N O T I C E

THIS DOCUMENT HAS BEEN REPRODUCED FROM MICROFICHE. ALTHOUGH IT IS RECOGNIZED THAT CERTAIN PORTIONS ARE ILLEGIBLE, IT IS BEING RELEASED IN THE INTEREST OF MAKING AVAILABLE AS MUCH INFORMATION AS POSSIBLE

Seasat Views Oceans and Sea Ice With Synthetic-Aperture Radar
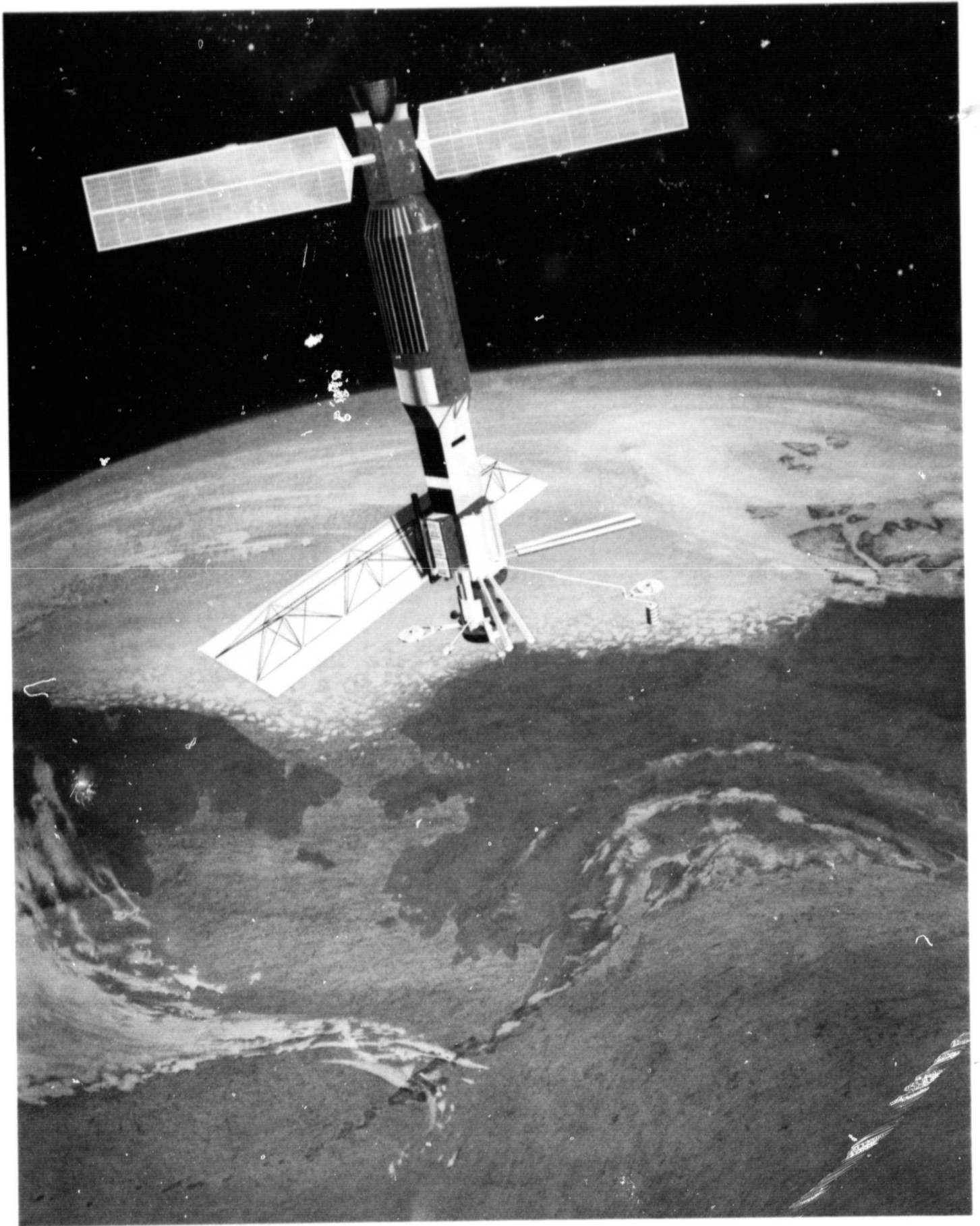
Lee-Lueng Fu
Benjamin Holt

February 15, 1982

NASA

National Aeronautics and
Space Administration

Jet Propulsion Laboratory
California Institute of Technology
Pasadena, California

Seasat Views Oceans and Sea Ice
With Synthetic-Aperture Radar

Seasat Views Oceans and Sea Ice With Synthetic-Aperture Radar

Lee-Lueng Fu
Benjamin Holt

February 15, 1982

Acknowledgements

Abstract

Fifty-one Seasat synthetic-aperture radar (SAR) images of the oceans and sea ice are presented to demonstrate the variety of information contained in this unique and extensive imagery. Forty-six are of the oceans, showing signatures of surface waves, internal waves, currents, mesoscale eddies, bottom topography, various coastal and atmospheric phenomena, and ships in the North Atlantic, the eastern North Pacific, the Gulf of California, the Gulf of Mexico, and the Caribbean. Five show various types of sea ice and its structural changes and drift motions in the Beaufort Sea area. Most images are presented with supportive illustrations, including observations made concurrently by other sensors on board Seasat or other satellites, weather maps, bathymetric charts, historical data, or the results of model calculations. The fundamental principles of a SAR and the characteristics of the Seasat SAR system and its images are briefly described. Maps showing the area covered by the Seasat SAR imagery, tables of key orbital information, and tables listing digitally processed SAR images are provided.

Contents

Figures

Image Locations

SAR Areal Coverage

Tables

CHAPTER 1
Introduction

Seasat, the first satellite dedicated to the use of microwave sensors for observation of the Earth's oceans, was launched on June 28, 1978, by the United States National Aeronautics and Space Administration; the project was managed by the Jet Propulsion Laboratory (JPL) of the California Institute of Technology. The satellite carried three microwave radars, one microwave radiometer, and one visible/infrared radiometer in a nearly circular orbit with an inclination angle of 108 degrees. Seasat circled the Earth 14 times a day at an altitude of 800 kilometers. On October 10, 1978, Seasat failed in orbit due to a massive short circuit in its electrical system. Fortunately, during most of its 105 days in orbit, Seasat returned a unique and extensive set of observations of the Earth's oceans. For more information about Seasat, the reader is referred to two series of articles: *Science* (1979) and *IEEE Journal of Oceanic Engineering* (1980).

One of the microwave radars on board Seasat was a synthetic-aperture radar (SAR). This instrument provided the first synoptic, high-resolution SAR images of the Earth's surface, including both the oceans and land; moreover, its operation was independent of the conditions of weather and sunlight. During its 98 days of operation, the Seasat SAR acquired images covering some 100 million square kilometers. This atlas is devoted to a description of the images of the oceans, including sea ice; the images of land areas have been compiled in a separate atlas by Ford et al. (1980).

Due to the high rate of data acquisition (~110 megabits per second), the SAR data were not recorded on board the satellite, but transmitted to the Earth and recorded on the ground. There were only five ground stations able to receive the SAR data, those at Goldstone, California; Fairbanks, Alaska; Merritt Island, Florida; Shoe Cove, Newfoundland, Canada; and Oakhanger, United Kingdom. Only when the SAR was in view of any of these receiving stations were its data received and recorded. Therefore, coverage of the oceans was limited to the North Atlantic, the Gulf of Mexico, the Caribbean, the

Mediterranean, the North Sea, the Norwegian Sea, the eastern North Pacific, the Gulf of California, and the Beaufort Sea.

Although the rationale for placing a SAR on board Seasat was its potential for monitoring the global surface wave field and polar sea ice conditions, the resultant images of the oceans revealed a much wider spectrum of oceanic and atmospheric phenomena, including internal waves, current boundaries, eddies, fronts, bathymetric features, storms, rainfalls, and windrows. Major aspects of the images have been discussed throughout the literature (e.g., Beal et al., 1981; Vesecky and Stewart, 1981; Teleki et. al., 1979; Apel, 1981; Gonzalez et al., 1981a; and Shuchman and Kasischke, 1979); however a comprehensive presentation of the images does not yet exist. This atlas is an attempt to bridge the gap. Its main purpose is to bring to the attention of the oceanographic community the wide variety of features seen in the images. Furthermore, we hope that, by introducing the images to this audience, the atlas will stimulate research on the mechanisms by which the SAR detects various ocean and ice features. Because most of these mechanisms are not yet well understood, quantitative interpretation of the SAR images is often lacking or inadequate, a problem that limits the value of a spaceborne SAR as a tool for the remote sensing of the oceans and sea ice. Some efforts toward solving this problem are found in Beal et al. (1981).

This atlas presents a number of representative SAR images of various natural and man-made phenomena occurring on the ocean surface and sea ice. The images were also selected to cover a wide range of geographic locations. While the number of images is limited, we tried on many occasions to give the reader a broader view with references to similar features on other images that are not included in this atlas.

Because of Seasat's premature failure, most surface experiments designed to validate interpretations of Seasat's observations were not carried out. Consequently, there is very little "surface truth" available for the interpretation of the SAR images. However, most images in this atlas are presented with illustrations that support the interpretative discussions that appear in the captions. The majority of these illustrations are drawn from observations made concurrently by other sensors on board Seasat or other satellites, weather maps, bathymetric charts, historical observations, or the results of model calculations. Some of these sources provide fairly convincing evidence, whereas others provide only plausible ideas. Therefore, most of our interpretations of the images are necessarily qualitative, and some can be considered only suggestive, not definitive.

Chapter 2 offers a brief introduction to the fundamental principles of a SAR and the characteristics of the Seasat SAR and its images. Chapter 3 presents 46 images of 9 categories of phenomena on the ocean surface. Chapter 4 presents 5 images of sea ice in the Beaufort Sea area. Of the 51 images, 13 were digitally processed and 38 were optically processed (see Chapter 2 for a discussion of the two kinds of processing). Appendix A provides maps showing the geographic areas depicted on the images. Appendix B is an index containing miscellaneous information about each of the images. Finally, to help familiarize the reader with the scope of the Seasat SAR images, Appendix C provides a series of index maps showing the coverage of all the Seasat images, tables of key orbital information, and tables listing digitally processed SAR images.

CHAPTER 2

Characteristics of the Seasat SAR
and Its Imagery

Of the five instruments on board Seasat, the synthetic-aperture radar (SAR) was the most complex. It had a data rate much higher than that of the others, its data required more complicated processing, and the interpretation of its data was less straightforward. Without some knowledge of the imaging system, however, one cannot fully understand the meaning of the resultant images. For this reason, we have devoted this chapter to a brief description of the Seasat SAR system.

2.1 The Principles of a Synthetic-Aperture Radar

A synthetic-aperture radar is a side-looking imaging radar operating on a moving platform. The radar transmits a series of short, coherent pulses to the ground (Figure 1) in a direction perpendicular to the flight path, producing on the ground a footprint whose size is inversely proportional to the antenna size. The image resolution in the range (across-track) direction, denoted by d_r, is determined by the effective pulse width, τ:

$$d_r = c\tau/2 \sin \theta \qquad (1)$$

where c is the speed of light and θ is the incidence angle of the radar pulse. Thus, a higher resolution in the range direction requires a shorter pulse width, which in turn requires a larger transmittal bandwidth and peak power. Range resolution, then, is ultimately limited by the available transmittal bandwidth and peak power. This limitation can be alleviated, as it was with Seasat, by the use of pulse compression techniques. Instead of the short pulses required by a specified resolution, longer pulses that change frequencies linearly with time
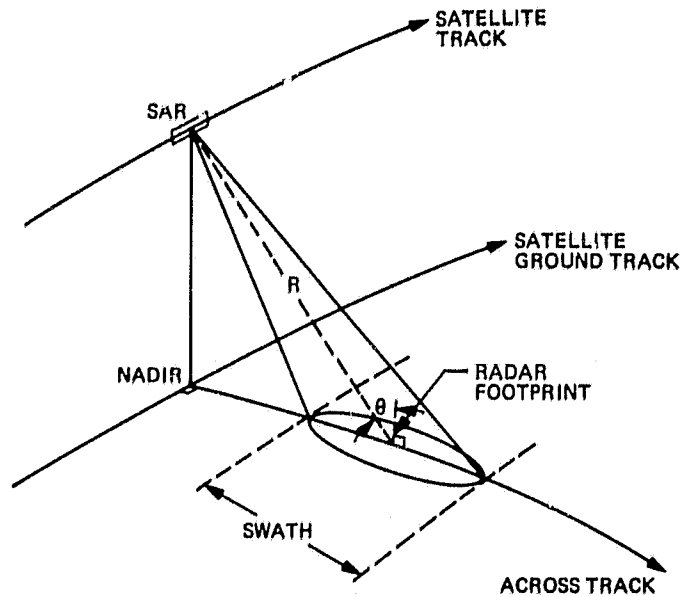
Figure 1. Seasat SAR imaging geometry.

over a bandwidth B (the chirp signals) can be used. Upon processing the received signals, the pulses can be compressed to obtain the desired resolution using matched filter techniques (Hovanessian, 1980). The ratio of the transmitted pulse width to its compressed value is simply τB (time-bandwidth product).

For a real-aperture radar, the resolution in the azimuthal (along-track) direction, denoted by d_a, can be written as

$$d_a = \frac{1}{2} \frac{R\lambda}{D} \tag{2}$$

where R is the distance between the radar and the target (slant range), λ is the radar wavelength, and D is the length of the radar aperture in the along-track direction. For a radar in space, the azimuthal resolution is then severely limited by the large value of R. This limitation can be alleviated by the concept of a synthetic aperture (e.g., Harger, 1970; Tomiyasu, 1978). The basic idea is the following: any particular target is illuminated by the radar beam for a finite time period, T, and

$$T = L/v \tag{3}$$

where v is the speed of the platform and L is the along-track dimension of the footprint (the azimuthal beamwidth) which can be written as

$$L = \frac{R\lambda}{D} \tag{4}$$

During this time period, the radial (slant-range) component of the spacecraft's velocity relative to the target is constantly changing, yielding a time-dependent Doppler shift in the frequency of the return pulses. This "Doppler phase history" can then be used to distinguish between targets within the same

4

footprint through a processing procedure similar to that used in the range processing. Thus the target's illumination is equivalent to that from a synthetic aperture of length vT, which is simply L. The resulting azimuthal resolution can be obtained from Equation (2) with D replaced by L, i.e.,

$$d_a = \frac{1}{2} \frac{R\lambda}{L} = \frac{1}{2} R\lambda \frac{D}{R\lambda} = \frac{D}{2} \qquad (5)$$

Therefore the azimuthal resolution is independent of the platform altitude and is dependent on only the antenna size — a unique advantage of SAR. However, the price paid is a complicated and time-consuming data processing procedure.

The processing of SAR data may be either optical or digital. For optical processing (e.g., Goodman, 1968; Harger, 1970; Rihaczek, 1977), the raw returning signal must be first recorded on photographic film. The resulting "signal film" is best described as a radar hologram on which the imaged targets are represented by overlapping Fresnel zone plates. To produce images, the signal film is illuminated by a laser beam which, through a complicated optical system, brings the radar hologram into focus on a plane where the images are formed to create an "image film." Alternatively, SAR imagery can be produced by a digital method that is equivalent to these optical manipulations (e.g., Wu, 1980). With more control of the data, the digital method produces images of generally better quality, but at a higher cost and a lower throughput rate, than the optical method. A comparison of the Seasat images processed by these two methods is presented in Section 2.3.

2.2 Characteristics of the Seasat SAR System

A detailed description of the Seasat SAR system can be found in Jordan (1980). Only a brief summary is given here; Table 1 summarizes the major characteristics of the system, Figure 2 is a sketch of the satellite showing the locations of different sensors, and Figure 3 is the functional block diagram.

Table 1. Characteristics of the Seasat SAR

Parameter	Value
Satellite altitude	800 km
Radar frequency	1.275 GHz
Radar wavelength	23.5 cm
System bandwidth	19 MHz
Theoretical resolution on the surface	25 m X 25 m
Number of looks	4
Swath width	100 km
Antenna dimensions	10.74 m X 2.16 m
Antenna look angle	20° from vertical
Incidence angle on the surface	23° ± 3° across the swath
Polarization	HH
Transmitted pulse length	33.4 μs
Pulse repetition frequency (PRF)	1463 to 1640 pps
Transmitted peak power	1000 W
Time-bandwidth product	634
Data recorder bit rate (on the ground)	110 Mbits/s (5 bits per word)

BUS

SOLAR ARRAY

FLIGHT PATH

TELEMETRY, TRACKING AND COMMUNICATION ANTENNA No. 2

SCATTEROMETER ANTENNAS

SYNTHETIC-APERTURE RADAR ANTENNA

SENSOR MODULE

TELEMETRY, TRACKING AND COMMUNICATION ANTENNA No. 1

MULTICHANNEL MICROWAVE RADIOMETER

VISIBLE-INFRARED RADIOMETER

LASER RETROREFLECTOR

SAR DATA LINK ANTENNA

ALTIMETER
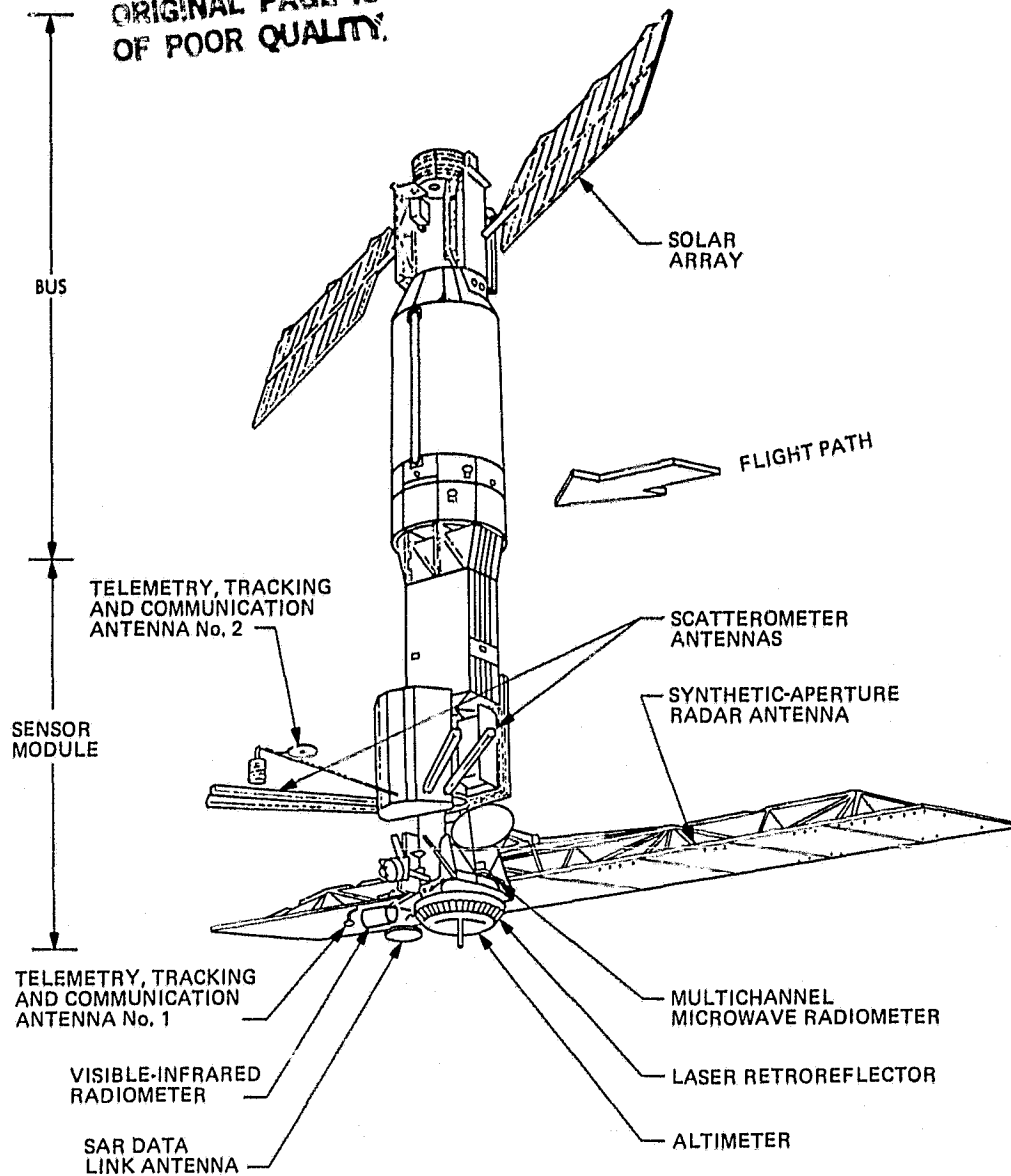
Figure 2. Seasat bus and payload configuration.

The radar antenna was a phased array system composed of eight mechanically deployed, electrically coupled, flat microstrip honeycomb panels (Figure 2). The antenna beam was centered at a boresight angle of 20 degrees from the nadir and had a beamwidth of 6.2 degrees in elevation; the beam illuminated a 100-kilometer swath that extended from 240 to 340 kilometers to the right of the spacecraft's ground track. To reduce the peak power required to achieve the specified range resolution, a chirped pulse with a bandwidth of 19 megahertz and a compression ratio of 634:1 was used.

A sensitivity time control (STC) device was incorporated in the receiver to compensate for the variation of the antenna gain with the elevation angle. The output of the receiver was sent directly to an analog data link along with the information on timing and reference frequencies.
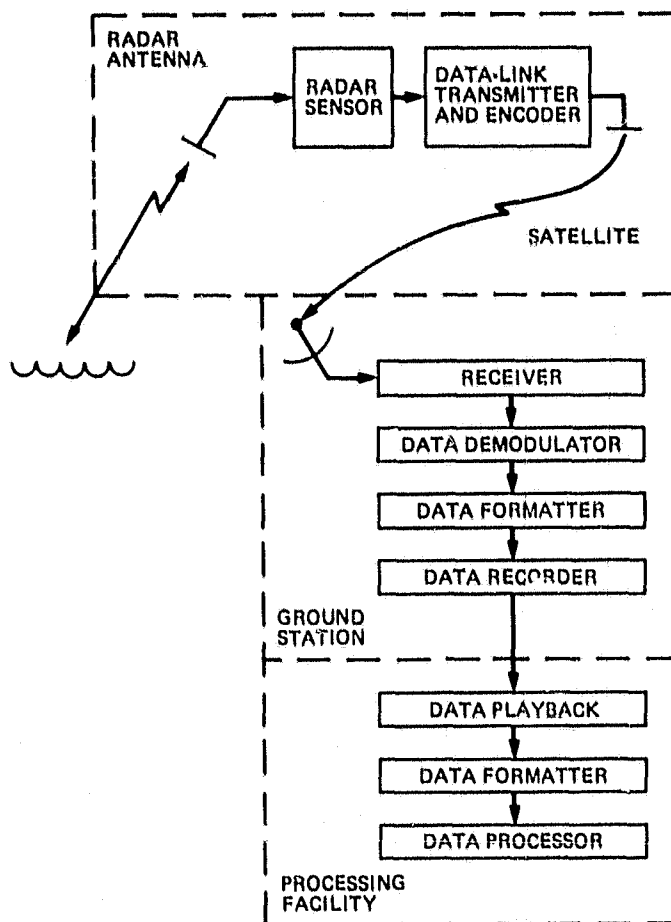
Figure 3. Seasat SAR system functional block diagram.

The data link translated the received L-band (1.275-gigahertz) signals to S-band (2.265-gigahertz) signals, orthogonally combined the offset video with both PRF and reference frequencies, linearly amplified the result, and transmitted the resulting signal to the ground.

After reception by a ground station of the data-link system, the signal was down converted and coherently demodulated with a reference signal to produce a video signal with frequencies from 2 to 21 megahertz. Concurrently, the link-induced Doppler shift was removed and the PRF and the spacecraft reference signal were both recovered. The signal was then digitized, formatted, and recorded on a high-density digital tape (HDDT) at a rate of about 110 megabits/second.

Most of the available SAR data have been processed optically; only limited data have been processed digitally. Characteristics of the images processed by both methods are described in the next section.

2.3 Characteristics of the Seasat SAR Images

The image characteristics and quality parameters that are most important for a qualitative interpretation of the SAR imagery of the ocean surface and ice are discussed below. Further information on the radiometric performance (e.g., contrast ratio, dynamic range, and amplitude transfer function), which is important for a more quantitative analysis, is given in Huneycutt et al. (1981).

2.3.1 Image Format

Optical image. The SAR 100-kilometer swath was divided into four subswaths to accommodate limitations in the processing of optical images at JPL. The data for each subswath were processed separately and recorded on 70-millimeter film. Each subswath film strip covers an area about 30 kilometers wide and overlaps the adjacent subswath by 6 to 7 kilometers. The length of a film strip usually covers a whole recorded pass, which varies from 800 to 4000 kilometers. An example mosaic of four subswath film strips is shown in Figure 4. Note that an across-track gradient of image brightness resulting from processor peculiarities is present in each subswath, causing a discontinuity in image

ILLUMINATION
DIRECTION →

N

0   20 km
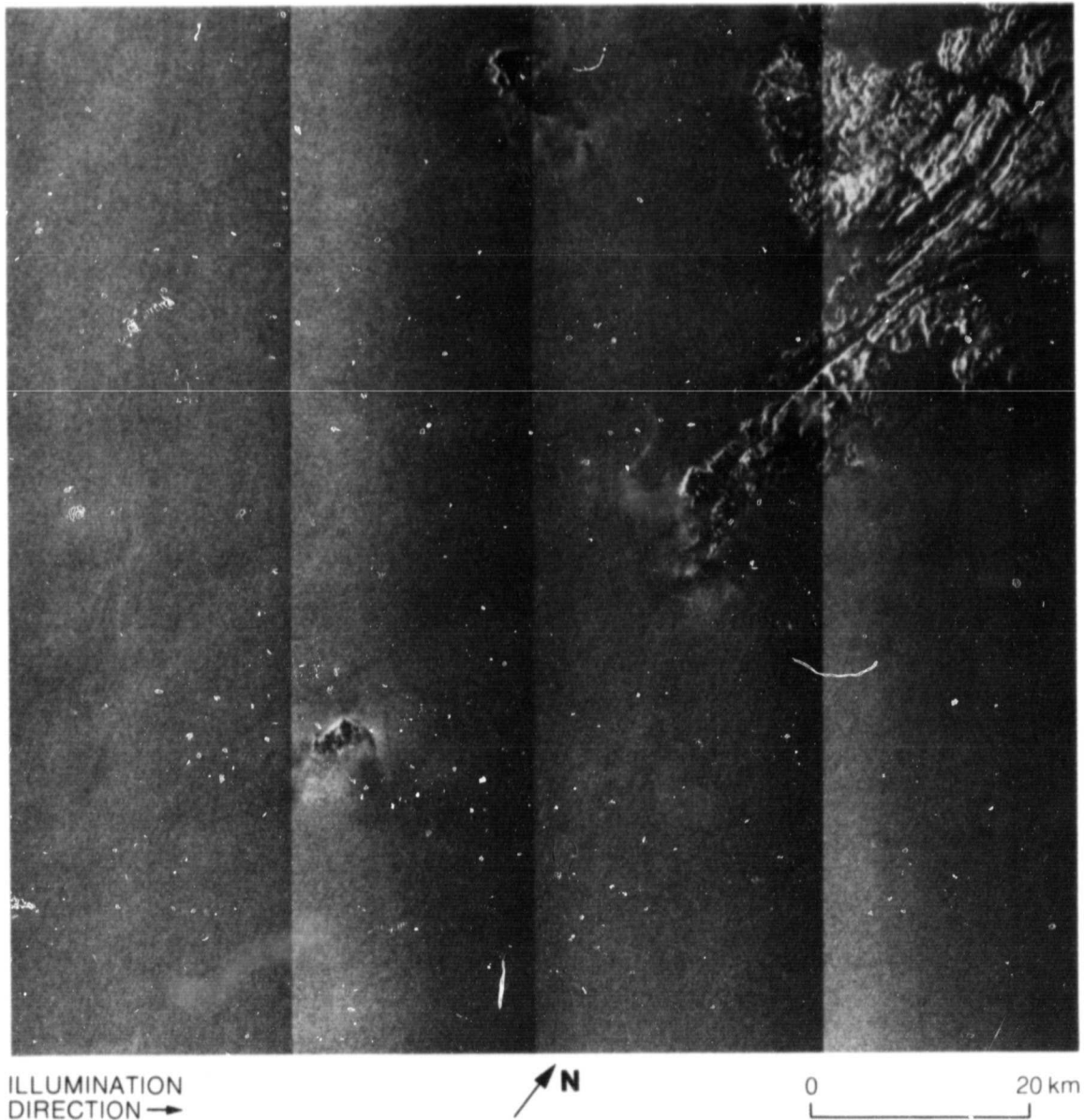
Figure 4. Optical image taken south of Shetland Island (upper right) and about 360 kilometers north of Scotland. The image center is at 59° 55′N and 2° 36′W (Rev. 1149; 0823 GMT, September 15, 1978).

brightness across the subswaths. The dots at the edges of each strip are timing marks representing a one-second flight distance on the ground — about 6.67 kilometers. Interesting features on this image are ocean waves traveling from west to east. Patterns of wave refraction/diffraction around the islands are well detected.

Digital image. Displayed in Figure 5 is the digital image of the scene shown in Figure 4. Digital images processed at JPL have a fixed 100-kilometer × 100-kilometer area format. Due to the Earth's rotation, the shape of the

ILLUMINATION
DIRECTION →

N

0   20 km
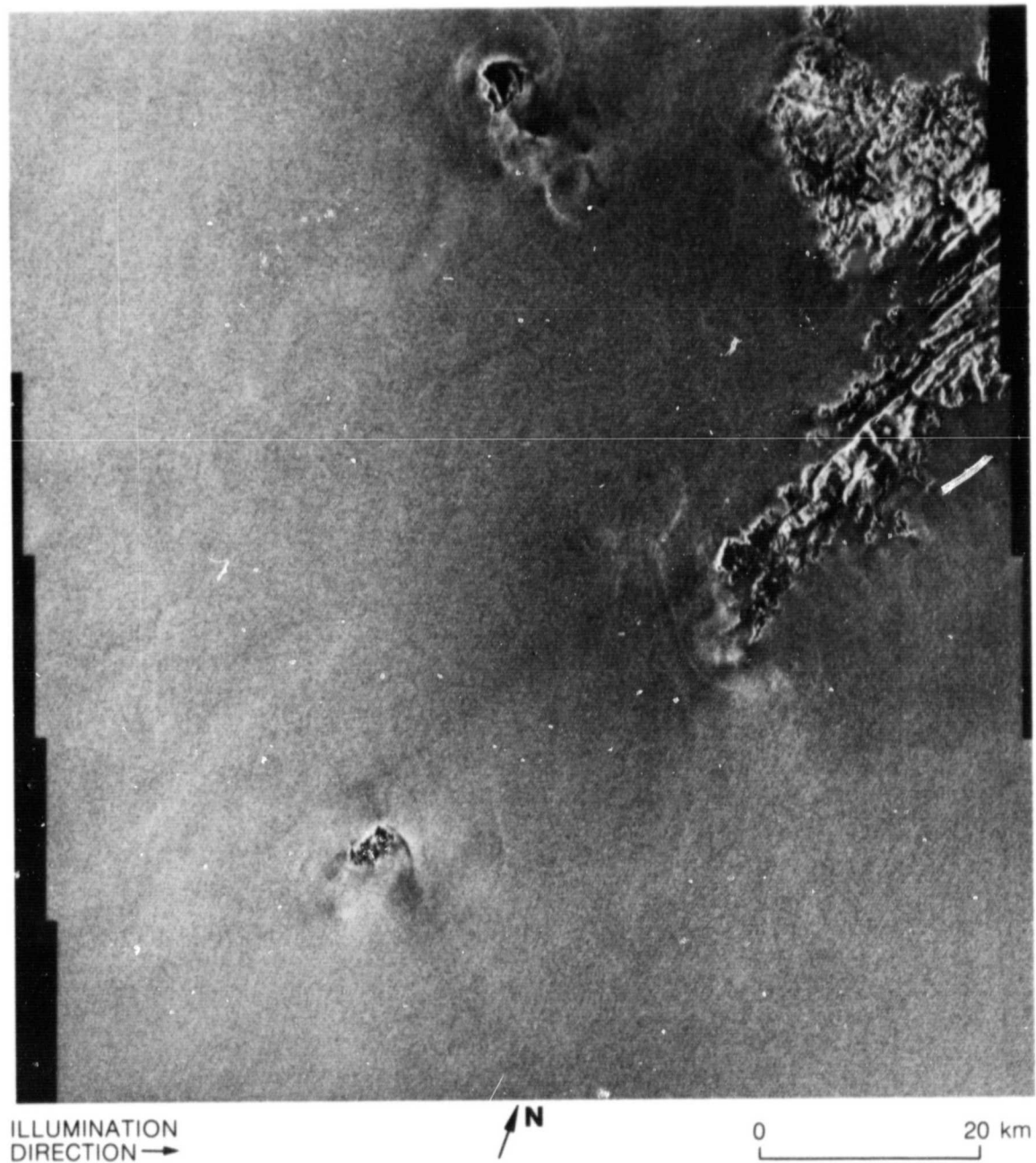
Figure 5. Digital image of the Figure 4 scene.

image is a parallelogram instead of a square. This is a common characteristic of all line-scanning sensors that view a laterally moving target (e.g., imagery of the Landsat multispectral scanner). The stepped edges parallel to the flight track are the result of special processing to correct for the distortion induced by the Earth's rotation (Wu et al., 1981).

2.3.2 Geometric Distortion

Because the across-track dimension of a target is detected by a SAR through its projection on the slant-range axis (the line connecting the target and the radar), the geometry of the SAR imagery is distorted in the across-track direction. As illustrated in Figure 6, the three targets A, B, and C have the same across-track dimensions on the ground, but have different projections (A′, B′, and C′) on the slant-range axis, with more compression occurring in the near range than in the far range. A straight line and a circle on the ground, then, will appear on the image as a curve and a distorted ellipse, respectively, as shown in Figure 6. This distortion is not corrected in the digital images now produced at JPL; however, it has been partially corrected in the optical images in such a way that the range-azimuth aspect ratio is maintained as unity at the center of each subswath. The resulting variation of pixel size in the range direction is about 25 percent for digital images and about 7 percent for optical images.
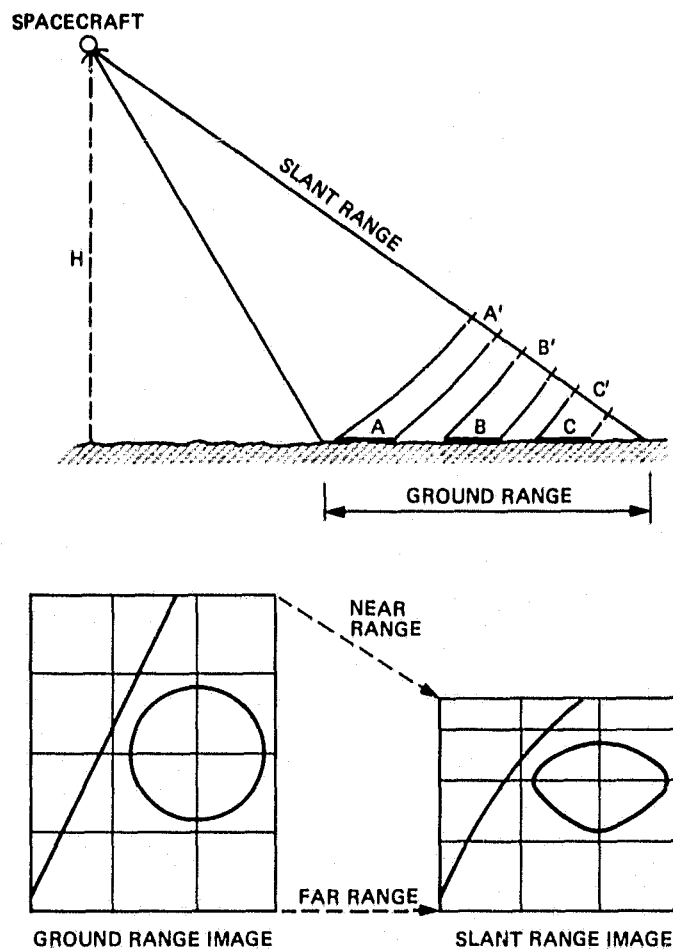
Figure 6. Geometrical distortion in the slant-range imagery.

2.3.3 Resolution

The specified resolution for the Seasat SAR was 25 meters in both range and azimuth. The current JPL digital processor is able to achieve this resolution; however, routinely processed images may have a resolution slightly worse than 25 meters due to errors in estimating the SAR processing (focusing) parameters. The resolution of routinely processed optical images is about 40 meters in both range and azimuth.

2.3.4 Image Location

The location of an image is very important for ocean studies. The location of an ocean optical image from a filmstrip that includes some landmarks can be estimated with an error of about 2 kilometers by using high-precision maps and spacecraft ephemeris data. An ocean optical image from a filmstrip without any landmarks can easily suffer a location error greater than 10 kilometers. Curlander and Brown (1981) have recently developed an algorithm that uses the spacecraft ephemeris along with the characteristics of the SAR system and the digital processing algorithm to obtain the location of digital images with an error of only a few hundred meters.

2.3.5 Speckle Effect

Because SAR is a coherent imaging system, the surface roughness at the scale of the radar wavelength produces a random interference pattern in the resulting image. This is why SAR images always look noisy. This speckle effect can be reduced by applying the technique of multiple-look processing. That is, several independent images of the same area, which are produced by using different portions of the synthetic aperture, are averaged together to produce a smoother image. The price paid, however, is degraded resolution. The number of independent images being averaged is usually called the number of looks. The size of a resolution cell is directly proportional to the number of looks. Because the two orthogonal components of the electric field of the return echoes are the sums of a large number of random variables, their probability distributions are Gaussian as the result of the Central Limit Theorem. Thus the speckle intensity of an N-look image has a chi-squared distribution with $2N$ degrees of freedom, with its standard deviation proportional to $1/\sqrt{N}$. Both the optical and digital images processed by JPL are four-look images: the resolution cell is four times larger than, and the speckle intensity is one-half that of a one-look image.

CHAPTER 3
Seasat SAR Images of Oceans

For a radar with an incidence angle of 23 degrees such as the Seasat SAR, backscatter from the ocean surface is produced predominantly by the Bragg resonant scattering mechanism (e.g., Valenzuela, 1978). That is, the surface waves traveling in the radar range direction with a wavelength of $\lambda/(2 \sin \theta)$, the "Bragg resonant waves," account for most of the backscattering, where λ is the radar wavelength and θ the incidence angle. For Seasat, the Bragg resonant waves are short gravity waves with a wavelength of 30 centimeters. What the SAR sees on the ocean surface is primarily the variation of these waves. Therefore, any phenomenon able to produce modulation in these waves is presumably detectable by the SAR. As demonstrated in the following nine sections, various features on the SAR imagery of the ocean surface can be identified with a wide spectrum of oceanic, atmospheric, and man-made phenomena.

3.1 Surface Waves

A major objective of the Seasat SAR was to explore its potential for monitoring from space the global ocean surface wave field, a field important for ship routing and offshore operations. Experience with airborne SAR had confirmed the ability of the radar to image the dominant ocean surface waves (Brown et al., 1976; Shemdin et al., 1978). A spaceborne SAR, however, needs a longer time (~2.3 seconds for Seasat) to synthesize its aperture than does an airborne SAR (generally less than 1 second); the spaceborne SAR, therefore, has an increased sensitivity to wave orbital motion. The influence of surface motion thus became an important concern in evaluating the Seasat SAR performance. During the 98-day period of operation of the Seasat SAR, several surface experiments — GOASEX (Gonzalez et al., 1979), JASIN (Vesecky, Assal, and Stewart, 1981), and DUCK-X (Beal, 1980) — confirmed the general ability of the Seasat SAR to detect the dominant ocean surface waves.

These experiments indicate that waves with a wavelength greater than 100 meters can be detected by the Seasat SAR under the condition that the significant wave height ($H_{1/3}$) exceeds 1 meter and the surface wind speed (U_{10}) exceeds 2 meters per second. Comparisons between satellite and surface observations indicate that the agreement is within about 15 percent in wavelength and about 25 degrees in wave direction. It has also been found that waves with a direction perpendicular to the satellite flight path (range waves) are generally more easily detected by SAR than are waves with a direction parallel to the satellite flight path (azimuthal waves).

The exact mechanisms by which surface waves are imaged by a SAR are not well understood yet. For a review of the recent progress on this subject the reader is referred to the paper by Vesecky and Stewart (1981), in which the following three mechanisms are extensively discussed:

(1) The sea-surface tilt caused by the long waves produces periodic variations in the local incidence angle, thus yielding modulation in the scattering cross section of short waves that backscatter the radio waves (the "tilting effect").

(2) The divergence of the surface velocity field due to long waves produces modulations in the height of the short waves (the "straining effect").

(3) The radial component (parallel to the line of sight) of the orbital motion of long waves produces a periodic azimuthal target displacement (the "velocity bunching effect").

The effects of both the first and second mechanisms are maximum for range waves and minimum for azimuthal waves, and vice versa for the third mechanism. These three mechanisms are by no means exhaustive; another mechanism of potential effect is the modulation by long waves of breaking short waves. The relative importance of the various mechanisms in wave imaging is still a subject of controversy and currently under intensive studies. It is anticipated that the results of the Maritime Remote Sensing Experiment (MARSEN), which will soon begin to appear, will shed some light on this subject.

By whatever mechanisms, long ocean surface waves were imaged by the Seasat SAR under a variety of weather conditions and sea states. Owing to its long swath, typically of several thousand kilometers, the Seasat SAR has provided for the first time information on the ocean surface wave field on a synoptic scale, offering a unique opportunity to study the generation and propagation of long ocean waves in the open ocean. For example, Beal (1981) demonstrated that by using the imagery of a spatially varying wave field in the North Atlantic Ocean, one could trace the storm center that had generated those waves, thus providing valuable information on how a swell would evolve from a typical extratropical cyclone. Gonzalez et al. (1981b) used the SAR imagery to study the wave generation by a hurricane in the eastern North Pacific. Shuchman and Kasischke (1981) demonstrated that SAR imagery could be used to study the refraction of a deep ocean swell by shoaling topography in a coastal area, a major concern of coastal engineers. These are just a few examples showing the potential of a spaceborne SAR in advancing our knowledge of ocean surface waves.

Following are five selected images showing the salient features of the surface waves observed by the Seasat SAR. Image 1 is chosen to illustrate the general detectability of the dominant surface waves propagating in an oblique direction with respect to the flight path. Image 2 shows the detectability of azimuthal waves. Image 3 shows nicely the dependence of SAR's ability to detect long waves on the existence of a wind field capable of generating short Bragg resonant waves. The spatial variation of the dominant wave field under a hurricane is illustrated in Image 4. Finally, the wave refraction patterns near islands and shoaling shelves are illustrated in Image 5.

1. Wave Travel Oblique to the Flight Path
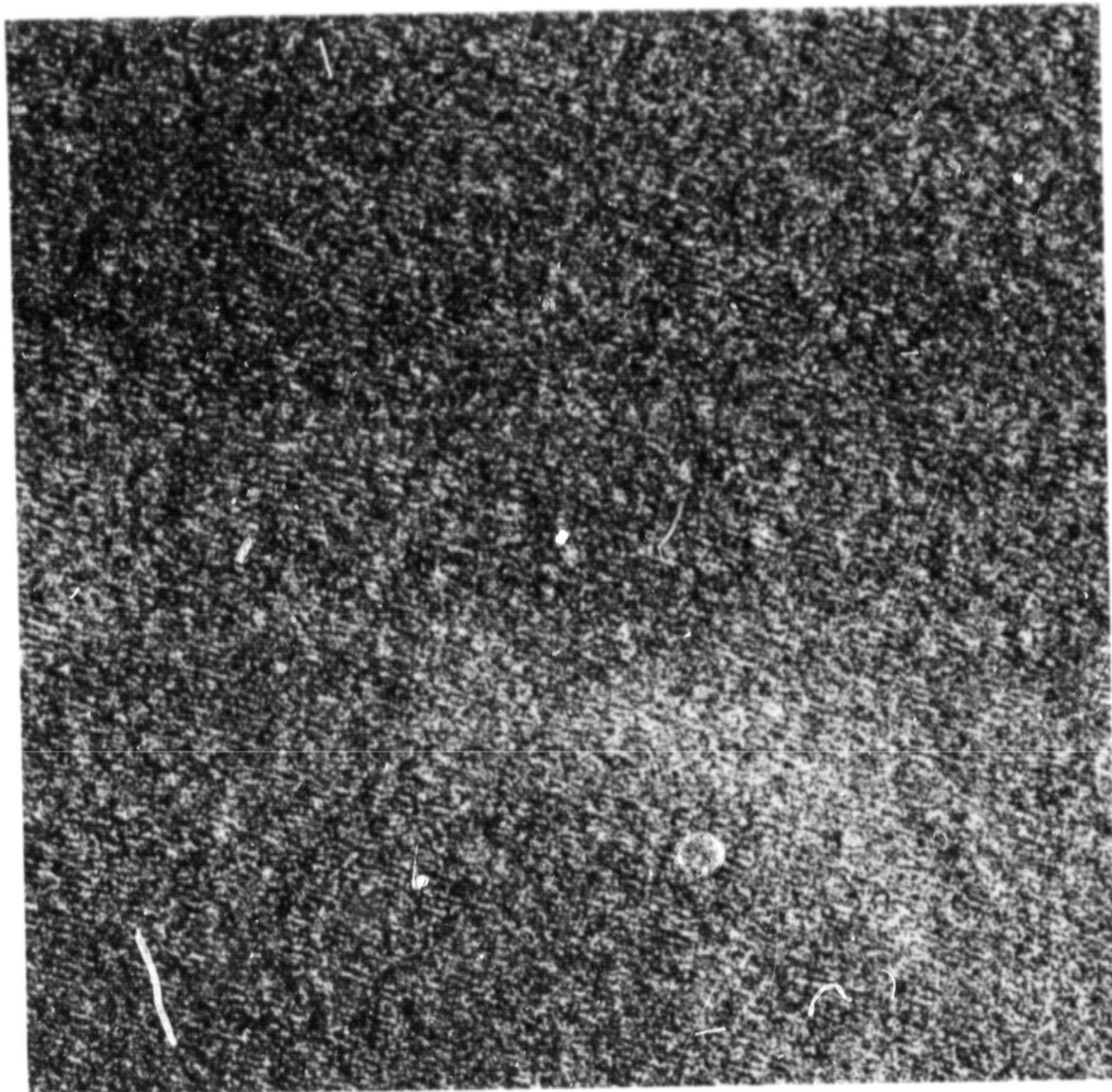
ILLUMINATION DIRECTION

N

0   5 km

This image of the North Atlantic Ocean, about 400 kilometers northwest of Scotland (59°N, 12.5°W), was taken where extensive surface observations were being made at the time of the Seasat overpass. These surface measurements were part of the Joint Air-Sea Interaction Experiment (JASIN, see Pollard, 1978).

During this overpass, the surface observations indicated a wave train moving in the direction of 50 degrees clockwise from true north, with a wavelength of 152 meters and a height ($H_{1/3}$) of 3 meters. The extensive linear striations on the image are thus manifestations of this wave train.

Graph (a) is the two-dimensional wave number spectrum[1] of the image intensity averaged over all directions. The dominant wavelength at the spectral peak is about
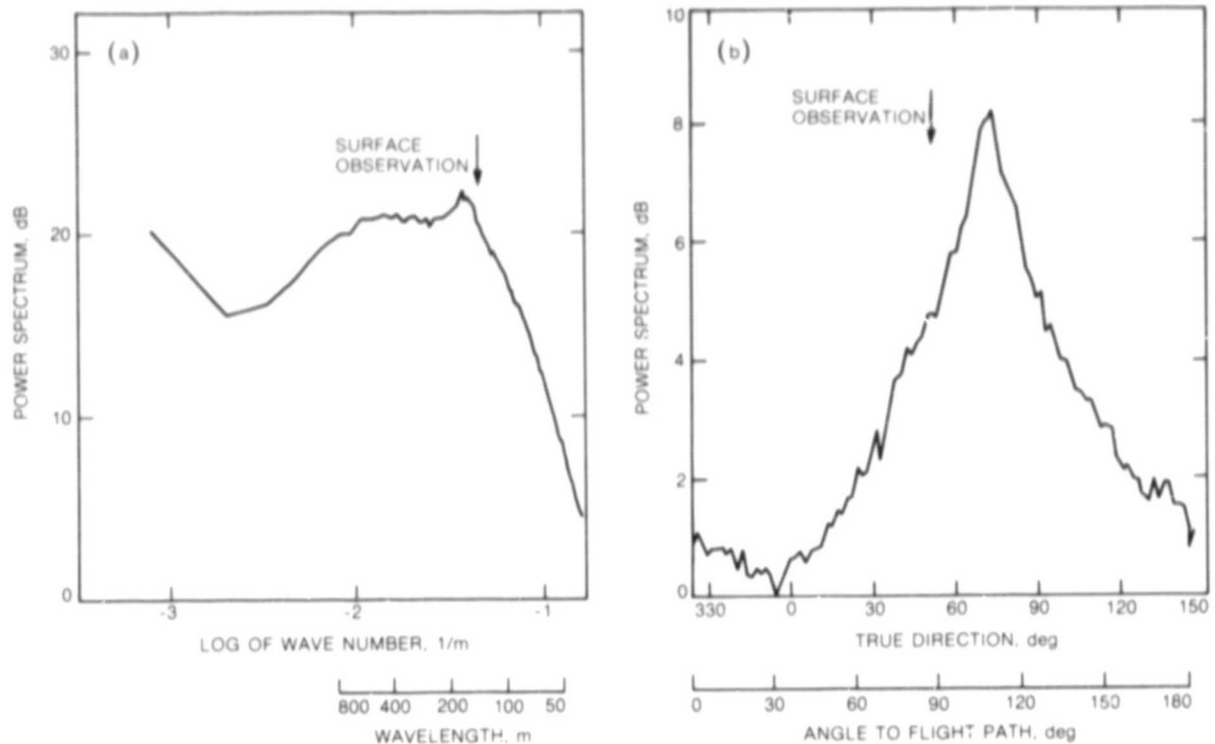
Spectra of the image intensity: (a) omnidirectional (surface observation was obtained by waverider buoys); (b) directional.

170 meters—slightly longer than that observed at the surface. Graph (b) is the directional spectrum[1] of the image averaged over a wavelength interval from 125 meters to 250 meters. The spectral peak is centered at 73 degrees clockwise from true north, with a half-power width of about 40 degrees.

The differences in wavelength and direction between satellite and surface observations are similar to the results of GOASEX (Gonzalez et al., 1979). The substantial directional spread can be seen on the image as the waviness of the crests, indicating that these waves were probably a locally generated wind sea rather than a swell. In fact, the North Atlantic Ocean north of 40°N was then dominated by a northeastward traveling storm, which reached its peak intensity on August 17 and 18 when winds of over 25 meters per second were reported some 1000 kilometers west of the JASIN area. On August 21, this storm had already passed the JASIN area and was about 700 kilometers north of it. The reported local winds were toward 55 degrees clockwise from true north with a speed of 13 meters per second, which is about the wind speed needed to generate a fully developed sea with a dominant wavelength of 150 meters.

(Rev. 791; 0725 GMT, August 21, 1978.)

2. Wave Travel Parallel to the Flight Path
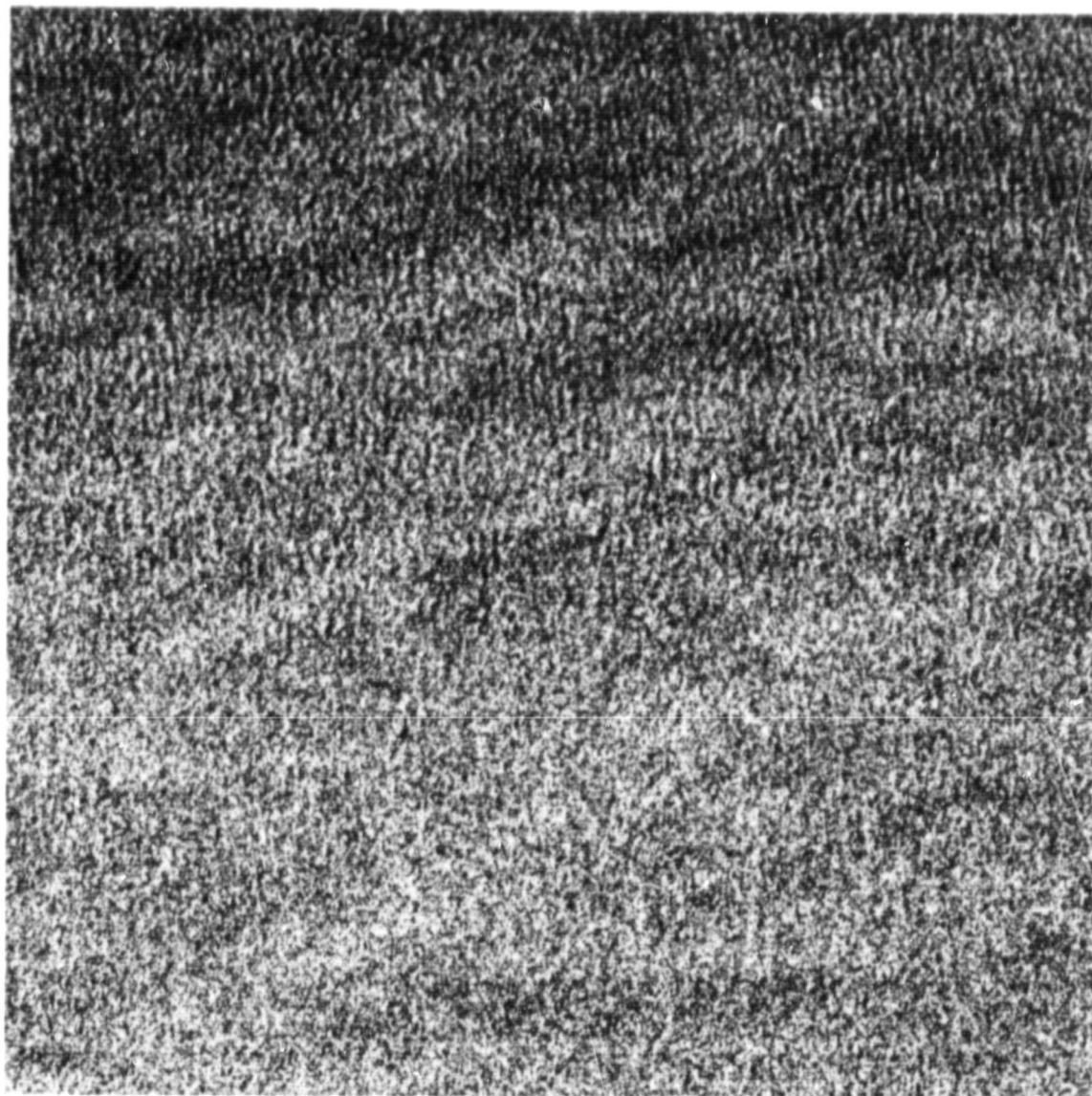
ILLUMINATION
DIRECTION

N

0   5 km

Waves traveling parallel to the flight path (azimuthal waves) are generally less detectable on SAR images than waves traveling in other directions, mainly because the effects of both tilting and straining, which are important imaging mechanisms for long waves, are least effective in this situation. However, the velocity bunching effect caused by the orbital motion of the long waves (Alpers and Rufenach, 1979) is most effective for azimuthal waves, so it is probably due to this effect that azimuthal waves have been occasionally detected by SAR.

This image shows such an example of waves traveling predominantly in the azimuthal direction in the Pacific Ocean about 100 kilometers west of Baja California, Mexico. Two wave trains in slightly different directions can be seen. The optical Fourier transform of this image (cf. Seasat Gulf of Alaska Workshop II Report, 1980) indicates that these two wave trains have roughly the same wavelength (about 225 meters), and

o   1200 GMT LOCATION AND DATE
●   0000 GMT LOCATION
• • •   TROPICAL DEPRESSION STAGE
– – –   TROPICAL STORM STAGE
———   HURRICANE STAGE
x x x x x   DISSIPATING STAGE
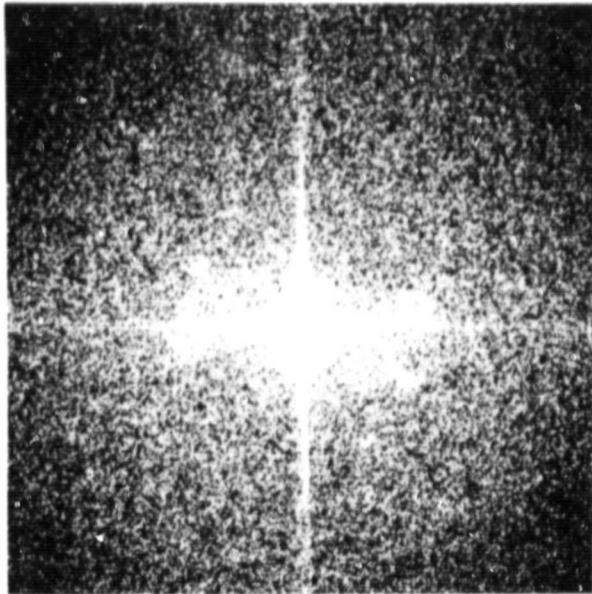
WAVELENGTH, m

Two-dimensional Fourier transform of Image 2 obtained by optical method. Horizontal axis is parallel to the flight path.
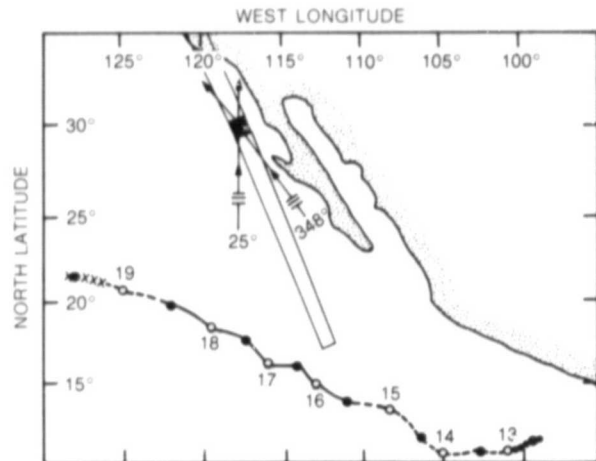
Path history of hurricane Gilma and the SAR swath. The image location is the black square, and the arrows represent wave directions.

propagate in directions of 348 degrees (or 168 degrees) and 25 degrees (or 205 degrees) clockwise from the flight direction. The 180-degree ambiguity of the wave directions can be resolved by considering the location of their source—hurricane Gilma, whose path history is shown on the chart (from Gunther, 1979). Apparently both wave trains were generated by this hurricane and propagated northward to the image site. The 348-degree waves were generated during the tropical storm stage of Gilma, while the 25-degree waves were generated after Gilma became a hurricane on July 16.

(Rev. 308; 1316 GMT, July 18, 1978.)

3. Waves Under a Spatially Variable Wind Field

ILLUMINATION
DIRECTION

N

0   5 km

To be seen by a SAR, long waves must modify the backscatter cross sections of those short capillary/gravity waves that satisfy the Bragg resonance condition of the incident electromagnetic waves. Because these short waves (wavelengths of a few tens of centimeters) are tightly coupled to the local winds, the presence of local winds with certain strength is thus essential to the detectability of long waves.

This image, taken at about 400 kilometers southwest of Vancouver Island, Canada, clearly illustrates the effect of wind on wave detectability. An eastward propagating swell (from open ocean to shore) with a wavelength of about 220 meters can be seen in the bright areas where the sea surface is roughened by local winds, while most of the swell signatures disappear in the dark areas where the sea surface appears smooth. The swell existed in the smooth areas as well, of course, but it was simply not detected by the SAR. The weather map shows conditions that existed about two hours before
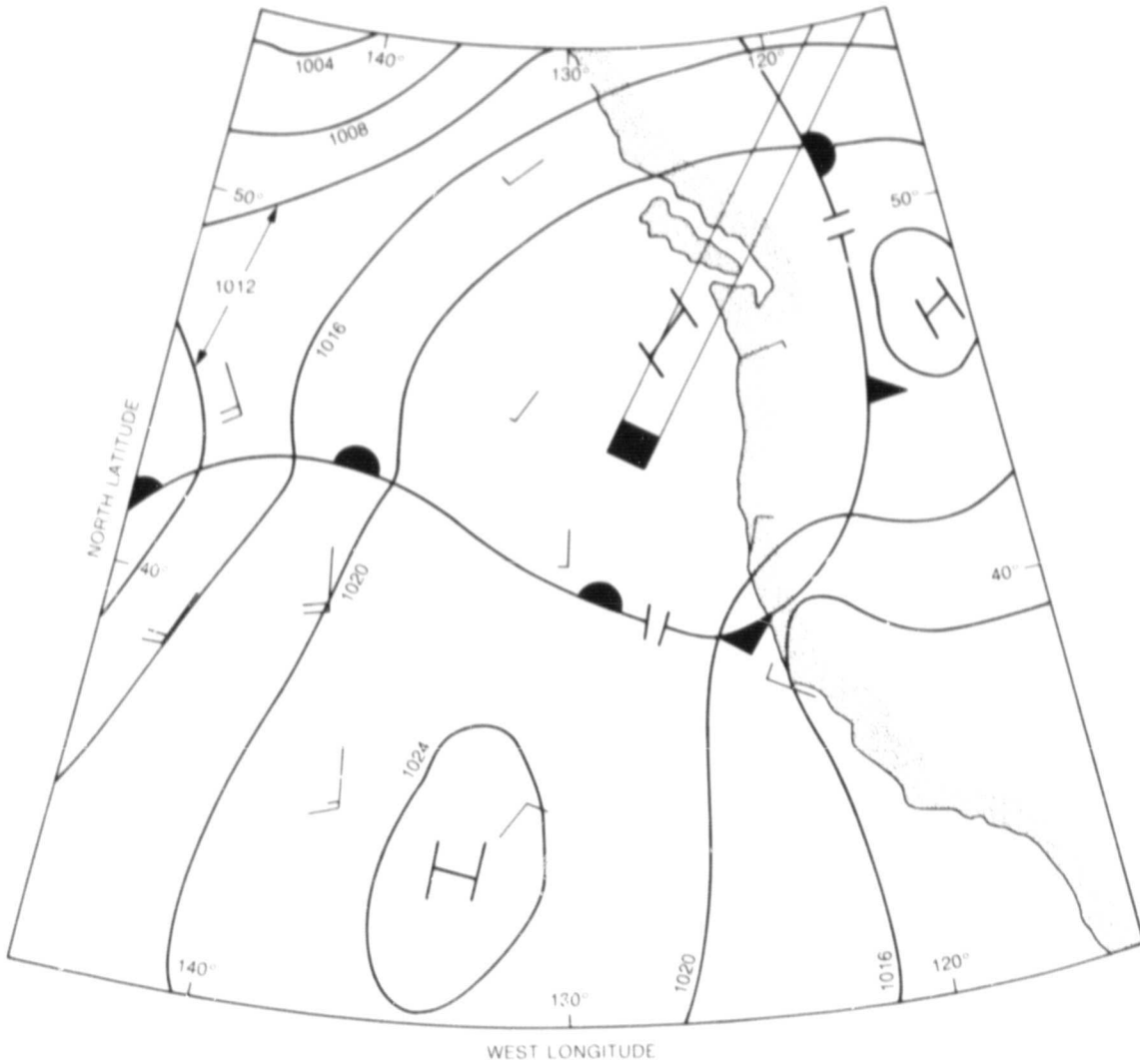
SAR swath superimposed on the surface weather chart of 0600 GMT, September 29, 1978. The image location is the black square.

this overpass; a light southerly wind field with a speed of about 2.5 meters per second was reported in this region. Data from the Seasat scatterometer also show a wind field with similar speed.

(Rev. 1349; 0834 GMT, September 29, 1978.)

4. Waves Generated by a Hurricane
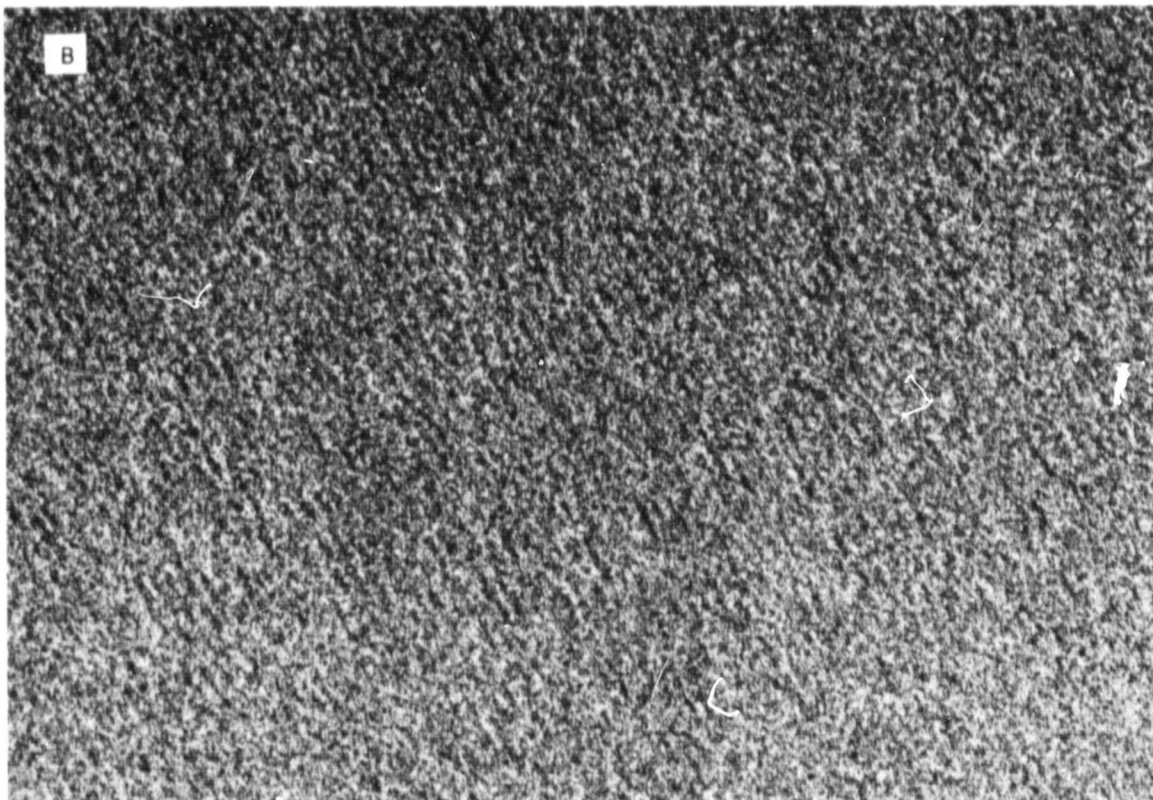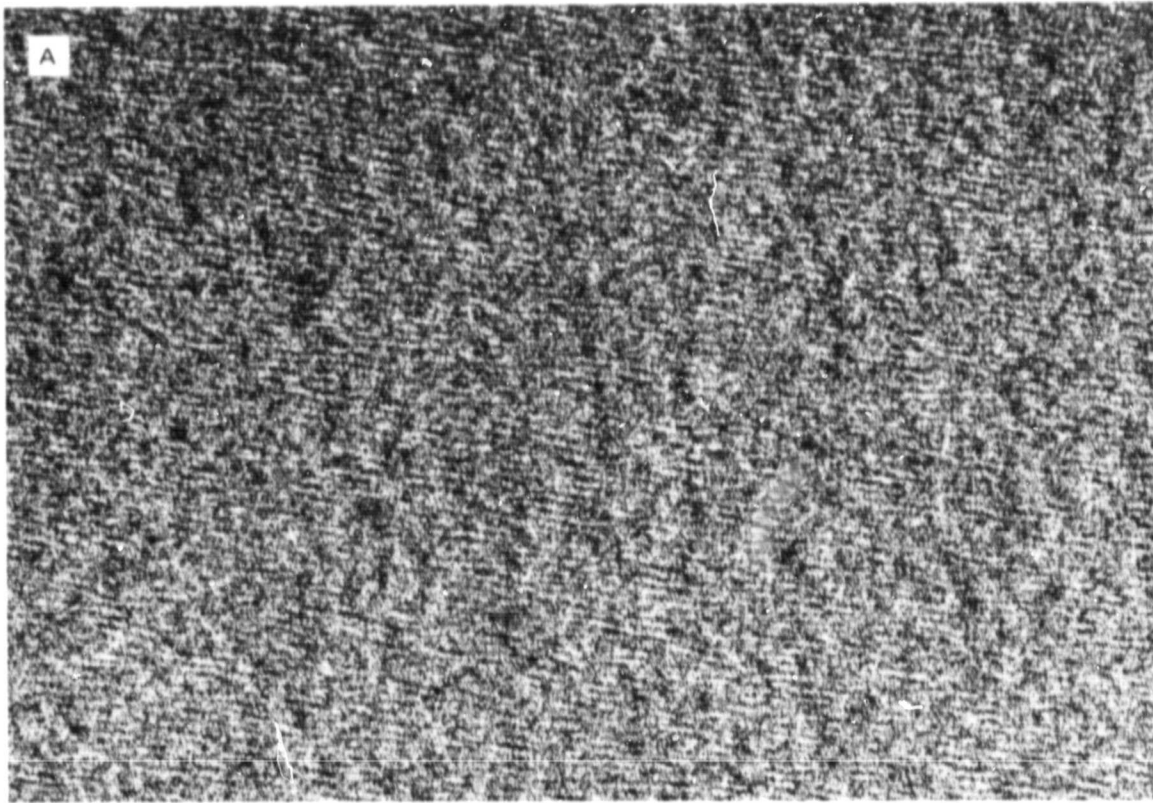
ILLUMINATION
DIRECTION

N

0   5 km
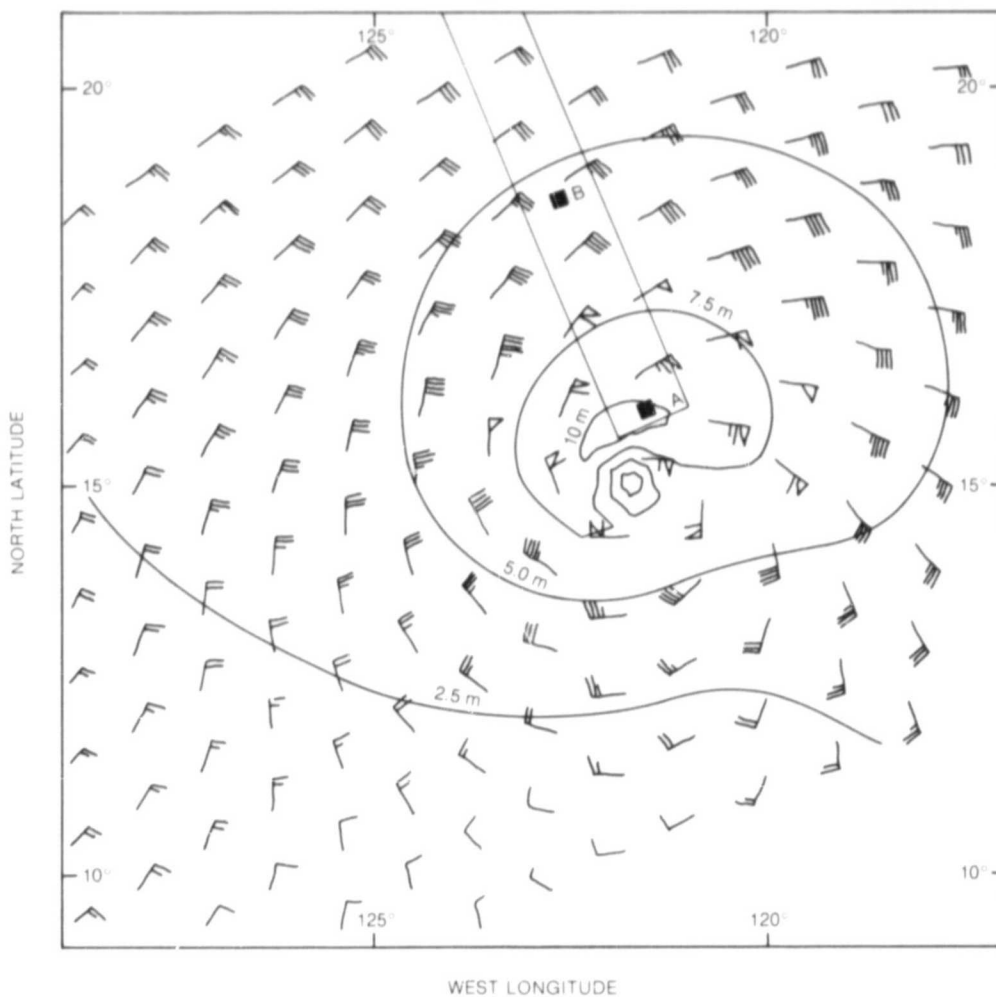
SAR swath superimposed on a chart of surface winds and significant wave height contours under hurricane Fico (from Teleki et al., 1979). The image locations are the black squares A and B.

As Seasat flew over hurricane Fico in the northeastern tropical Pacific Ocean, its SAR swath fell within 100 kilometers of the hurricane's center. Above, the SAR swath is superimposed on a chart of surface winds and significant wave heights; the chart was synthesized from models of hurricane winds and waves (Cardone et al., 1977; Ross and Cardone, 1978). The hurricane's center was moving westward at a speed of about 22 kilometers per hour.

Waves with different wavelengths and directions can be seen on the two images of the two areas indicated on the chart as A and B. Waves in area B were propagating northwestward with a wavelength of about 280 meters while waves in area A were propagating to the west-southwest with a shorter wavelength of about 165 meters. Although the large orbital velocities associated with high waves tend to degrade image resolution (Alpers and Rufenach, 1979), these images indicate that waves with heights greater than 5 meters can still be seen by a SAR. The spatial variation of the wavelength and wave direction relative to the hurricane's center is consistent with previous observations (e.g., Elachi et al., 1977; King and Shemdin, 1978).

SAR imagery of waves generated by hurricanes and severe storms is extremely useful in validating directional wave-prediction models, because this is the only available large-scale information on such waves.

(Rev. 251; A: 1336 GMT, B: 1337 GMT, July 14, 1978.)

5. Wave Refraction by Bottom Topography

0   10 km

N

ILLUMINATION
←DIRECTION
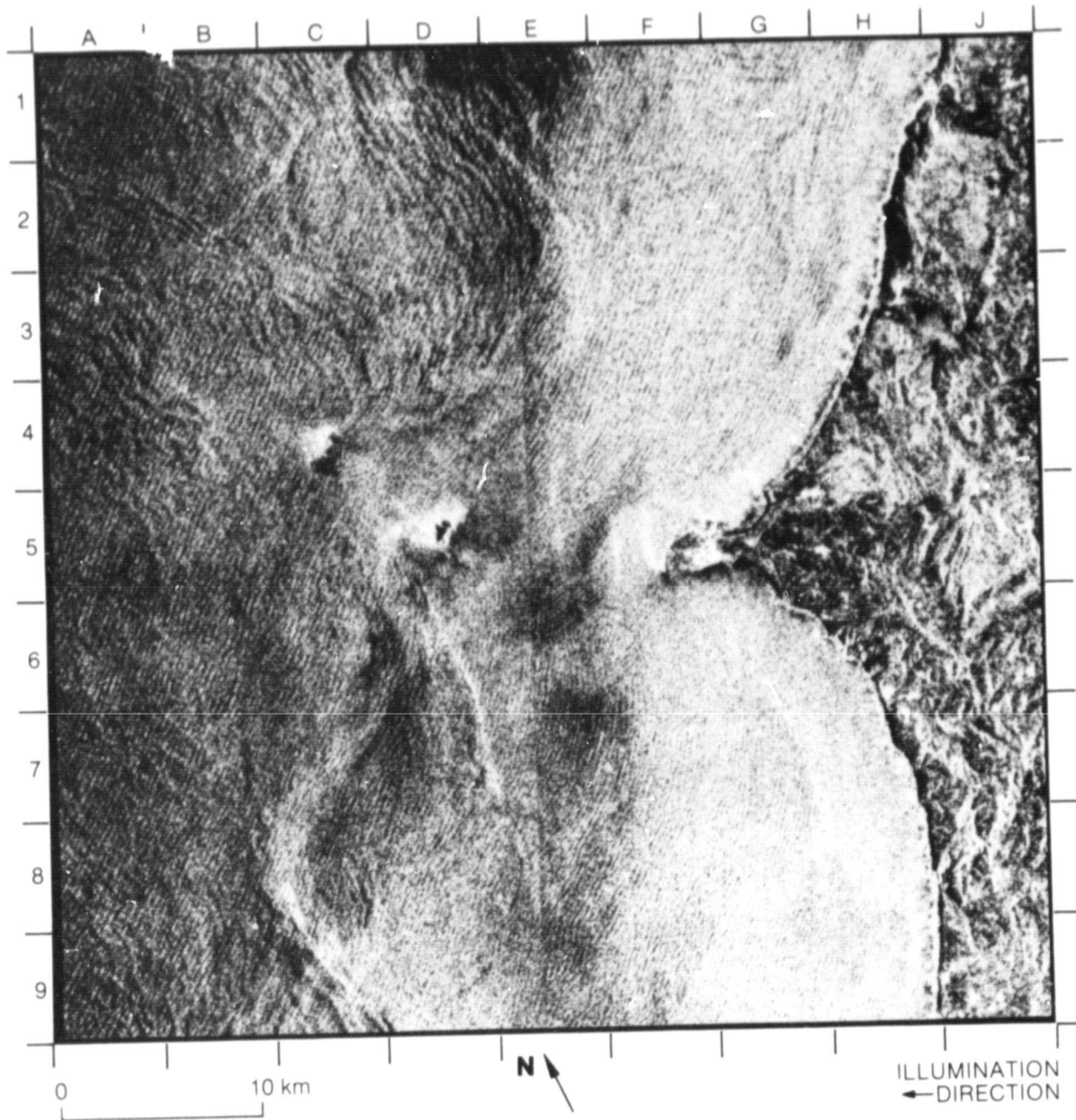
The refraction of impinging deep ocean waves by varying bottom topography in near-shore areas is one of the major concerns of coastal engineers. This image shows how deep ocean waves are refracted by the bottom topography west of Portugal.

A long-crested wave train with a wavelength of about 310 meters propagated from the northwest onto the coast. Interesting refraction patterns can be seen around the two islands at C4 and D5 (refer to the bathymetric chart for bottom topography). The wavelength decreases and the wave crests bend toward the islands, forming a wave convergence zone behind the islands where the wave heights should be anomalously high. Because of the small size of these two islands, wave diffraction effects might also be important in explaining some of the severe bending of the wave crests behind the islands.

Besides these two islands, the major topographic feature in this area is the submarine ridge extending offshore from the cape at F5 and F6. This ridge causes a
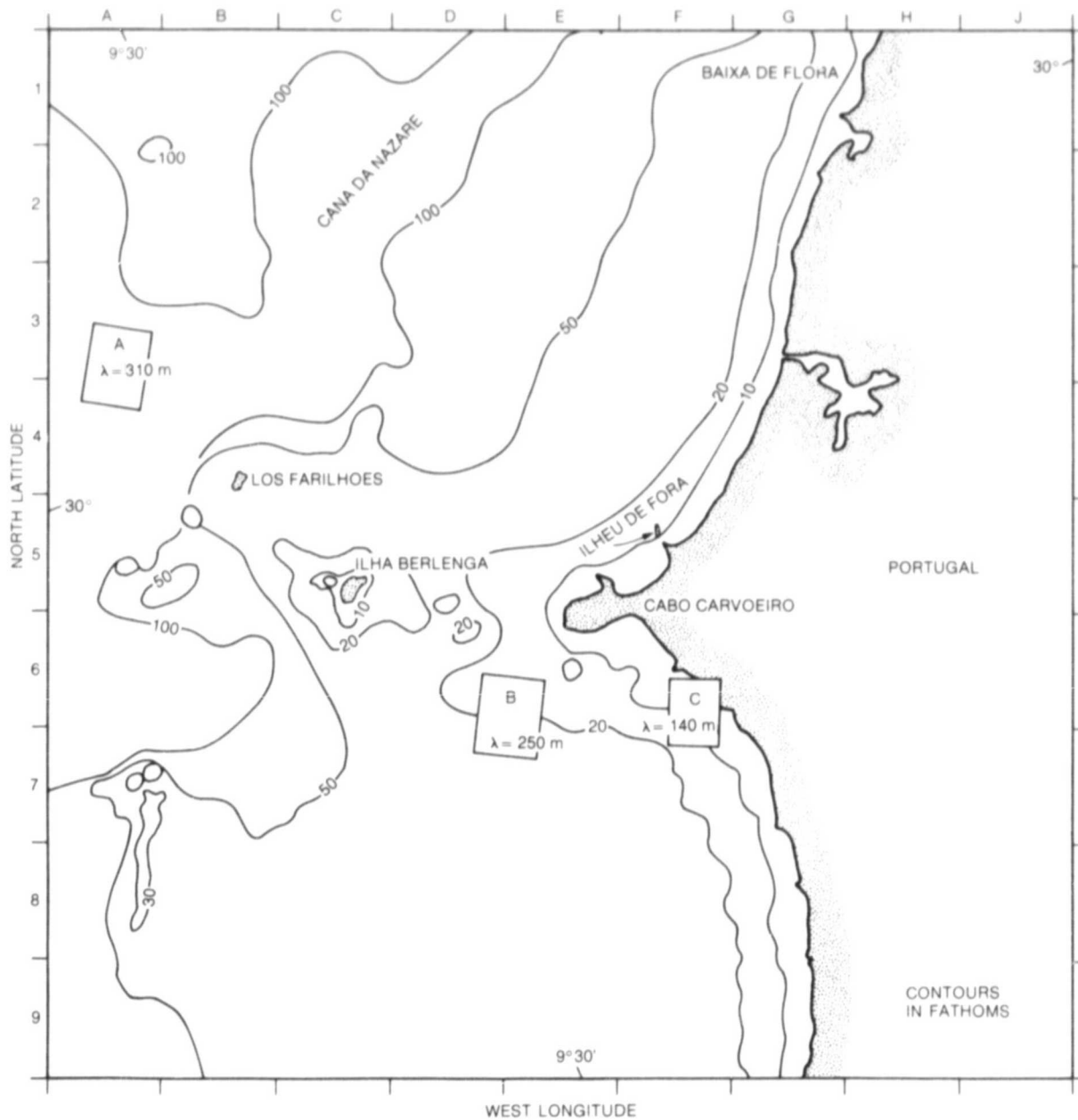
Bathymetric chart of the imaged area. Lambda values within boxes A, B, and C are wavelengths within those areas.

large-scale bending of the wave crests toward itself, resulting in another wave convergence zone over the ridge. This confirms that a submarine ridge in coastal areas is always associated with high waves.

The decrease of wavelength with bottom depth is illustrated at the three areas indicated as A, B, and C on the chart. The observed wavelengths are consistent with the results of calculation based on bottom depths and the theoretical dispersion relation. By examining the weather map of the North Atlantic a few days before this overpass, it was found that these waves were generated about two days earlier by the same storm that generated the waves in the JASIN area shown in Image 1.

(Rev. 785; 2143 GMT, August 20, 1978.)

3.2 Internal Waves

Alternating bands of rough and smooth sea surface are a common phenomenon in coastal waters under low winds. They have been well documented as surface manifestations of large amplitude internal waves trapped in the highly stratified summer seasonal thermocline (Ewing, 1950; LaFond, 1962; Curtin and Mooers, 1975). Before the launch of Seasat, these surface patterns had been detected in aerial photographs (Shand, 1953), in the Landsat imagery (Apel et al., 1975), and in airborne SAR imagery (Elachi and Apel, 1976). The Seasat SAR has demonstrated that internal wave signatures can be also well detected by a spaceborne SAR. During its short lifetime, Seasat collected a great deal of SAR imagery of internal waves in a variety of geographic locations. Among other features, internal waves constitute a major element in the wealth of information contained in the Seasat SAR imagery.

It is generally believed that internal waves are seen by a radar and/or a camera mainly as a result of either or both of two mechanisms: (1) the surface currents associated with the internal wave field sweep together surface oils and materials in the surface water convergence zones, resulting in severe damping of short capillary/gravity waves to form slicks (Ewing, 1950); (2) the interaction of the short capillary/gravity waves and the surface current field induced by the internal waves results in a periodic modulation in the height of the capillary/gravity waves, thus producing the banded patterns of roughness and slicks with occasional occurrence of highly peaked, long-crested waves that are the result of resonant interactions (Gargett and Hughes, 1972; Hughes, 1976). The field experiment conducted by Hughes and Grant (1978) indicates that the surface wave field is more sensitive to internal wave currents at lower wind speeds. Their experimental results can be well explained by a theory based on the second mechanism described above (Hughes, 1978), suggesting that the second mechanism was dominant during that experiment. Comparisons of airborne SAR imagery with surface observations indicate that the image intensity is correlated with both the mean square height and slope of the surface wave field (Gower and Hughes, 1979). With a theory relating the surface wave field to the internal wave amplitude and surface winds, information on the internal wave amplitude can be obtained from the imagery and simultaneous wind information. However, such a theory is not available yet.

Characteristics of the internal waves observed in the Seasat imagery are similar to those observed in the Landsat imagery (Apel et al., 1975) and can be summarized as follows:

(1) Most of these waves are found in coastal areas with wave crests more or less parallel to the bottom topography.

(2) These waves generally propagate onto the shores in separate groups with the distance between groups ranging from about 10 to 60 kilometers.

(3) The wavelength within each group decreases monotonously from several kilometers at the leading edge to several hundred meters at the trailing edge.

(4) The crests range in length from about 10 to 100 kilometers.

(5) The crests are characterized by either narrow bright lines in a dark background or by relatively wider dark lines in a bright background, indicating that these waves can be detected at a substantial range of wind speed.

These near-surface internal waves are generated mainly through the interaction of tidal currents and abrupt topographic features (Lee and Beardsley, 1974; Gargett, 1976; Maxworthy, 1979). Because these waves have large amplitudes, nonlinearity must be retained in the dynamics, and these waves are better described as solitary wave trains rather than linear wave trains (Osborne and Burch, 1980). When these waves travel over a shoaling bottom, they eventually break and produce intense mixing, which may have important effects on biological primary production in coastal waters (Haury et al., 1979). This mixing effect should also have potential impacts on modeling the diffusion processes in the coastal environment. Mollo-Christensen and Mascarenhas (1979) demonstrated that satellite-derived information on these waves can be used to map the heat content in the upper ocean, thus making this information important in modeling the climate of coastal areas. How significant the generation of these waves is in draining the tidal energy is also an interesting question for tide modelers.

We have selected seven images to illustrate the internal waves observed in various geographic locations. Image 6 is a scene of the Gulf of California, showing prominent wave packets in a semienclosed basin with strong tidal currents and topographic variations. Images 7, 8, 9, and 10 are scenes of the Mid-Atlantic Bight, the Florida coast, the Oregon-Washington coast, and the Labrador Sea off Hudson Strait, respectively, showing internal waves near continental shelves. Images 11 and 12 were selected to illustrate some of the limited examples of internal waves in the deep ocean, the Ormonde Seamount (off Portugal) and the Azores.

6. Gulf of California

ILLUMINATION
DIRECTION →

N
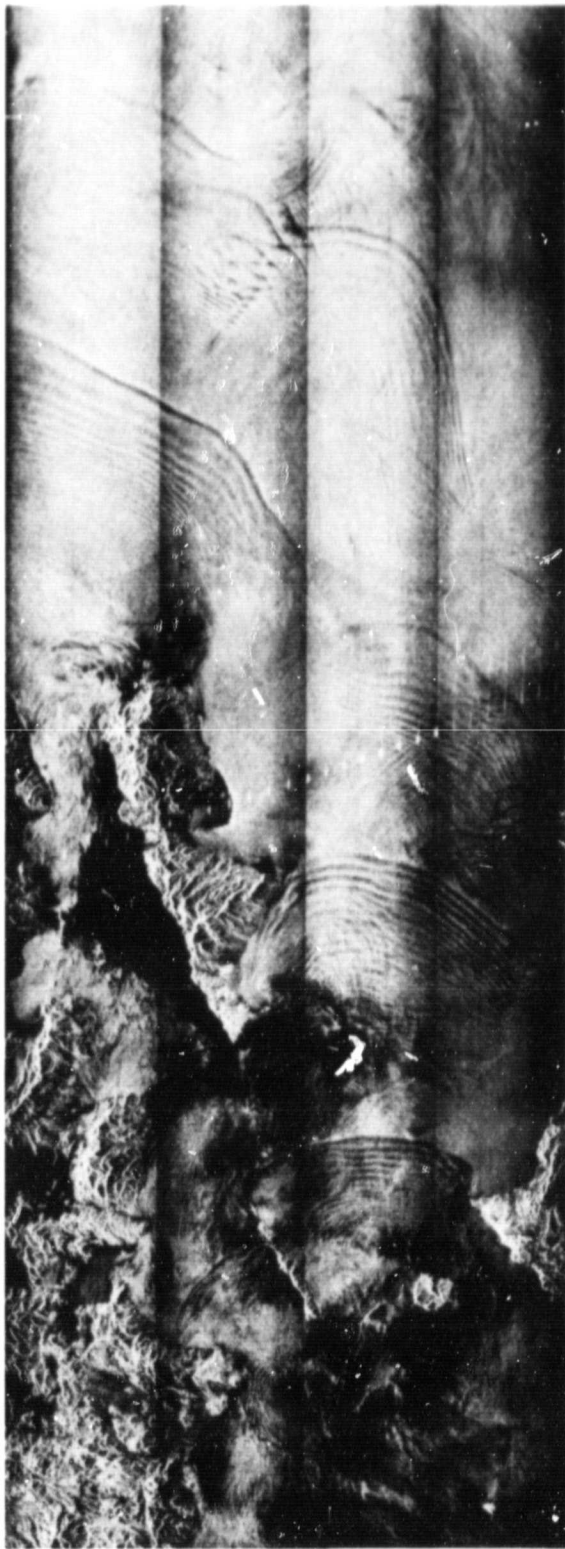
0   25 km
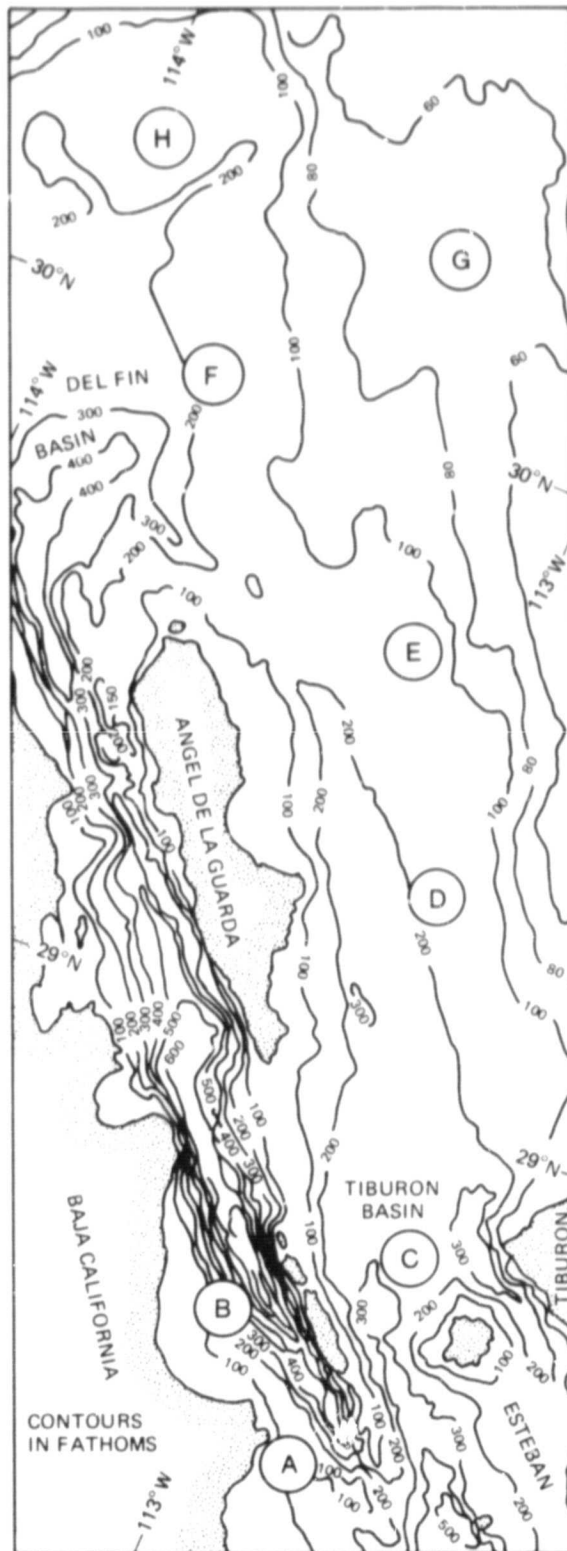
Bathymetric chart of the imaged area (from Fisher et al., 1964). Encircled letters indicate the locations of wave groups discussed in the text.

Signatures of internal waves have been observed in the imagery of the Gulf of California from numerous overpasses. The wave activities are primarily confined to north of 28°N in the Gulf. Eight major wave groups can be identified on this image (labeled as A through H on the bathymetric chart) along with many minor ones.

The occurrence of these waves is associated with the twice-a-month cycle of spring tides when the tidal range is over 6 meters near the northern end of the Gulf; there is very little wave activity during the neap tides. Presumably these waves were generated as a result of the interaction of strong tidal currents and bottom topography, which is shown on the bathymetric chart. North of 28°N, strong variations of bottom relief are located to the southwest of Tiburon and to the west of Angel de la Guarda, and those wave groups identified in the image were apparently generated in these two regions.

Within a particular wave group, the wavelength and amplitude (inferred from the brightness modulation) decrease with the distance from the leading crest—a common characteristic of near-surface internal waves. The maximum wavelength is on the order of 2 kilometers except for groups A and B, which have wavelengths less than 1 kilometer. Assuming that wave groups C, D, and E were generated in successive tidal cycles with a period of 12.42 hours (M_2 tide), the inferred group speed was about 1.2 meters per second.

The pronounced patterns between groups G and H are indications of strong interactions, probably a manifestation of interacting solitary waves. The ultimate breaking of these waves as they propagate northward over the shoaling bottom could be an important mixing mechanism in the northern end of the Gulf.

Note that the series of bright segments across the center of the image are not oceanic features, but are caused by system calibration pulses.

(Rev. 1355; 1811 GMT, September 29, 1978.)

7. Mid-Atlantic Bight

The sharp shelf break off the east coast of the United States is well known for the generation of near-surface internal waves. Signatures of internal waves have been
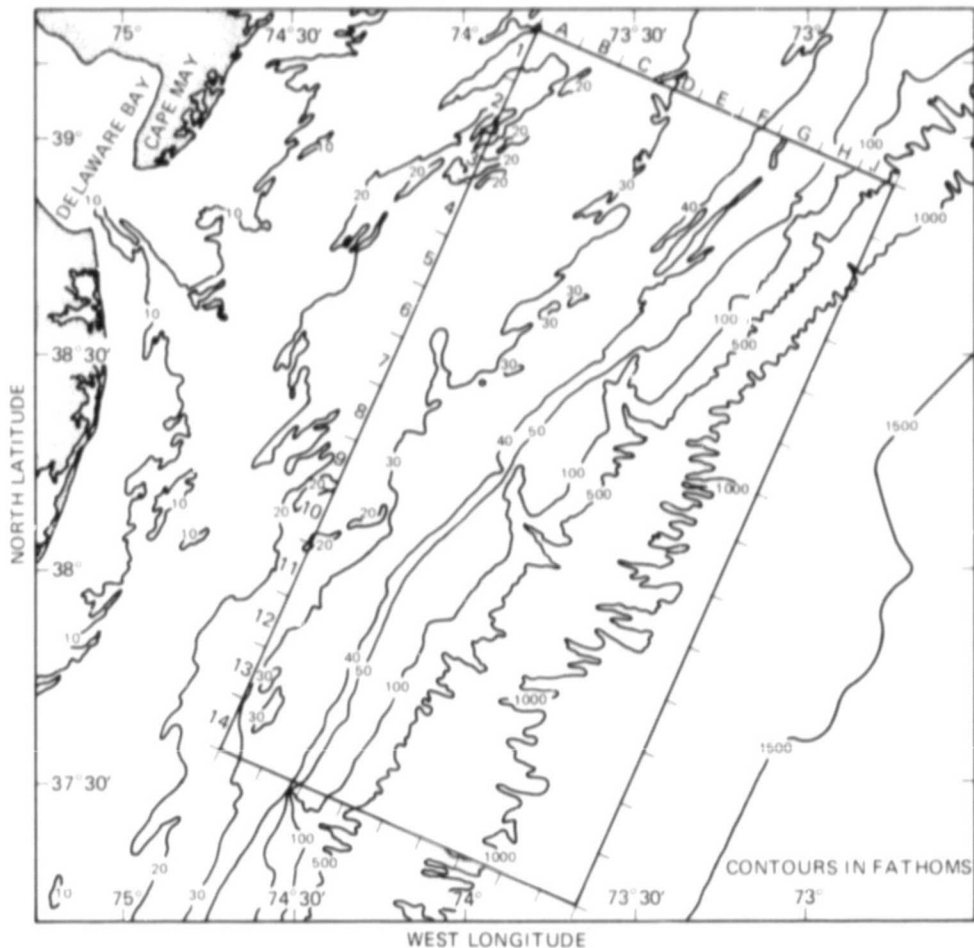
Bathymetric chart of the imaged area, which is enclosed by the rectangle.

observed in many images of the continental shelf from Florida to Nova Scotia (including the Gulf of Maine). This image covers an area southeast of Delaware Bay, the central area of the Mid-Atlantic Bight. Numerous packets of internal waves with long, linear wave crests can be seen. The corresponding bottom topography is shown on the bathymetric chart.

In general, the wave crests are parallel to the bottom contours with the crest length on the order of 50 kilometers. Most of the waves seem to propagate shoreward from the shelf break, which roughly corresponds to the seaward boundary of the major wave activities. These characteristics are generally consistent with the hypothesis that these waves are generated through the interaction of tidal currents and the shelf break. However, there is no clear evidence for waves propagating seaward from the shelf break. The maximum wavelength in these packets is about 1.3 kilometers, and the estimated group speed is about 0.3 meters per second. The number of wave crests in a particular packet can be as high as 30. The few wave packets with crests perpendicular to the shelf break (at E6, B13, and B14) were probably generated over the submarine canyons nearby when tidal currents were parallel to the shelf break.

This image also illustrates that internal wave signatures can be seen under different surface roughness conditions. In the smooth (dark) region, the wave crests are identified as narrow bands of enhanced roughness (brightness); in the rough (bright) region, the wave crests are identified as relatively wider bands of enhanced smoothness (darkness).

(Rev. 931; 0240 GMT, August 31, 1978.)
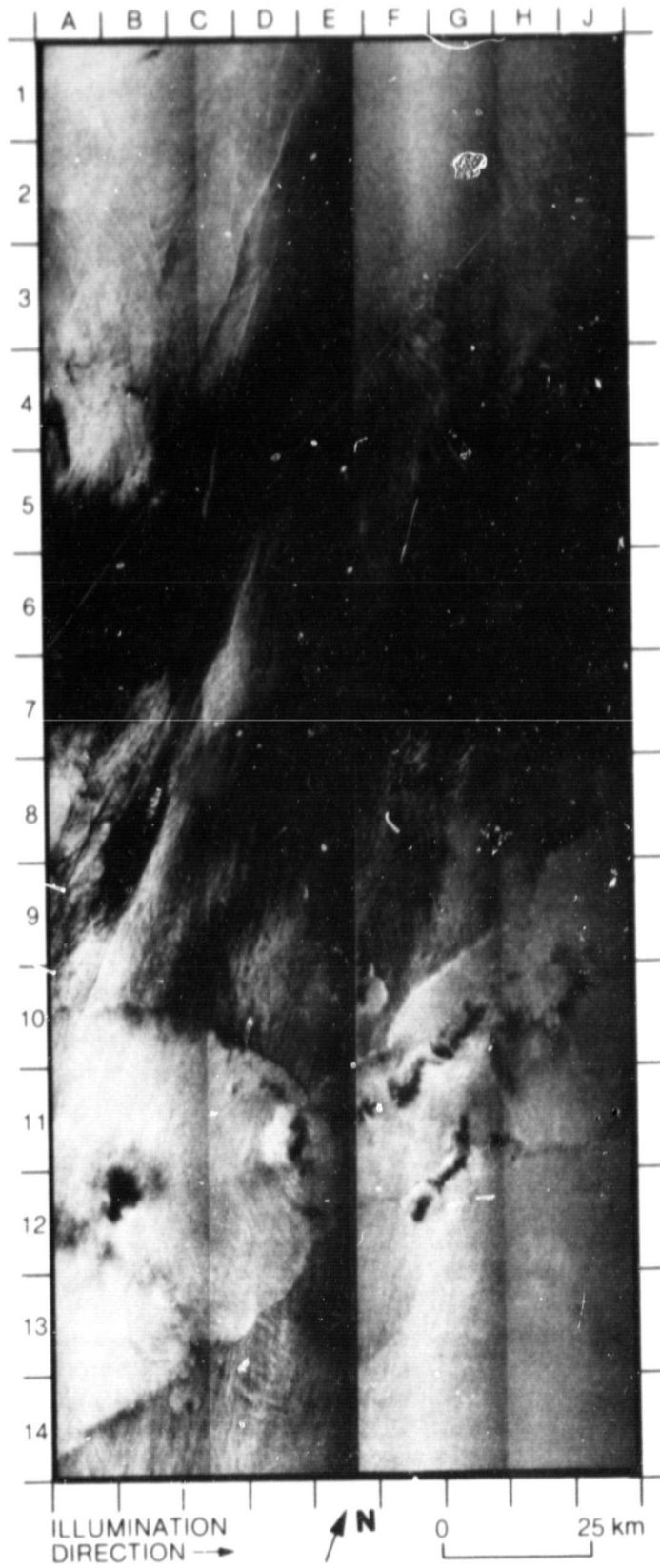
31

ILLUMINATION
DIRECTION →

N

0   25 km
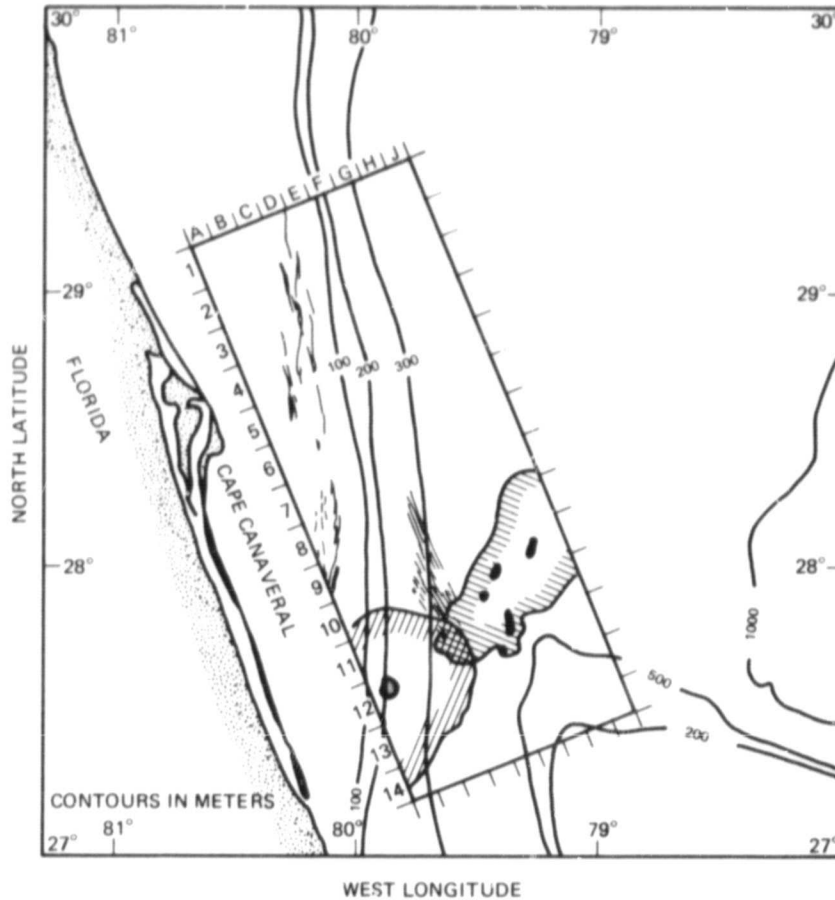
Bathymetric chart of the imaged area, which is enclosed by the rectangle. Prominent wave packets are indicated by groups of roughly parallel fine lines.

This image shows an area off Cape Canaveral, Florida, where the Gulf Stream flows along the shelf break. Signatures of internal wave packets are seen immediately shoreward of the shelf break, which is represented by the 100-meter and 200-meter contours on the bathymetric chart. These waves are characterized by their linear crests and short wavelengths (less than 300 meters) that are possibly due to the effect of the shear associated with the Gulf Stream, which flows close to the 200-meter contour line. The proximity of these waves to the shelf break indicates their topographic origin. The role of the Gulf Stream in the generation of these waves is unclear.

The circular-shaped feature centered at B12 is the signature of a tropical rain cell (cf. Image 39) confirmed by surface observations (Ross, 1981). The distinct boundary represents the associated squall line, and the dark spot at the center is an area of heavy rainfall that damps most of the short waves. A second rain cell, overlapping the first, extends from D11 to J11. North of these rain cells is a highly collimated wave-like pattern (from D10 to E11) with a wavelength of about 400 meters. This cannot be a swell because of its limited extent. If this is an internal wave packet, the following questions may arise: What is its source? Why is it so collimated with a constant wavelength? The answers are, of course, very likely associated with the presence of the Gulf Stream. In fact, similar features have also been observed in other areas of the Gulf Stream (Images 15 and 16).

(Rev. 163; 1004 GMT, July 8, 1978.)

9. Oregon-Washington Coast

Internal wave signatures have also been observed in the imagery of the west coast of the United States. Because this area generally lacks a wide continental shelf like that off the east coast, topographically generated near-surface internal waves here are primarily confined to areas immediately adjacent to the shore.

Major wave activities observed by the SAR are found near Vancouver Island, Canada, the coasts of Oregon and Washington, and Baja California, Mexico. Very little wave activity is found between 35°N and 40°N.

This image shows the internal wave patterns near the mouth of the Columbia River at the border between Oregon and Washington. The most prominent feature is the bright, circular wave packet from B3 to C5, apparently radiating from a subsurface sediment spit at the river mouth (see the bathymetric chart). A relatively weak signature

34
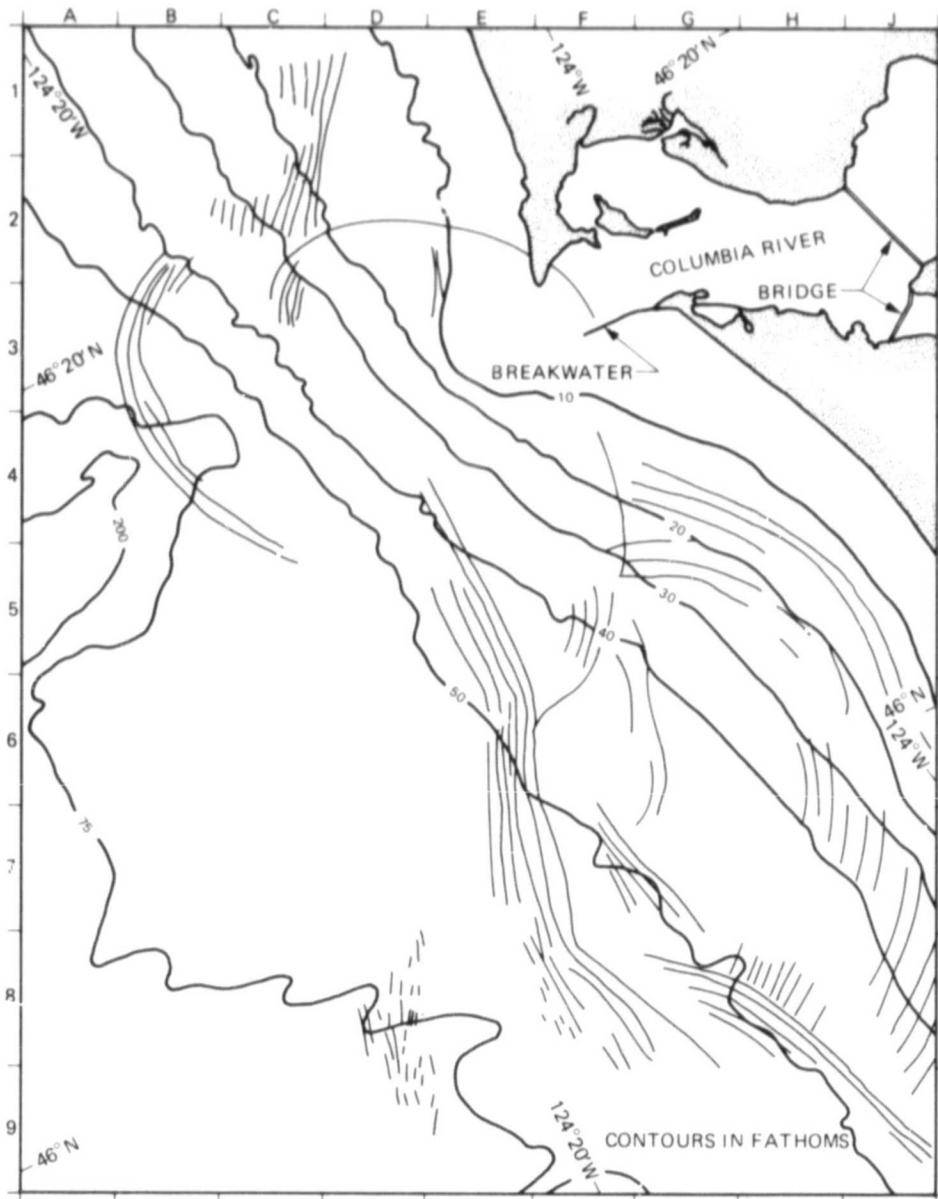
Bathymetric chart of the imaged area. Prominent wave packets are indicated by groups of roughly parallel fine lines.

of a similar wave packet can be seen from C3 to E2. All other wave packets shown were probably generated further offshore over a submarine canyon. The maximum wavelength of these wave packets is about 1 kilometer. Note that some of the wave signatures are partially wiped out by patches of surface roughness, suggesting a rather highly variable wind field.

Also seen on this image are breakwaters at the river mouth and two bridges inside the estuary (ref: bathymetric chart).

(Rev. 761; 0527 GMT, August 19, 1978.)

10. Labrador Sea (Off Hudson Strait)

ILLUMINATION
DIRECTION ➡

N

0   20 km
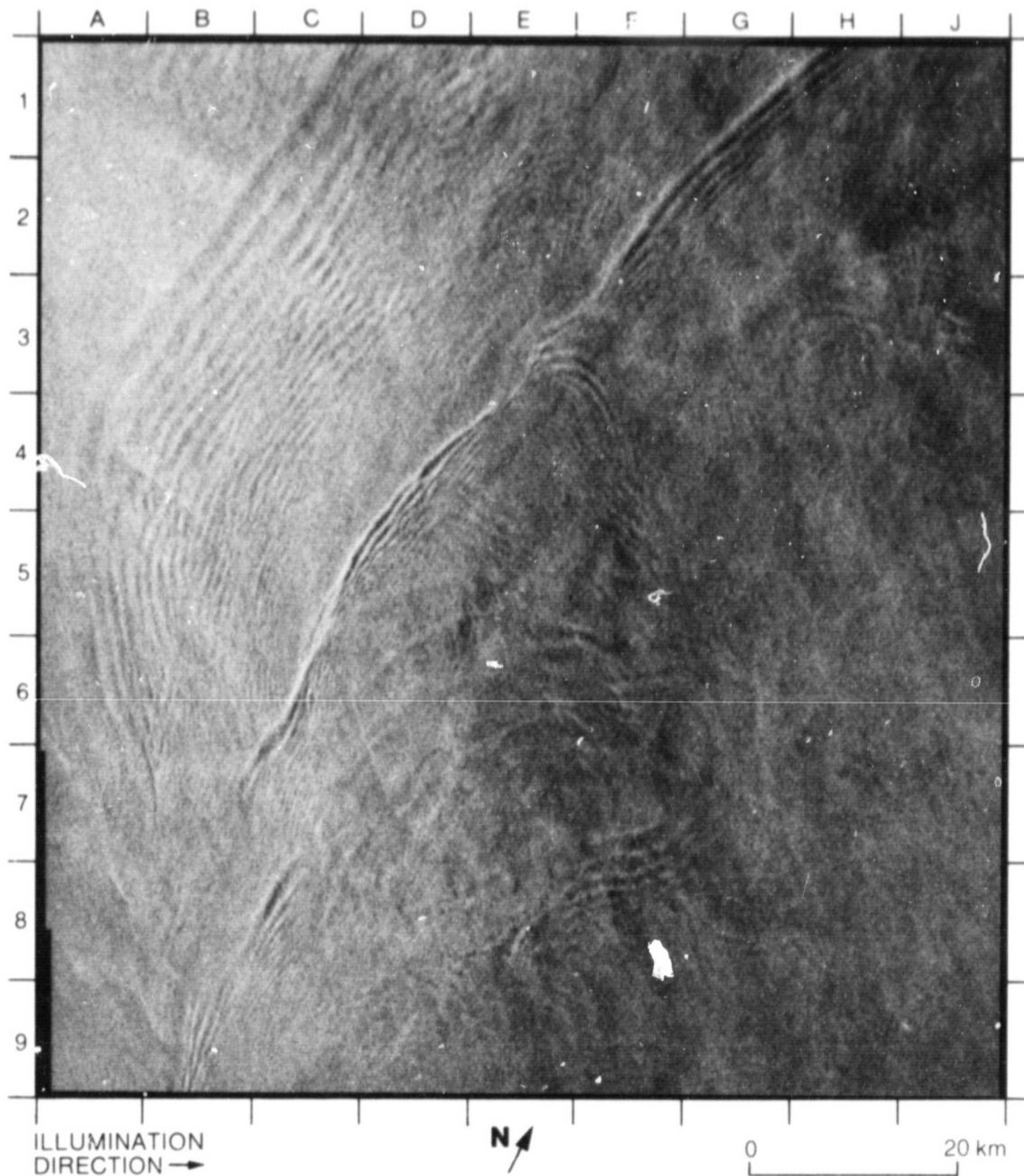
Internal wave-like features are also observed at high latitudes. This image shows a scene in the Labrador Sea about 150 kilometers east of Hudson Strait, Canada. The two long-crested wave packets oriented in the north-south direction are the major features here (D1 to A6 and H1 to B7). They are roughly parallel to the large-scale bottom topography (see the bathymetric chart).
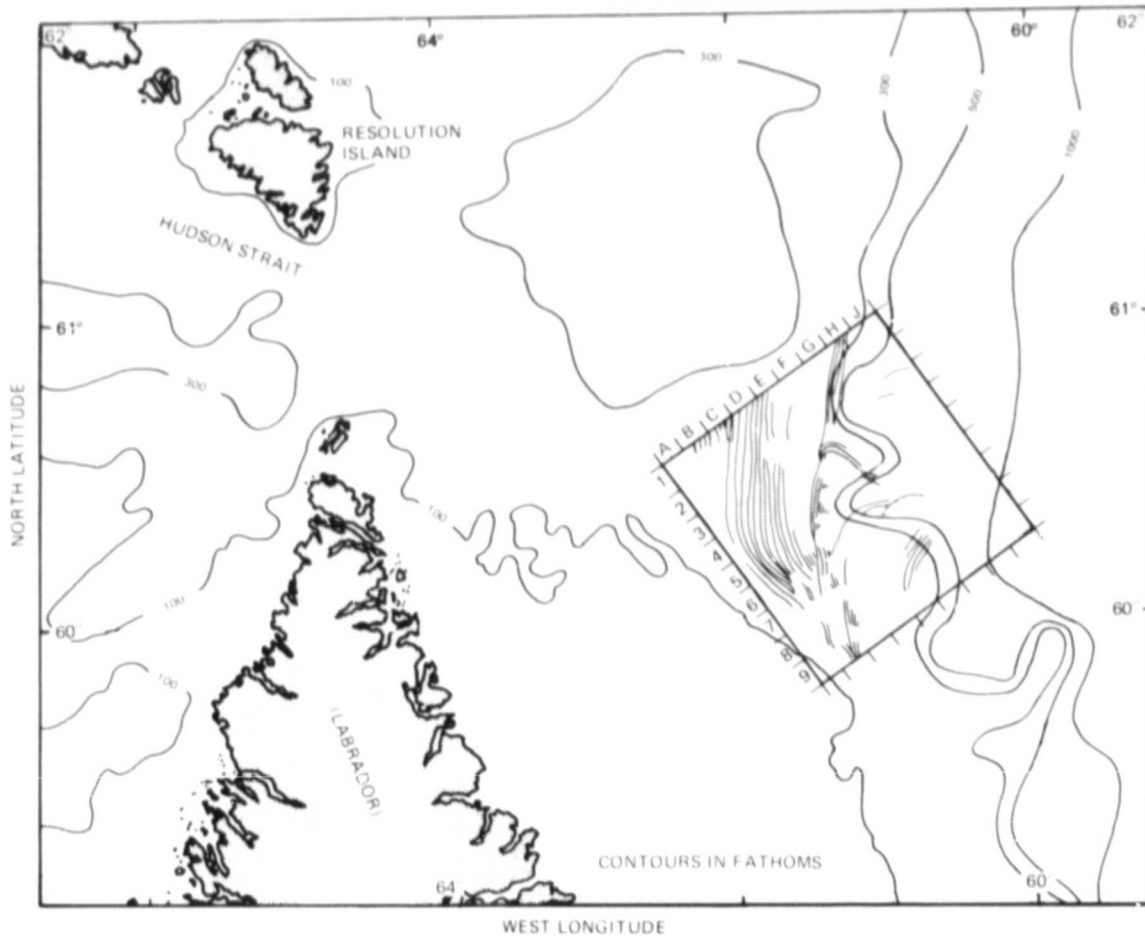
36

Bathymetric chart of the imaged area, which is enclosed by the rectangle. Prominent wave packets are indicated by groups of roughly parallel fine lines.

According to LeBlond et al. (1981), the mean currents in the imaged area are characterized by the convergence of the Baffin Current that flows southward along the shelf break (300- and 500-fathom contours) and an eastward flowing current from the Hudson Strait, with the merged current known as the Labrador Current. So the relatively long wave crests and their pronounced curvature at A4 and A5 are probable manifestations of the influence of the currents on internal wave propagation.

The local tides are predominantly semidiurnal with a range of about 5 meters. If these waves were tidally forced, the inferred group speed was about 0.65 meters per second. Note the strong dispersion of the wave crests—the wavelength at the leading edge of the packets increased from about 0.9 kilometers to about 2.7 kilometers in 12.4 hours.

(Rev. 1395; 1331 GMT, October 2, 1978.)

0   20 km

N

ILLUMINATION
←DIRECTION
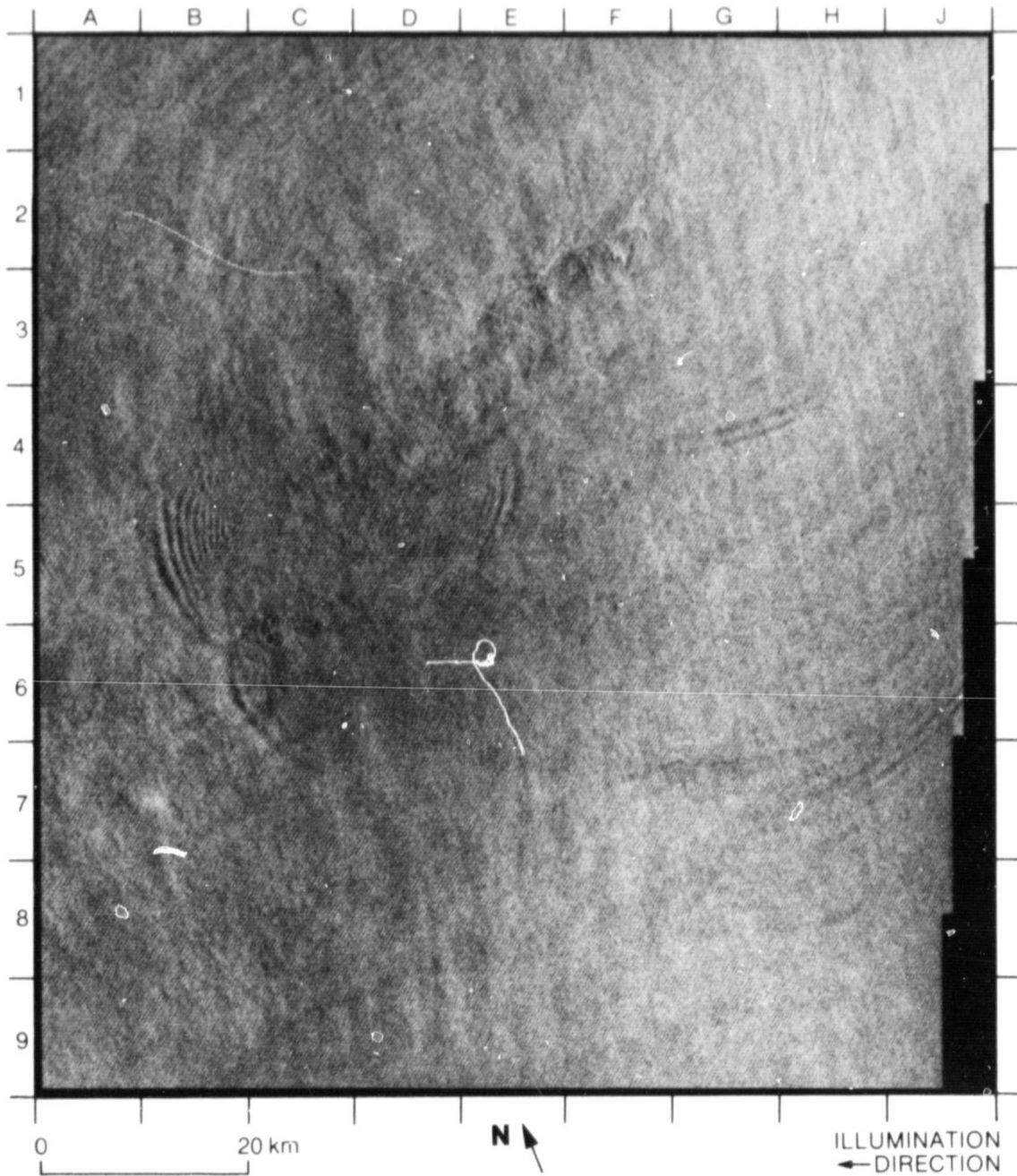
    Although most of the internal wave activities detected by Seasat were found in near-shore regions, we have some limited evidence from SAR images that these waves exist near seamounts in the deep ocean. This image shows such an example.

    Located about 200 kilometers southwest of Portugal on the Gorringe Ridge between the Tagus Abyssal Plain and the Horseshoe Abyssal Plain (see the bathymetric chart), Ormonde Seamount is one of two seamounts with summit depths less than 200 meters; the depth of the plains is generally greater than 4000 meters. The internal wave packets shown on this image are indicated on the bathymetric chart by line drawings. The three wave groups at B5, C6, and E5 have the same characteristics as those waves observed in the near-shore areas, with the wavelength decreasing
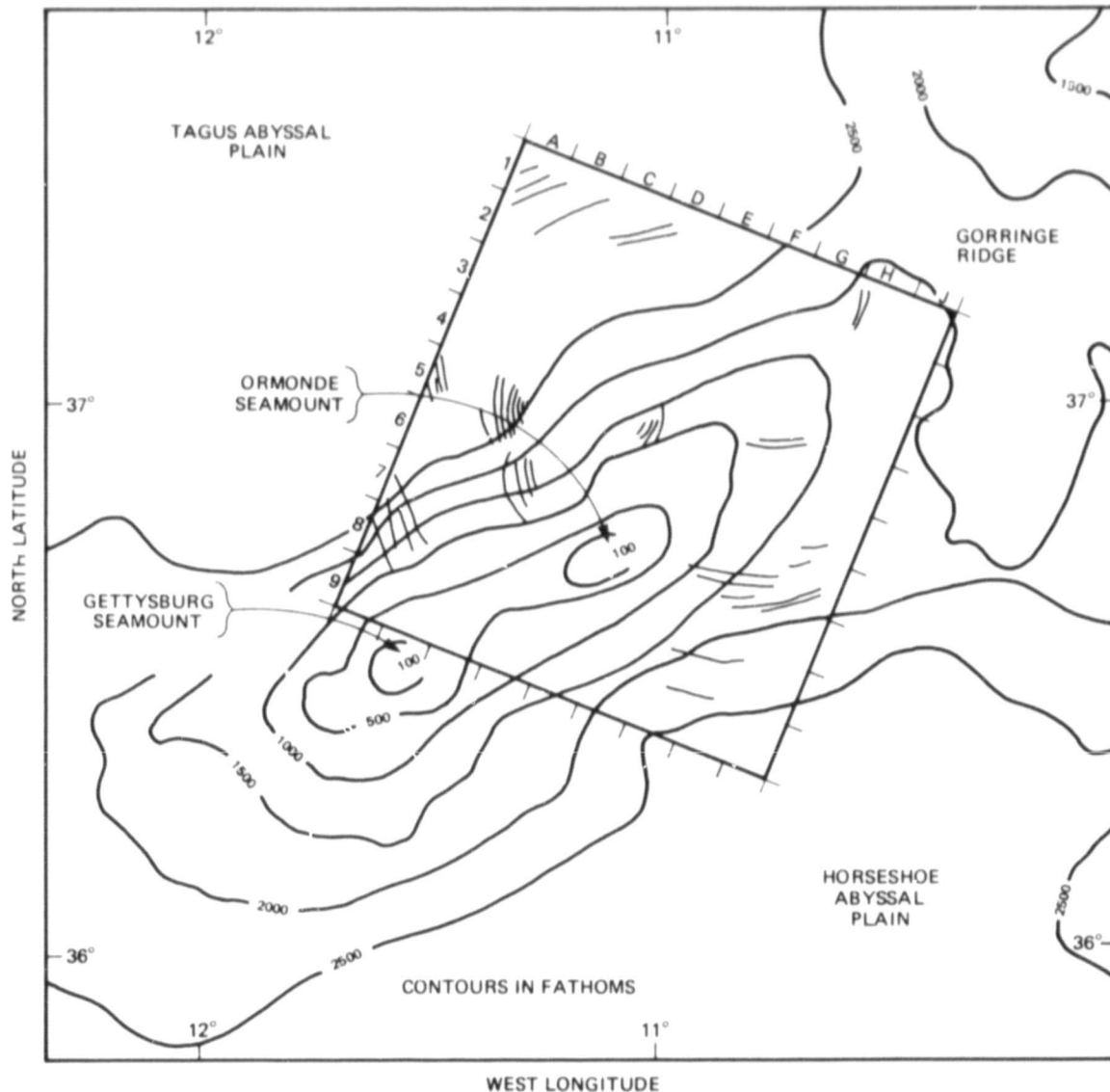
Bathymetric chart of the imaged area, which is enclosed by the rectangle. Prominent wave packets are indicated by groups of roughly parallel fine lines.

from about 1.2 kilometers at the leading edge to about 0.6 kilometers at the trailing edge. The maximum length of the wave crest is on the order of 10 kilometers, much shorter than those found near shores. The most likely generation mechanism for these waves is the interaction of the Ormonde Seamount and the tides. Similar internal wave patterns were also found near the Rockaway Seamount at 35°N and 50°W in Revolutions 1403 and 1446, and in the JASIN area (between Scotland and Iceland) in Revolution 7€2 (not shown in this atlas). In the lower part of the image are some less-organized striations with quite different characteristics from those described above; they might also have been internal waves from different sources.

The image was taken from the same pass as that of Image 5, and the swell described there also appears on this image.

(Rev. 785; 2144 GMT, August 20, 1978.)

0   25 km   N   ILLUMINATION
                                     ←DIRECTION
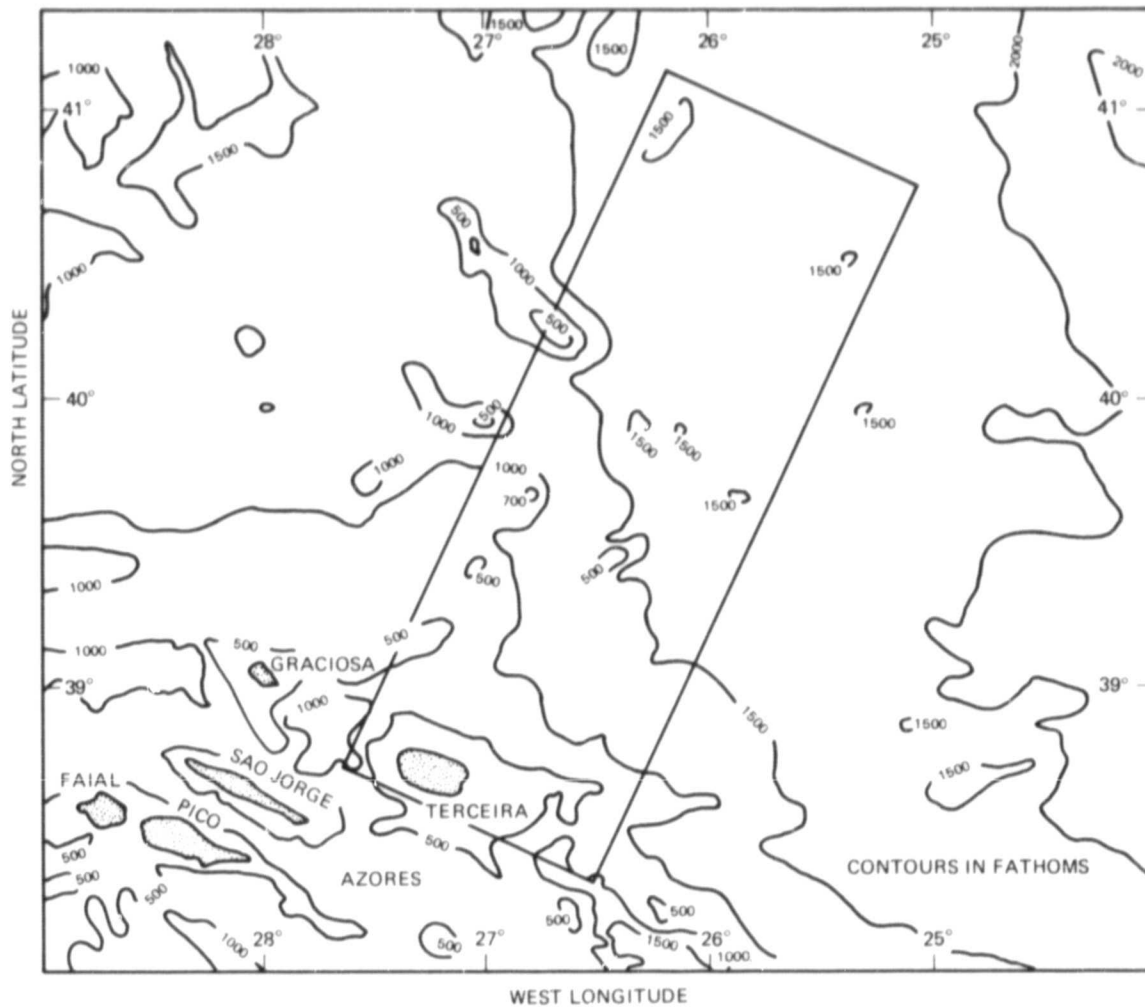
Bathymetric chart of the imaged area, which is enclosed by the rectangle.

The Azores are a group of islands on the Mid-Atlantic Ridge. This image covers an area near the Azores northeast of Terceira, which is the island at the lower end of the image.

This area has a high concentration of internal wave-like features. Unlike other areas where internal waves are characterized by isolated packets in a somewhat uniform background, this area is filled with highly "packed" internal wave-like patterns, indicating the abundance of internal wave sources. Similar patterns have been observed in other overpasses in this area (e.g., Revolutions 599, 642, 714, and 757).

Anomalously high energy of internal waves and tides near the Mid-Atlantic Ridge at about 27°N was reported by Fu (1981). The most plausible energy source of these waves is the strong tides interacting with the very rough bottom topography, which is shown on the bathymetric chart. The bottom depth in most of the imaged area is greater than 2000 meters (approximately 1100 fathoms). The topography is characterized by scattered seamounts superimposed on a large-scale slope associated with the ridge. If these ocean surface features are indeed tidally-generated internal waves, the associated rate of tidal dissipation near the Mid-Atlantic Ridge should be an interesting quantity for tide modelers.

(Rev. 556; 2142 GMT, August 4, 1978.)

41

3.3 The Gulf Stream System

The western boundary current of the North Atlantic Ocean is generally referred to as the "Gulf Stream System." It begins in the Caribbean Sea, and flows around the Gulf of Mexico and the east coast of the United States until reaching Cape Hatteras, where it begins to flow eastward into the open ocean and gradually loses its identity in the eastern North Atlantic after it passes the Grand Banks south of Newfoundland. This is the swiftest boundary current of the world's oceans and carries the largest amount of water. Observations of the current and studies of its dynamics appear in the monograph by Stommel (1965) and a recent review paper by Fofonoff (1980).

Detection of the Gulf Stream boundaries by an airborne SAR has been reported by several investigators (e.g., Moskowitz, 1973; Weissman et al., 1980). The narrow swath (10 kilometers) of an airborne SAR, however, limits its value in mapping large-scale ocean currents. On the other hand, Hayes (1981), by analyzing the extensive imagery taken by the Seasat SAR off the east coast of the United States, demonstrated that the Seasat SAR was able to detect a variety of features associated with the Gulf Stream. It is apparent that the relatively wide swath (100 kilometers) of a spaceborne SAR has the potential to monitor the evolution of large-scale current systems in the ocean.

Such large-scale currents as the Gulf Stream are seen by a spaceborne SAR through several mechanisms. First, a change in surface wind stress that generates Bragg resonant waves (see page 13) usually occurs across a current boundary as a result of the difference in water temperature on the two sides of the current, with smaller wind stress occurring on the colder side where the boundary layer above the sea surface is more stable (Weissman et al., 1980). Second, due to wave-current interactions (e.g., Phillips, 1977), the Bragg resonant waves are modulated when they travel across a current boundary, resulting in either an increased or a decreased backscatter, depending on the orientation of the wave field relative to the current. Third, under a uniform wind field, the velocity of the air relative to the water surface is different within a current than outside a current, thus resulting in a variable surface wind stress. Fourth, the line-of-sight component of a current produces an azimuthal displacement of its image, thus making the current detectable on SAR imagery.

Although the major western boundary currents of the world's oceans are presumably detectable by a spaceborne SAR, only the Gulf Stream System was covered by the Seasat SAR swaths. Following are five images selected to illustrate features associated with the Gulf Stream System from the Gulf of Mexico to Cape Hatteras. Image 13 shows the current off Cape Hatteras as it leaves the continental slope and enters the open ocean. Images 14 and 15 illustrate the deflection and meandering of the current induced by an abrupt topographic feature off South Carolina – the Charleston Bump. Image 16, a scene off the Florida coast, shows the current immediately adjacent to the shelf break. Finally, Image 17 presents some features of the Loop Current in the Gulf of Mexico.
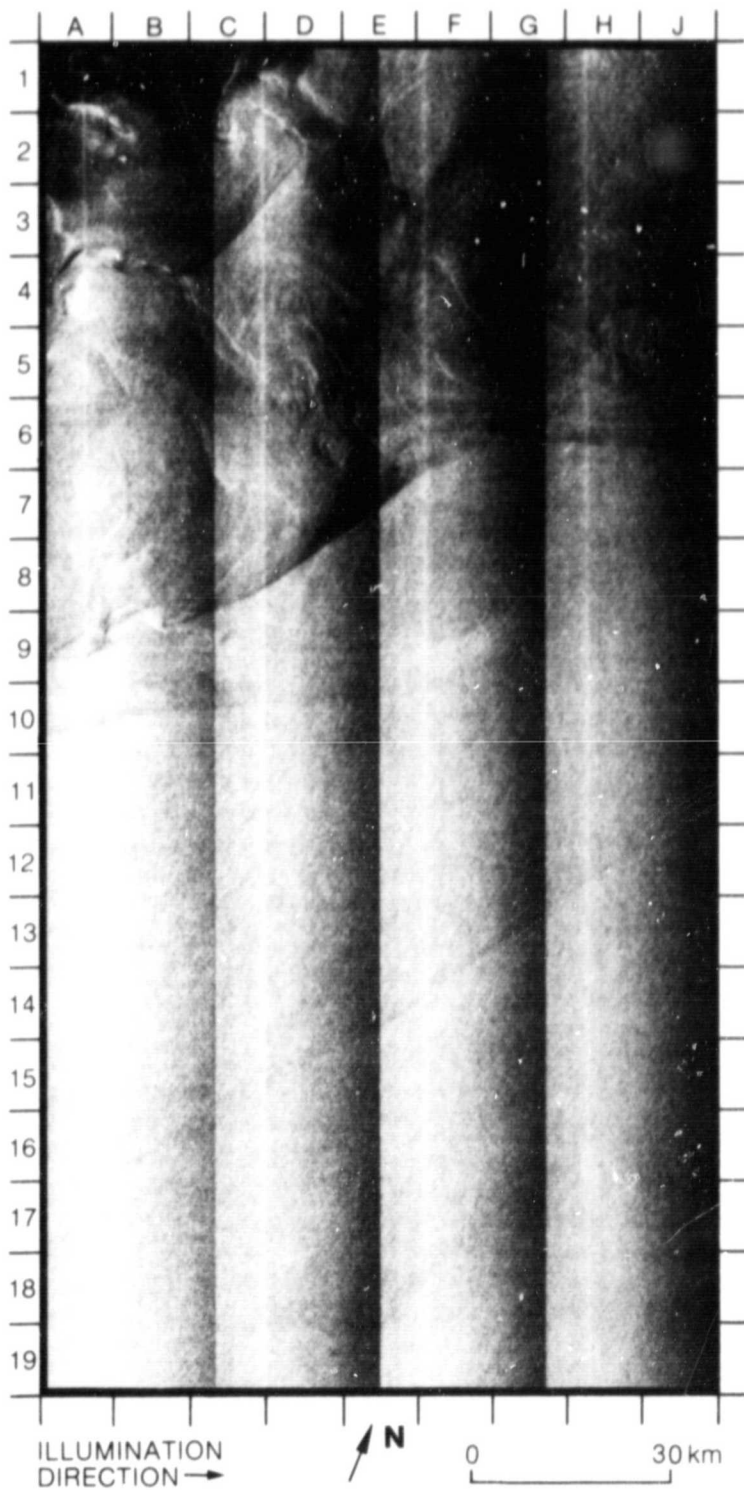
The Gulf Stream flows adjacent to the continental slope from the Florida straits up to Cape Hatteras, where the current begins to flow seaward off the continental slope into the deep ocean. This image shows signatures of this current at about 100 kilometers east of Cape Hatteras (see the bathymetric chart opposite Image 14 for the location of this image).
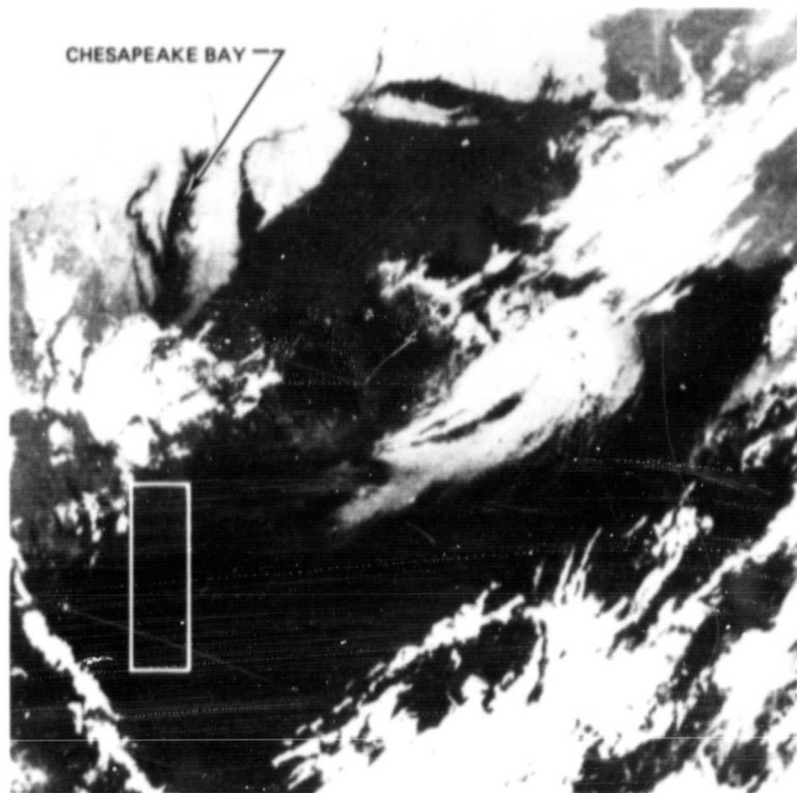
Infrared image of the North Atlantic Ocean off the northeast coast of the United States. The area of the SAR image is enclosed by a rectangle. The dark circular feature southeast of Chesapeake Bay is the same warm ring shown on Image 18.

The most prominent feature on the image is the along-track change in intensity from a uniformly bright region into a variably dark region across the sharp boundary extending from A9 to J6. Based on extensive surface observations, Ross (1981) interpreted this change to be a result of a shoreward decrease in surface wind speed across the northern boundary of the Gulf Stream. Here the sea surface temperature rapidly decreased shoreward of the current, resulting in an increased stability above the sea surface. Thus this sharp change in image intensity should correspond to the northern boundary of the Gulf Stream.

The infrared image of this area was taken by the very high resolution radiometer (VHRR) on board the NOAA-5 satellite at 0019 GMT, September 29, 1978, 9 hours after the Seasat overpass. Note that the boundary between the warm Gulf Stream water (dark region) and the cold shelf water (gray region) roughly corresponds to the boundary on the SAR image. South of this boundary, several weak, linear features can be seen on the SAR image; they were probably induced by the current shears of the Gulf Stream. North of this boundary, the small-scale wedge-like features are pools of warm water (Ross, 1981), which are possible manifestations of small-scale mixing between the Gulf Stream water and the shelf water (see Image 26).

(Rev. 1339; 1520 GMT, September 28, 1978.)
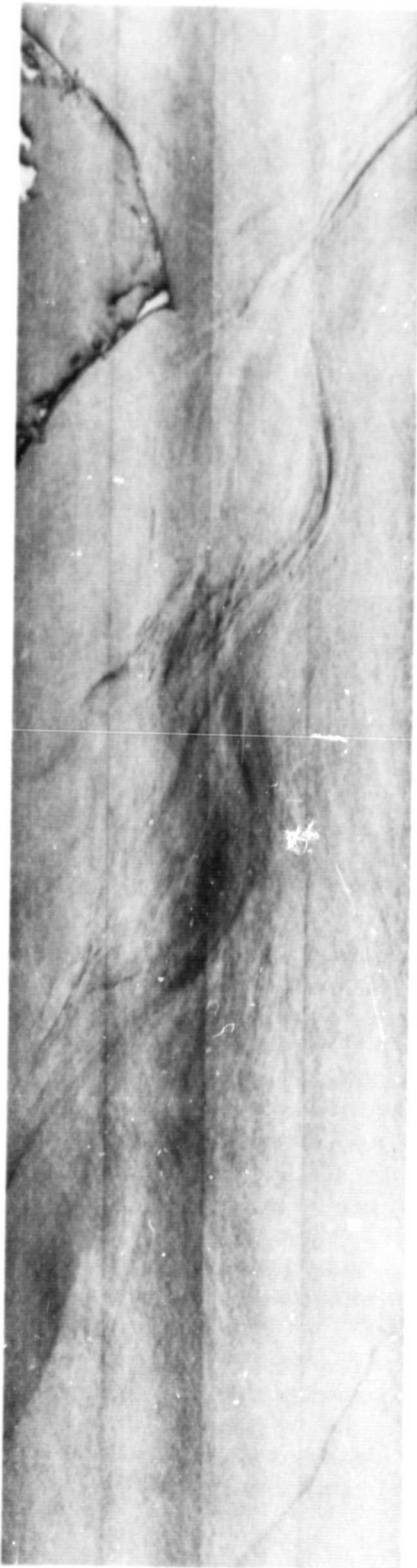
```
0          50 km                    N          ILLUMINATION
|_____|                       ↑          ←DIRECTION
```
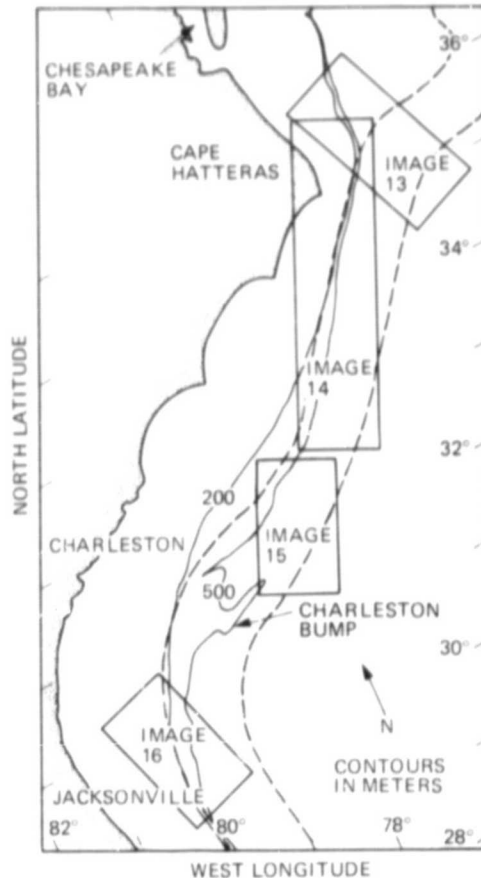
Map showing the geographic locations of Images
13 through 16 and the path of the Gulf Stream
(dashed lines) between Florida and Cape Hatteras.

It is well known that a persistent seaward deflection of the Gulf Stream occurs near 32°N as it flows over a submarine ridge (known as the "Charleston Bump") protruding from the continental slope off Charleston, South Carolina, and that this deflection is followed by large-scale wave-like fluctuations of the current downstream of this topographic feature (Brooks and Bane, 1978; Legeckis, 1979). This image shows such wave-like features in the Gulf Stream south of Cape Hatteras.

The Charleston Bump is located about 160 kilometers upstream of this image (see the bathymetric chart). The apparent "wavelength" inferred from this image is about 100 kilometers, with a peak-to-peak lateral displacement of about 25 kilometers. Based on an analysis of 3 years of satellite infrared imagery, Legeckis (1979) found that these wave-like disturbances generally propagated downstream at an average speed of 40 kilometers per day with wavelengths ranging from 90 to 260 kilometers. The dashed lines on the bathymetric chart represent the Gulf Stream boundaries derived from the Weekly Sea Current Chart prepared on August 30, 1978, by the Coast Guard Oceanographic Unit for the Department of Transportation, using satellite infrared imagery and ship reports. Note that the wave-like features discussed above and the linear features at the lower right corner of the image agree very well with the weekly averaged positions of the shoreward and the seaward boundaries of the Gulf Stream, respectively.

(Rev. 931; 0240 GMT, August 31, 1978.)

15. The Gulf Stream Off Charleston, South Carolina
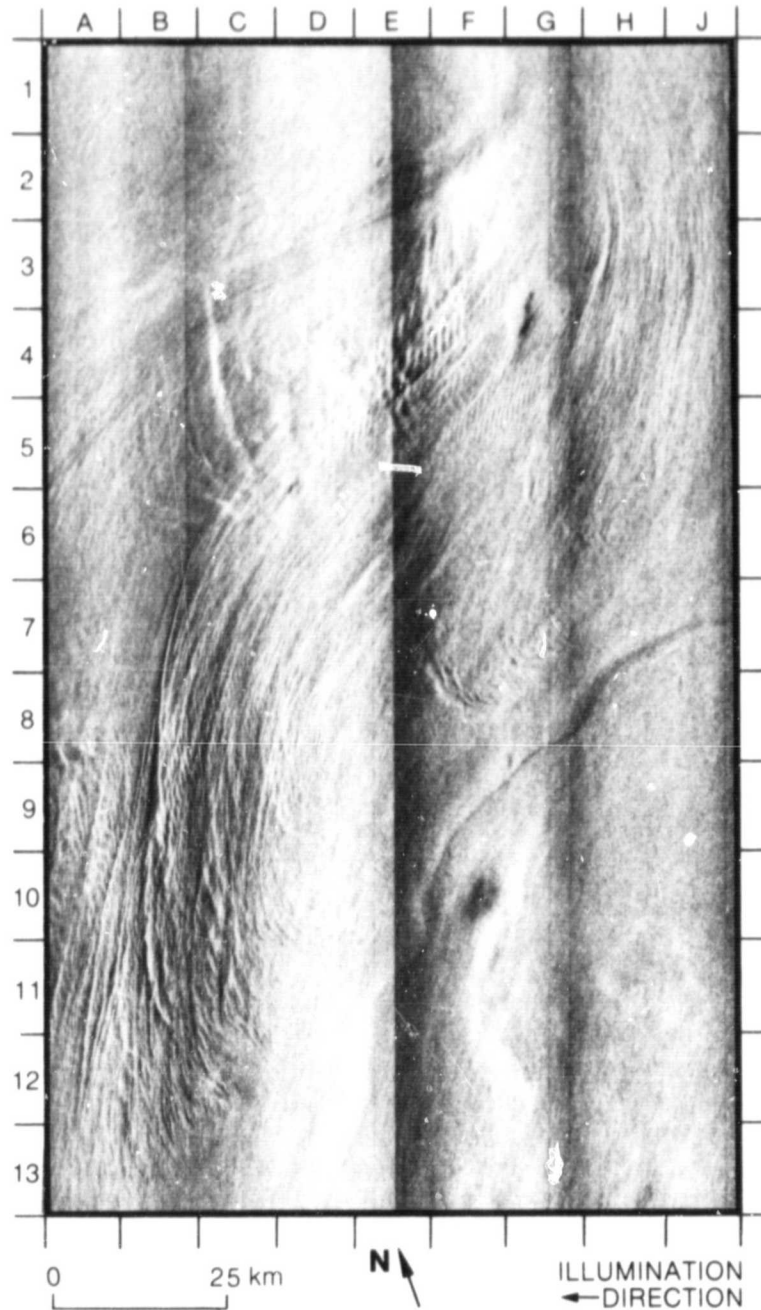
This image shows the Gulf Stream in the eastward deflection zone just northeast of the Charleston Bump (see the bathymetric chart opposite Image 14 for location). The bathymetric chart above, superimposed on the image, shows with dashed lines the Gulf Stream boundaries derived from the Coast Guard Weekly Sea Current Chart prepared on July 26, 1978. The two prominent linear features on the image (from G1 to A5 and from J7 to D13) are probably signatures of the two current boundaries. Note their correlation with the underlying bathymetry. The latitude at which the current axis becomes eastward is about 32.2°N, consistent with the findings of Brooks and Bane (1978).
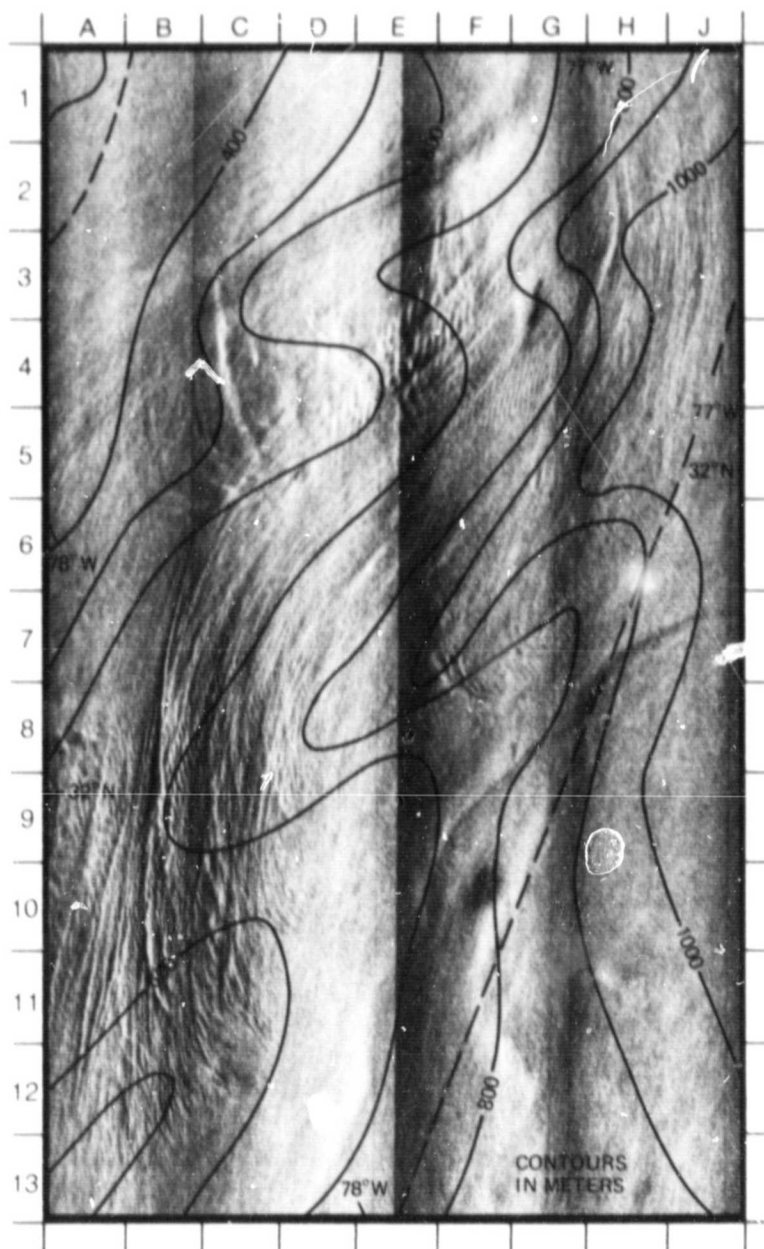
Bathymetric chart superimposed on Image 15. The dashed lines represent the thermal boundaries of the Gulf Stream (after Hayes, 1981).

Note the small-scale linear striations trapped between the two current boundaries. Their wavelengths range from 300 to 1200 meters, and their long crests are more or less parallel to the current boundaries. Because these features have never been observed by surface measurements, the physics of their generation and interaction with the Gulf Stream is essentially unknown (also see Images 8 and 16). However, a plausible account was given by Mollo-Christensen (1981), who proposed that these striations were the surface effects of the adjustment of the bottom boundary layer to changes in the interior flow.

A ship and its wake can be seen at F8 (see Section 3.9 for ship detection). (Rev. 400; 0006 GMT, July 25, 1978.)
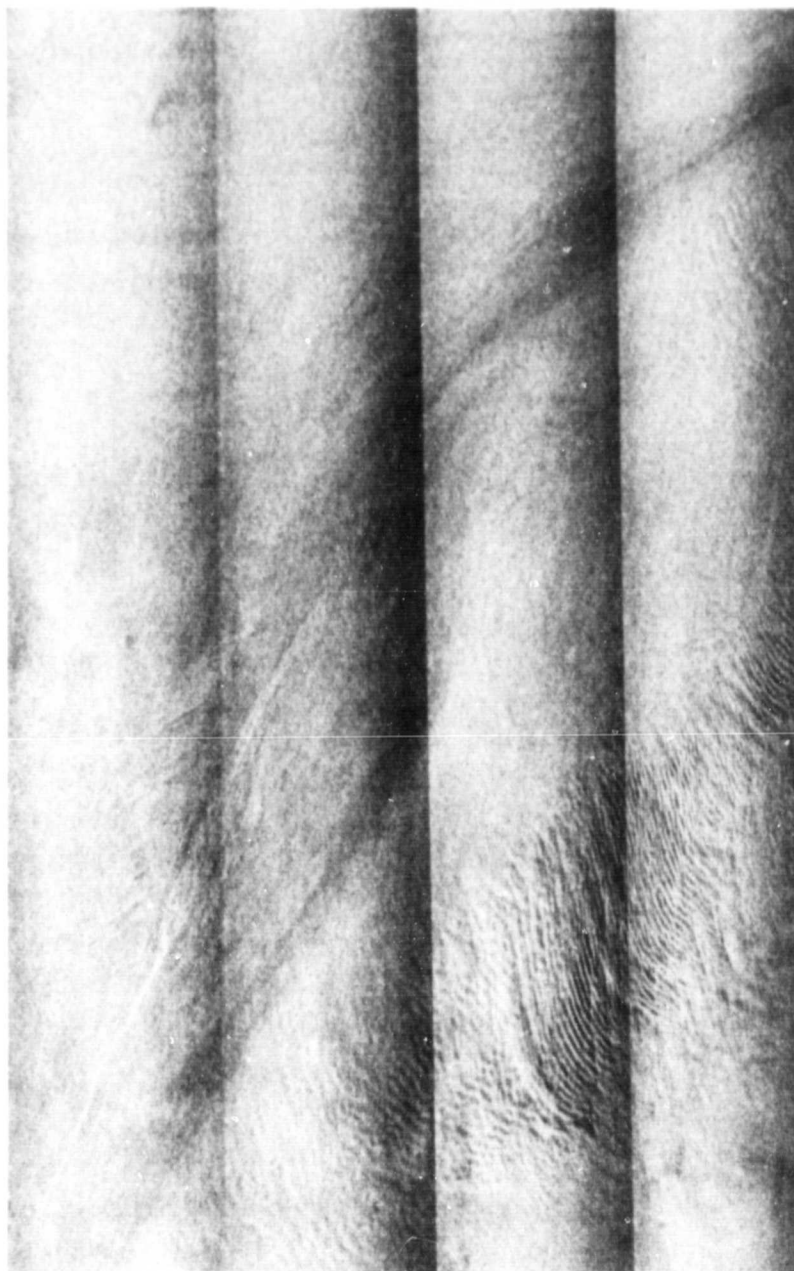
ILLUMINATION
DIRECTION →

N

0   25 km

Upstream of the Charleston Bump, the Gulf Stream is very stable; its shoreward boundary follows closely the shelf break between the 100-meter and 200-meter contours, as shown on this image taken about 100 kilometers east of Jacksonville, Florida (see the bathymetric chart opposite Image 14 for location).

The ribbon of low intensity extending from upper right to lower left marks the shoreward boundary of the Gulf Stream. Note the high correlation between this boundary and the bathymetry shown on the chart that is superimposed on the image. The
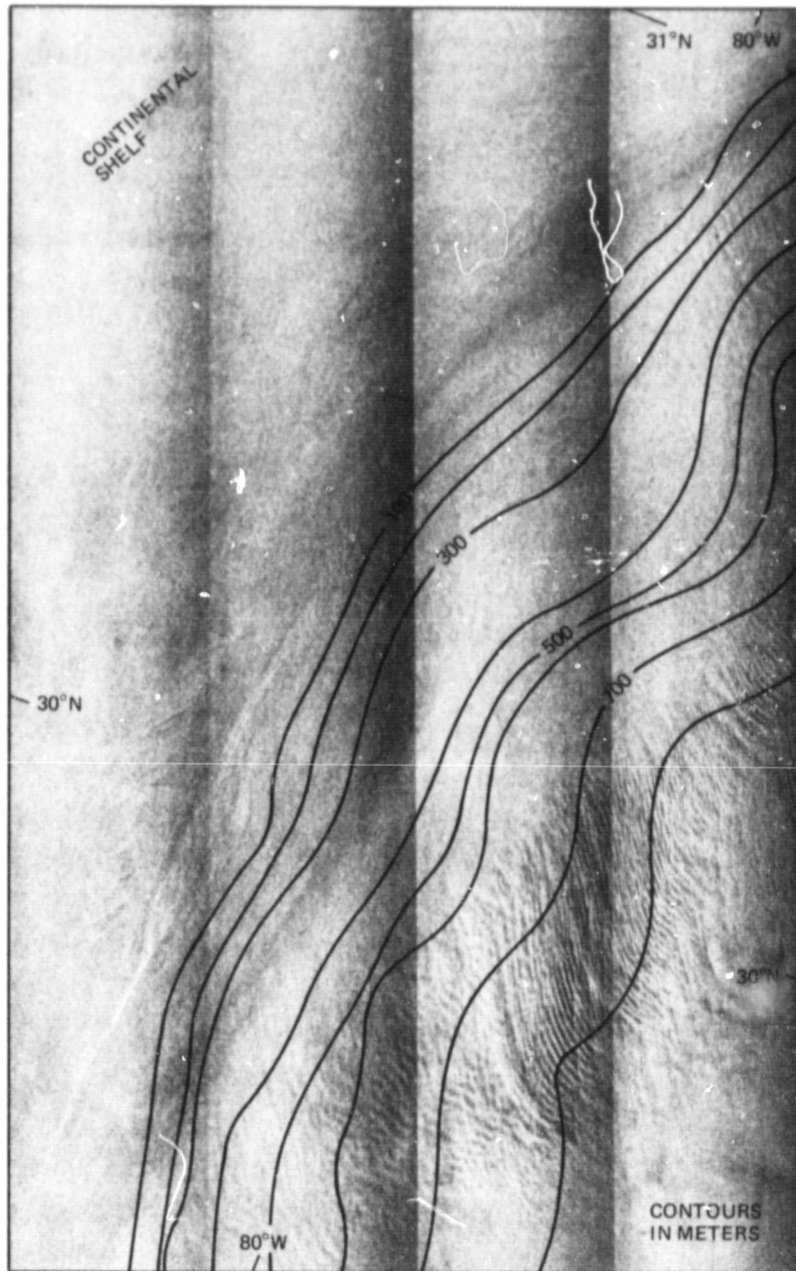
Bathymetric chart superimposed on Image 16.

inflection of the current seen in the center of the image is evidently associated with the bathymetric features. To the east of the current boundary are small-scale linear striations similar to those found in Images 8 and 15.

(Rev. 1110; 1444 GMT, September 12, 1978.)
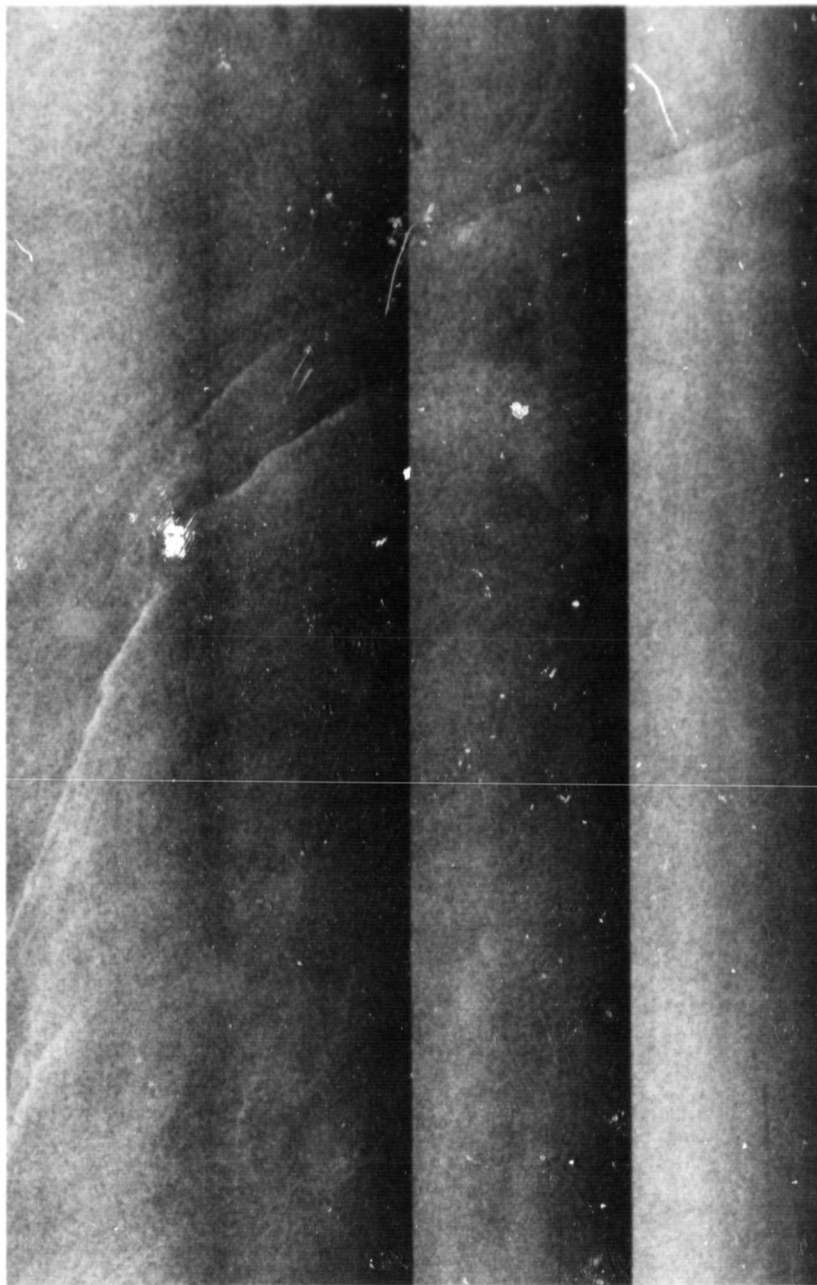
ILLUMINATION
DIRECTION →

N

0   25 km

The Loop Current is that portion of the Gulf Stream System in the eastern part of the Gulf of Mexico between the Yucatan Channel and the Florida Straits. The fragmentary, linear features on this image are probably signatures of the Loop Current.

The surface temperature contrast associated with the Loop Current is too weak in summer to be detected by infrared imagery, and another means must be used to confirm the SAR observations. In the absence of any concurrent in situ observations of
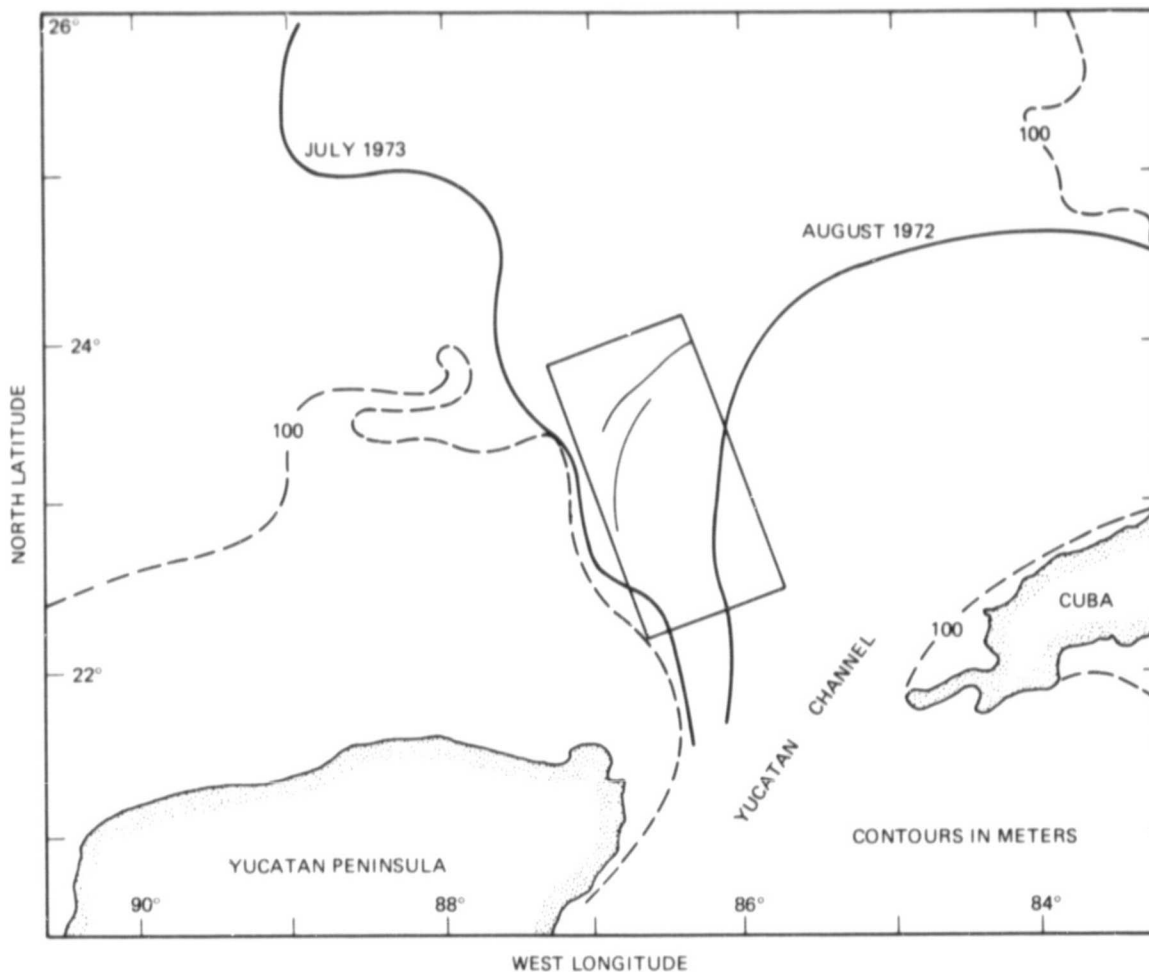
Map showing the positions of the Loop Current (thick lines) during August 1972 and July 1973. The current signatures are indicated by thin lines.

this current, we can compare this image only with previous observations. Therefore, a rectangle representing the image area is superimposed on an isotherm map; the isotherm was 22 degrees Celsius at a 100-meter depth, based on in situ measurements (adapted from Maul, 1977). This isotherm has been used as an indicator for the position of the Loop Current (Leipper, 1970). Although the path of the Loop Current has both annual and interannual variabilities (Behringer et al., 1977), this figure suggests that the features on the image are within the probable region of the Loop Current. Similar features have also been detected in Revolutions 472, 637, 759, 838.

(Rev. 393; 1147 GMT, July 24, 1978.)

53

3.4 The Gulf Stream Rings and Eddies

East of Cape Hatteras the path of the Gulf Stream develops wave-like meanders. They have a wavelength of 200 to 400 kilometers and propagate downstream with growing amplitudes that can reach 400 kilometers near 60°W (Hansen, 1970). West of 60°W, however, the meanders have grown so large that they occasionally close on themselves to form eddies of closed circulation. These eddies are then shed from the Stream into the surrounding water, where they are called "Gulf Stream rings."

Rings with clockwise circulation north of the Gulf Stream carry warm, highly saline Sargasso Sea water into the cold slope water of low salinity; they are usually called "warm-core rings" because of the relatively high temperature of the cores. Rings with counterclockwise circulation south of the Stream carry the slope water into the Sargasso Sea; they are usually called "cold-core rings" because of the relatively low temperature of the cores.

Because the rings transport enormous amounts of mass, heat, momentum, and chemical and biological substances, they are an important part of the general circulation of the western North Atlantic Ocean (e.g., the Ring Group, 1981; Lai and Richardson, 1977; Saunders, 1971).

Further east, the Gulf Stream is somewhat stabilized by the confining effects of the Grand Banks of Newfoundland and its extension, the Southeast Newfoundland Rise (Fofonoff, 1980). After passing the Grand Banks, however, the Gulf Stream enters another unstable regime and undergoes a drastic change: it divides erratically into two branches with intense eddy shedding (e.g., Mann, 1967; Clarke et al., 1980; Mountain and Shuhy, 1980). Cold eddies with water properties characteristic of this region have been found drifting to the south of the Gulf Stream about 1000 kilometers west of the Grand Banks (McCartney et al., 1978) and are sometimes called "Gulf Stream Extension rings."

Owing to their time-varying nature, the Gulf Stream rings and eddies are difficult to observe with shipborne instruments alone. Fortunately, remote sensing from a satellite is a powerful means to detect and track them. Infrared imagery detects the temperature contrasts associated with the rings and eddies (e.g., Legeckis, 1978), and satellite-tracked buoys monitor the movements and currents of the rings on an all-weather, long-term basis (Richardson et al., 1977; Cheney et al., 1980). However, the ability of a spaceborne SAR to detect rings and eddies was not realized before the launch of Seasat, and the first SAR images that showed them were indeed a pleasant surprise. The imaging mechanisms for rings and eddies, though not well understood yet, should be quite similar to those for currents, as discussed on page 43.

From the many images of the Gulf Stream area, we have selected five that show typical rings and eddies. Images 18 and 19 show two different warm-core rings on the Continental Slope off the United States' northeast coast, and they reveal quite different characteristics. Image 20 appears to show a cold-core ring in the Sargasso Sea, though direct supporting evidence is lacking, and Images 21 and 22 each show a cold eddy near the Grand Banks.

18. A Warm-Core Ring Off Delaware Bay

0   20 km   N↑   ILLUMINATION
←DIRECTION
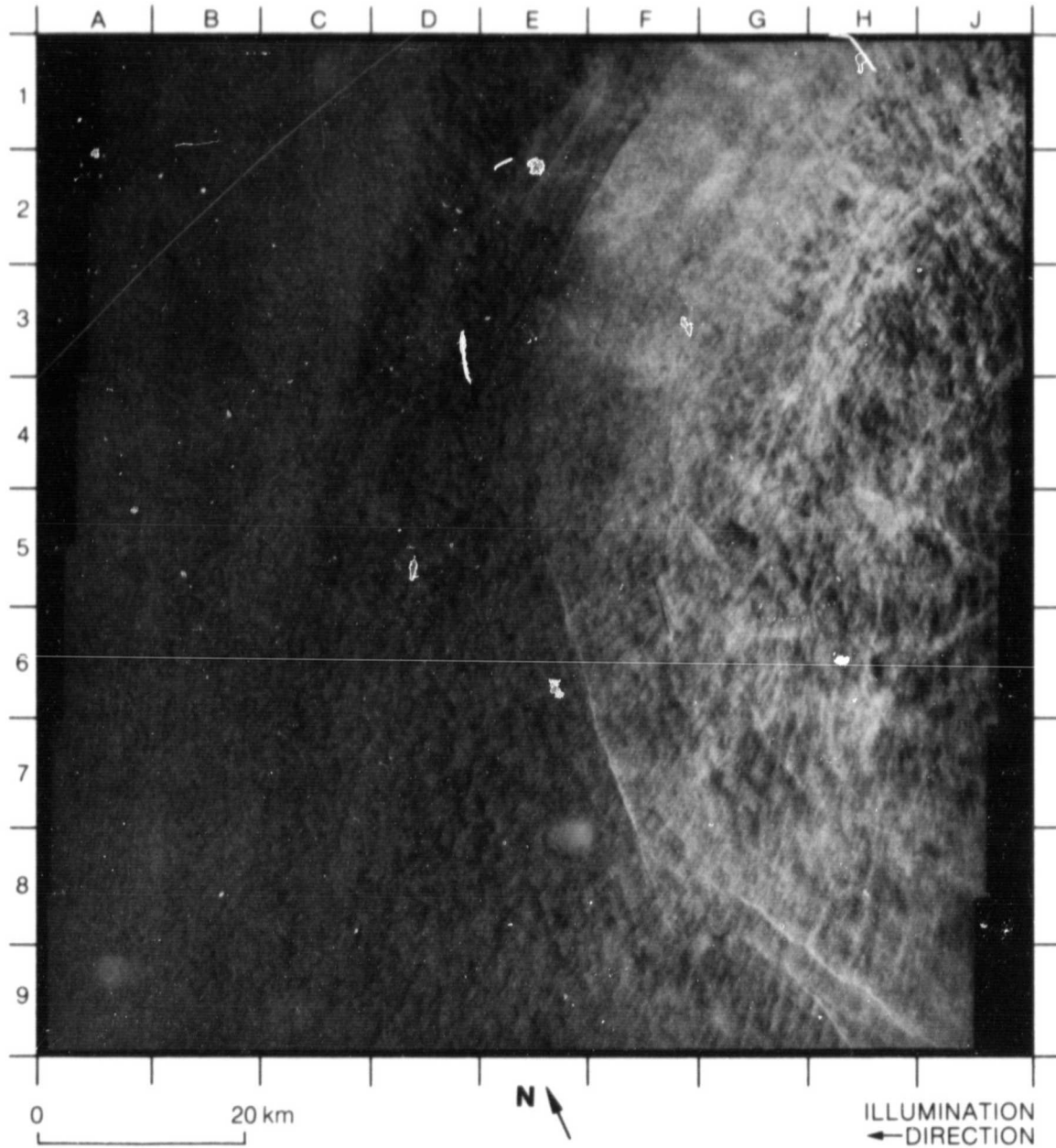
On the right of the image is the western portion of a warm-core ring about 100 kilometers southeast of Delaware Bay. The ring was repeatedly observed during four other overpasses (Revolutions 1275, 1318, 1404, and 1447) and some characteristics common to all of its images have been identified (Lichy et al., 1981). The area within the ring generally has a higher intensity than the surrounding area with a boundary characterized by concentric curvilinear lines (from E1 and F1 to H9 and J9). These lines are bright in the southern part of the ring and dark in the northern part. Small-scale patches of high and low intensities (the mottled texture) surround the ring and wave-like patterns (J2 to J5) occur near the ring center. The cause of these features is not understood; however, they are most likely associated with the current shears and temperature contrasts produced by the ring.
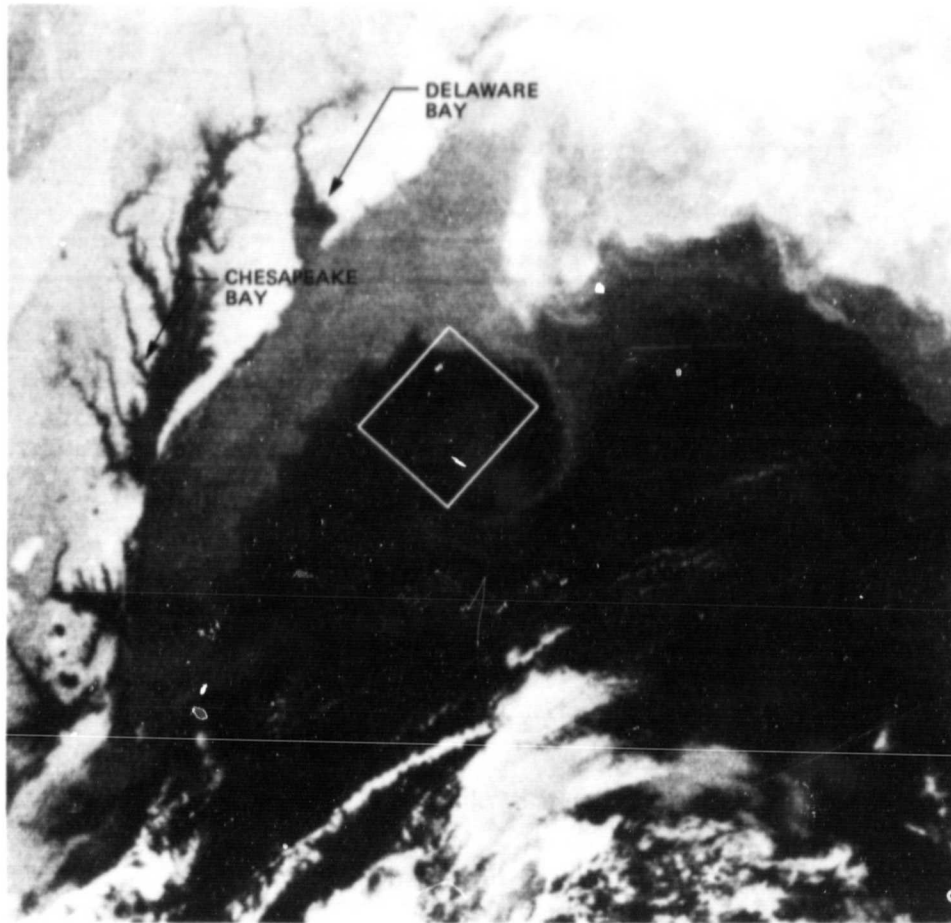
Infrared image of the area off Delaware Bay. The area of the SAR image is enclosed by a rectangle.

A NOAA-5 infrared image of the same ring was taken at 0021 GMT, September 21, 1978, about 4 hours before the Seasat pass. In this image the warm-core ring is most distinctly outlined along its eastern boundary, which is formed by a strip of the cold shelf water (bright area) embedded in the relatively warm slope water (dark area) as a result of the clockwise motion of the ring water. However, the western boundary clearly seen in the SAR image is invisible in the infrared image due to the weak thermal contrast at the boundary.

The SAR image also shows an east-west traveling swell (with a wavelength of about 145 meters) and a southward moving ship at F6.

(Rev. 1232; 0408 GMT, September 21, 1978.)
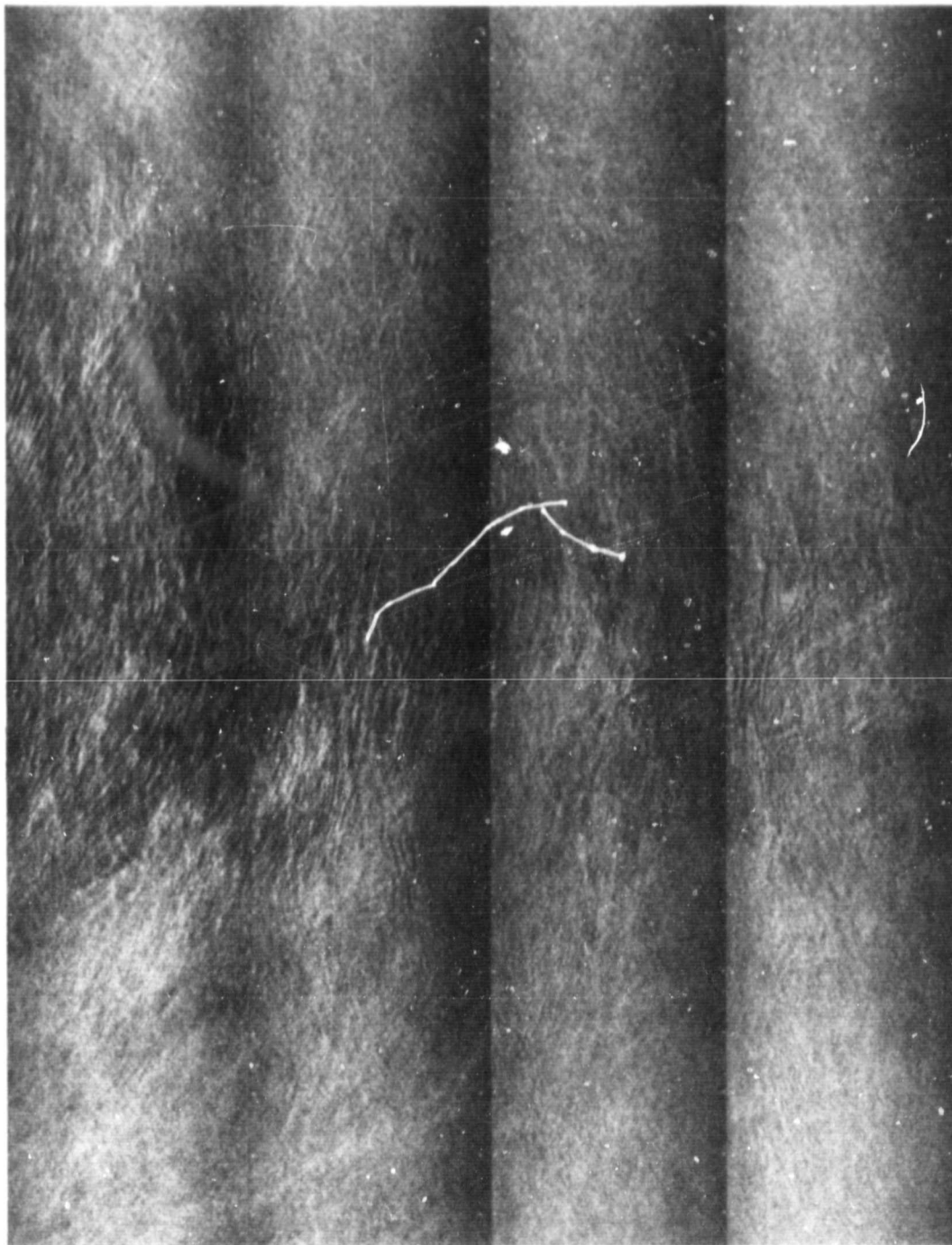
ILLUMINATION
DIRECTION ➝

N

0   20 km

The curvilinear features on the left of this image are manifestations of the eastern edge of a warm-core ring with characteristics that differ considerably from those shown on the preceding image. Instead of brighter than the surrounding area, this ring is darker. No mottled patterns or bright (or dark) lines around the ring edge are found on this image. Rather, this ring has an appearance of more extended wave-like patterns.
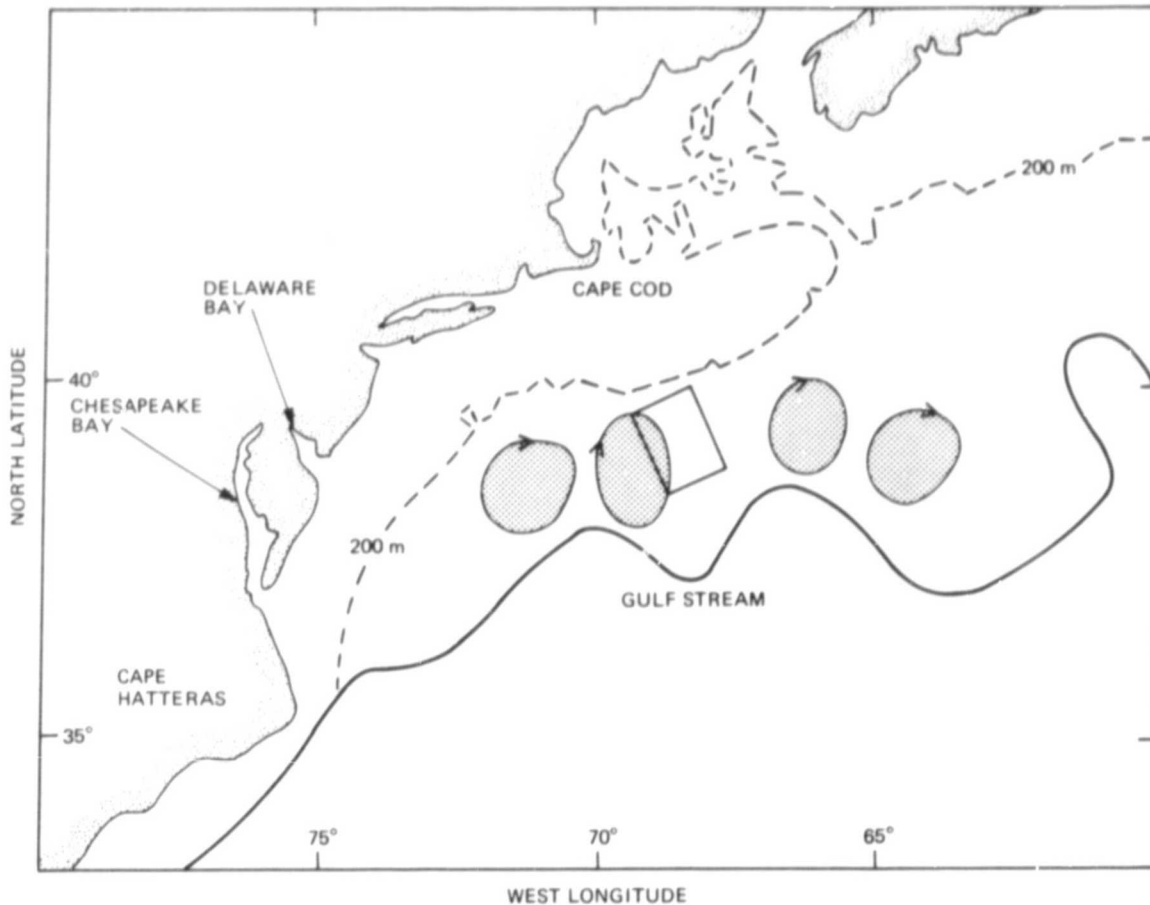
Positions of the Gulf Stream and its warm rings on August 27, 1978. The imaged area is enclosed by a rectangle.

The positions of the Gulf Stream and its warm-core rings on the day of the Seasat pass are shown on the map (adapted from *gulfstream*, 1978). The map indicates that the SAR image caught the eastern edge of a ring. To the west of this ring lies the ring of Image 18, which was taken a month later. Because no warm-core rings have ever been completely imaged by the SAR, we do not know whether the observed differences between these two images are due to an east-west asymmetry in image characteristics of a warm-core ring, or some other phenomena.

(Rev. 880; 1233 GMT, August 27, 1978.)

20. A Cold-Core Ring in the Sargasso Sea

ILLUMINATION
DIRECTION →

N

0   25 km
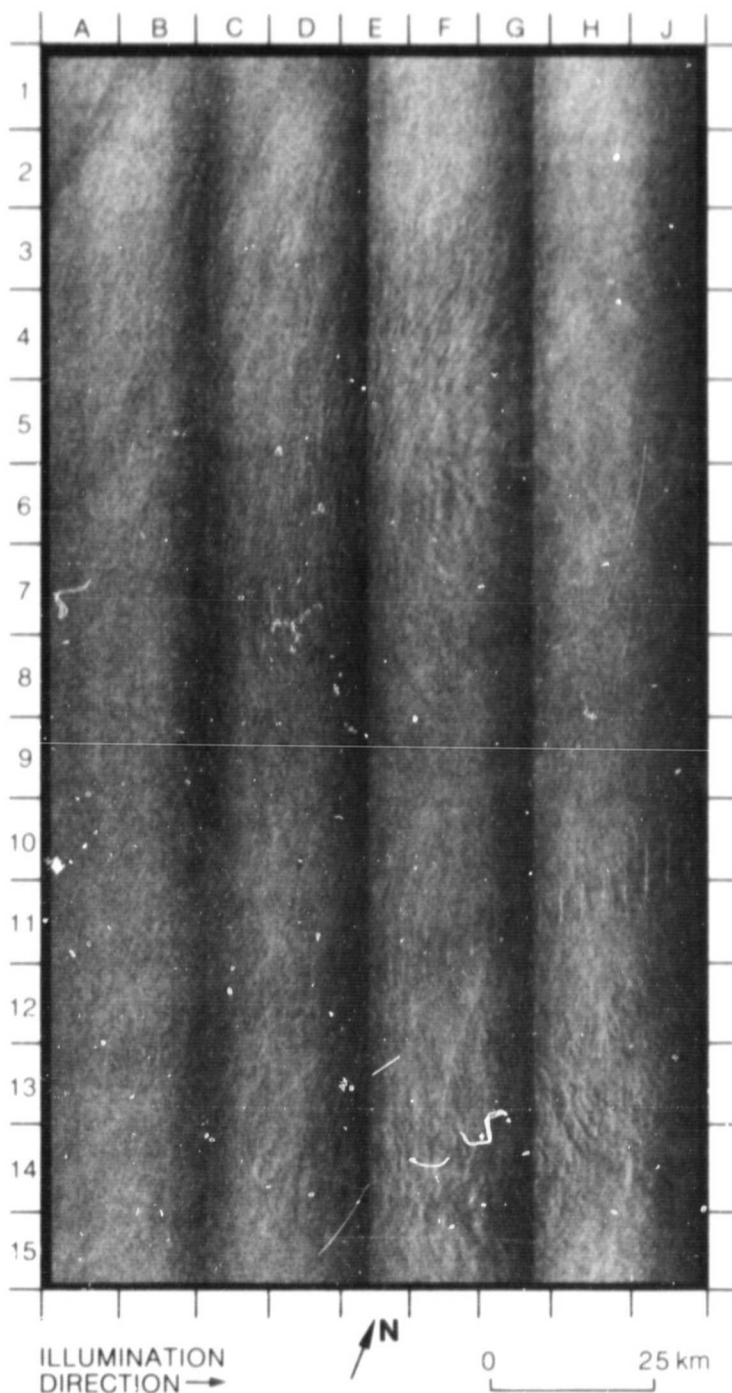
The boundary of a cold-core ring appears in this image, which covers an area south of the Gulf Stream in the Sargasso Sea. Using information from buoys and infrared imagery, a cold-core ring was tracked through this area for some time during the Seasat mission. The map, adapted from Cheney (1981), shows the position of the image, the tracks of the cold-core ring, and the path of the Gulf Stream as inferred from satellite infrared images taken on August 26, 1978. Although the ring was not tracked for nearly six weeks before and after this image was taken, what evidence we have indicates that the ring was quite probably at the position of this image.
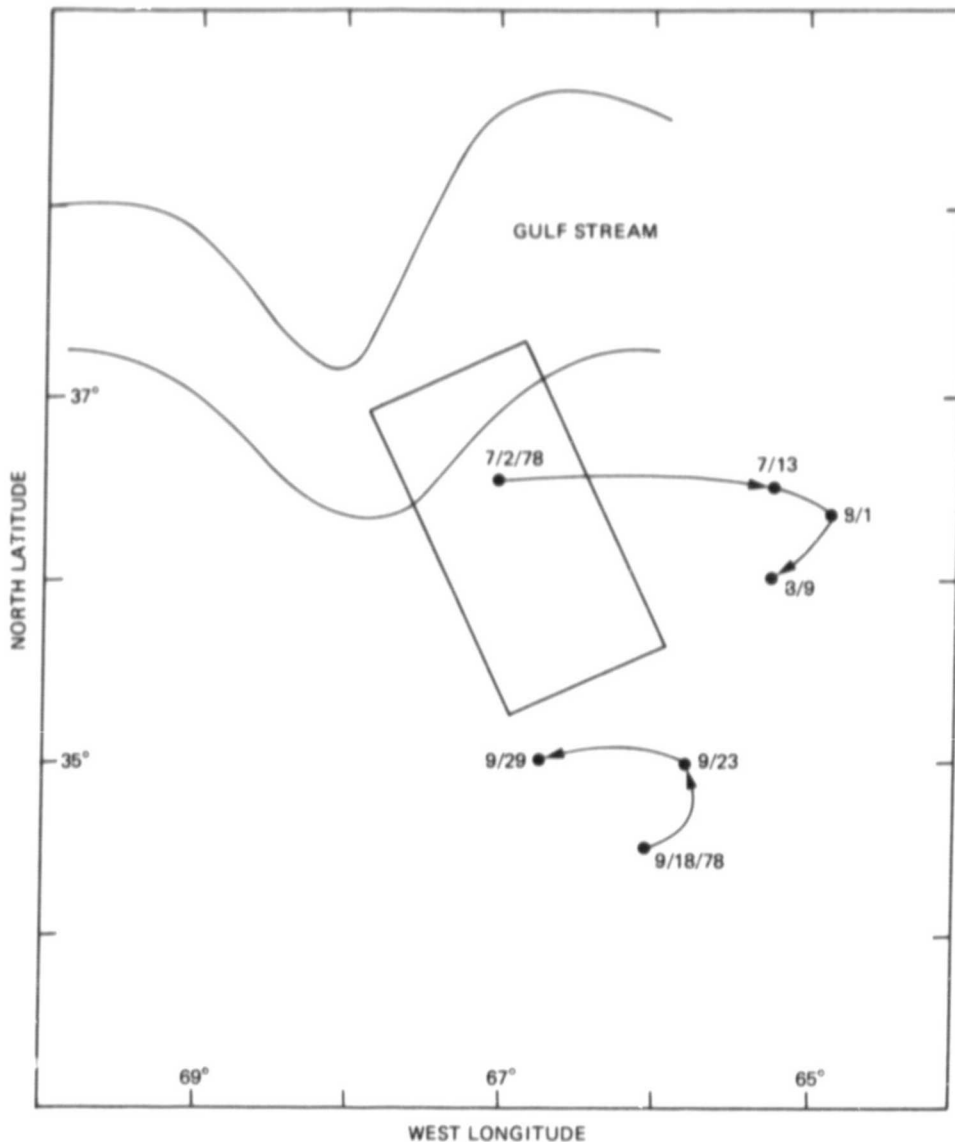
The solid circles represent the locations of the cold-core ring at the dates labeled. The imaged area is enclosed by a rectangle.

The two weak linear features on the image (from B1 to A3 and from D1 to A6) appear to be the southern boundary of the Gulf Stream, and the two features with some curvature centered on G6 and H13 appear to be the cold-core ring. The highly organized linear striations between F3 and C8 are probably produced by the strong shears developed between the Gulf Stream and the counterclockwise flow of the ring. It is not clear why there are two separate features associated with the ring. Perhaps they were due to the strong interaction of the Gulf Stream and the ring.

According to surface observations (Cheney, 1981), the same ring should have been imaged by the Seasat SAR in Revolution 1267 on September 23, 1978; however, no convincing features of a ring can be found on that image.

(Rev. 880; 1232 GMT, August 27, 1978.)

21. A Cold Eddy South of the Grand Banks of Newfoundland
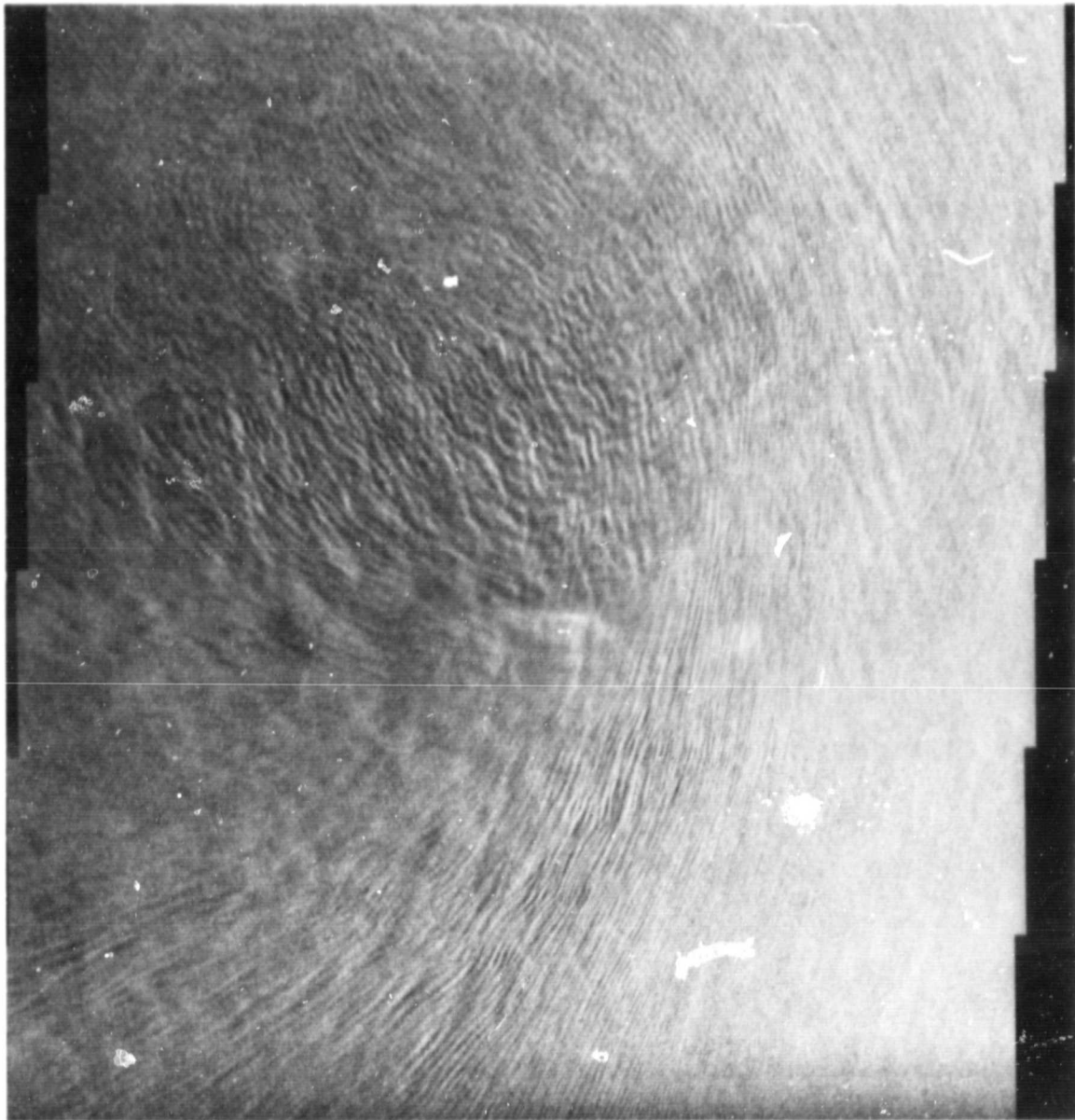
0   20km   N↑   ILLUMINATION
                                   ←DIRECTION

The circular feature with relatively low intensity and mottled texture at the upper left quadrant of the image is a cold eddy being formed south of the Grand Banks of Newfoundland. The surrounding water appears slightly brighter and has curvilinear striations about 100 kilometers long with spacings ranging from 400 to 1300 meters. The contrast in brightness is probably due to the temperature difference between the eddy and the surrounding water (see page 43); however, the reason for the change in texture is not known. The highly coherent striations suggest that they are aligned with strong currents. Variations in sea-surface roughness in this area due to the presence of cold eddies have also been reported by LaViolette et al. (1980), who used airborne radar observations and sun-glint patterns on satellite images.
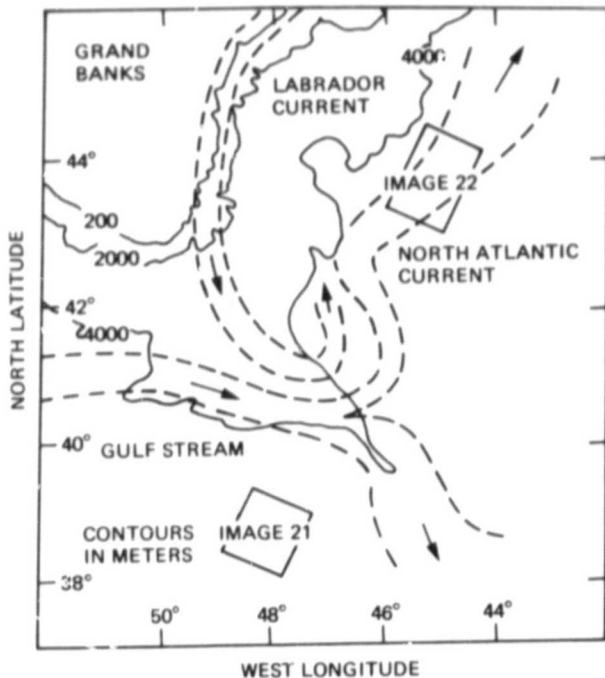
A schematic map of the time-averaged current system. The locations of Images 21 and 22 are enclosed by rectangles.
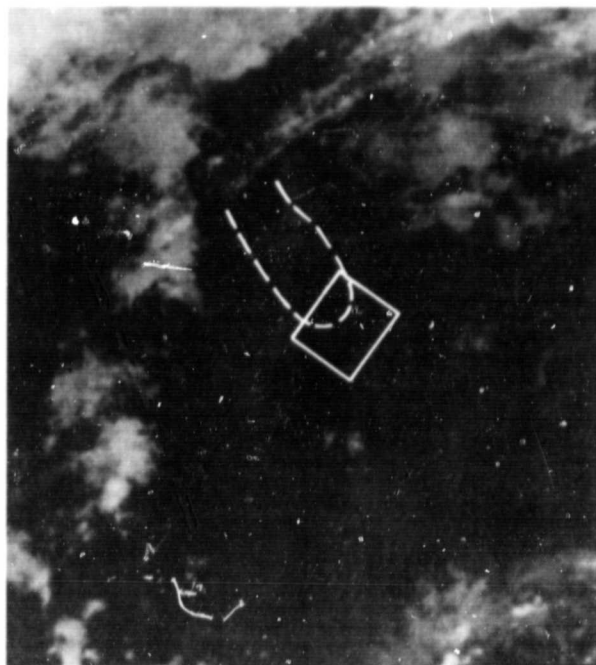
Infrared image of the area south of the Grand Banks. The area of the SAR image is enclosed by a rectangle.

The time-averaged current system in this area, together with the locations of Images 20 and 21, is shown on the map. As mentioned earlier (page 55), however, the current system in this area is highly time-dependent with eddies frequently shed to the south of the Gulf Stream, bringing cold, fresh Labrador Sea water into the Atlantic. Observations of cold eddies in the imaged area have been reported by Mann (1967) and Mountain and Shuhy (1980).

The infrared image of this area, taken by a satellite of the Defense Meteorological Satellite Program (DMSP) 3 days after the Seasat pass, indicates that the eddy on the SAR image indeed corresponds to a southward intrusion of cold water (the slightly lighter area enclosed by a dashed line on the infrared image), which perhaps led to the birth of a Gulf Stream Extension ring (page 55).

(Rev. 1231; 0227 GMT, September 21, 1978.)

22. A Cold Eddy East of the Grand Banks of Newfoundland

0   20 km   N↑   ILLUMINATION
←DIRECTION
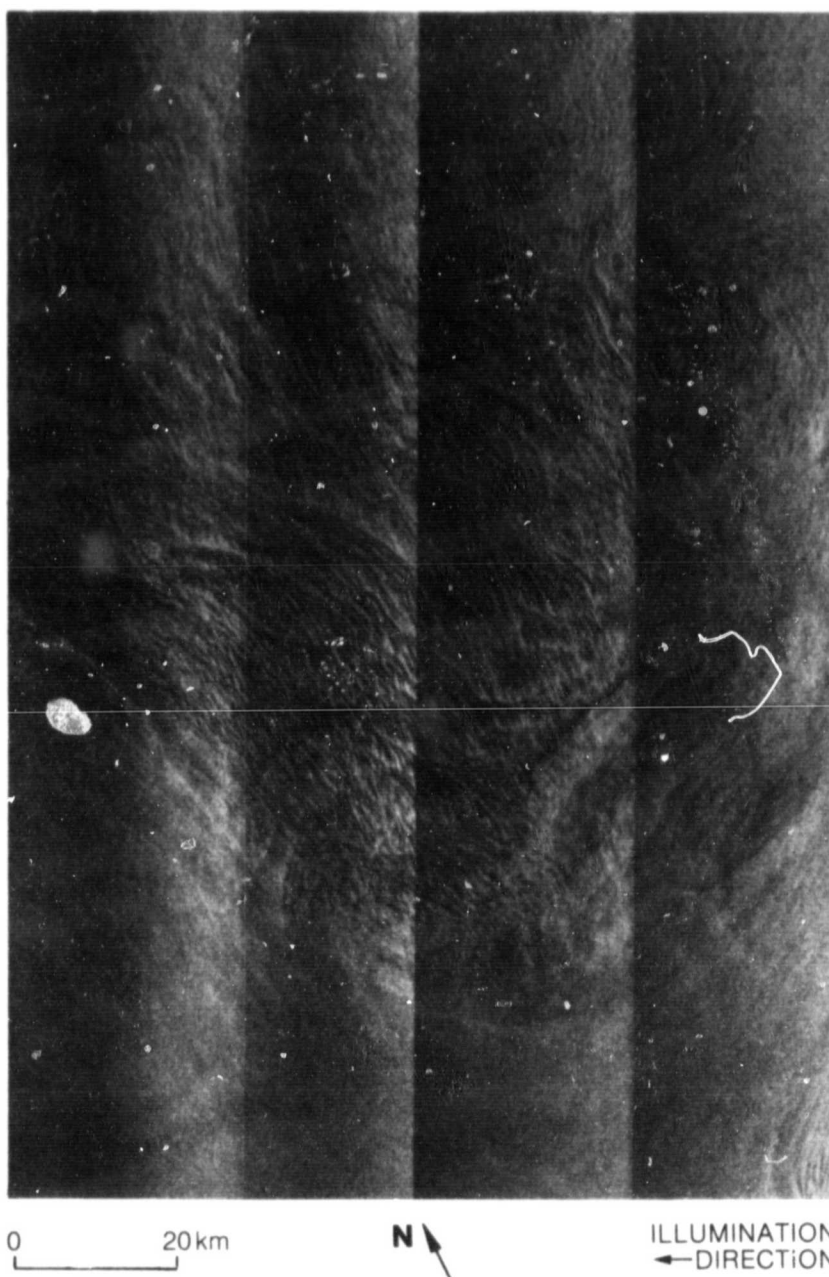
East of the Grand Banks, the northern branch of the Gulf Stream (the North Atlantic Current shown on the map opposite Image 21) is another current with intense meandering and eddy shedding. The resultant mixing of Gulf Stream water with Labrador Sea water has a great influence on the characteristics of the upper waters of the northern North Atlantic. We show here an image of a cold eddy in this dynamic region.

With a distinct, semicircular boundary to the south and west, this eddy is characterized by a more pronounced change in image texture than is the eddy shown on Image 21. The surrounding water has a more or less uniform intensity without the long striations of Image 21, whereas the eddy itself has complex surface signatures that vary from a mottled surface in its southern part to long striations in its northern part, where its boundary is rather diffuse.
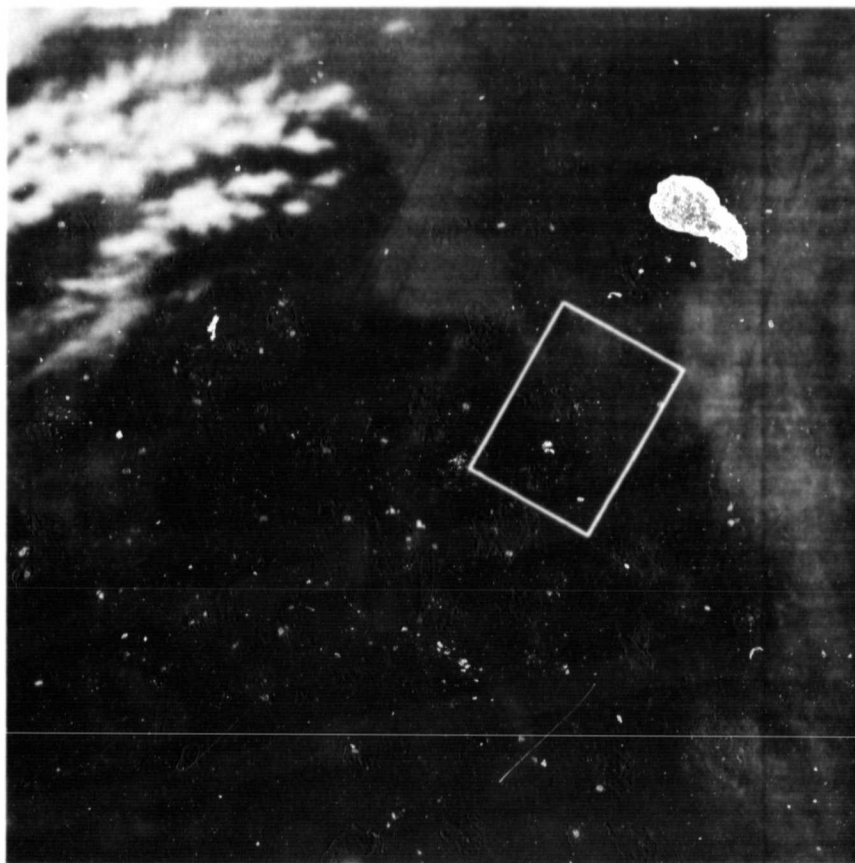
Infrared image of the area east of the Grand Banks. The area of the SAR image is enclosed by a rectangle.

This area was covered by clouds for an extensive period of time before and after the Seasat pass; the closest infrared image we can find without clouds in the area is the DMSP image taken 13 days earlier. It shows a complex gradation of intensities, representing waters of varying temperatures. Southwest of the SAR imaged area, the S-shaped dark strip corresponds to the warm water of the North Atlantic Current, and the bright area to the west and north corresponds to the cold water of the Labrador Current with its eddies and meanders. Although the SAR imaged area was then occupied by a large cold eddy, it seems more likely that the eddy detected by the SAR 13 days later was something else, perhaps the cold feature northwest of the SAR imaged area (note its similarity in shape to the SAR-detected eddy).

(Rev. 1360; 0303 GMT, September 30, 1978.)

3.5 Large-Scale Variabilities of the Eastern North Pacific

In the Pacific Ocean, the Seasat SAR collected extensive imagery covering most of the eastern North Pacific within 1000 kilometers of the west coast of North America (See Figure A-1). Because the eastern part of an ocean generally has less variability than the western part (cf. Wyrtki et al., 1976), the imagery of the eastern North Pacific shows fewer features than that of the western North Atlantic. However, some large-scale features were repeatedly observed by the SAR in two dynamic regions of the eastern North Pacific—the California Current and the North Pacific subtropical front. In this section we present two images showing some typical features in these two regions.

The California Current flows southward along the west coast of the United States. It forms between latitudes 40°N and 50°N and is fed from the west by a broad zonal flow—the West Wind Drift of the North Pacific (for a comprehensive review see Hickey, 1979). The flow is broad (the width is of a few hundred to 1000 kilometers) and slow (velocities are generally less than 20 centimeters per second), with complex spatial and seasonal variabilities. At most times, the current is masked by meanders and detached eddies, and is hardly well-defined. For this reason, shipborne observations of the current have suffered serious sampling problems; remote sensing by satellite infrared radiometers, however, has provided high-resolution, broad-coverage observations of the current (e.g., Bernstein et al., 1977). Unfortunately, parts of the California Current are often covered by clouds and fog, making the need for microwave remote sensing imperative. Image 23, showing an area off the coasts of California and Oregon, demonstrates the potential of a spaceborne SAR for detecting the variabilities of the California Current.

The North Pacific subtropical front is a narrow region of strong north-south gradients of temperature and salinity (e.g., Roden, 1975). It lies in the Ekman convergence zone between the northeasterly trade winds and the westerlies, with its position varying from 25°N to 35°N. The surface signature of the front varies from a sharp change in both temperature and salinity in winter and spring to a sharp change in salinity alone in summer and fall. The front has a complex structure in both the horizontal and the vertical, with frequent occurrences of multiple fronts. Image 24, a view of the frontal region, shows some complex patterns that might be caused by current shear associated with the front.

23. Eddies and Meanders of the California Current

ILLUMINATION
DIRECTION →

↑N

0   50 km
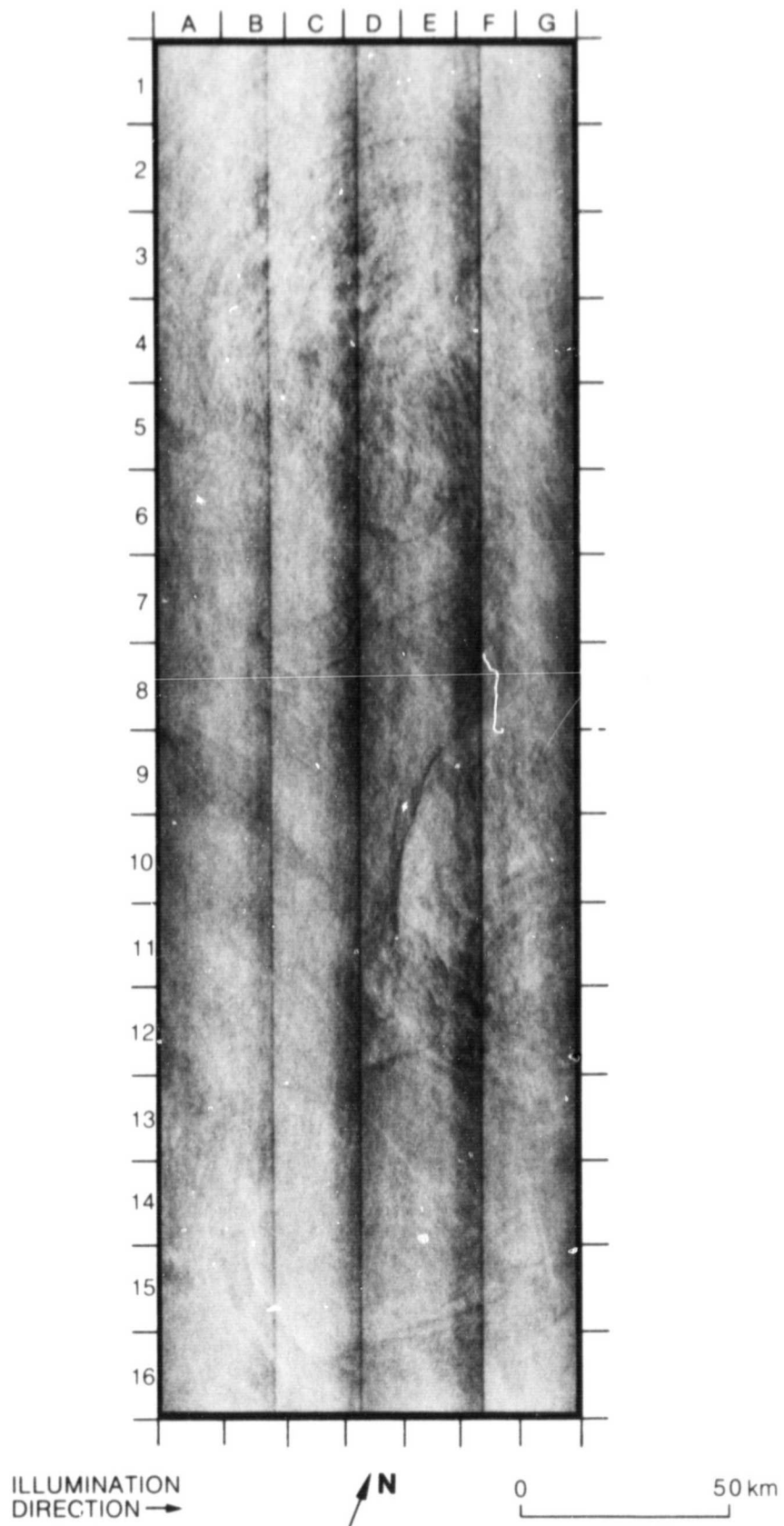
ORIGINAL PAGE
BLACK AND WHITE PHOTOGRAPH
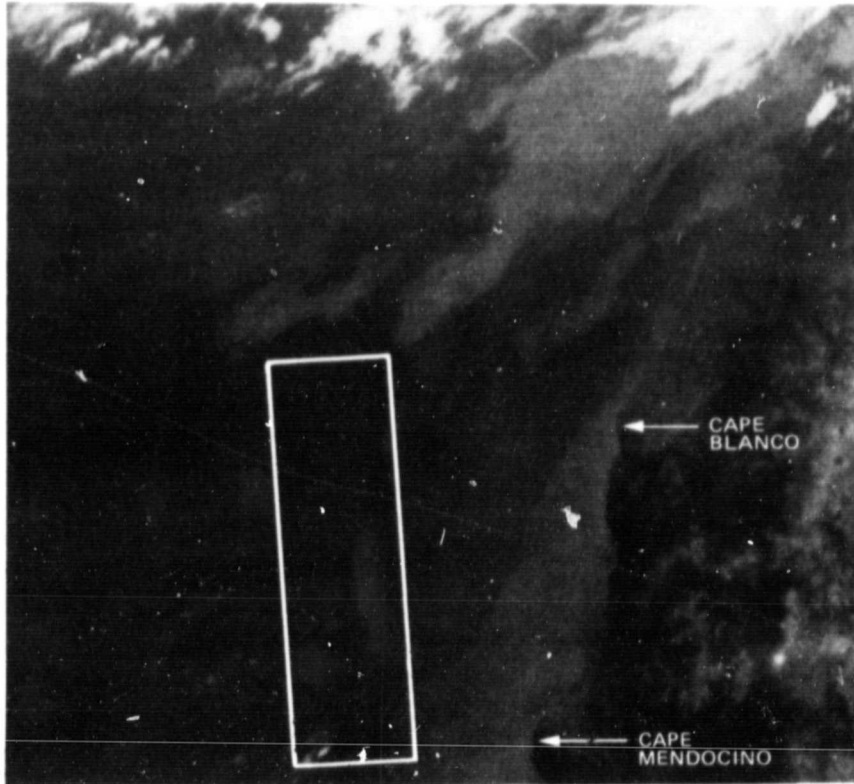
Infrared image of the area off northern California and southern Oregon. The area of the SAR image is enclosed by a rectangle.

This image shows an area about 200 kilometers off the Pacific Coast near the border of California and Oregon. Centered on D3/D4 and G10/G11 are two eddy-like features with diameters of 100 kilometers. Their outer edges appear to be connected by a slightly dark band extending from A4/A5, through G8, to D12. The band is probably the manifestation of a meandering current interacting with the two eddies.

The infrared image of this area was taken by the NOAA-5 satellite about eleven hours before the pass. The SAR imaged area (enclosed by the rectangle) has a generally darker tone (higher surface temperature) than the near-shore area; however, the eddies and meanders detected by the SAR are not seen on the infrared image. The near-shore area between Cape Blanco and Cape Mendocino is characterized by a band of cold shelf water (the light gray area) that extends well into the warmer offshore water near Cape Mendocino. The offshore tip of this cold-water band may be expressed on the SAR image by the group of lines from G14/G15 (where they appear dark) to C15/C16 (where they become light).

Other SAR images showing similar features in this area include those from Revolutions 222, 466, and 761.

(Rev. 710; 1532 GMT, August 15, 1978.)

The prominent features on this image are the short filaments near the upper edge of the image and a long curvilinear feature extending from E4 to G9. While this image was taken near the region of the North Pacific subtropical front, we do not have any information on the origin of these features; however, they were repeatedly observed by the SAR (e.g., Revolutions 273, 474, and 761) and likely are persistent oceanic phenomena.
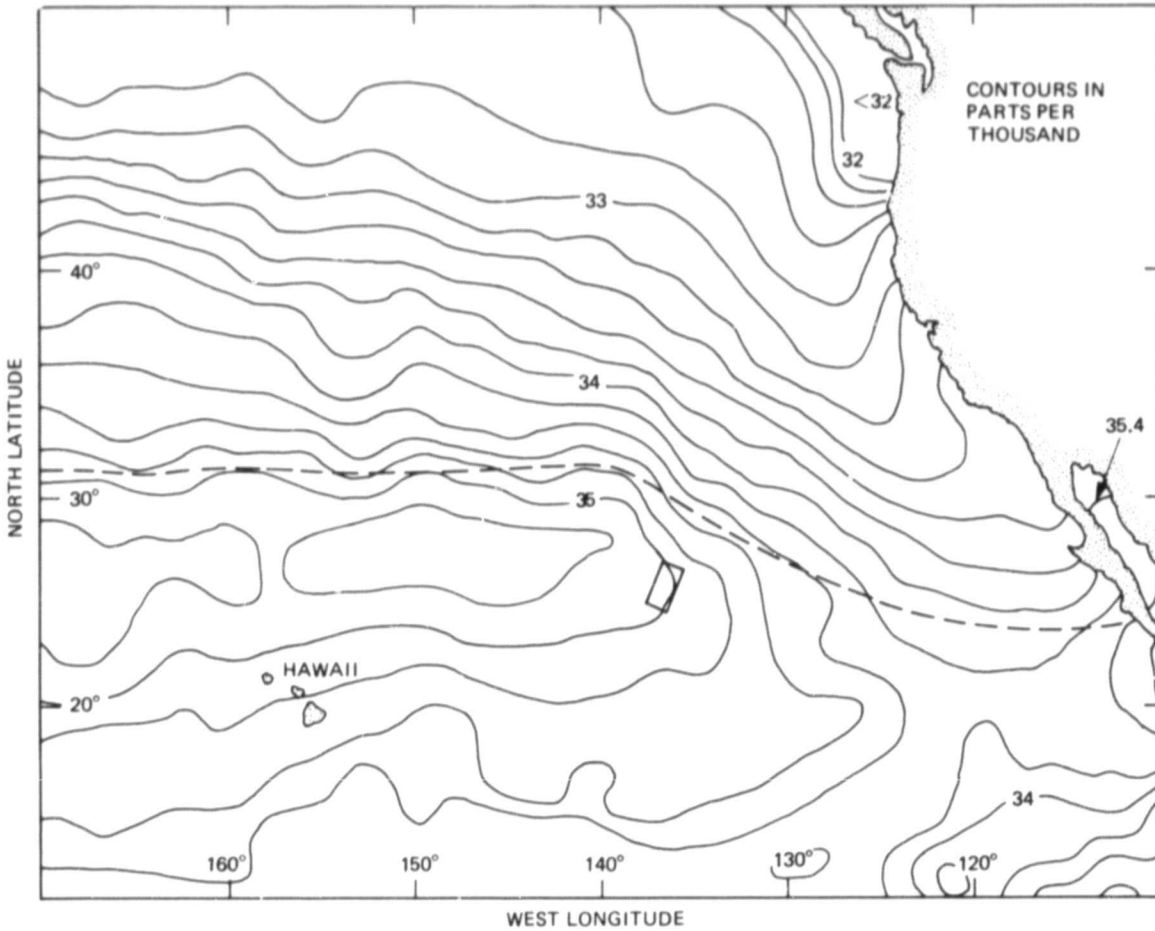
Surface salinity distribution in the eastern North Pacific (after Robinson, 1976). The dashed line represents the subtropical front, and the small rectangle denotes the location of the SAR image.

The annual mean distribution of surface salinity and a schematic representation of the subtropical front in the eastern North Pacific are shown on the map. The SAR imaged area is in a region where the lines of constant salinity run in a nearly north-south direction, roughly consistent with the orientation of the observed features. Because a front usually results from the convergence of surface currents, the observed features might be manifestations of the subtropical front convergence zone.

(Rev. 230; 0301 GMT, July 13, 1978.)

3.6 Coastal Phenomena

The importance of monitoring oceanic phenomena in the coastal zones has long been recognized by oceanographers and meteorologists; these phenomena bring the most direct and critical effects of the oceans on human society. Various sensors and techniques have played important roles in monitoring coastal waters from space: infrared radiometers on board the NOAA satellites have been routinely used to produce maps of sea-surface temperatures in certain coastal areas; the coastal zone color scanner on board Nimbus-7 has begun to provide information on ocean color that can be used to monitor the primary biological productivity in coastal waters (Hovis et al., 1980). In this section we present six Seasat SAR images to demonstrate that various coastal phenomena can be detected from space also through their effects on sea surface roughness.

As the result of one or several of the coastal processes that include coastal upwelling, seasonal cooling, and river discharge, a band of relatively cold and fresh water usually forms on the continental shelf. The exchange and mixing of this shelf water with the warmer and saltier offshore water often produces pronounced variations in sea-surface roughness detectable on the SAR images. Image 25 shows the offshore intrusion of shelf water that results from the seasonal upwelling off California; Image 26 shows many features of the interaction of the shelf water off the northeast coast of the United States with the Gulf Stream; Image 27 shows features probably associated with cross-shelf mixing on the continental shelf off Texas.

Where the continental shelf is not extended seaward, strong offshore boundary currents are directly affected by the coast and its geometry. Flow separation with vortex shedding occurs at coastal headlands and other places of strong coastal curvature. Image 28 shows several small vortices generated at the Yucatan coast by the Yucatan Current. A series of similar vortices, generated by a highly variable coastal current, also appears to the south of Grand Bahama Island, as shown in Image 29.

It is well known that oil-containing films on the sea surface damp short capillary-gravity waves and thus smooth the sea surface (e.g., Hühnerfuss and Garrett, 1981). The oil discharged from natural offshore oil seeps often contaminates the coastal waters and produces slicks that can be identified on the SAR images as dark bands within bright areas. Image 30 shows typical oil slicks from natural seepage, and drilling platforms south of Santa Barbara, California.

25. Coastal Eddies Off Point Arena, California
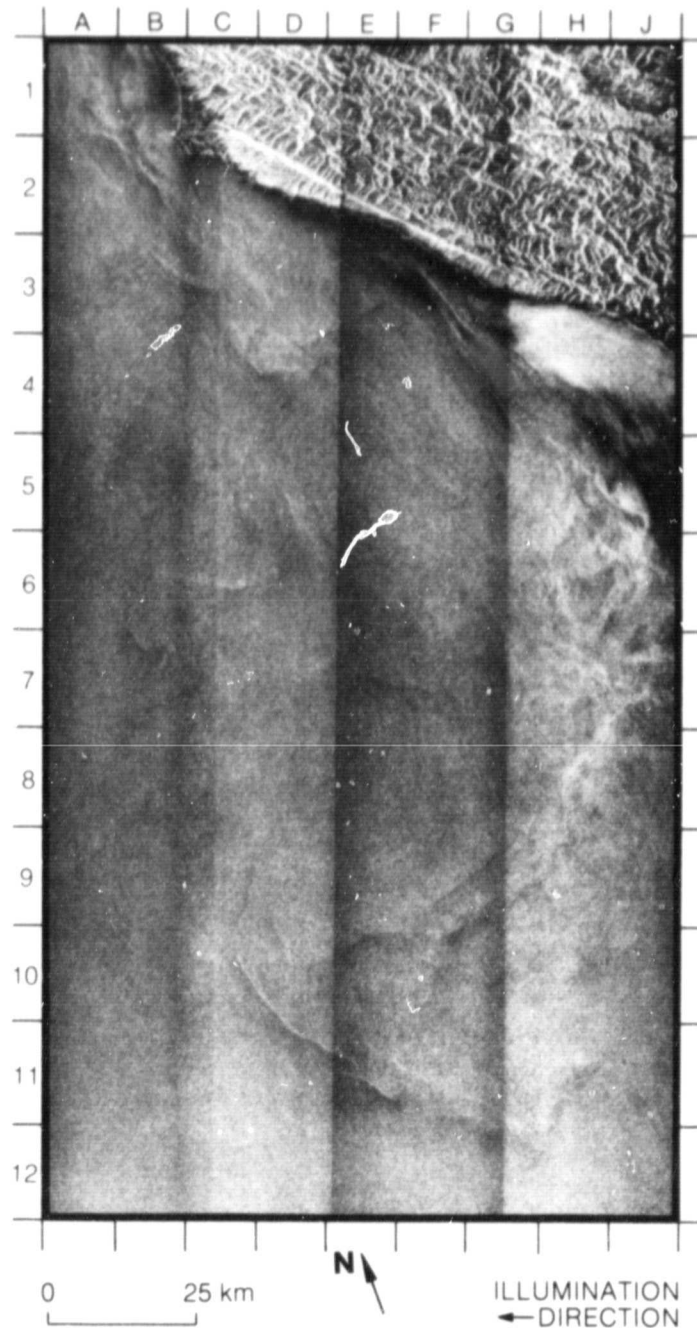
This image of the coastal waters south of Point Arena (at B2), California, shows a large-scale, tongue-like feature protruding from the coast into the ocean (from H5, through C10, to H11). The feature is characterized by small-scale swirls (H5 to J7) and filaments of low and high image intensities (H8 to E11). Another feature of smaller size and weaker signatures can be seen south of Point Arena (B3 to C6/D6).

Off the coast of California, the annual upwelling season ends usually in August. Then begins the process of intense exchange between the cold coastal water resulting from the upwelling and the relatively warm offshore water. This process produces various eddies and plumes (Sverdrup et al., 1942, p. 725) as shown on the image.
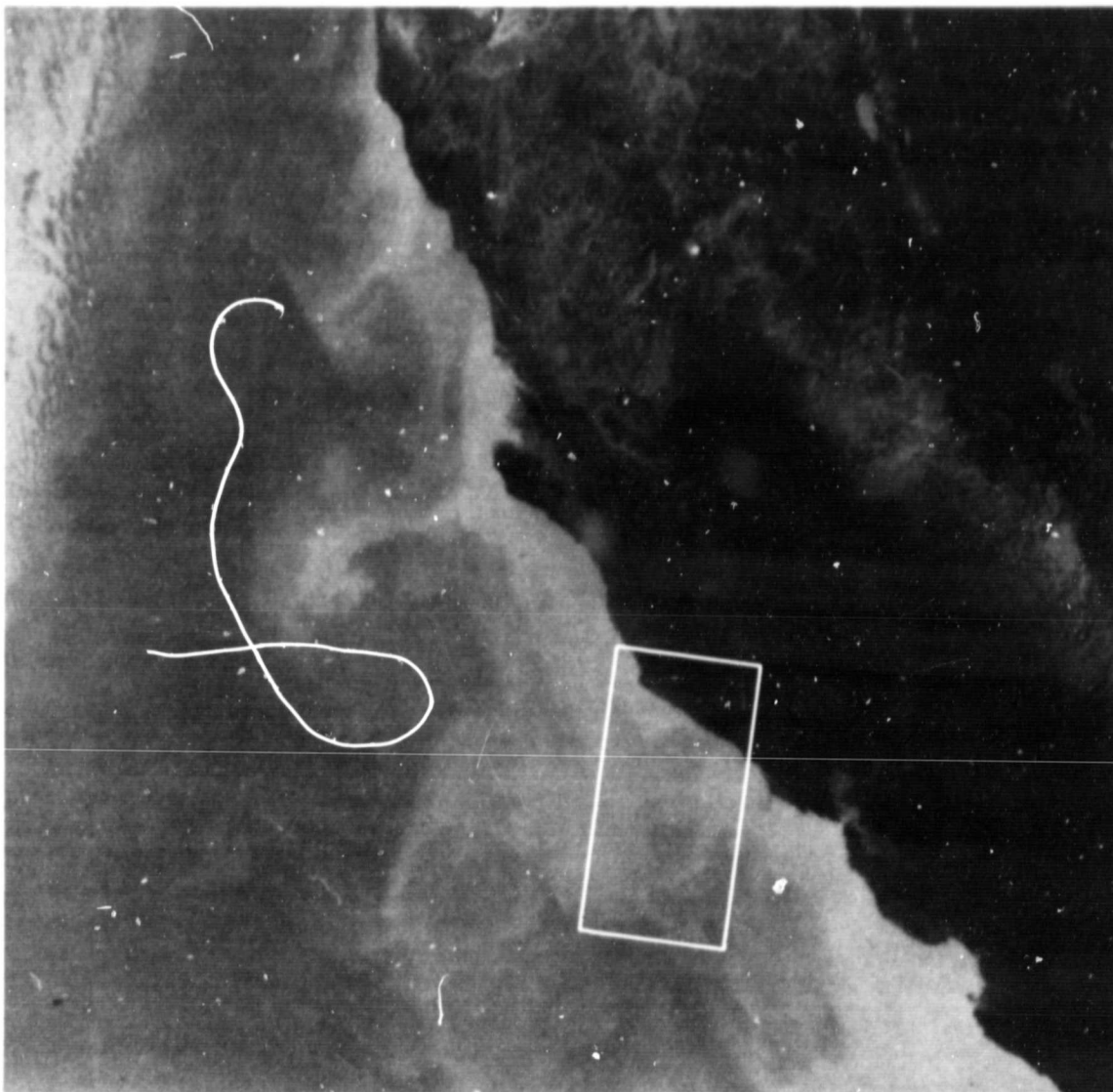
Infrared image of the area off northern California. The area of the SAR image is enclosed by a rectangle.

The NOAA-5 infrared image was taken about ten hours after the Seasat pass. This image reveals a large-scale pattern of the mingling of the cold (light gray) and warm (dark gray) waters. Offshore intrusions of tongue-like plumes of cold water are the major characteristics. Note that the shapes and positions of the cold-water plumes in the area of the SAR image (enclosed with a rectangle) correspond very well to those features on the SAR image. Three days later, the same area was imaged by the SAR again (Revolution 1449); however, due to low winds in the coastal zone, these features were only vaguely detected.

Also shown on the SAR image are a few packets of internal waves in the near-shore areas (A1 to B2 and F3 to J5), and short-crested surface waves in most of the area.

(Rev. 1406; 0821 GMT, October 3, 1978.)
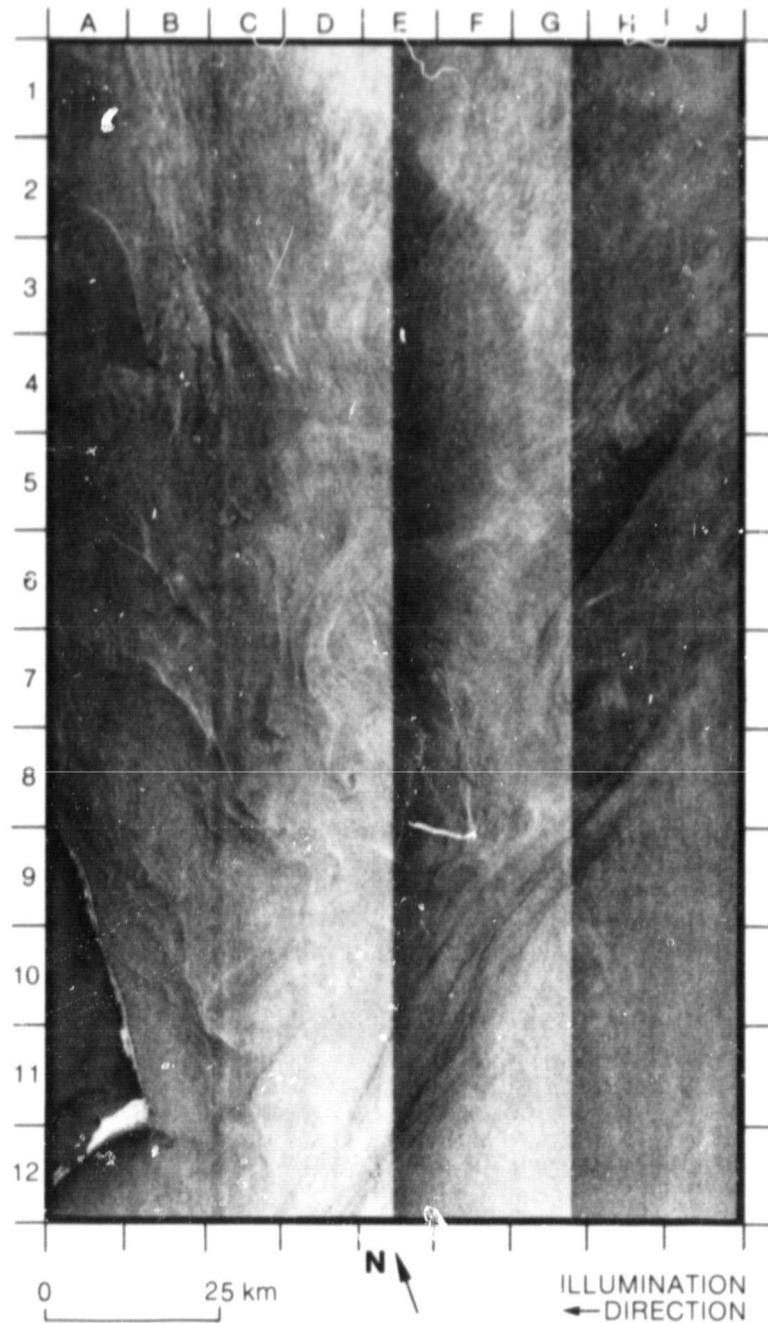
This image shows an area northeast of Cape Hatteras (A9 to A12) where the Gulf Stream meets the colder and fresher southward flowing shelf water (see the map). The shoreward boundary of the Gulf Stream is delineated by the dark filaments extending from D12 to J7 and from G7 to J4. Several small cyclonic (counterclockwise) vortices (H4/H5, G7, F8/F9, and D8/E8) are formed as a result of the strong shear between the Gulf Stream and the flow of the shelf water. The numerous short, bright filaments on the shoreward side of the image are probably associated with small pools of warm water shed from the Gulf Stream into the shelf water (cf. Image 13). The slight change in brightness across a line from D1 to G4 appears to be associated with the transition from
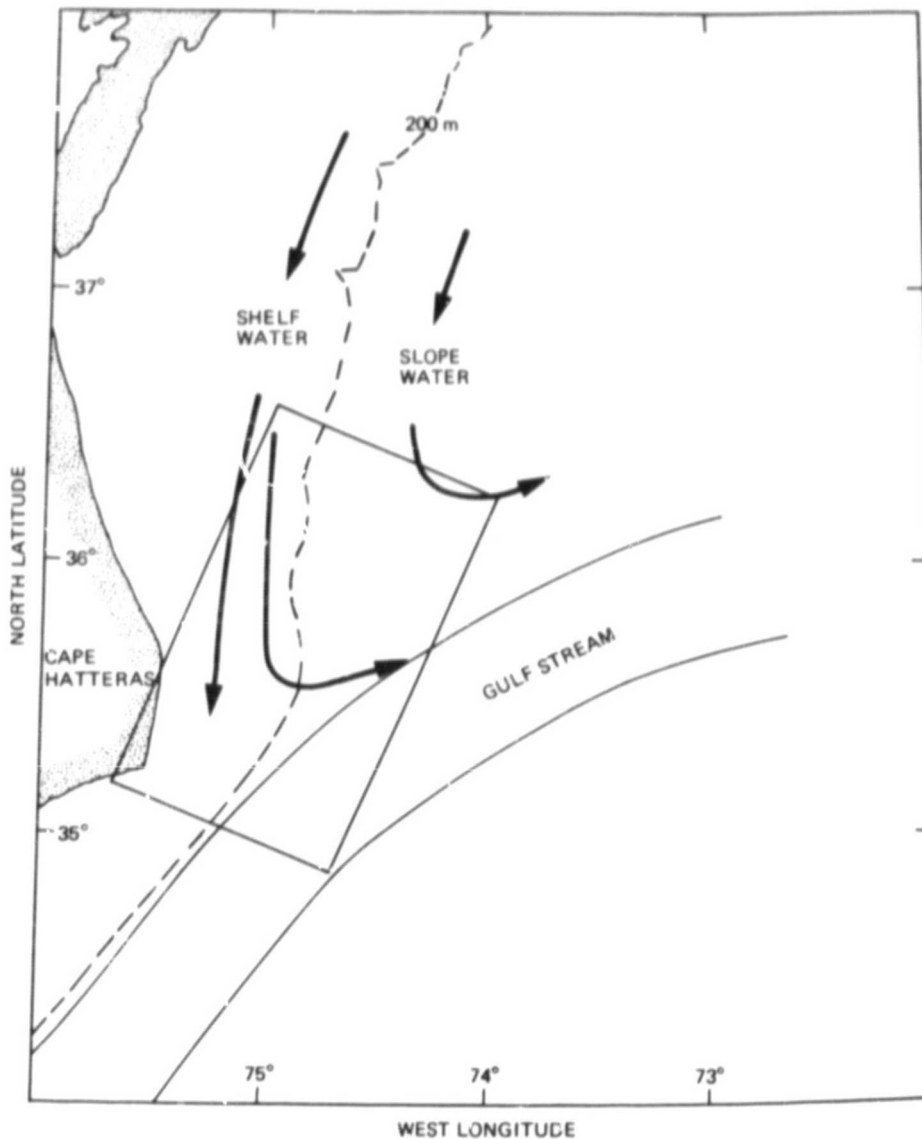
A schematic map of the currents off Cape Hatteras. The area of the SAR image is enclosed by a rectangle.

shelf water to slightly warmer slope water (see the map). These features are characteristic of most images of the area (e.g., Revolutions 974, 1253, 1296, 1447, and 1468).

As a result of its interaction with the Gulf Stream, shelf water is entrained by the Gulf Stream and carried downstream for about 2000 kilometers, resulting in both surface and subsurface bands of relatively cold and low-salinity water along the northern boundary of the Gulf Stream (e.g., Fisher, 1972; Ford et al., 1952). The transport of shelf water by the entrainment process has been estimated to be 40,000 cubic meters per second (Kupferman and Garfield, 1977), a significant fraction of the total along-shore transport of shelf water on the Mid-Atlantic Bight.

(Rev. 1404; 0500 GMT, October 3, 1978.)

77

27. Coastal Eddies Off Galveston, Texas

ILLUMINATION DIRECTION →

↗N

0   25 km
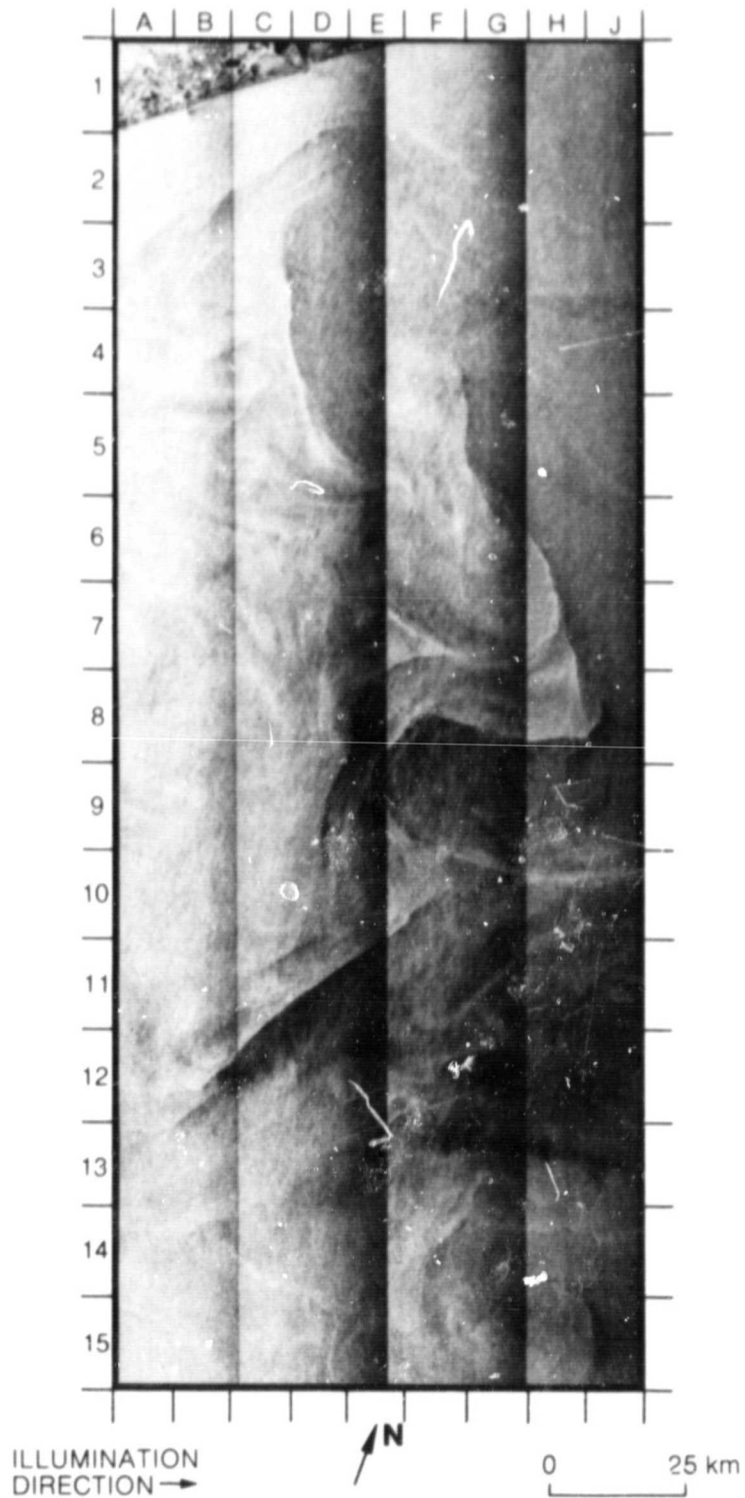
This image of the Gulf of Mexico south of Galveston (F1/G1), Texas, shows some prominent eddy-like features from the coast to the shelf break (see the chart for image location and bathymetry). These features are characterized by large filaments with sharp changes in brightness (e.g., C12 to F10, E9 to J8, J8 to G4, and E5 to D3).
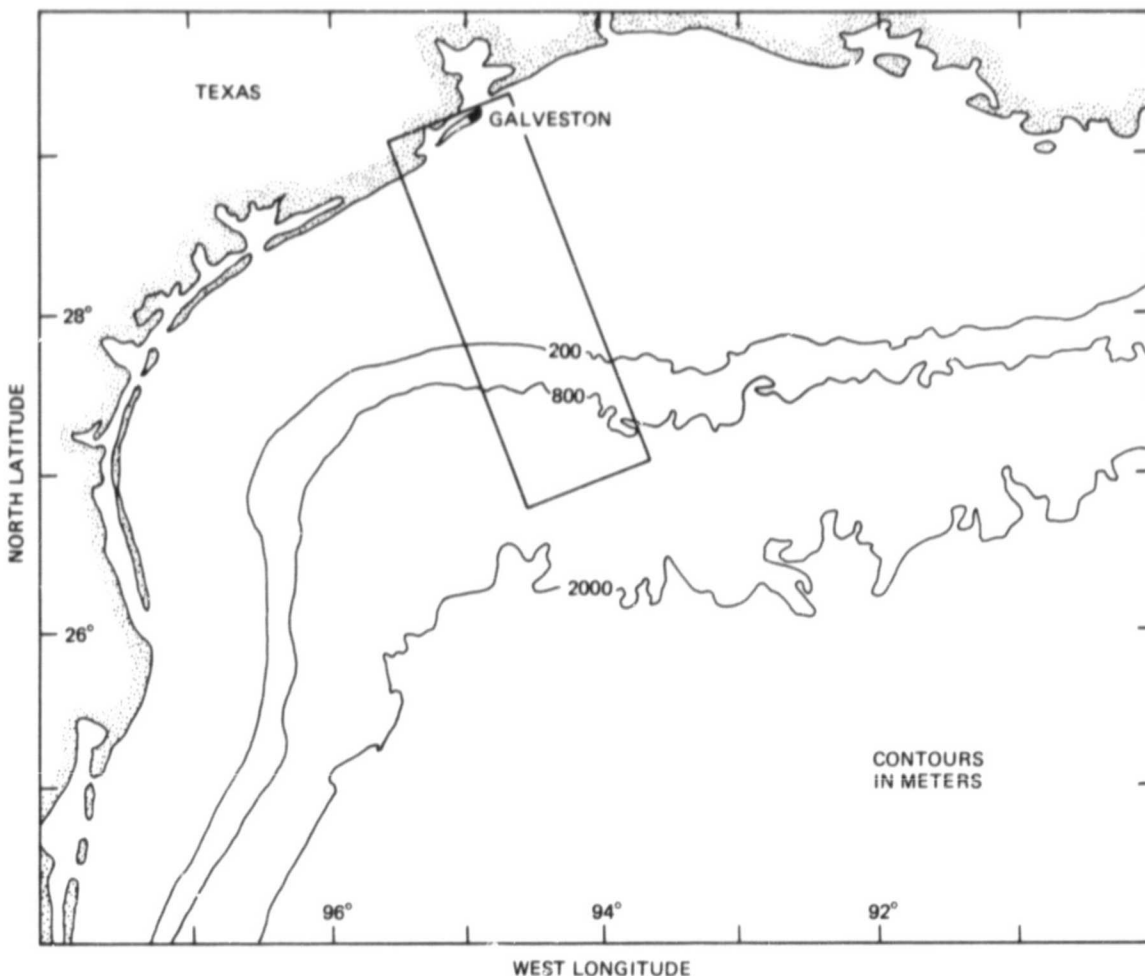
Bathymetric chart of the imaged area, which is enclosed by a rectangle (from Uchupi, 1971).

Additionally, there are numerous small patches of brightness changes in most of the imaged area. Similar features have been observed over most of the shelf off Texas (e.g., Revolutions 221, 422, 508, and 659).

The circulation on the shelf off Texas has a strong seasonal variability. In the winter, a predominantly wind-driven shelf current flows southwestward along the coast, whereas in the summer this current weakens and even reverses occasionally (e.g., Smith, 1980a). The temperature and salinity of the shelf water also have a pronounced seasonal variation. In the winter there is a rapid shoreward decrease in both temperature and salinity on the shelf, whereas this gradient disappears in the summer (Smith, 1980b), indicating that some cross-shelf mixing events occur. Therefore, the eddy-like features on the image may be the manifestations of the mixing.

Numerous small ships can be seen on the image as bright point targets (e.g., G2, G3, F6, F8, and F9).

(Rev. 465; 1234 GMT, July 29, 1978.)

79

28. Small Vortices East of the Yucatan Peninsula

ILLUMINATION DIRECTION →

N

0   25 km
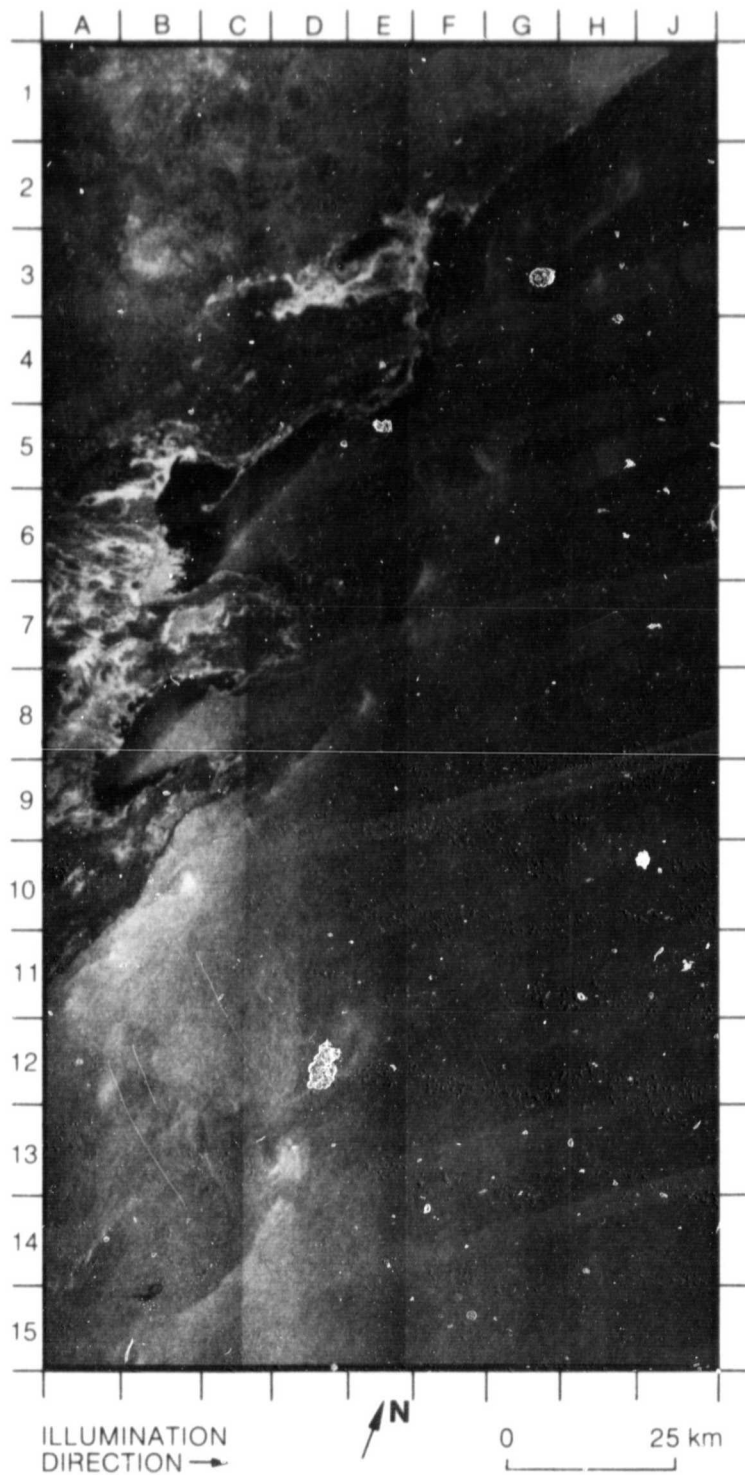
Flowing northward along the east coast of the Yucatan Peninsula (the land on the image) is the Yucatan Current, which is the boundary current of the northwestern Caribbean Sea (see the map) and becomes the Loop Current (cf. Image 17) after entering the Gulf of Mexico. This is a swift current with maximum speeds up to 2 meters per second (e.g., Molinari, 1976). Because there is no extended continental shelf off the
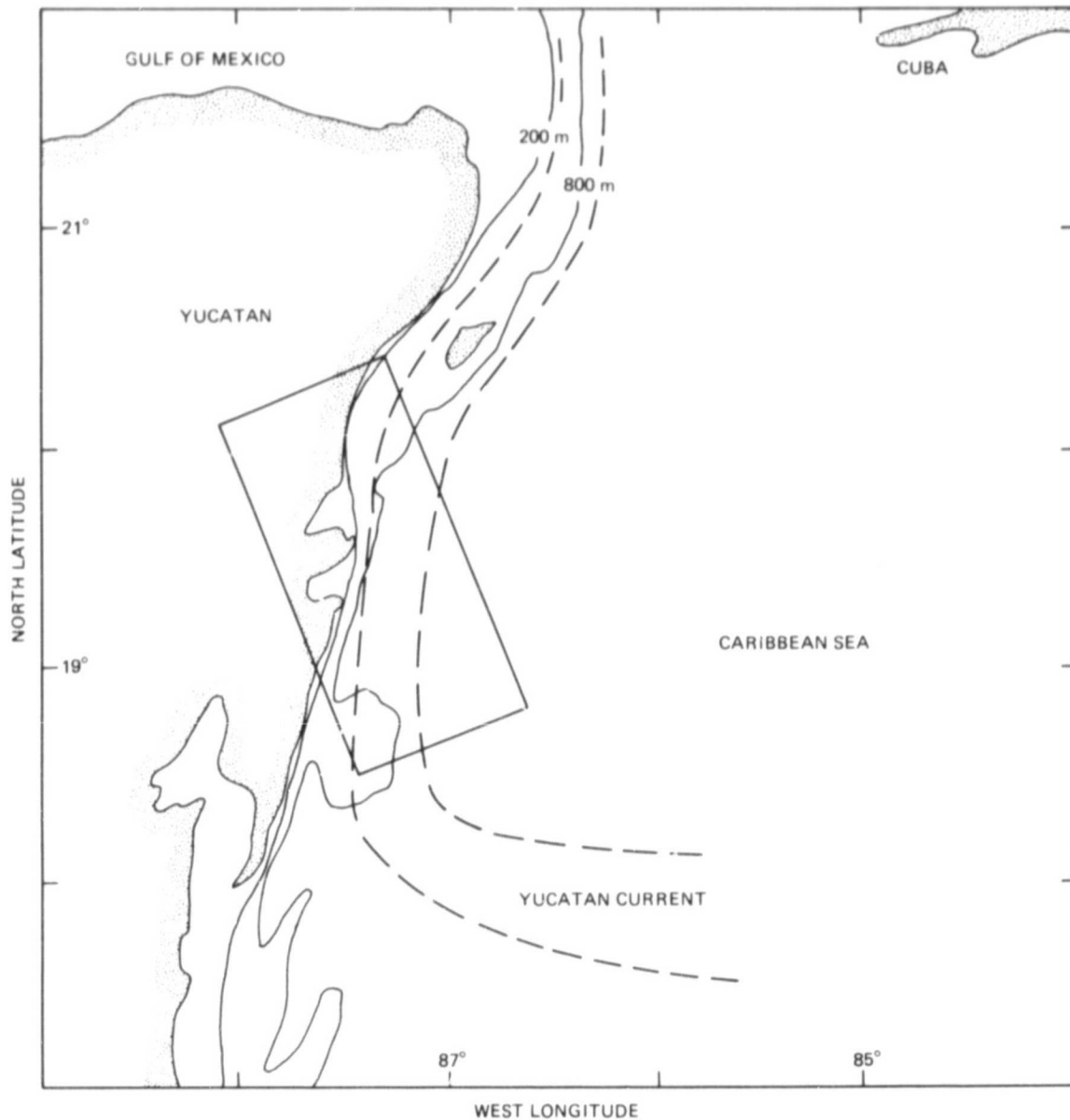
Map of the northwestern Caribbean Sea (Cayman Basin) (from Uchupi, 1971); the area of the SAR image is enclosed by a rectangle.

east coast of Yucatan, this current flows immediately adjacent to the coast, producing a very intense shear zone. The resultant shear instabilities and the flow separation induced by coastal headlands (C9, D7, and E4/E5) generate numerous small (less than 10 kilometers in diameter) cyclonic vortices (e.g., H2/J2, G5/F6, G9/H9, and C13/D13), transporting cyclonic vorticity from the coast into the current. This indicates that the lateral friction in the coastal zone should play a significant role in modeling the Yucatan Current.

Similar features in this area were detected by the SAR also during Revolution 759. (Rev. 795; 1355 GMT, August 21, 1978.)

29. Small Vortices South of Grand Bahama Island

ILLUMINATION DIRECTION ⟶

↗N

0 ——— 20 km
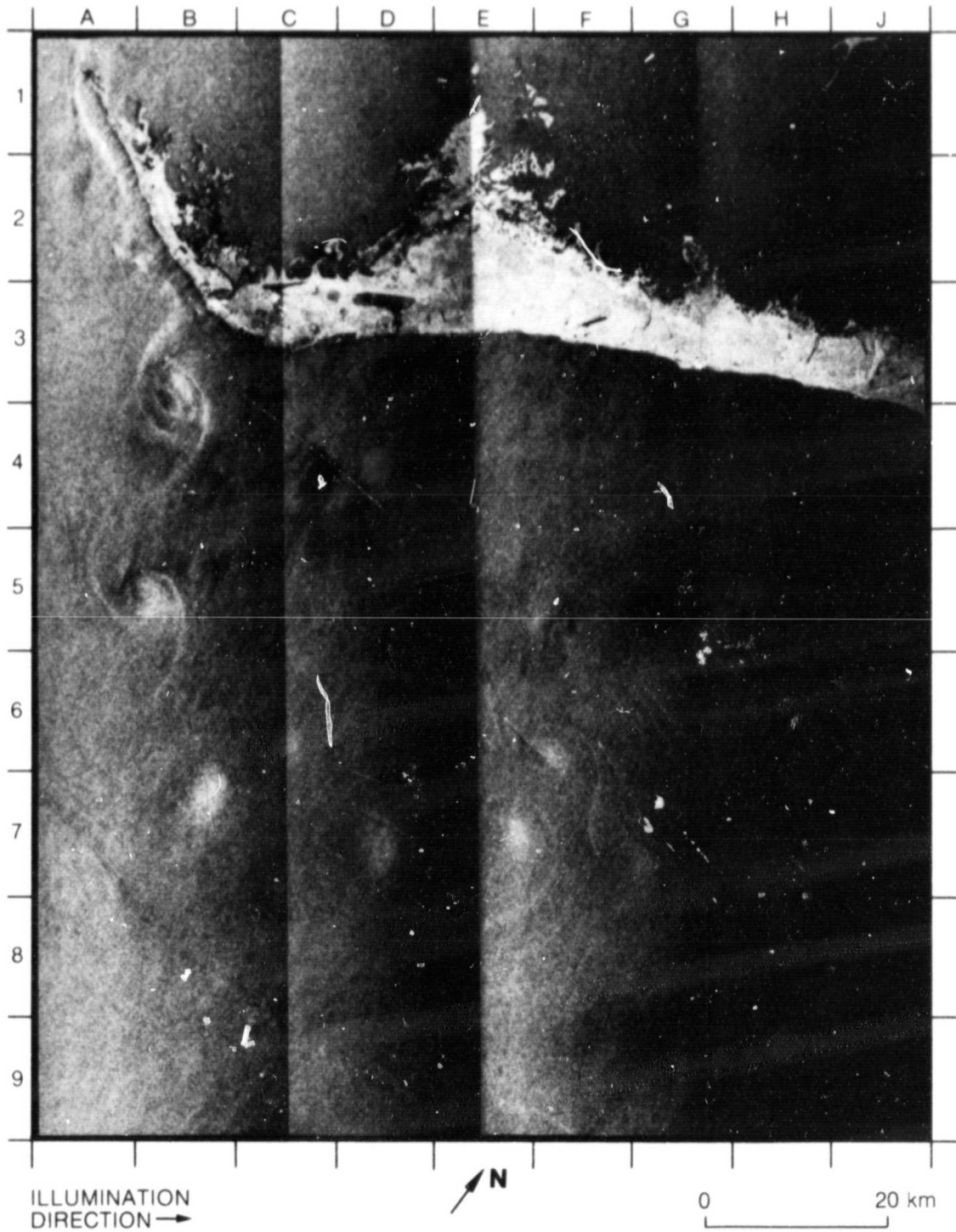
A series of well-organized cyclonic vortices can be seen on this image, which shows an area south of Grand Bahama Island and east of the Gulf Stream (see the bathymetric chart for location of the image). From the arrangement of these vortices, it seems that they are generated by a southeastward flow sweeping along the coast from A1 to B3, and that the flow weakens and deflects to the east after leaving the coast. Note that the three vortices at E6/F6, E7, and F7/G7 are squeezed together because of the deceler-
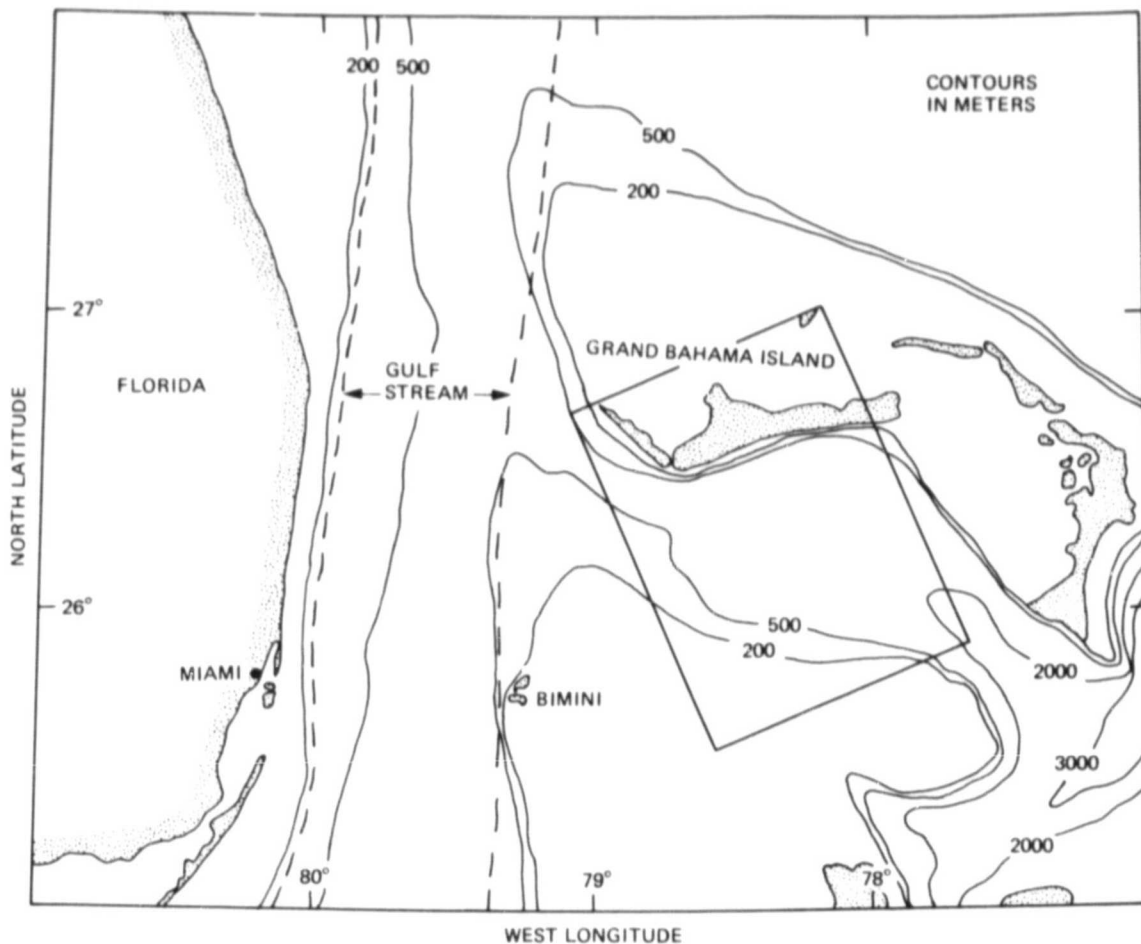
Bathymetric chart of the area of Grand Bahama Island; the area of the SAR image is enclosed by a rectangle.

ating flow. When the vortices are first formed (B3), they have distinct, detailed characteristics—a dark center surrounded by concentric circles with two "tails" extending outward from the vortex's boundary; these characteristics fade away when the vortices begin to decay. Some of the vortices are connected with one another by their tails, like the vortex street generated by obstacles in laboratory-simulated flows (cf. Batchelor, 1967, Plate 2).

The origin of the southeastward flow is not clear. Because the vortices were not observed on any other images of this area, of which some were taken at the same local time as this image, it seems unlikely that this flow was associated with any steady currents or tides.

The current-meter observations reported by Lee (1977) indicated that the coastal currents in the area were generally aligned with bottom depth contours. The currents were highly variable and unpredictable in direction and speed. Maximum speeds of about 0.4 meters per second were recorded, and dominant time scales ranged from 3 to 18 days.

Additionally, three ships appear on the image at H4, E6, and D6.

(Rev. 1325; 1547 GMT, September 27, 1978.)

30. Oil Slicks and Platforms Off Santa Barbara, California

ILLUMINATION DIRECTION →

N

0   20 km

This image shows most of the Santa Barbara Channel where numerous natural seeps of oil, tar, and gas exist in the coastal zone. One of the most prolific groups of oil seeps is located offshore between Santa Barbara and Coal Oil Point (see the map for location). The numerous dark bands in the coastal area from A1 to D3 (as sketched on the map) are oil slicks resulting from this group of seeps. Estes et al. (1980) showed that the slick patterns observed on the image were consistent with the results of a numerical model that used concurrent meteorological and oceanic conditions to simulate the hourly patterns of slicks from these seeps. They also showed that other dark areas on the image were basically due to low winds (about 2 meters per second), which had masked any oil slick signatures that might have been produced by the seeps southeast of Santa Barabara.
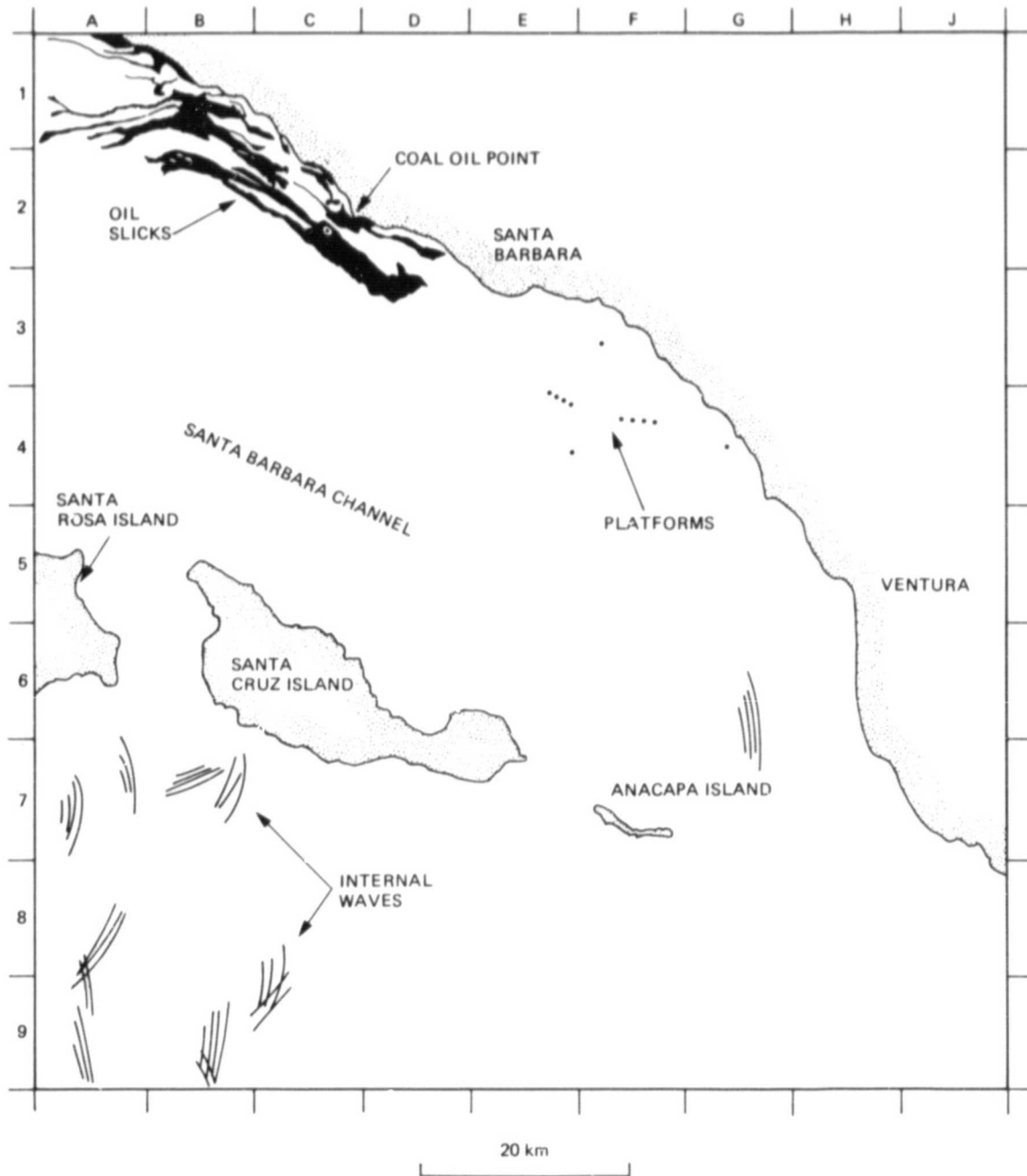
Map of the imaged area off Santa Barbara, California.

Twelve offshore platforms appear on the image as bright points (represented by black dots on the map). Eleven are located southeast of Santa Barbara, and the twelfth is located southwest of Coal Oil Point.

Several packets of internal waves are seen south of Santa Cruz Island and Santa Rosa Island, in a region of rapidly changing topography.

(Rev. 308; 1317 GMT, July 18, 1978.)

3.7 Bathymetric Features

In certain shallow ocean regions imaged by the Seasat SAR, surface expressions are detected, often with surprising detail, that appear to be induced by the local bathymetry. The most striking examples occur in images of shallow-water areas where strong currents flow over uneven bathymetry. These images show pronounced surface expressions closely delineating the bottom features. In other areas, particularly near islands and coral reefs, more subtle changes in surface expression that reflect the bathymetry have been imaged.

The mapping of bathymetric features in the ocean is most commonly done by echo sounding. Recently, multispectral scanners and ocean color scanners, mounted on aircraft and satellites, have proved effective in detecting shallow-water bottom features, using primarily the blue-green band of the visible spectrum that can penetrate the water column (Bina and Ombac, 1979; Egan, 1980; Lyzenga 1981; Lohmann and van der Pieppen, 1981). It had been thought that the only application of SAR in studying shallow-water bottom features would be the detection of surface-wave transformations caused by bathymetric features (Active Microwave Workshop Report, 1975). Later, surface effects from sand bars were actually imaged by a radar over the North Sea (de Loor and Van Hulten, 1978). However, the extent to which a radar system can detect the effects of bathymetric features on the ocean surface was perhaps first realized from the Seasat SAR imagery.

The mechanisms by which bathymetric features affect the ocean surface and thereby the radar backscatter are largely unknown. One likely explanation is that variations in the bathymetry affect a steady or tidal flow to produce surface variations that in turn induce variations in the Bragg resonant waves (Phillips, 1981). Initial studies by Kasischke et al. (1980) on Seasat SAR imagery showed that abrupt changes in bathymetry caused either an increase or decrease in radar backscatter, and that the type of response may be related to the direction of the flow.

The following five images show surface expressions that are the result of bathymetric features. Image 31 of the English Channel and Image 32 of Nantucket Shoals show distinct patterns of the underlying bathymetry. Image 33 in the Caribbean shows the outline of a fairly deep bank and an eddy downstream of the bank. Image 34 is an example from the extensive imagery over the Tongue of the Ocean in the Bahama Bank region. Variations in current flow induced by bottom topography at a river mouth are shown in Image 35.

ILLUMINATION
DIRECTION →

N

0   20 km

The English Channel near the Straits of Dover is characterized by tidal ranges up to 7 meters, reversing tidal currents with velocities at times over 1.5 meters per second, and extensive sand bars on both sides of the Straits and along the coasts of France and England. The sand bars in the Channel are long, narrow ridges from 10 to 30 meters in depth, with some shallower than 5 meters. Together with the high volume of ship traffic, these sand bars make navigation in the Channel hazardous.

By comparing this image of the English Channel, just east of the Straits of Dover, with the bathymetry map, it can be seen that the surface patterns detected by the SAR follow closely the sand-bar patterns present in that area. The more prominent patterns are over bars 20 meters (11 fathoms) or less in depth (e.g., B4, B5, and D6). The predicted tidal currents at the time of the image were flowing southwestward with a speed of 0.5 to 1 meter per second, as indicated on the bathymetry map. Note that most of the sand bars have a region of low radar backscatter on their upstream sides and a band of higher backscatter on their downstream sides (e.g., E5, F5, G4, and H3). Wave-like features, with crests perpendicular to the tidal flow, occur throughout the image (e.g.,
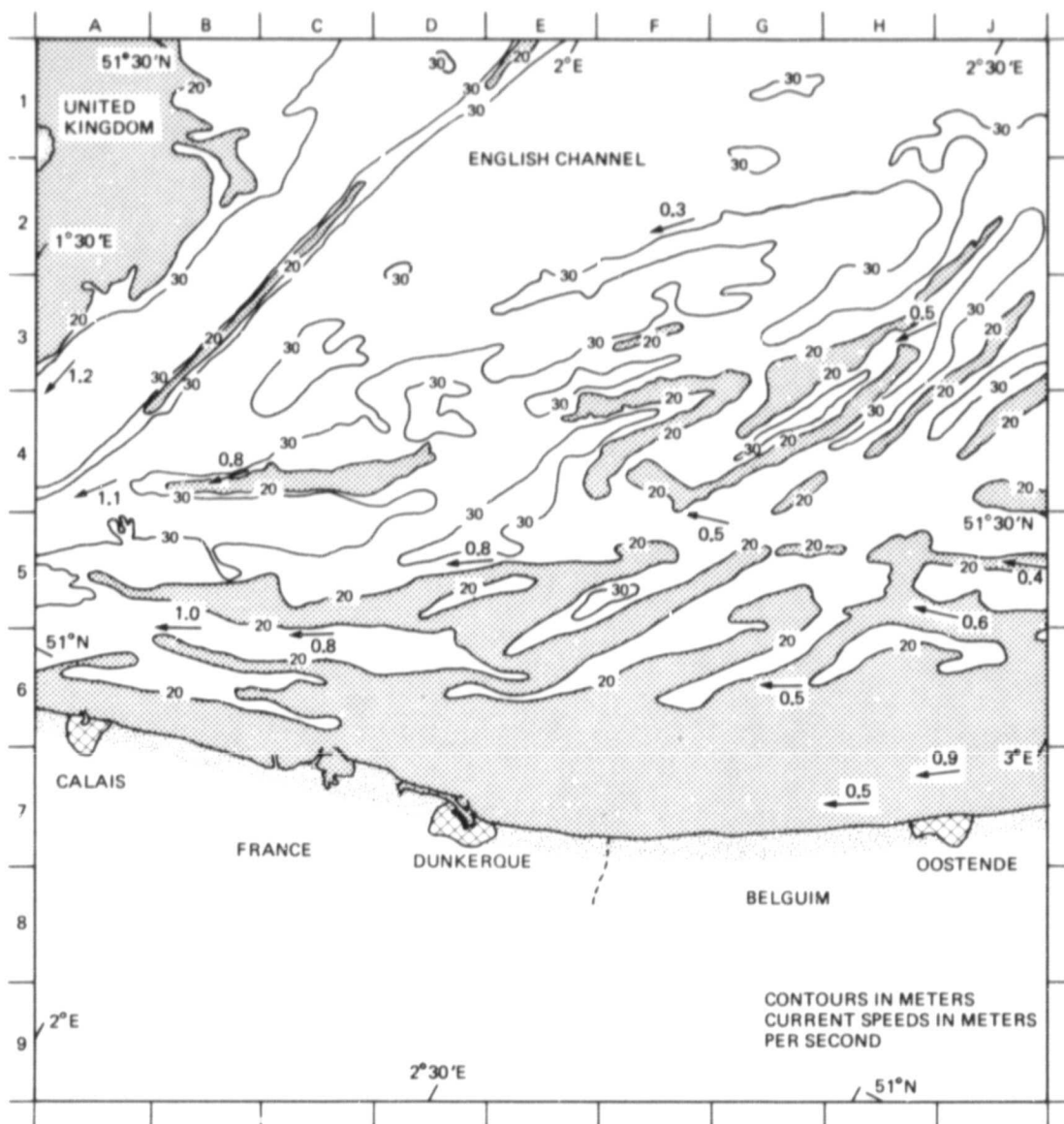
Bathymetric chart of the imaged area. Tidal current directions and velocities, from the table on the original chart cited in Appendix B, are indicated.

C4, B5, and F3). Perhaps the more intense appearance of these waves on the western portion of the image is due to the higher current velocities there.

Three other passes that imaged the Straits of Dover were analyzed (Revolutions 719, 1430, and 1473), but none showed the detailed, bathymetrically related surface patterns seen on this image. Although the tidal current velocities present during these three passes were comparable to those present during the pass of this image, the predicted water levels at Dover for the three passes were 3 to 6 meters higher than those for this image, indicating that the currents may have been less altered by the effectively deeper sand bars.

At least 25 ships can be identified on this image, many shifted from their stern wakes (see Section 3.9).

(Rev. 762; 0646 GMT, August 19, 1978.)

32. Nantucket Shoals

ILLUMINATION DIRECTION →

N

0   20 km
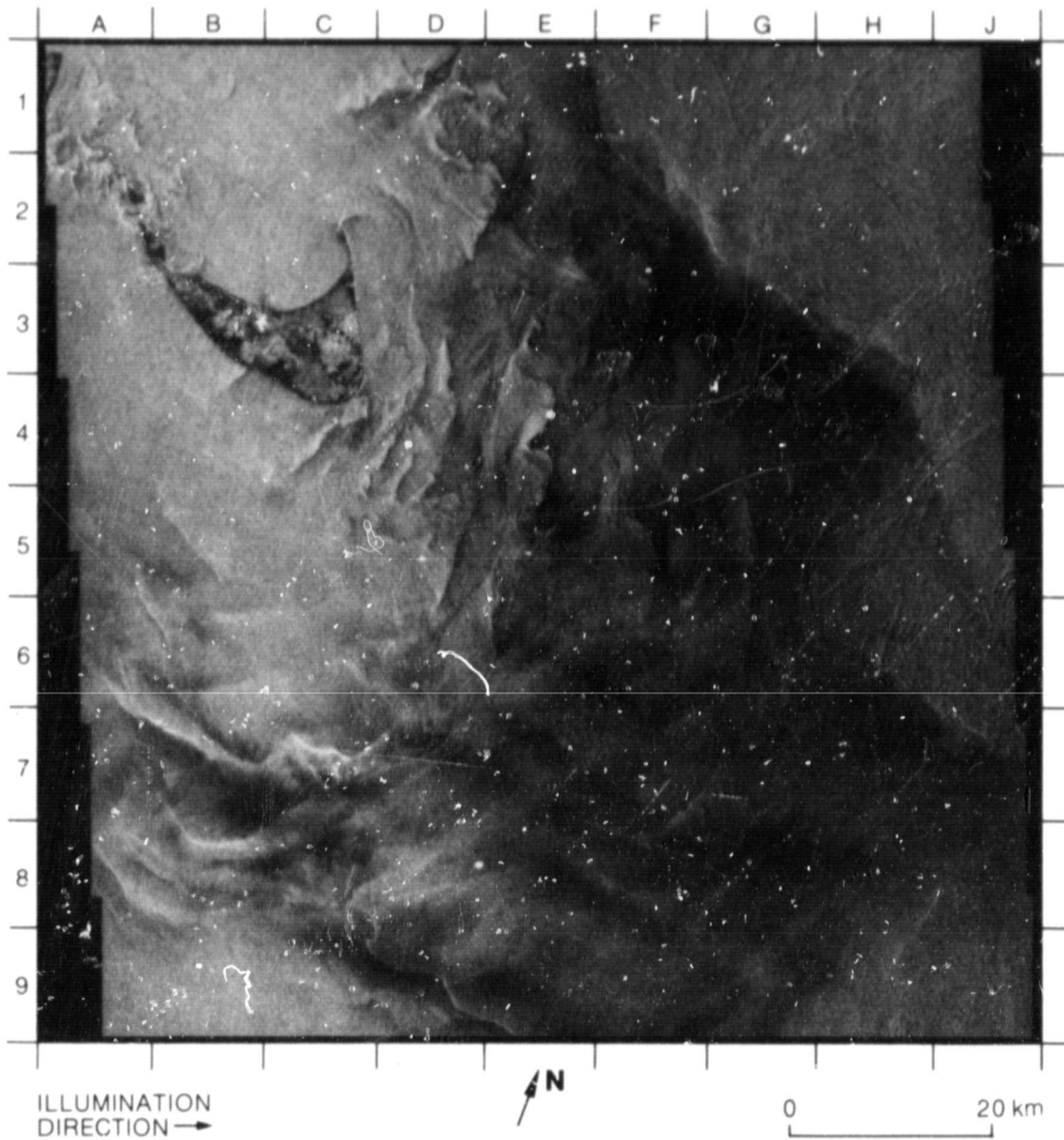
Nantucket Shoals are shallow-water areas to the south and east of Nantucket Island, south of Cape Cod, and are characterized by ridges and shoals separated by deeper channels. The surface expressions on this image, the only SAR image taken of this area, reflect closely the bathymetric patterns shown on the map, with the more intense and distinct patterns occuring over areas shallower than 10 fathoms (18 meters) (e.g., C4, D4, and E4).
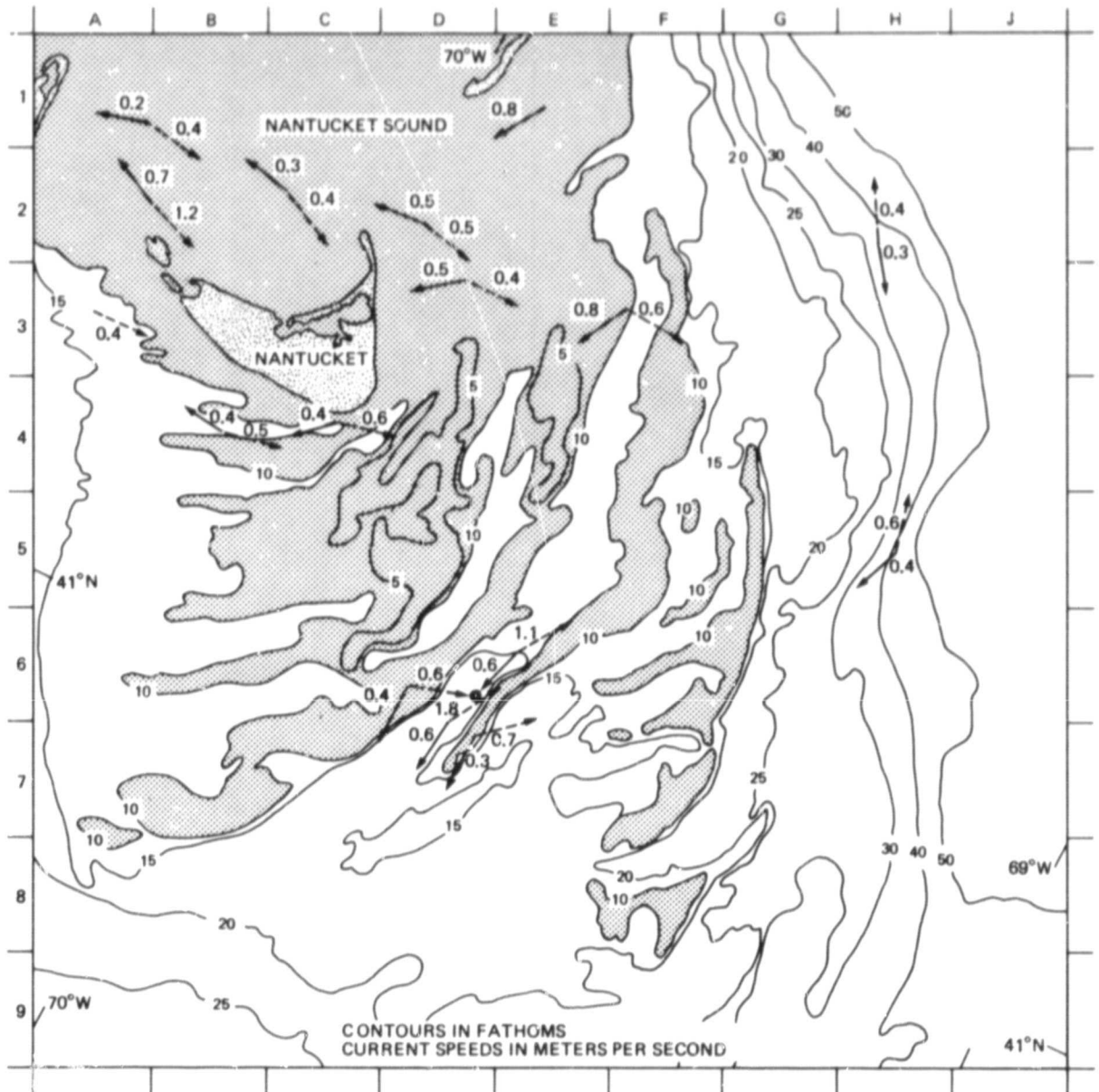
Bathymetric chart of the imaged area. Tidal current directions and velocities (from *Tidal Current Tables*, 1978) are indicated for both the SAR image (solid arrows) and the Landsat image (dashed arrows).

While the mean tidal range in this region is low (about 1 meter), the tidal currents are rotary rather than reversing, so there is continuous flow with varying speeds and directions. The predicted currents at the time of this image were 0.25 to 0.75 meters per second to the southwest over the main shoal area, as indicated on the bathymetry map, and were at small angles to the main orientation of the bottom topography. Wave-like features, similar to those observed in the English Channel (Image 31), occur ove. shallow areas of 10 fathoms or less in depth and have crests generally perpendicular to the direction of current flow. Also, a narrow line of low radar backscatter borders the shoals on the upstream side, while over the shoals the surface expressions have a higher backscatter (cf. Kasischke et al. 1980).
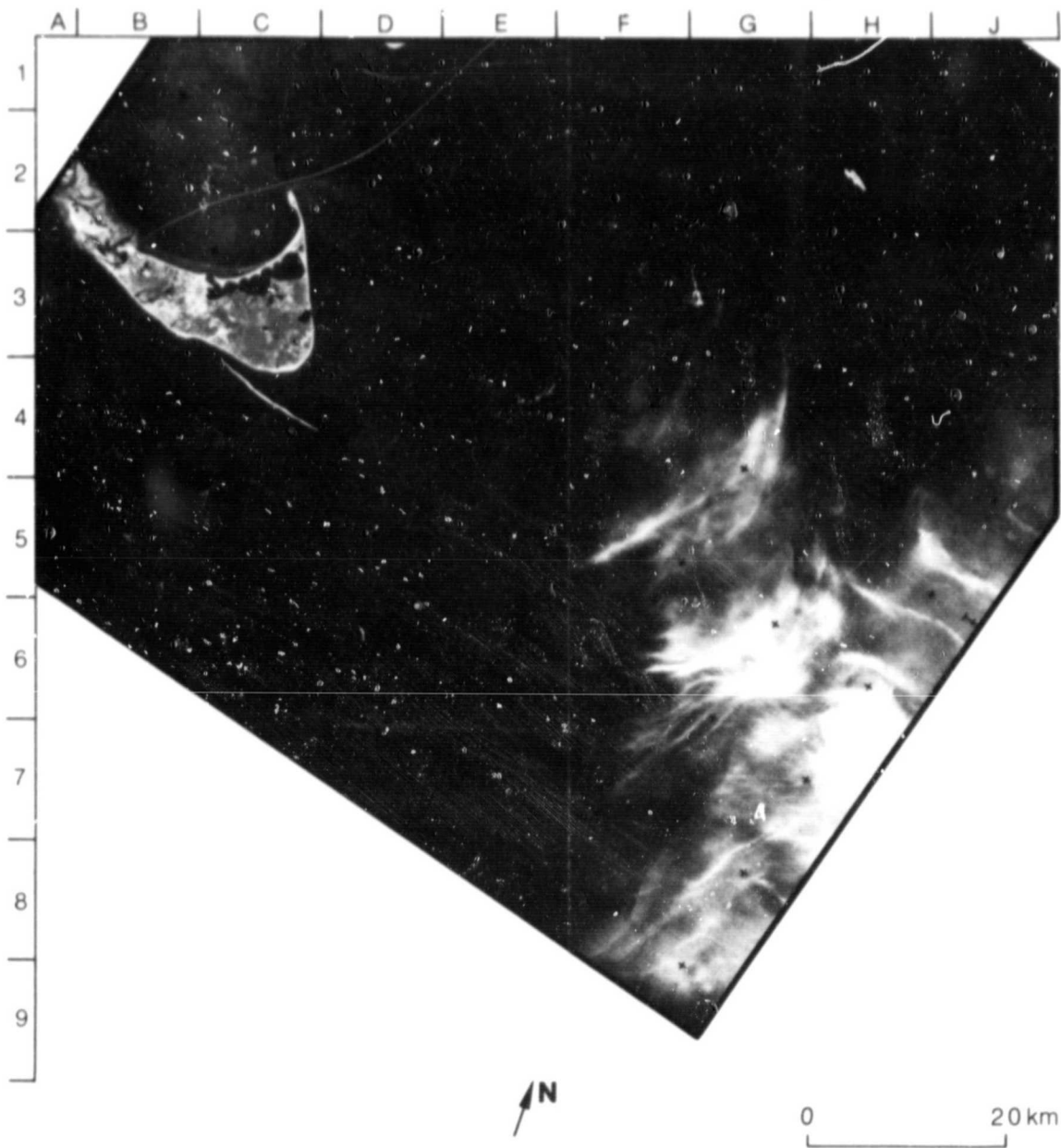
Landsat RBV image of the Nantucket Shoals.

The Landsat return beam vidicon (RBV) image, taken on August 19, 1978, also shows some effects of the bathymetry. The bright streaks on this image (D4, D5, and E3 to E6) indicate that the sun's rays are being scattered by increased surface roughness in those narrow areas. The tidal currents at the time of this image, as indicated on the bathymetry map, are generally in the direction opposite those at the time of the SAR image. When this image is compared with the bathymetry map, it can be seen that the bright streaks appear on the downstream side of the ridges and shoal areas.

Internal wave packets can be seen on both the SAR image (G1, H1, and J6) and the Landsat image (H3 and J2).

(Rev. 880; 1234 GMT, August 27, 1978.)

33. Misteriosa Bank in the Caribbean Sea

ILLUMINATION DIRECTION →

N

0   20 km

Misteriosa Bank is a part of the Cayman Ridge located between Mexico and the Cayman Islands south of the Yucatan Channel; it has depths ranging from 9 to 12 fathoms. The isolated position of Misteriosa Bank—distant from any coastal areas—makes this image unique among the images in this section. The shape of the bank (see bathymetry map) is delineated on the SAR image by a thin dark line on the southern side of the bank (A15, B16, and C15) and a bright line on the northern side (A15 to C15). Misteriosa Bank was included in three other passes, Revolutions 400, 1440, and 1483, but was imaged only on the latter two. Easterly winds of 2.5 to 5 meters per second occurred during Revolution 400, while weak, easterly winds of 0 to 2.5 meters per
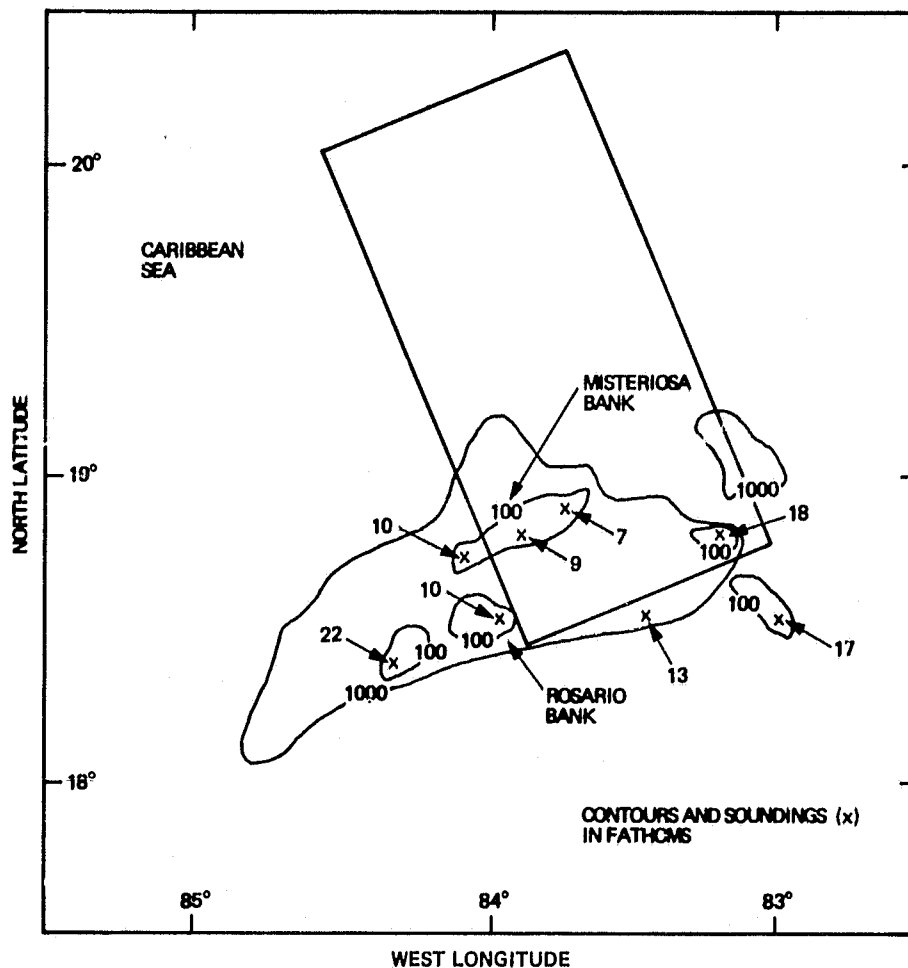
Bathymetric chart of the imaged area, which is enclosed by the rectangle.

second existed during the other three passes (note dark areas on this image). Another surface expression on this image (G18/G17) is near a topographic bump with a depth of 33 meters (18 fathoms), but this was not imaged by the other three passes.

The surface expressions of these bathymetric features are probably affected by the steady surface currents that flow northwestward in this part of the Caribbean at speeds from 0.4 to 0.6 meters per second (Molinari et al., 1981). In particular, note the curvilinear patterns that may result from current shear northeast of the bank (B12 to D14) and the bright delineation of the northern border on the downstream side.

Also seen on this image is apparently one half of an eddy with a diameter of approximately 65 kilometers (centered on A5). This eddy was not imaged three days later, presumably because it moved westward. The eddy could not be confirmed by NOAA-5 infrared imagery because the sea surface temperature gradient was weak at that time of year. However, Molinari (1976) and Molinari et al. (1981), in studying the surface currents of the Caribbean with drifting buoys, found that eddies occurred downstream of the Cayman Ridge and other ridges in the Caribbean. These eddies were shed from the currents as they were deflected by the major topographic features and carried away by the net westward drift.

Also seen in this image are 4 ships (D4, D7, C2/C3, and E13).

(Rev. 1397; 1640 GMT, October 2, 1978.)

34. Tongue of the Ocean in the Bahama Bank
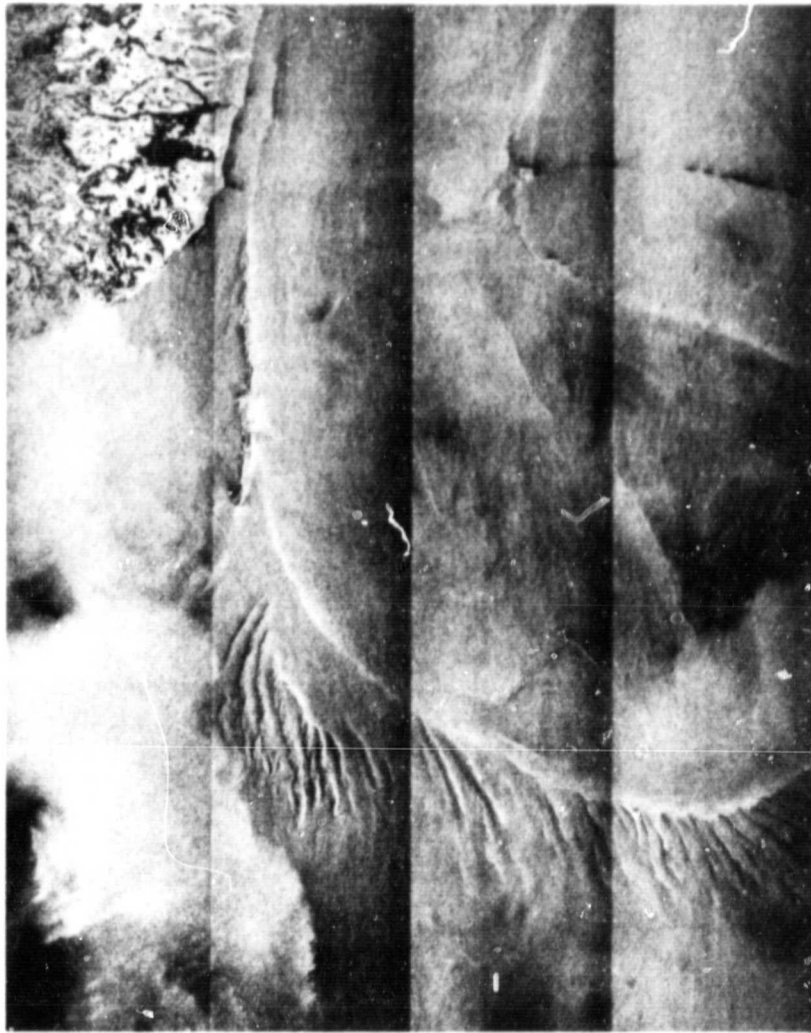
ILLUMINATION DIRECTION → ↑N 0 ____ 20 km

Tongue of the Ocean (TOTO), the tongue-like feature enclosed by a bright line on the image, is a deep channel with depths greater than 1500 meters. This channel extends into the shallower Bahama Bank (less than 200 meters in depth) along the east margin of Andros Island. The bright, continuous line surrounding TOTO is caused by the coral reefs and extensive carbonate deposits at the margins. Near the southern end, tidal currents have formed navigable channels over 5 meters deep separated by long sand bars that are nearly exposed. The SAR imaged this area on 12 separate passes, producing the most extensive data set of any area that has surface expressions affected by bathymetric features.

The patterns of the sand bars, which surround the southern end of TOTO, are easily seen on this image, with the western side of the bars delineated by a dark band and the eastern side by a bright band. The channels separating the sand bars have a uniform return of intermediate intensity. Currents are thought to have produced these surface expressions, but, at the time of this writing, information on the tidal currents is not available, nor is the surface circulation well known, although the Environmental Atlas of TOTO (1967) notes that the currents in the area are exceedingly variable and have speeds usually less than 1 meter per second.

0   25 km

↑ N
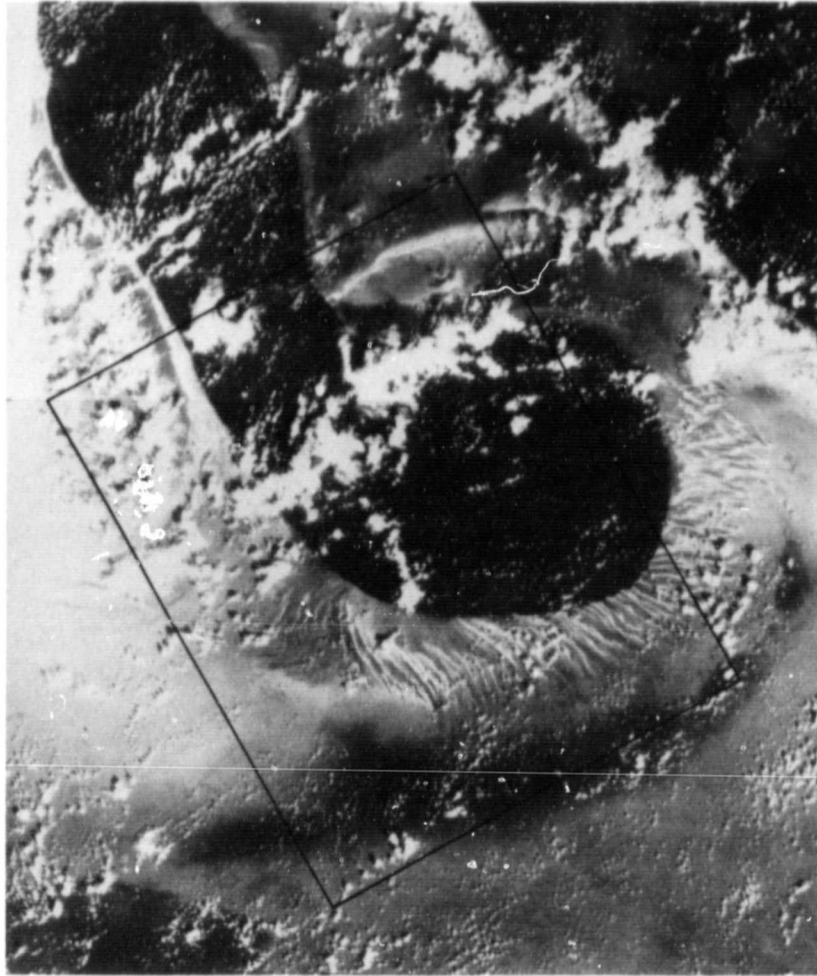
Landsat MSS image (Band 4) mosaic of the Tongue of the Ocean. The area of the SAR image is enclosed by a rectangle.

Predicted tidal amplitudes were determined at Andros Island for the 12 passes. Although the tidal range for the Bahama region is only 0.6 to 1.0 meter, the passes that had little or no surface expression occurred generally during the highest tides, while the passes with the strongest surface expression occurred during the lowest tides, with three exceptions: one pass (Revolution 1325) had very little expression at a time of low tide while two passes (Revolution 1239 and this image) had strong expressions but occurred at times of high tides. Also of note is that Revolution 1239 had a surface pattern opposite of this image, with a dark line on the eastern side of the sand bars and a bright line on the western side, indicating, perhaps, that the currents for the two passes were in opposite directions.

The Landsat multispectral scanner (MSS) image was obtained on October 31, 1978, using blue-green light (Band 4), which penetrates water to depths greater than 10 meters. The sand bars appear white and are separated by the gray channels. TOTO itself is dark and Andros Island is masked by cloud cover.

(Rev. 1411; 1612 GMT, October 3, 1978.)

95

35. The Kuskokwim River, Alaska
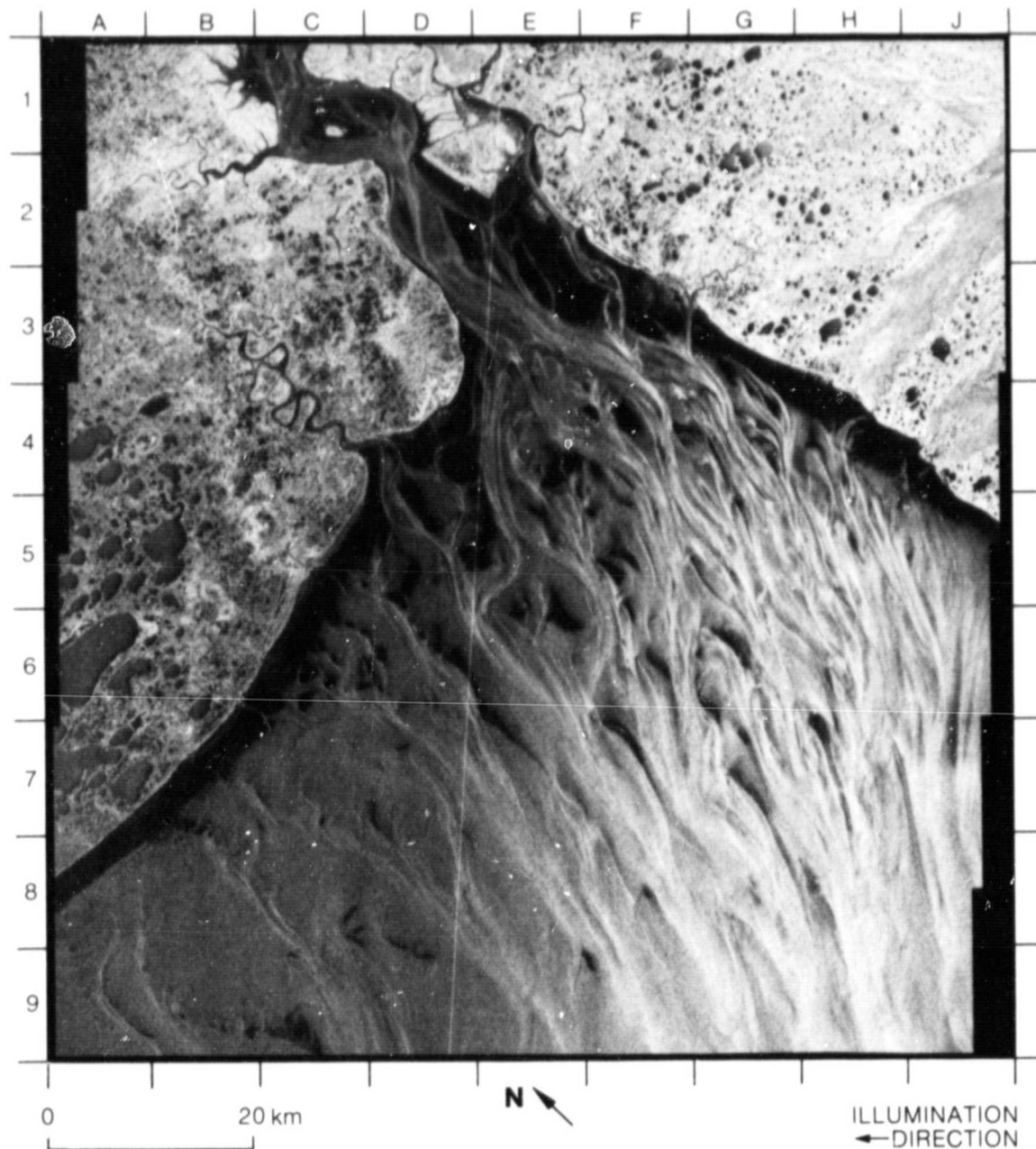
The Kuskokwim River in Alaska flows into the southeastern Bering Sea, where it forms large sediment deposits in the Kuskokwim Bay. As this image shows, many of the sediment deposits (dark areas) are exposed throughout the bay (e.g., D5, E5, and G6), and are separated by channels (bright areas) from 7 to 14 meters deep. The river flow should be substantial due to the runoff from the seasonal snowmelt at this time of year and the additional component from the ebb tidal current of 0.8 meters per second. The linear variations within the channels themselves may be a result of the shear and strain

Landsat MSS image (Band 4) of the Kuskokwim River.

of the current as it is deflected around the sediment deposits. Another SAR image (Revolution 720) shows similar patterns of less intensity.

The Landsat MSS image, obtained on July 30, 1978, in the blue-green band, shows the channels brighter than the shallow areas. The tidal current at this time was also in the ebb phase at a velocity of 1.7 meters per second.

The white line in the middle of the SAR image is a radar system calibration pulse.
(Rev. 232; 0612 GMT, July 13, 1978.)

3.8 Atmospheric Phenomena

Because of the short response time of the Bragg resonant waves to wind forcing—some tens of seconds for moderate winds greater than 2 meters per second (cf. Phillips, 1977, p. 169)—rapid time and/or spatial variations of surface winds resulting from various atmospheric phenomena have a great influence on the strength of the radar backscatter. In fact, the study by Jones et al. (1981) has shown that the SAR backscatter cross section is a function of wind speed. Additionally, heavy rainfalls also have strong effects on radar backscatter by attenuating small-scale roughness on the surface, including the Bragg resonant waves.

In this section we present five images to demonstrate the variety of atmospheric phenomena observed by the Seasat SAR. A hurricane in the tropical Pacific Ocean appears on Image 36, with its center and spiral arms clearly detected. Image 37 shows a well organized tropical storm in the Gulf of California. Off the coast of El Salvador, Image 38 shows a squall system associated with a tropical storm. Shown on Image 39 is a cluster of tropical rain cells southeast of New Orleans in the Gulf of Mexico. Image 40 shows signatures of windrows in the North Atlantic between Scotland and Iceland. Image 41 shows an anomalous feature that appears to be the result of atmospheric effects.

36. Hurricane Iva in the Tropical Eastern Pacific

This image of hurricane Iva in the tropical eastern Pacific Ocean was taken when she had reached her maximum intensity with an estimated wind speed of 34 meters per second (see Gunther, 1979, for Iva's developing history). She was moving west-north-westward at a speed of about 18 kilometers per hour. The relatively dark region at G9/H9/J9 can be identified as the hurricane's center where the surface wind is much weaker than that in the surrounding area. Two of the spiral arms of the hurricane are detected on the image; one of them extends from J2 to C8 and the other from A10 to J11. Barely discernible in the three far-range subswaths are waves with a wavelength of about 180 meters. The spatial variation of wave directions suggests that the source region was about 80 kilometers east of the hurricane's center.
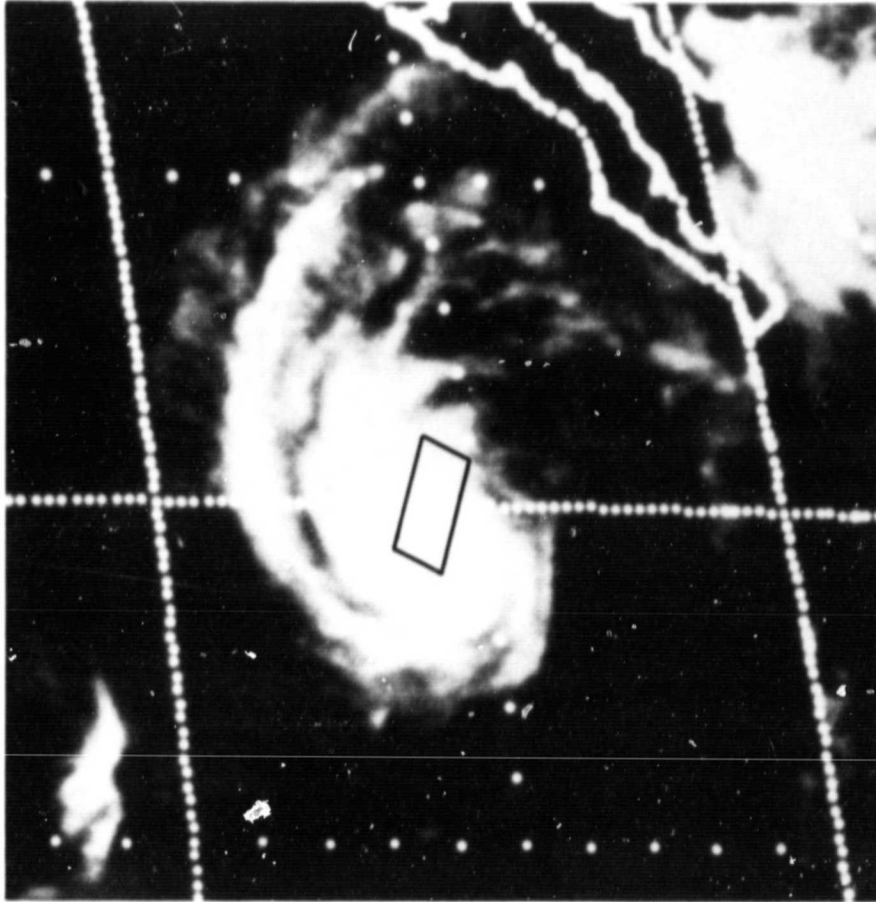
GOES infrared image of the area southwest of Baja California, Mexico. The area of the
SAR image appears as a parallelogram instead of a rectangle due to the geometric
distortion of the GOES image.

The infrared image of Iva was taken by a Geostationary Operational Environmental
Satellite (GOES) at the time of the Seasat pass. The hurricane is manifest by its
cyclonic, spiral cloud patterns. While the infrared image delineates the overall cloud
structure of a hurricane, the SAR image reveals the small-scale patterns of a hurri-
cane's surface winds and waves that have been previously unattainable by any other
remote sensors. Together with the data from other sensors on Seasat, this image has
been used by Gonzalez et al. (1981b) to study in some detail the winds and waves
generated by Iva.

(Rev. 674; 0342 GMT, August 13, 1978.)

37. A Tropical Storm in the Gulf of California

ILLUMINATION
DIRECTION →

↑N

0   20 km

Shown on this image is a small-scale, well-organized tropical storm near the mouth of the Gulf of California. Except for its small size, the storm has all the characteristics of a hurricane: e.g., the cyclonic spiral arms and a well-defined center of low winds (G5/H5).
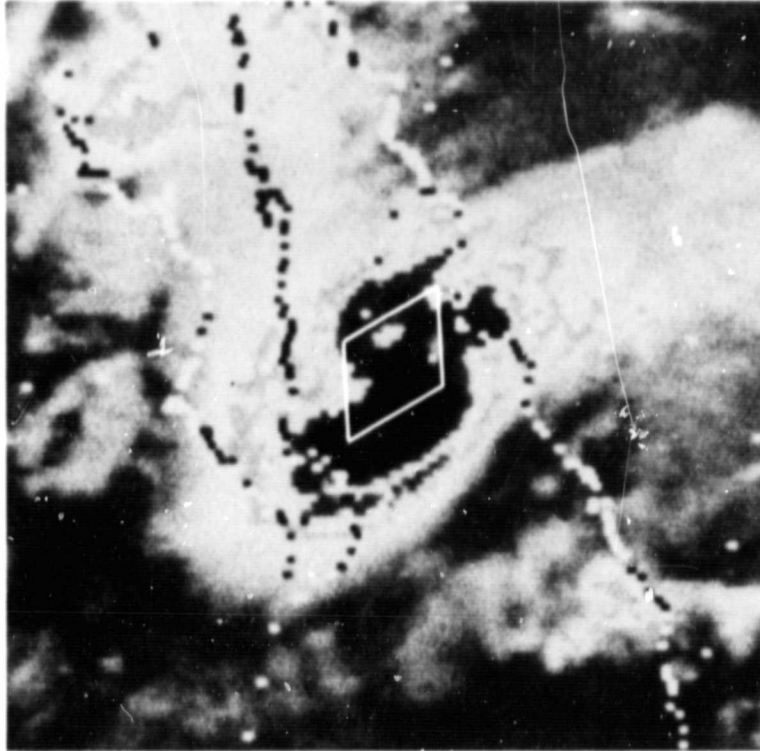
Enhanced GOES infrared image of the southern part of the Gulf of California. The area of the SAR image is enclosed by a parallelogram.

Although this tropical storm has not been documented on the weather charts we have searched, its presence has been confirmed by examining the GOES images of this area. Opposite the image is an enhanced GOES infrared image taken about 40 minutes before the Seasat pass. In the area of the SAR image (enclosed by solid lines) is the typical cloud pattern of a tropical storm. The black area that predominates within and spreads beyond the SAR image outline indicates a cloud-top temperature below −50 degrees Celsius, a result of the deep convection association with the storm. The area of the storm signatures on the infrared image is much larger (about 300 kilometers in diameter) than that on the SAR image, indicating that only the high-velocity core of the storm has been detected by the SAR.

(Rev. 480: 1343 GMT, July 30, 1978.)

38. Squall Lines South of El Salvador

ILLUMINATION DIRECTION → ↑N 0   25 km
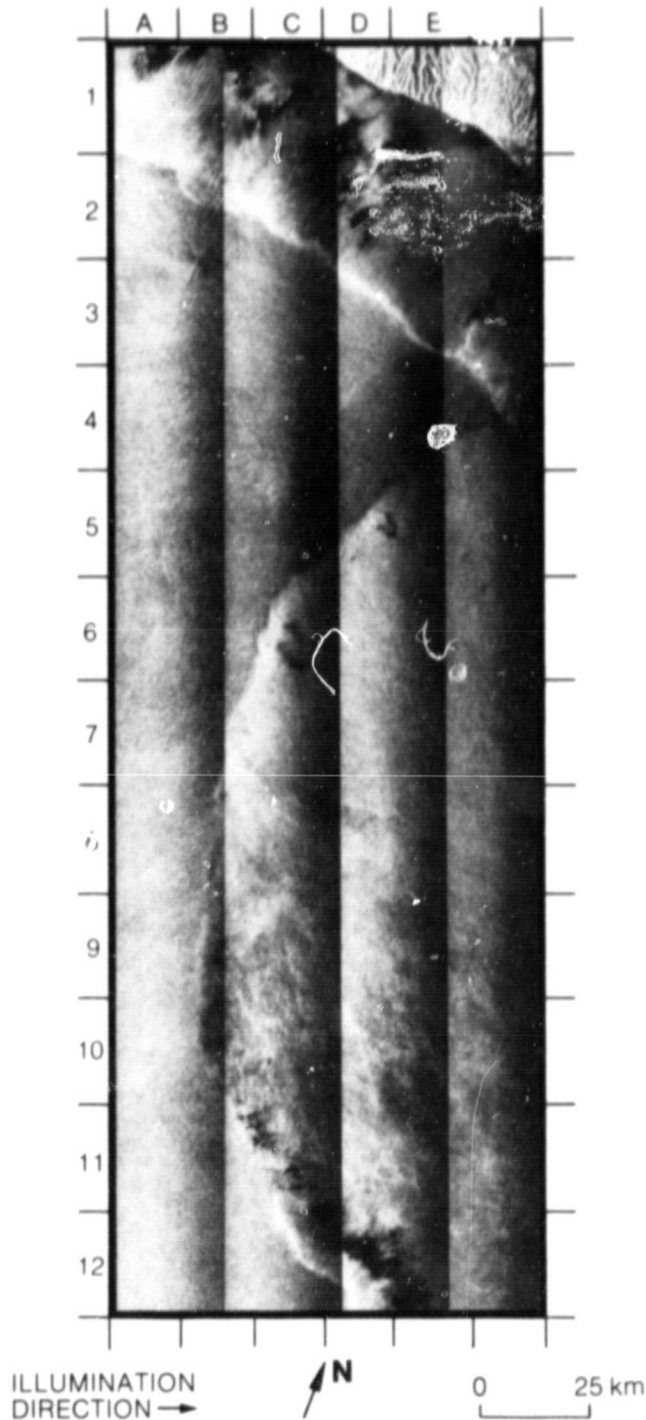
This image of the sea surface south of El Salvador shows two bright, curvilinear strips (A1/A2 to F4, and F4 to D12), which are signatures of local squall lines associated with tropical storm Greta. The visible-channel image taken by a GOES Satellite about 30 minutes before the Seasat pass shows the center of Greta about 300 kilometers northwest of the SAR imaged area. Note that the cloud pattern in the SAR imaged area has a weak feature similar to that extending from F4 to D12 on the SAR image.
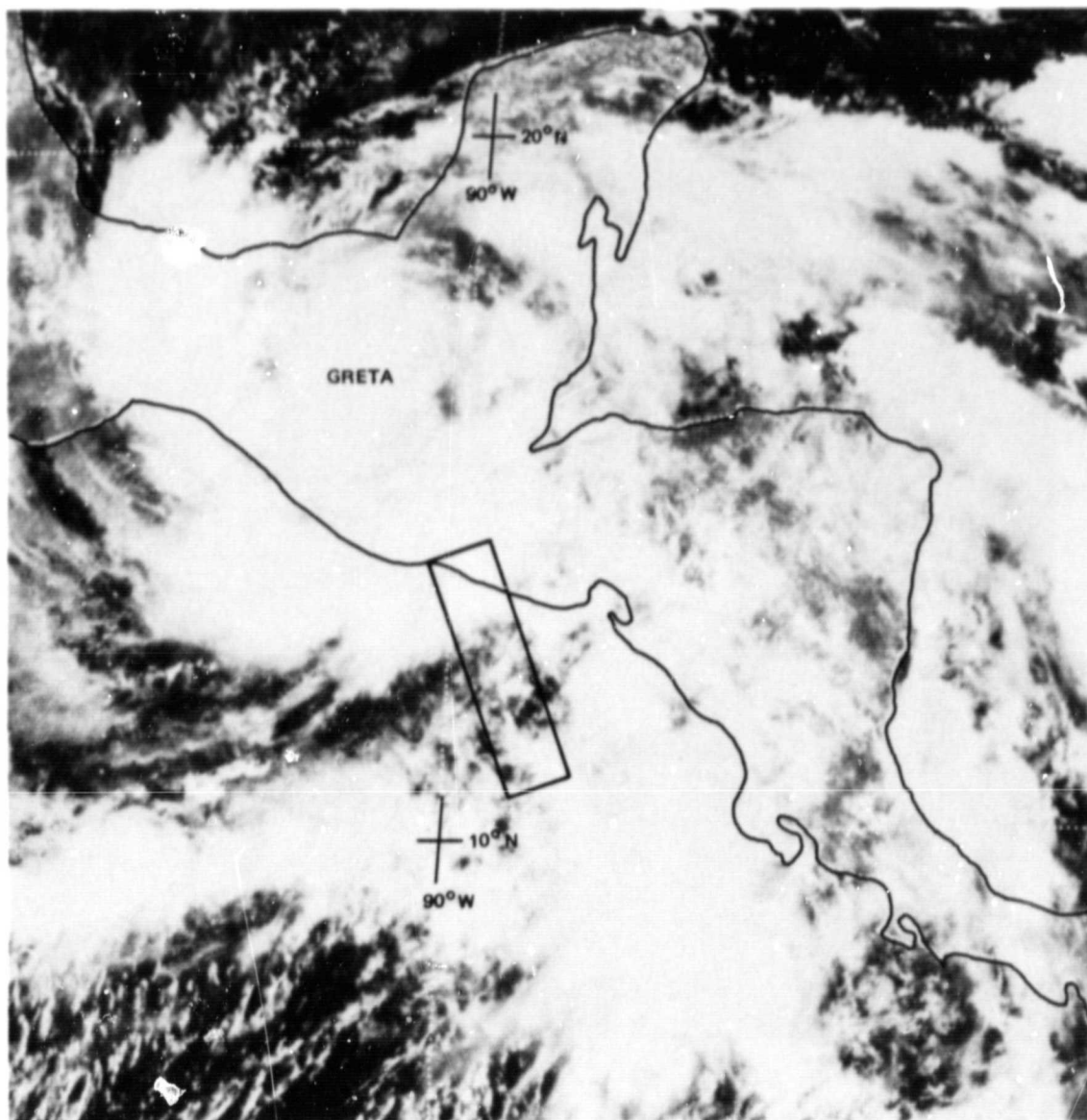
GOES visible-channel image of the tropical storm Greta centered on El Salvador. The area of the SAR image is enclosed by a rectangle.

Squall lines are regions of local gusty winds that produce high radar backscatter (cf. Image 8). The wind observations by the Seasat scatterometer showed a spatially variable wind field of 5 to 9 meters per second in the imaged area, but the structure of the squall lines could not be resolved by the 50-kilometer resolution cell of the scatterometer. The rain rate observations by the Seasat scanning multichannel microwave radiometer (SMMR) suggest that the dark spots at the upper and the lower ends of the image were probably caused by rain. However, the SMMR data at the upper end of the image are probably not reliable due to the proximity to land.

Also seen on this image are packets of internal waves at A1 and B1.

(Rev. 1211; 1616 GMT, September 19, 1978.)

39. Tropical Rain Cells in the Gulf of Mexico

ILLUMINATION DIRECTION →

↑N

0   20 km
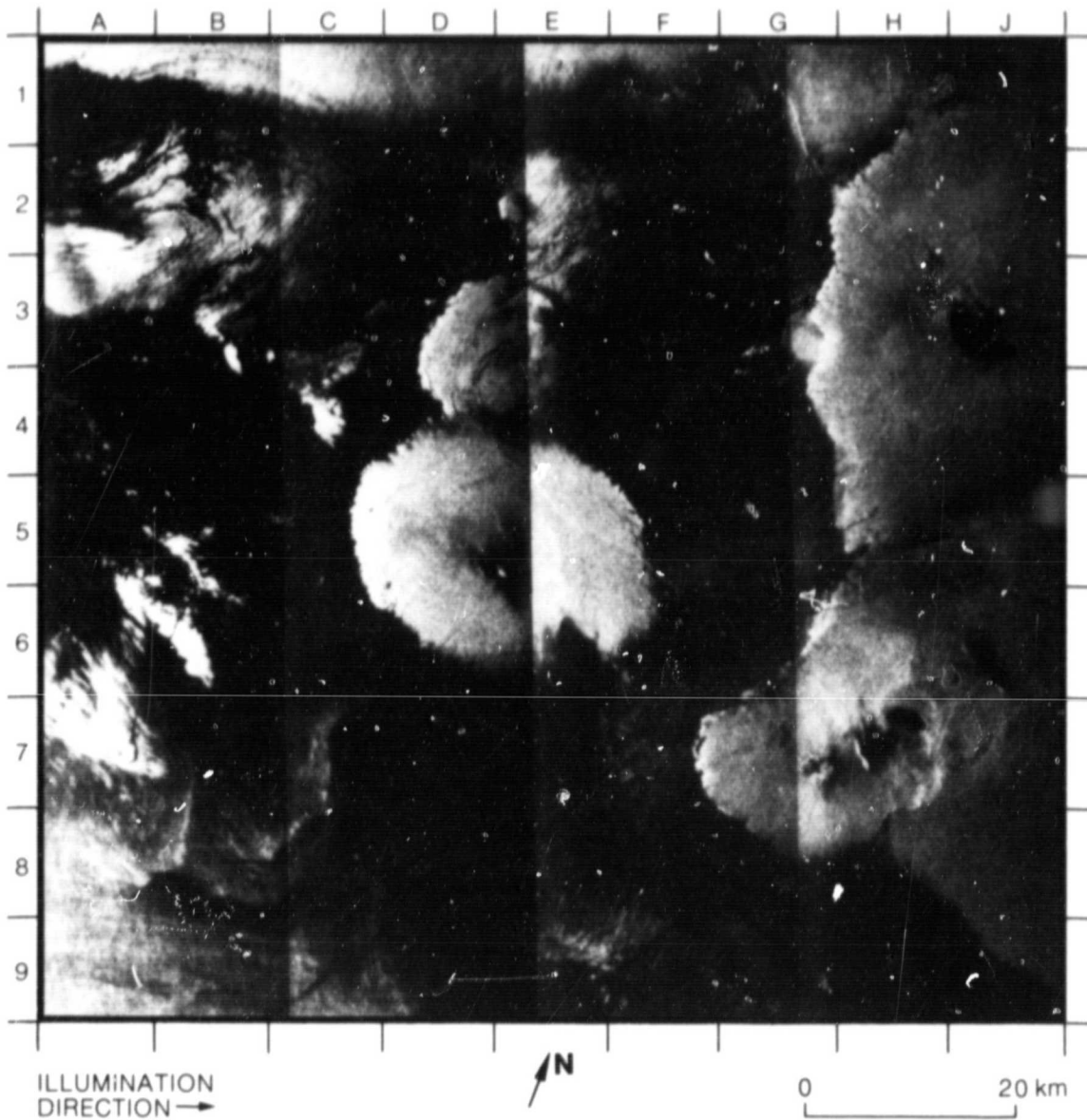
Several tropical rain cells (e.g., E5, J3, and H7) appear in the Gulf of Mexico, about 160 kilometers east-southeast of New Orleans. The cell centers have a low radar return because the sea surface is smoothed by the heavy rainfalls that damp the short capillary/gravity waves, whereas the areas surrounding the cell centers have a nigh radar return because the sea surface is roughened by the wind squalls that carry the cold, descending air away from the cell centers. The distinct boundaries between the wind squalls and surrounding calm water are squall lines (cf. Images 8 and 38).
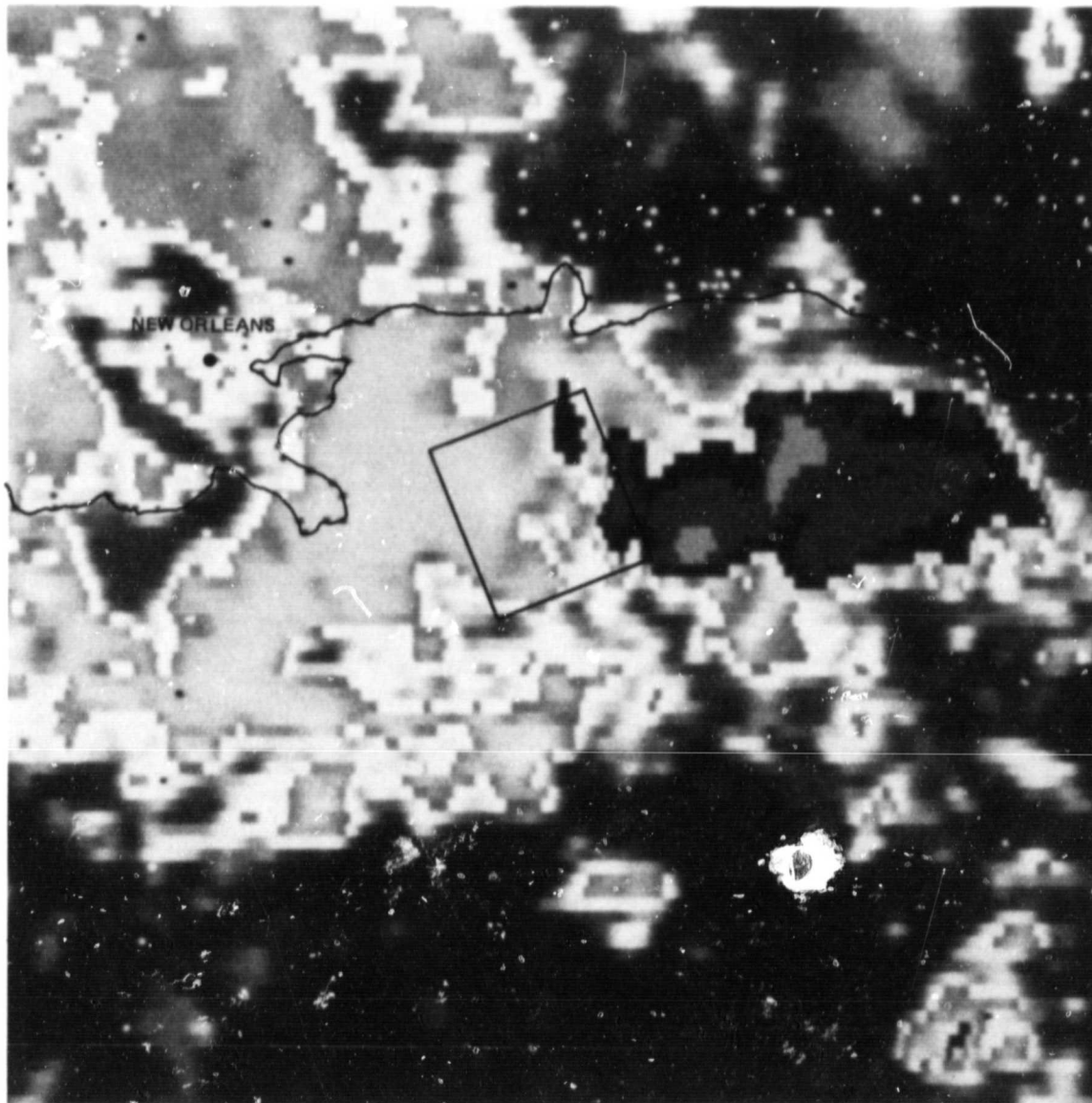
Enhanced GOES infrared image of the Gulf of Mexico off New Orleans, Louisiana. The area of the SAR image is enclosed by a rectangle.

The enhanced GOES infrared image of this area, taken about 13 minutes before the Seasat pass, indicates that the SAR imaged area was on the western edge of a convective storm system (the elongated dark region) with cloud-top temperatures generally below −30 degrees Celsius. Note that the rain cells on the SAR image are represented by two dark spots (cold clouds) and a less distinct, brighter (warmer clouds) feature at their corresponding locations on the infrared image. This comparison indicates that the rain cell at E5 of the SAR image was probably decaying.

Also discernible on the SAR image is a north-bound ship (E1) with its stern wake (see Section 3.9) and a small internal wave packet south of it.

(Rev. 1096; 1514 GMT, September 11, 1978.)

40. Windrows in the North Atlantic Ocean

ILLUMINATION DIRECTION →

N

0   20 km
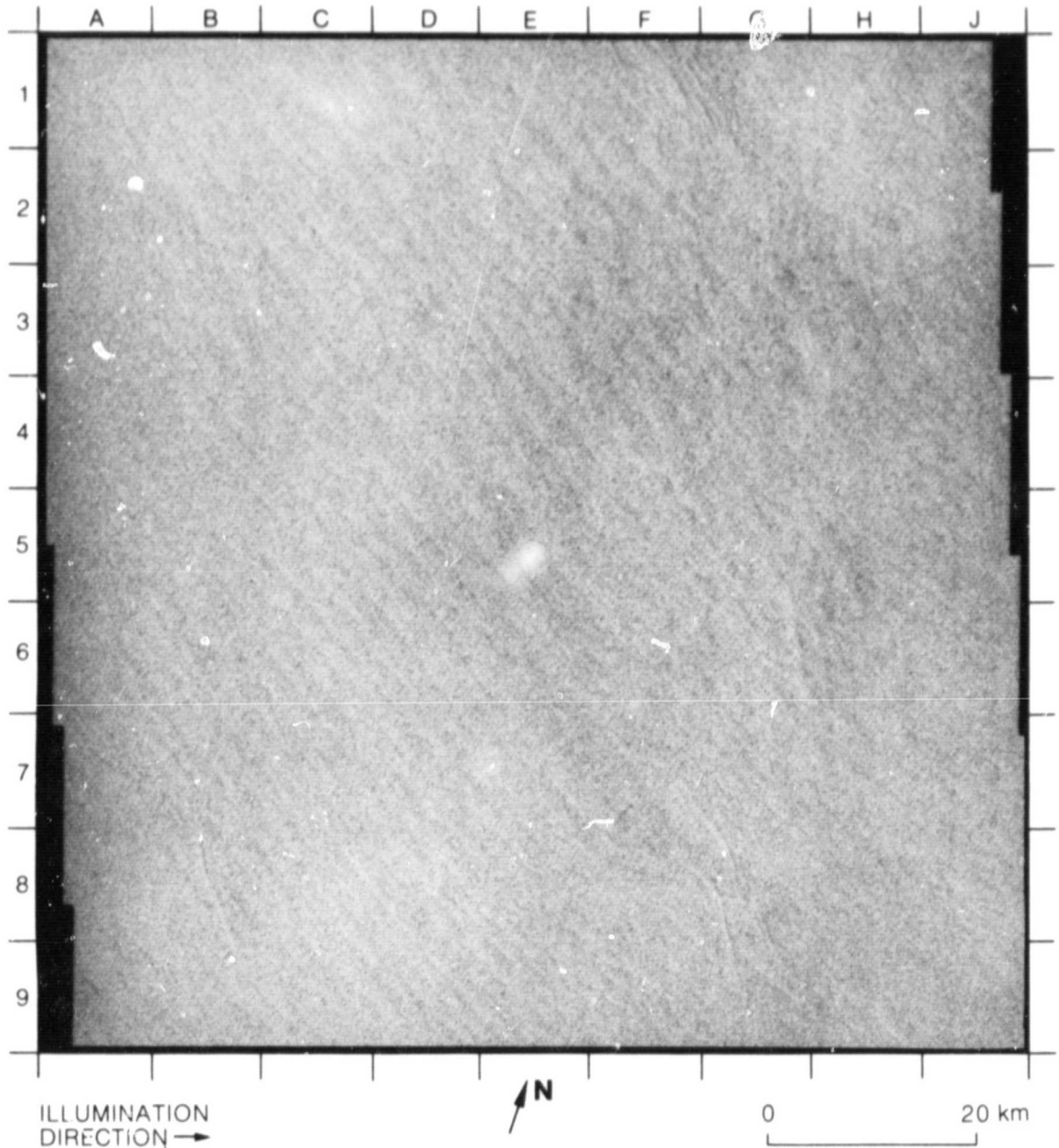
The long, linear striations aligned diagonally on the image are manifestations of windrows above the sea surface. Windrows, sometimes called roll vortices, are secondary, crosswind circulations resulting from instability mechanisms in the planetary boundary layer of the mean wind field (e.g., LeMone, 1973). Their structure is periodic in the crosswind direction with the row axes roughly parallel to the mean wind, resulting in a periodic crosswind modulation in the mean wind speed (and hence in the radar scattering cross section). The horizontal wavelength of windrows is usually 2 to 4 times the thickness of the planetary boundary layer. Existence of windrows is revealed usually by cloud streets at the top of the boundary layer (Kuettner, 1971), and sometimes by organized patterns of soaring seagulls (Woodcock, 1941).
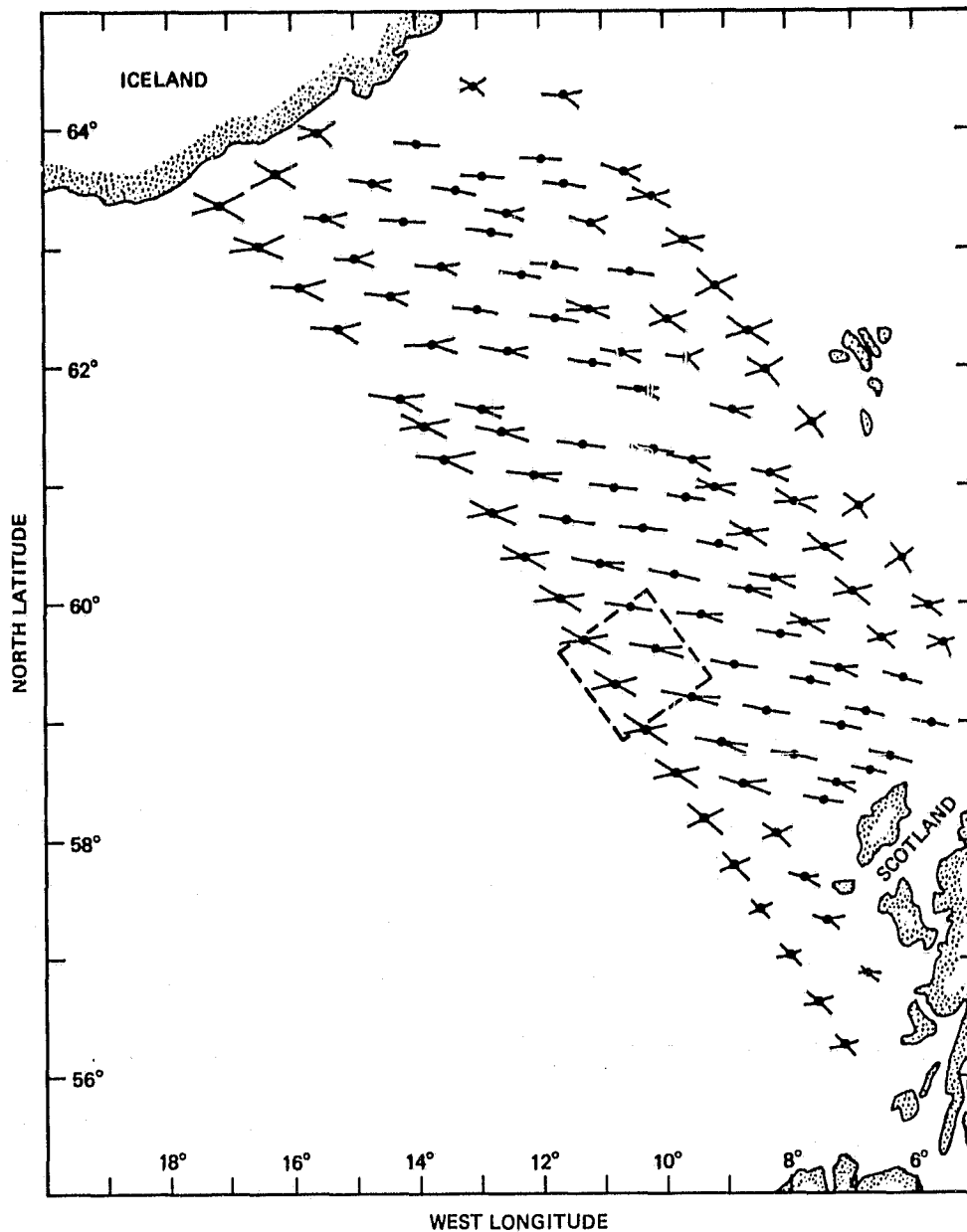
The sticks centered on the solid circles represent the possible wind directions at each resolution cell of the Seasat scatterometer. There is a two- to fourfold ambiguity at each resolution cell. The area of the SAR image is enclosed by dashed lines.

The wavelength of the striations is estimated to be about 2 kilometers, a typical value for windrows. The map shows wind directions in this area as observed by the Seasat scatterometer during the same overpass. Note that the wind directions, regardless of uncertainties, are roughly parallel to the striations on the image. The wind speed in the imaged area was about 12 meters per second, strong enough to generate windrows.

Some weak signatures of internal waves generated by nearby seamounts can be seen at G7/G8 and F1/G1.

(Rev. 1006; 0815 GMT, September 5, 1978.)

41. An Anomalous Feature South of Long Island, New York
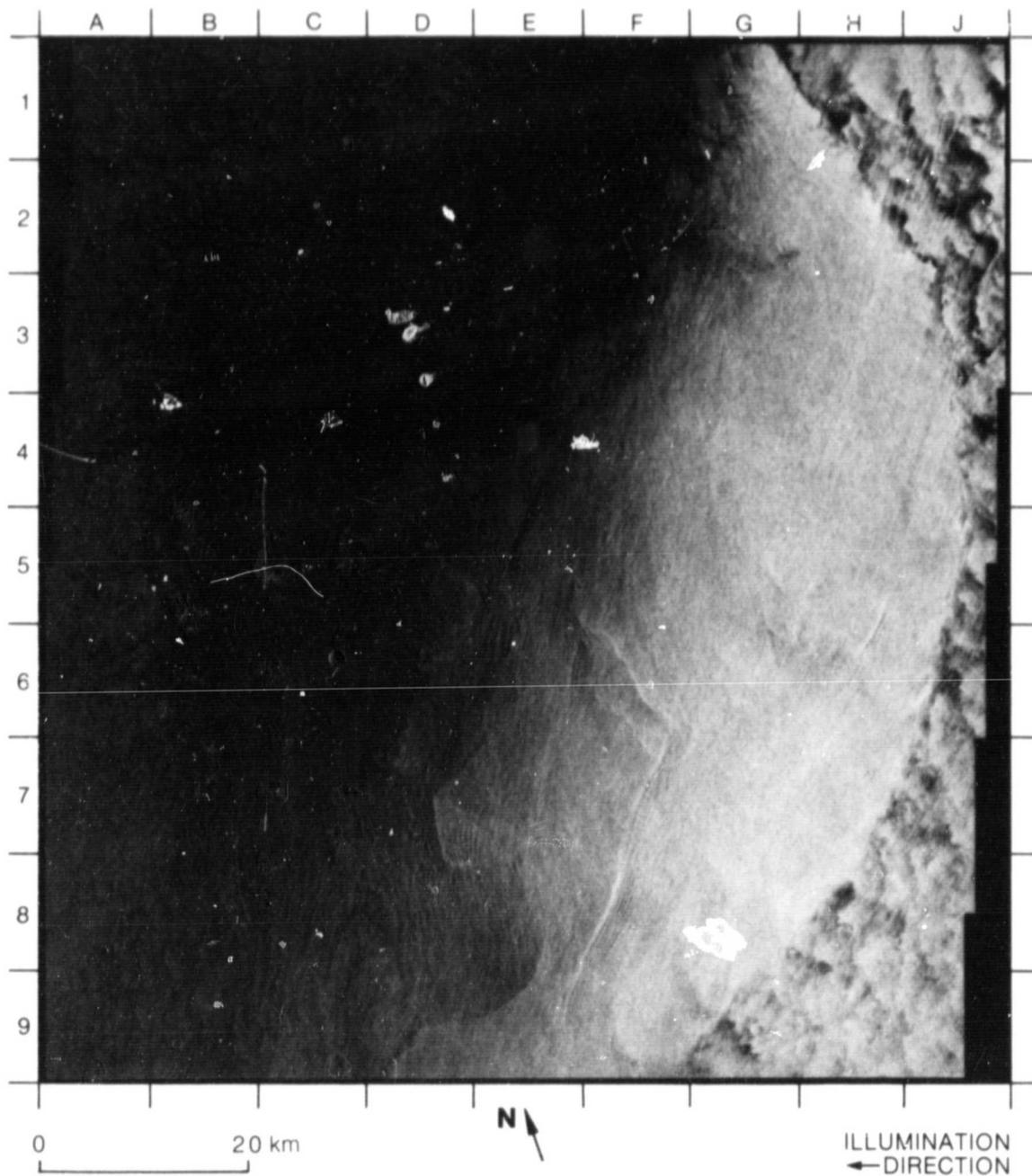
On the right of the image (see the map for location), a drastic change in image texture occurs across an arc-shaped boundary, which separates a region of uniformly bright return from a region of mottled appearance. About 90 percent of the arc is covered by the image. This is one of the most puzzling features imaged by the Seasat SAR; we have no convincing evidence whatsoever to confirm its origin. Concurrent NOAA satellite infrared images of this area show no signs of any thermal structures on the sea surface, indicating that this feature was not a Gulf Stream ring (cf. Section 3.4). Moreover, this feature is not visible on the SAR images of this area taken three days before and six days after this image (Revolutions 1275 and 1404), indicating that the
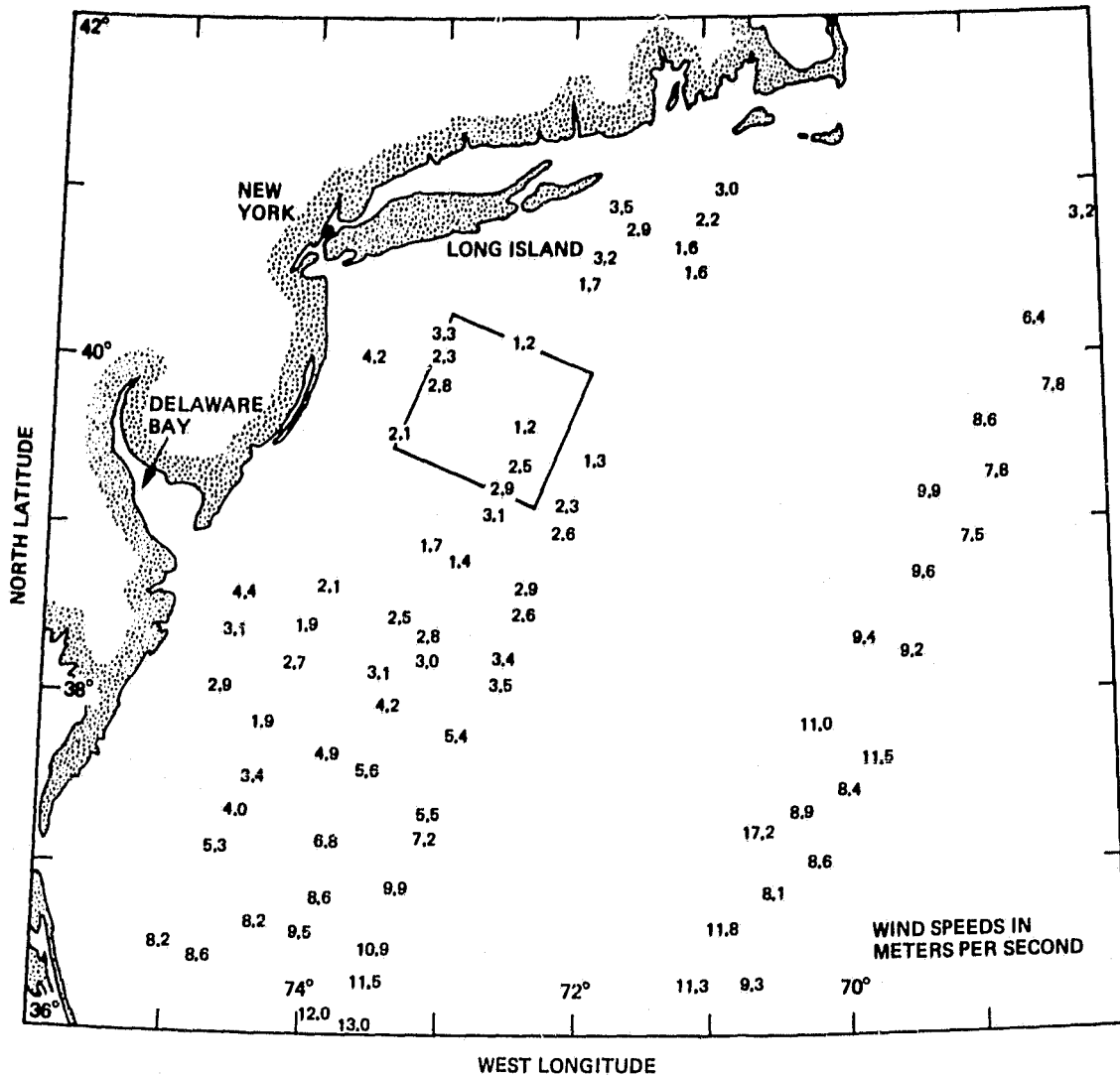
Wind speeds as measured by the Seasat scatterometer. The area of the SAR image is enclosed by a square.

time scale of this feature was much shorter than that of most large-scale oceanic phenomena. Therefore, this feature seems most likely to have been caused by some atmospheric phenomena. However, from both NOAA satellite images and weather maps, there is no evidence of any significant weather features in the area at that time. The wind speeds measured by the Seasat scatterometer during the pass are shown on the map. Apparently the SAR imaged area was in the region of lowest wind. The extended dark area on the image indicates that the wind speed there was less than the threshold (approximately 2 meters per second) for generating Bragg resonant waves. The bright and uniform area to the right indicates an increased wind speed, and the arc-shaped feature might be the boundary of small-scale instabilities in the wind field.

Some curvilinear dark bands at the left edge of the image (e.g., A2 and A5/A6) were probably caused by oil-containing pollutants. Also seen on the image are numerous internal wave packets, of which most are generated over the Hudson Canyon, which lies near the center of the image.

(Rev. 1318; 0433 GMT, September 27, 1978.)

3.9 Ships and Their Wakes

The high resolution of the Seasat SAR revealed ships and their wakes on a large portion of the ocean imagery. Both stationary and moving ships appear typically as bright point targets, with moving ships accompanied by a stern wake. Less often, one side of a ship's bow wake can be seen, and only rarely can both sides of a bow wake be detected.

Detection of a ship by SAR depends on its size, shape, structure, and orientation to the radar beam, and also on the general sea state and wind velocity; high winds and waves tend to mask the ship's image. Several research ships with known positions, including those in JASIN and GOASEX, were illuminated by the SAR but not imaged, probably due to high sea states and clutter, and their relatively small size (Vesecky and Stewart, 1981).

A ship's motion produces both a stern wake and a bow wake, each having different characteristics on the SAR images. The turbulence in a ship's stern wake will temporarily dampen any capillary waves and small surface gravity waves, resulting in a low radar backscatter. The bow wake is V-shaped and has a characteristic angle of 39 degrees in deep water. Contained within this limiting wedge are waves of varying wavelengths and angles of propagation. At normal ship speeds, waves at the boundary of the wedge dominate the pattern, making the characteristic bow wake of 39 degrees visible. However, if a ship's velocity is either too high or too low, the waves in the interior of this limiting wedge become dominant, making the apparent wake angle less than 39 degrees (Lighthill, 1978). In any case, the increase in surface roughness at the boundary of the bow wake causes an increase in radar backscatter. Wind and surface waves seem to overcome the signature of a bow wake more rapidly than that of a stern wake, which persists over a greater distance.

A ship with a velocity component in the range direction of the SAR will produce a shift in the Doppler frequency of the returned signal. This results in the azimuthal displacement of the ship's image relative to its wake. The speed of the ship can be estimated from the amount of this displacement, the velocity of the spacecraft, the ship's direction of travel, and its distance from the spacecraft nadir point (Elachi and Brown, 1977; Jain, 1978).

Five images have been selected to show the appearance of ships and their wakes under various conditions. The first image is an example of a ship in the open ocean with only its stern wake visible. Image 43 shows a ship with only one side of its bow wake visible. The three ships in image 44 appear in calm areas, with at least one ship having a narrow bow wake. Image 45 shows a ship in the Atlantic Ocean with a quite long stern wake that may be a result of oil discharge from the ship. The two moving ships in Image 46 are displaced from their stern wakes because of shifts in the Doppler frequency.

42. Ship With Stern Wake
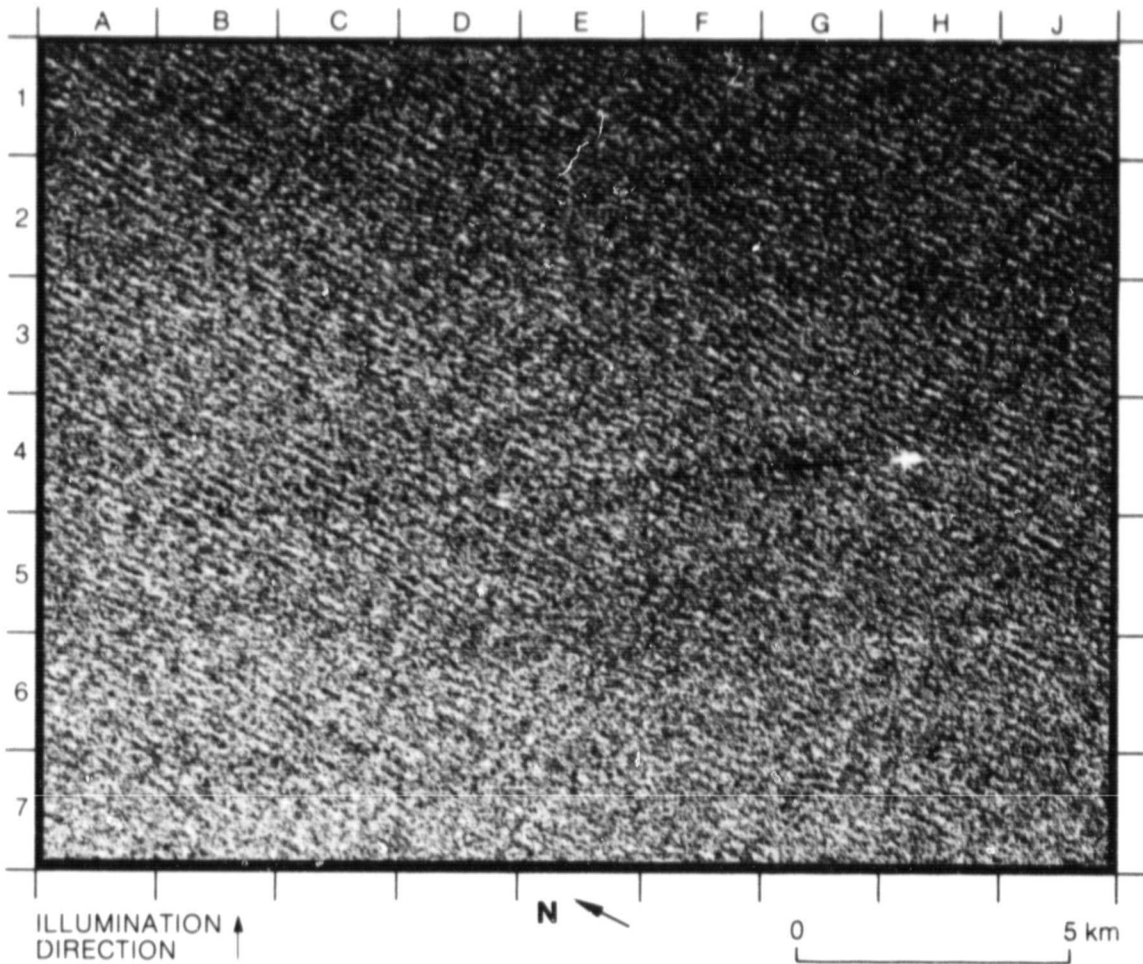
The stern wake of this large, bright ship (H4) in the Pacific Ocean is visible for about 12 kilometers, while the bow wake is not seen. The sea state is fairly high with surface waves of approximately 250 meters in wavelength and wind speeds greater than 7 meters per second (Seasat Gulf of Alaska Workshop II Report, 1980). The ship's heading places it on a direct route from Port Valdez, Alaska, to a port in California, indicating that it may be an oil tanker.

(Rev. 1126; 1741 GMT, September 13, 1978.)

43. Ship With Bow Wake
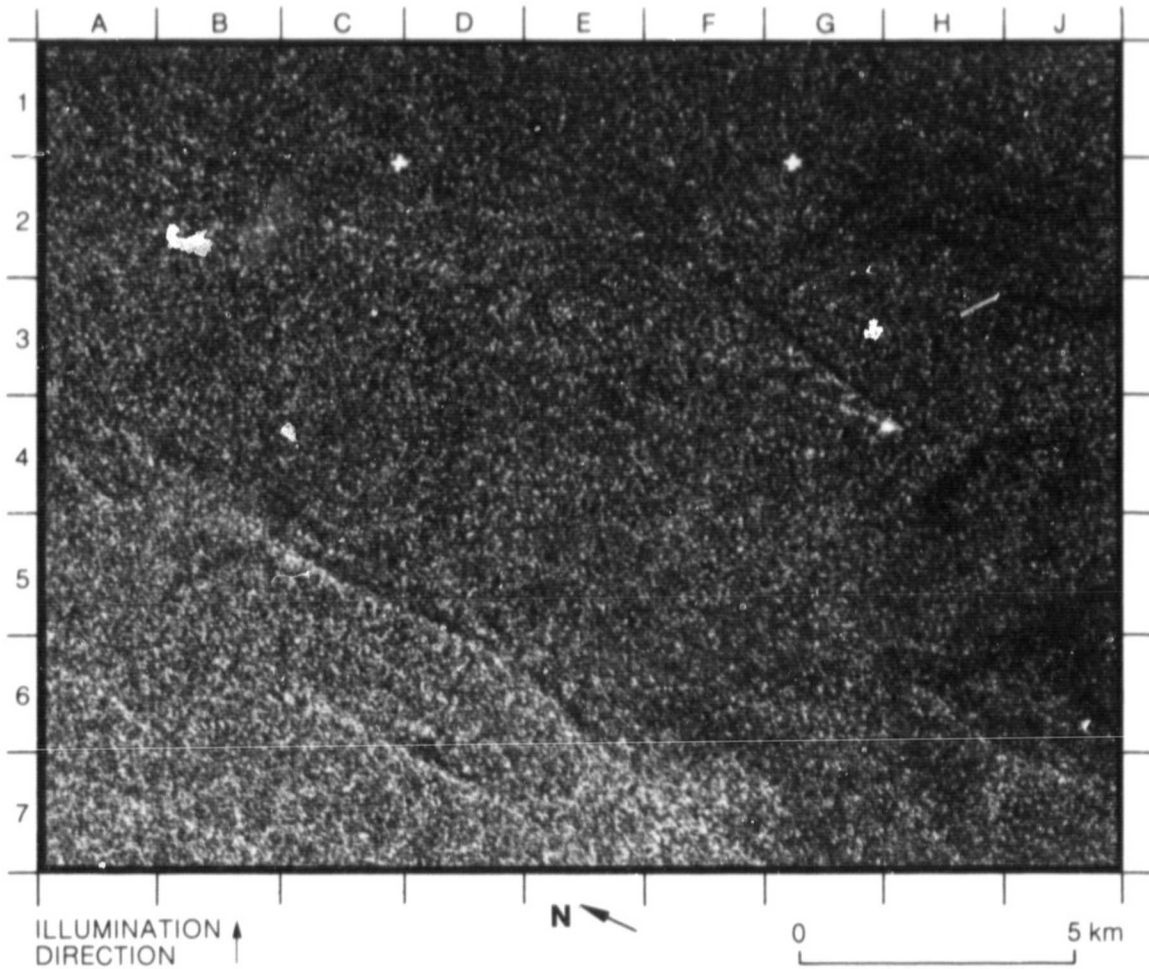
This ship (H4), with one side of its bow wake and its calm stern wake visible, is traveling in a southward direction 130 kilometers off Chesapeake Bay. The angle formed between the bow wake and the stern wake is very close to 19.5 degrees, half of the characteristic angle of the full bow wake. It is not clear why the other side of the bow wake was not imaged. The ship is displaced from its stern wake because of range motion. Also, several groups of internal waves are seen propagating shoreward.
(Rev. 1253; 1455 GMT, September 22, 1978.)

44. Ships in a Calm Ocean With Bow Wakes

ILLUMINATION DIRECTION

N

0   10 km
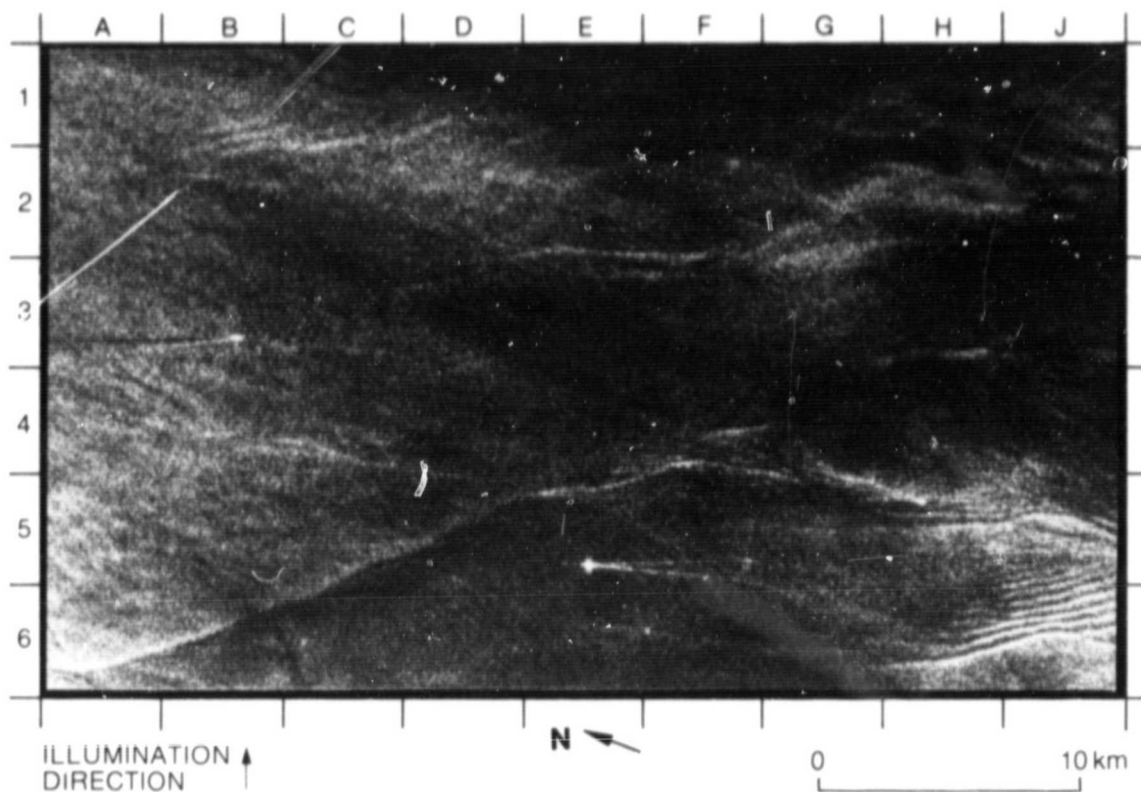
This image, 40 kilometers off the Florida Coast near Cape Canaveral, shows three ships (B3, E5, and H5), all with slightly different wake appearances. Although the surface is calm, only one of the ships (E5) has a clearly visible bow wake, which forms an angle of 7 degrees; however, no stern wake can be distinguished. Another ship (B3) has a stern wake with low backscatter and the faintly visible portion of a bow wake. The wake of the third ship (H5) almost disappears in the surface expression of the internal wave groups whose crests are somewhat parallel to the ship motion.
(Rev. 407; 1118 GMT, July 25, 1978.)

45. Ship With Long Stern Wake

ILLUMINATION DIRECTION

N

0   10 km
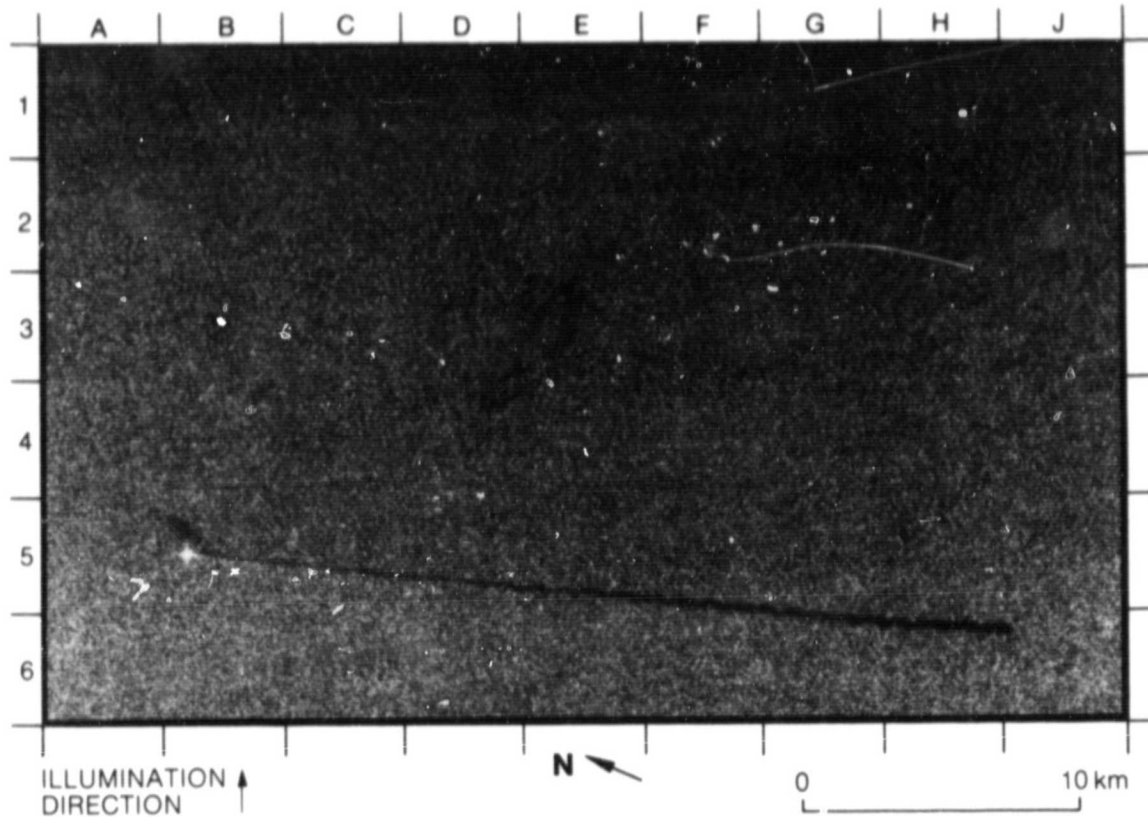
This ship (B5) in the Atlantic Ocean has a stern wake that extends for 30 kilometers, and no visible bow wake. Apparently, the ship is discharging oil or an oil-contaminated liquid. The oil disperses with time, causing the wake to widen and the short surface waves to damp. The ship is roughly 500 kilometers from the coast, heading for Delaware Bay.

(Rev. 1210; 1442 GMT, September 19,1978.)

46. Ships Displaced From Their Stern Wakes

ILLUMINATION
DIRECTION

N

0   10 km
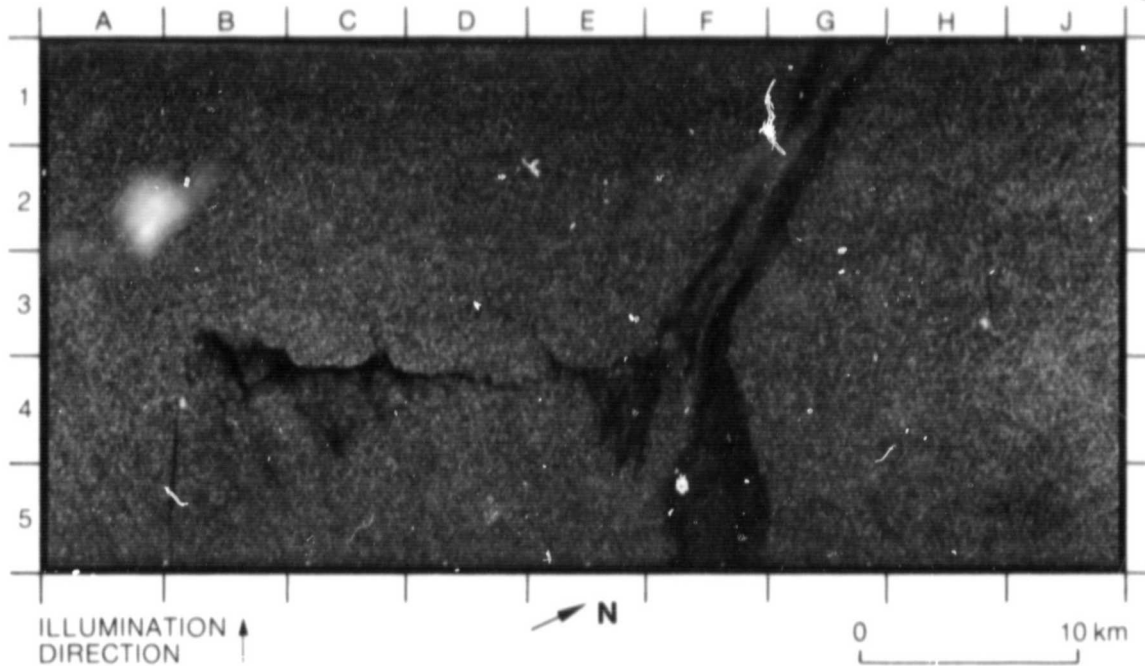
Each of the two ships (A4 and H3) on the image are displaced from their stern wakes because of shifts in Doppler frequency produced by their motion. Each ship has a velocity direction nearly perpendicular to the spacecraft flight direction. The ship at H3 is moving toward the radar and produces a positive shift in Doppler frequency that displaces it forward of its wake. The ship at A4 is moving away from the radar, causing a negative shift in Doppler frequency and a displacement rearward of its wake. The velocities of the two ships are estimated to be 9 meters per second (18 knots) for the H3 ship and 7.5 meters per second (15 knots) for the A4 ship, as discussed on page 112. The extensive, dark streaks between the two ships may be pollutants dispersed by winds and surface currents. Three days later, these streaks were still visible.

(Rev. 1404; 0504 GMT, October 3, 1978.)

CHAPTER 4
Seasat SAR Images of Arctic Sea Ice

In addition to the study of surface waves, a secondary objective of the Seasat SAR was to determine its potential for the remote sensing of sea ice, which has an important role in the global climate through its contribution to the Earth's heat budget, and in such coastal operations as oil exploration, fishing, and ship routing. The effectiveness of SAR in early sea-ice studies has been reviewed by Page and Ramseier (1975) and in the Active Microwave Workshop Report (1975). AIDJEX, a comprehensive experiment in the Arctic Ocean using an airborne SAR in combination with both passive and active microwave sensors, and coincident surface measurements, led to increased understanding of the motion (Leberl et al., 1979), age, dynamics, and backscatter characteristics of sea ice (Campbell et al., 1978). Additionally, two other satellite sensors have proved valuable for sea-ice studies, but both have key functional disadvantages that can be overcome with a SAR. The electronically scanning microwave radiometer (ESMR) on the Nimbus-5 satellite utilized brightness temperature characteristics to distinguish between various ice types and to determine the concentration, movement, and structure of these ice types on an annual basis with a resolution of only 30 kilometers (Campbell et al., 1978 and 1980; Gloersen et al., 1978). The multispectral scanner (MSS) on Landsat has tracked ice floes and observed the structural and seasonal morphological changes within pack ice (Williams and Carter, 1976). However, the prevailing inclement weather conditions of the polar regions restrict the use of the MSS to essentially cloud-free days. A space-borne SAR, however, can produce a high-resolution view of

the dynamics of sea ice on a repeated basis, unrestricted by weather or the time of day.

The primary sea-ice experiments intended for the Seasat SAR were to determine the radar backscattering coefficient of various ice types and observe the structure, dynamics, and motion of ice from sequential passes. Imagery was acquired on an almost daily basis over the Beaufort Sea, with more than 100 passes recorded. Without the coincident surface and aircraft observations, scheduled to begin during the winter months of 1978 and 1979 in support of Seasat, but not taken due to the satellite's early failure, the task of calibrating the SAR backscatter was very difficult. However, much useful information can still be obtained from the SAR imagery on the major morphological features, structural changes, and drift motion of sea ice (Teleki et al., 1979).

The morphology of sea ice changes significantly with time. Newly formed sea ice, including both shore-fast ice and floes associated with pack ice, is relatively thin and has a smooth surface. After this initial formation, the ice is continuously subject to temperature fluctuations, compressive and shearing forces from the motion of other ice floes, surface currents, and wind stresses. These factors result in structural changes in the ice such as ridge formation and an overall increase in thickness and surface roughness. Additionally, the ice floes undergo a seasonal metamorphosis in the summer as the snow and ice surface melts, causing desalination and subsequent recrystallization within the ice floes. As the result of all these processes, first-year floes have angular edges and moderately rough surfaces with some ridges, while multiyear floes have rounded edges and hummocked surfaces with numerous ridges.

Some discrimination by SAR between the various types of sea ice is possible since the imaging mechanism is primarily a function of the surface roughness characteristics of the ice. The low radar backscatter from new ice distinguishes it from the higher radar backscatter from both first-year and multiyear ice, but not from a smooth ocean surface, unless the time of year is considered (new ice is more likely to form in winter than in summer). The radar backscatter characteristics of both first-year and multiyear ice have been found to be so similar at the single wavelength, incidence angle, and polarization used by the Seasat SAR that it is very difficult to distinguish between them (Onstott et al., 1980). This problem is compounded by the lack of coincident surface and aircraft observations and by the fact that Seasat was operational during only one season, leaving only the different shapes of first-year and multiyear ice to aid in their identification.

Eight images were selected to illustrate a range in types of sea ice and ice dynamics. Image 47 is a characteristic scene of pack ice within the main Beaufort Sea region. Included is a small ice island, presumably broken off from Ellesmere Island. This ice island was tracked by the SAR over an 80-day period. Image 48 shows shore-fast ice breaking up and drifting away from land. Images 49A and B show the rapid structural changes that can occur within pack ice during a 3-day period, and include a large ice island. Images 50A, B, and C demonstrate the rapid changes in morphology and drift motion that can occur during two successive 3-day periods at the boundary between the ice pack and open water. Image 51 shows the complex interaction between surface waves and small ice floes at the pack-ice margin.

47. Pack Ice

ILLUMINATION
DIRECTION

N

0   20 km
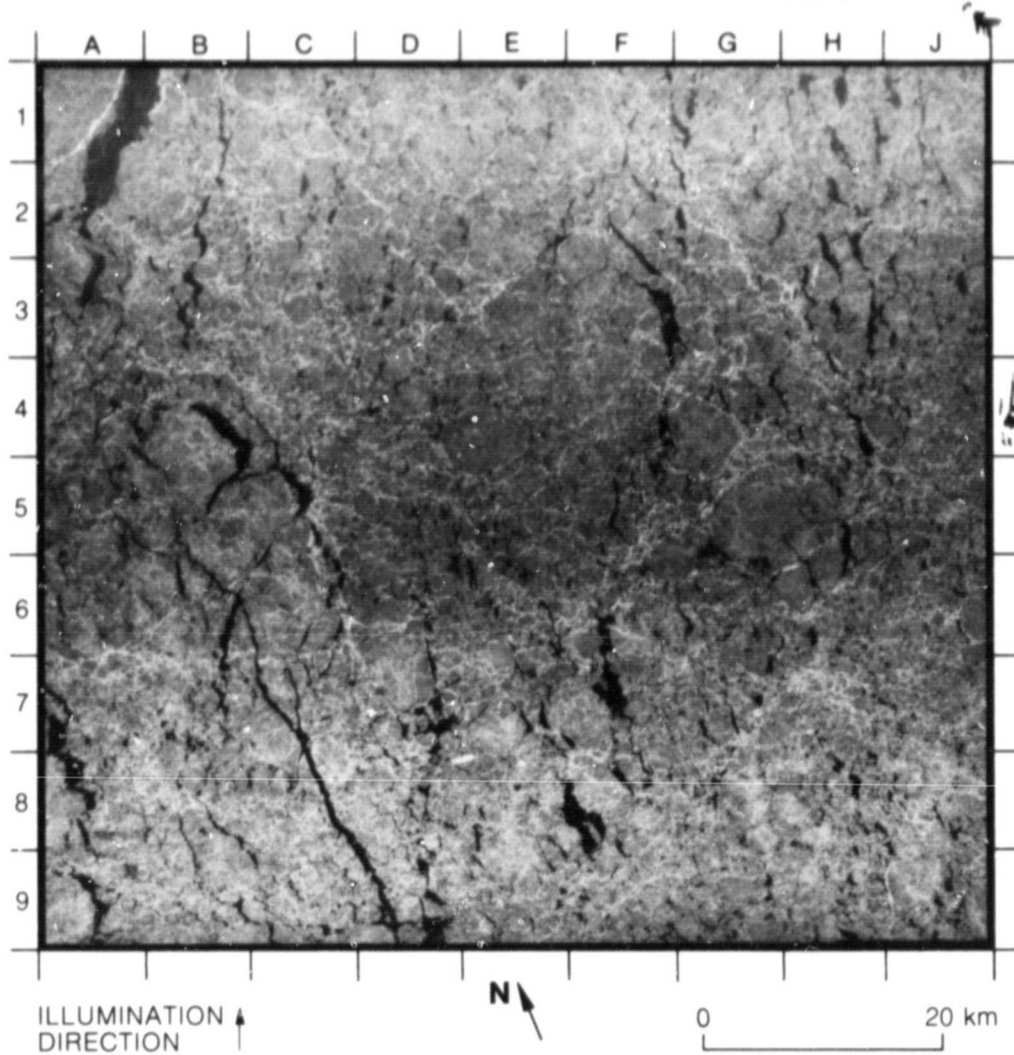
Pack ice within the central Beaufort Sea consists primarily of an aggregate of both multiyear and first-year ice floes, some as large as 10 kilometers in diameter (F3, G5). Identification of multiyear and first-year ice contained within this image is difficult at the single wavelength, incidence angle, and polarization of the Seasat SAR. However, the shapes of the floes can provide clues. Multiyear floes (3 to 5 meters thick) are rounded from extensive grinding, while first-year floes (1 to 1.5 meters thick) tend to be more angular. Ridging and rafting of floes caused by compressive forces results in bright, linear features that often border the floes (A1). The leads between floes appear as dark linear bands (B4 and C7 to D9), indicating either a calm ocean surface or recently frozen ice.

Of special interest is the bright, anomalous feature entrapped within the ice pack (D8/E8). The feature, with small ice floes cemented to it, is probably an ice island calved from the ice shelf on Ellesmere Island in the Arctic Ocean. Its small-scale surface roughness near the L-band wavelength of 23.5 centimeters produces a radar backscatter high enough to saturate the dynamic response of the photographic film. This was unavoidable because the anomaly was always viewed with its long axis roughly parallel to the flight direction of the satellite, and more than one viewing angle was impossible. Imaging from a different angle might have produced less backscatter, and, in turn, brought the image out of saturation to reveal more detail of the anomaly's
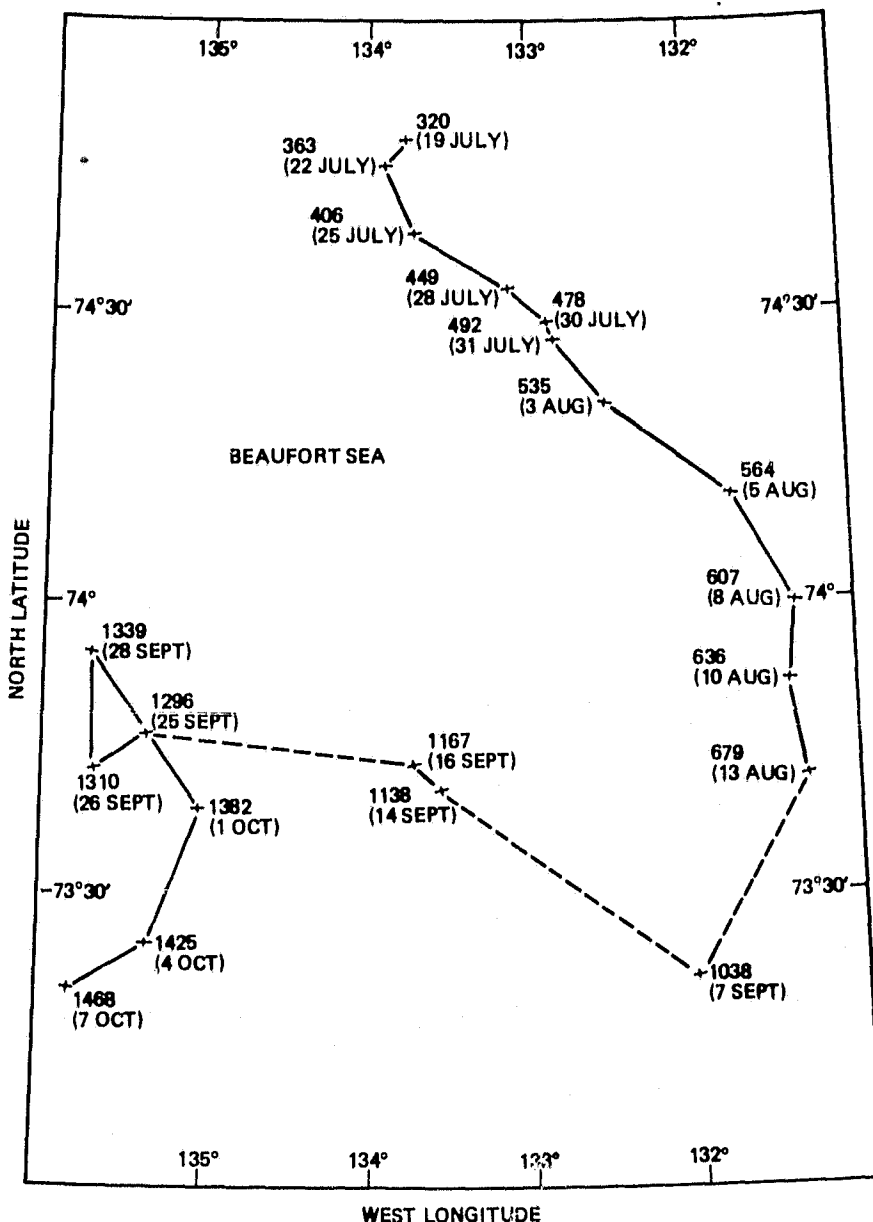
Drift motion of an ice island. The crosses indicate the position and orientation of the ice island plus the revolution number and date. The dashed lines indicate a significant gap in the SAR coverage of this feature.

surface structure. This feature was imaged by the Seasat SAR on 20 separate passes, many of these over 3-day repeat sequences, providing a unique opportunity for the study of the drift of an ice island within pack ice. During the 80-day period from July 19 to October 7, the anomaly traveled circuitously approximately 435 kilometers, an average of 5.4 kilometers per day, as shown on the map. The greatest drift velocity was found to be between September 28 and October 1, when it averaged 12.2 kilometers per day.

(Rev. 1468; 1612 GMT, October 7, 1978.)
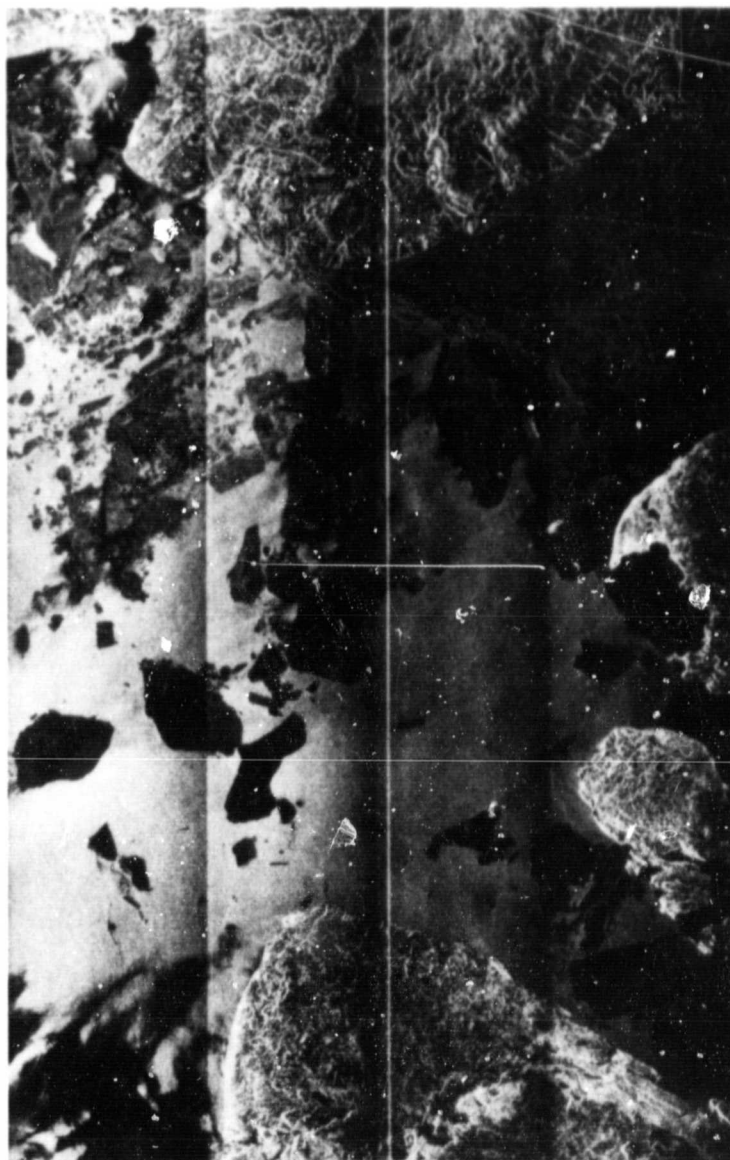
48. Shore-Fast Ice

ILLUMINATION
DIRECTION →   N   0   25 km

Warming temperatures caused the break up of large blocks of first-year, shore-fast ice from the frozen Prince of Wales Strait and several smaller bays (see the map for location) as seen in this image. Shore-fast ice begins to form in undisturbed areas next to land and continues to form outward as conditions permit. Both the large blocks and the more highly fragmented chunks of shore-fast ice are drifting southward into the Amundsen Gulf. The ice itself has a low radar backscatter as the result of its smooth surface, while the bright linear features within the ice are closed cracks resulting from thermal stress and tidal and mechanical forcing. The open water, uniformly roughened by wind stress, is clearly distinguishable from the shore-fast ice. Prince of Wales Strait was clear of ice 47 days later, as indicated on other SAR imagery.

(Rev. 220; 0954 GMT, July 12, 1978.)
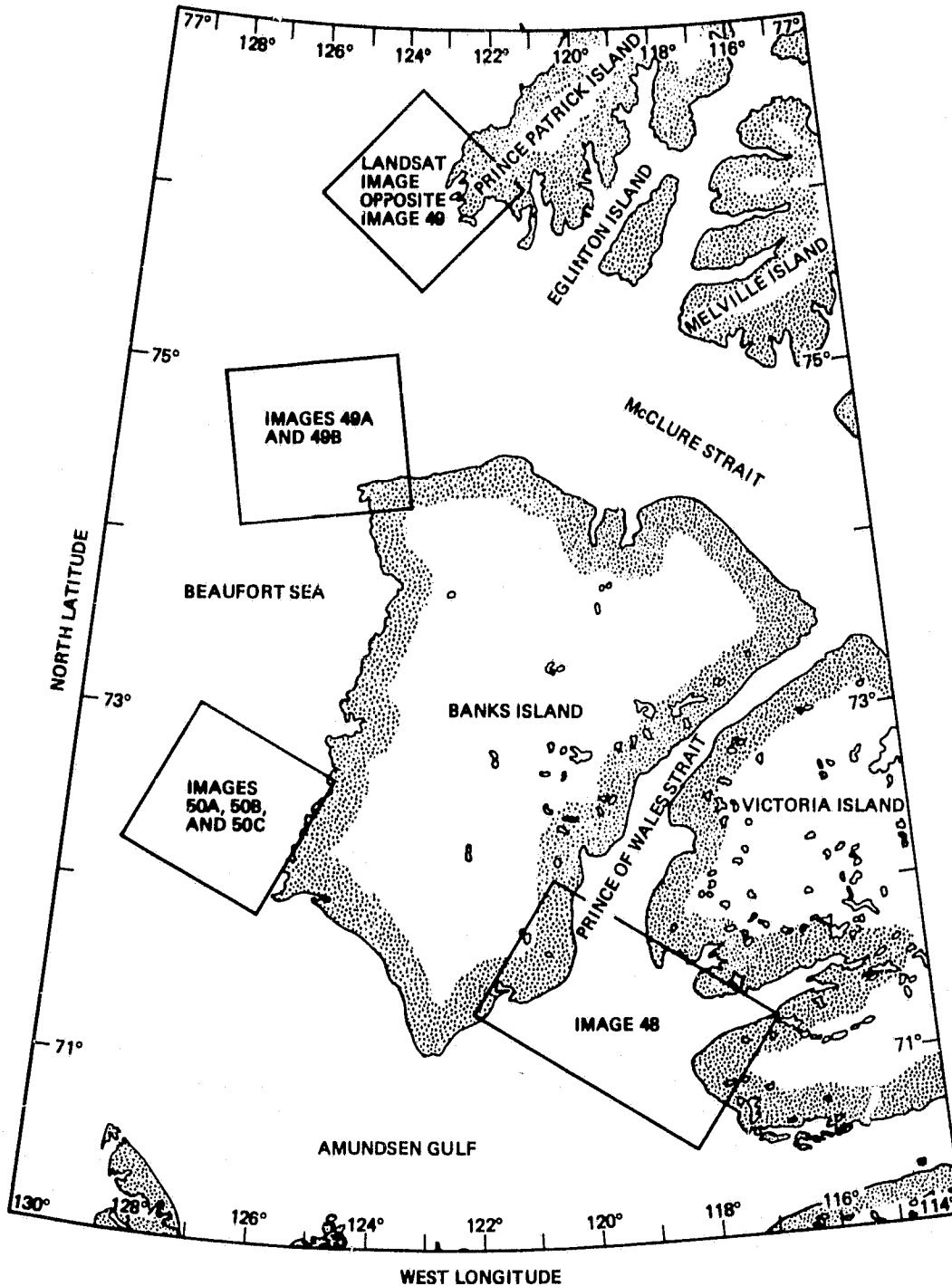
Map of Banks Island and the Beaufort Sea showing locations of polar ice images.

49. Structural Variations Within Pack Ice

ILLUMINATION DIRECTION

N

0   20 km
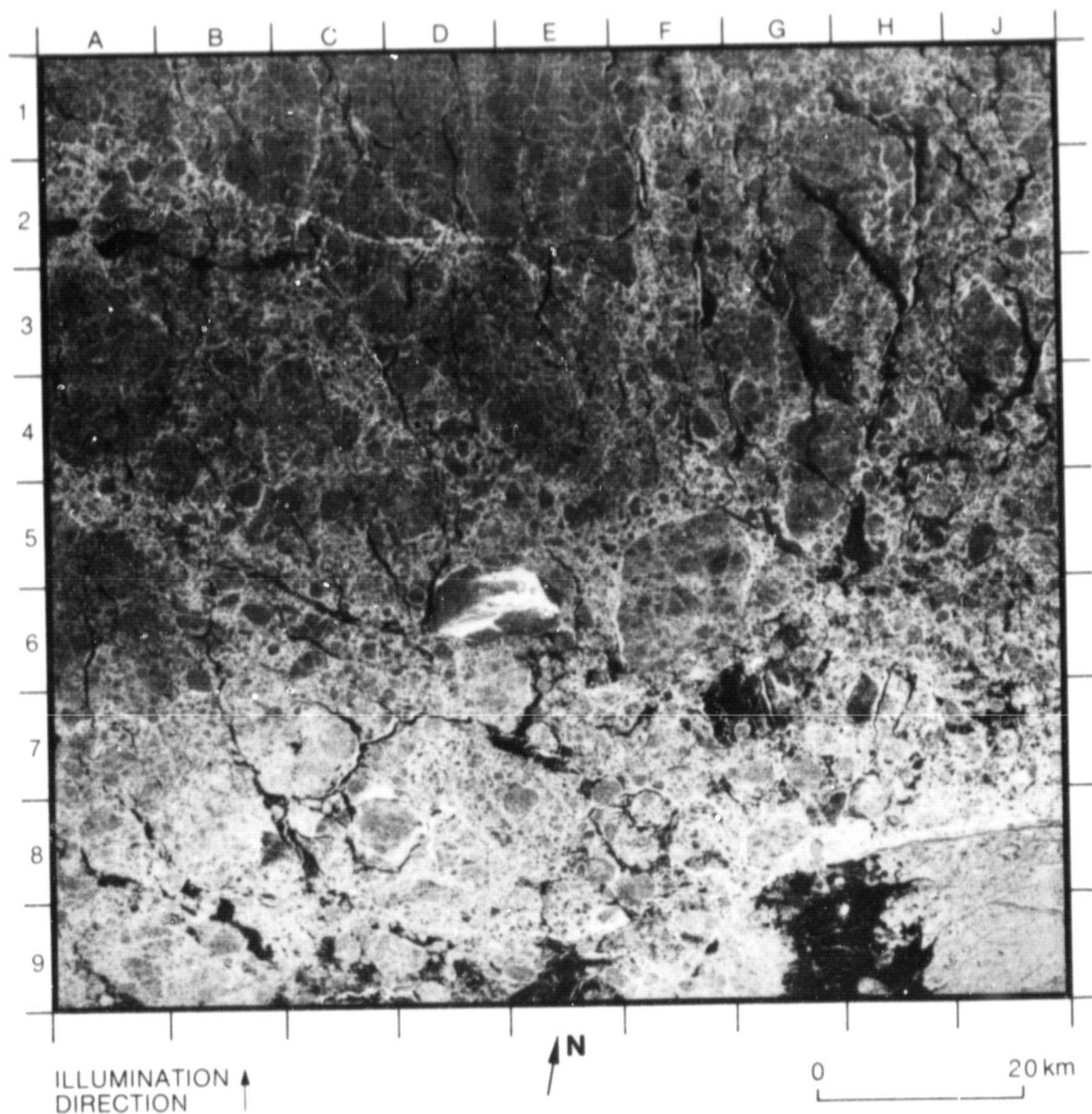
Structural changes can occur rapidly within the main ice pack, as seen in these two images taken 3 days apart north of Banks Island (see the map opposite Image 48 for location). Multiple polynyas have widened up to 5 kilometers from narrow leads between the cemented first-year and multiyear floes. Their dark appearance indicates either open water or recently frozen ice. The western portion of the pack ice moved approximately 15 kilometers toward the south, while the ice directly north of Banks Island showed little motion and remained compacted along the coast.

ILLUMINATION
DIRECTION

N

0   20 km
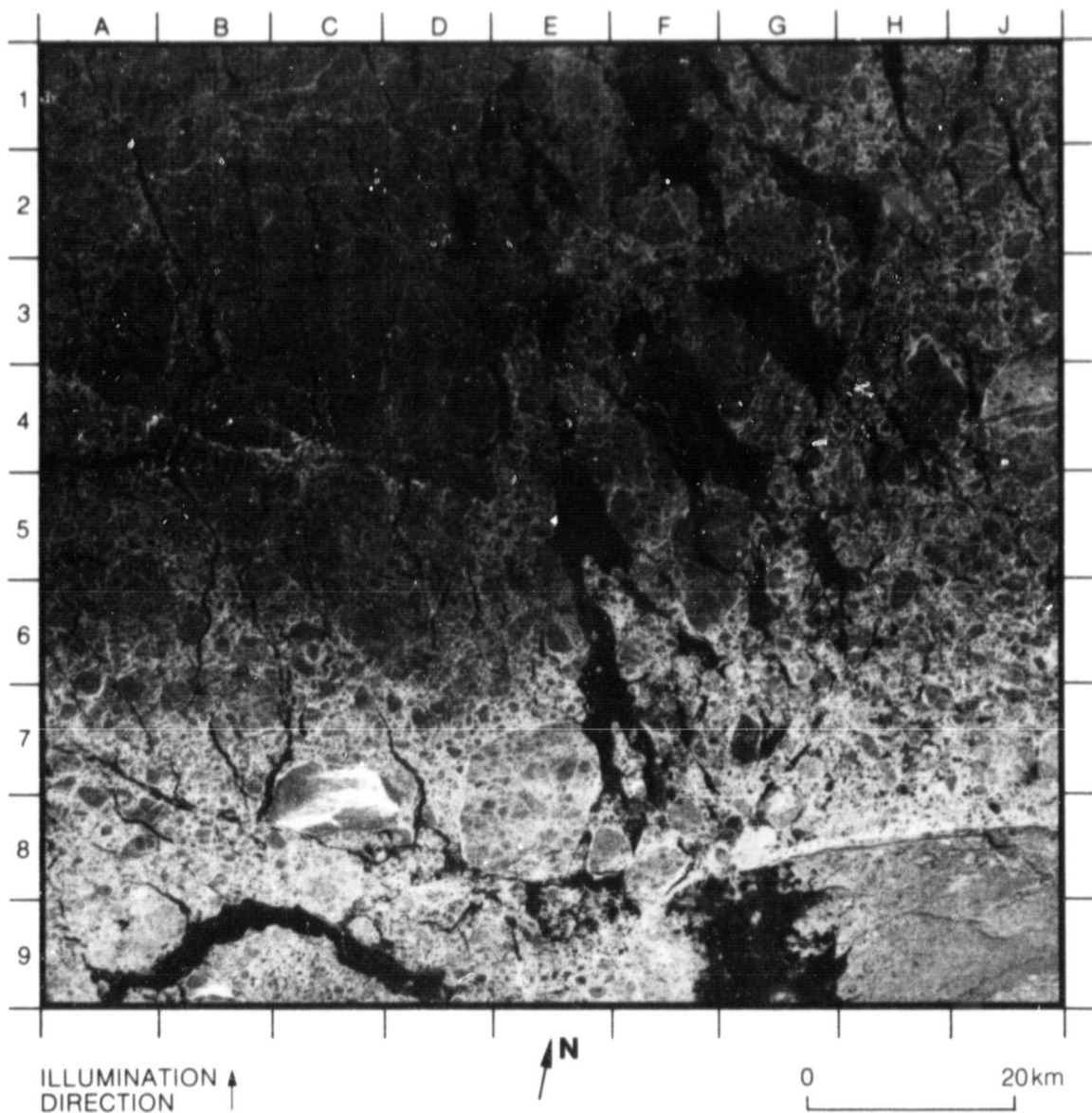
The large feature with a unique radar backscatter is Fletcher's Ice Island, commonly referred to as T-3 (D6 on Image 49A, and C8 on Image 49B), which is a tabular block of ice, 7 kilometers by 12 kilometers in area, calved from the Ellesmere Island ice shelf. The high radar backscatter may be due to the ice island's regular pattern of low, corrugated ridges and scattered deposits of rock debris (Rodahl, 1954). Fletcher's Ice Island was discovered in 1946 and has been tracked continuously since then, remaining within the anticyclonic gyre of the Beaufort Sea. It was imaged by Seasat on eight separate passes from August 16 to October 6, traveling 157 kilometers over 61 days in a south-westward direction. The positions have been confirmed by the tracking of T-3 from a NOAA satellite.

127-

Landsat MSS scene at Prince Patrick Island showing Fletcher's Ice Island.

In the Landsat image obtained on July 5, 1978, the ice island (E5) is located near Prince Patrick Island (see the map opposite Image 48 for location). Prince Patrick Island is encircled by dark ice which, in this case, is shore-fast ice. The ice island is still snow-covered while the surrounding pack ice has undergone its seasonal melt, with the ice surfaces now mottled with ponds from melting snow and ice. On the shoreward edge of the ice island, the small, dark bay, which is not clearly discernible on the SAR images, is old sea ice that has remained compacted in that bay for many years. From the time of the Landsat image to the time of Image 49B, the ice island rotated over 90 degrees in a clockwise direction.

(A: Rev. 1409: 1310 GMT, October 3, 1978. B: Rev. 1452; 1322 GMT, October 6, 1978.)

50. Ice Motion and Morphology at Pack-Ice Margins

ILLUMINATION DIRECTION

N

0   25 km
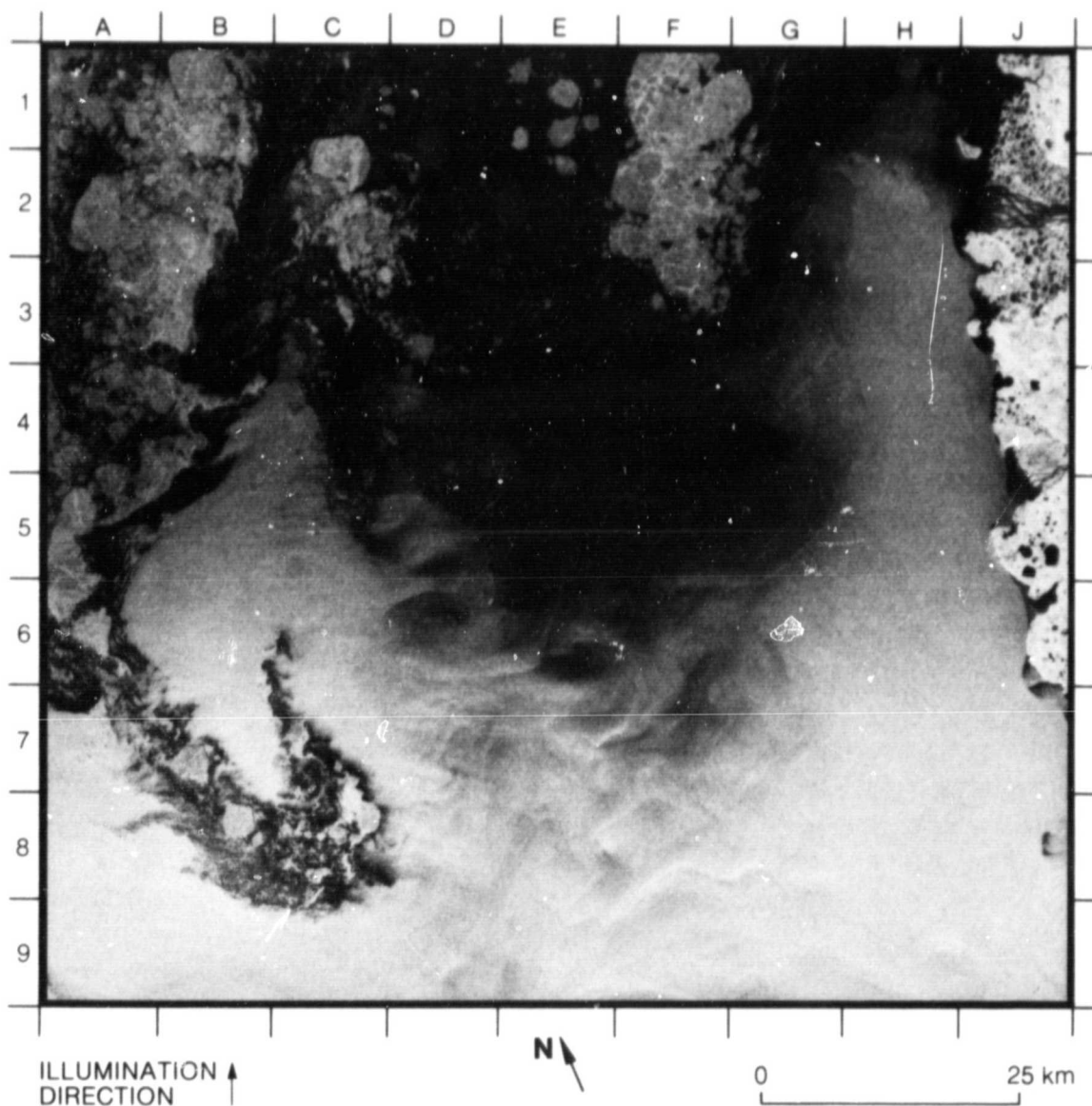
As indicated by these three images taken off the coast of Banks Island (see the map opposite image 48 for location) over a 6-day period, the motion and morphology of ice at the pack-ice margins may be highly variable. Ice motion at the pack ice margin is affected by both wind stress and surface currents; however, without any adequate surface truth data, it is very difficult to determine the dominating forcing mechanism. Individual floes of the fragmented pack ice were identified and tracked to determine the short-term drift motion. The first image (A) consists primarily of open water, whose surface appearance is affected both by wind stress and small-scale

ILLUMINATION
DIRECTION

N

0   25 km
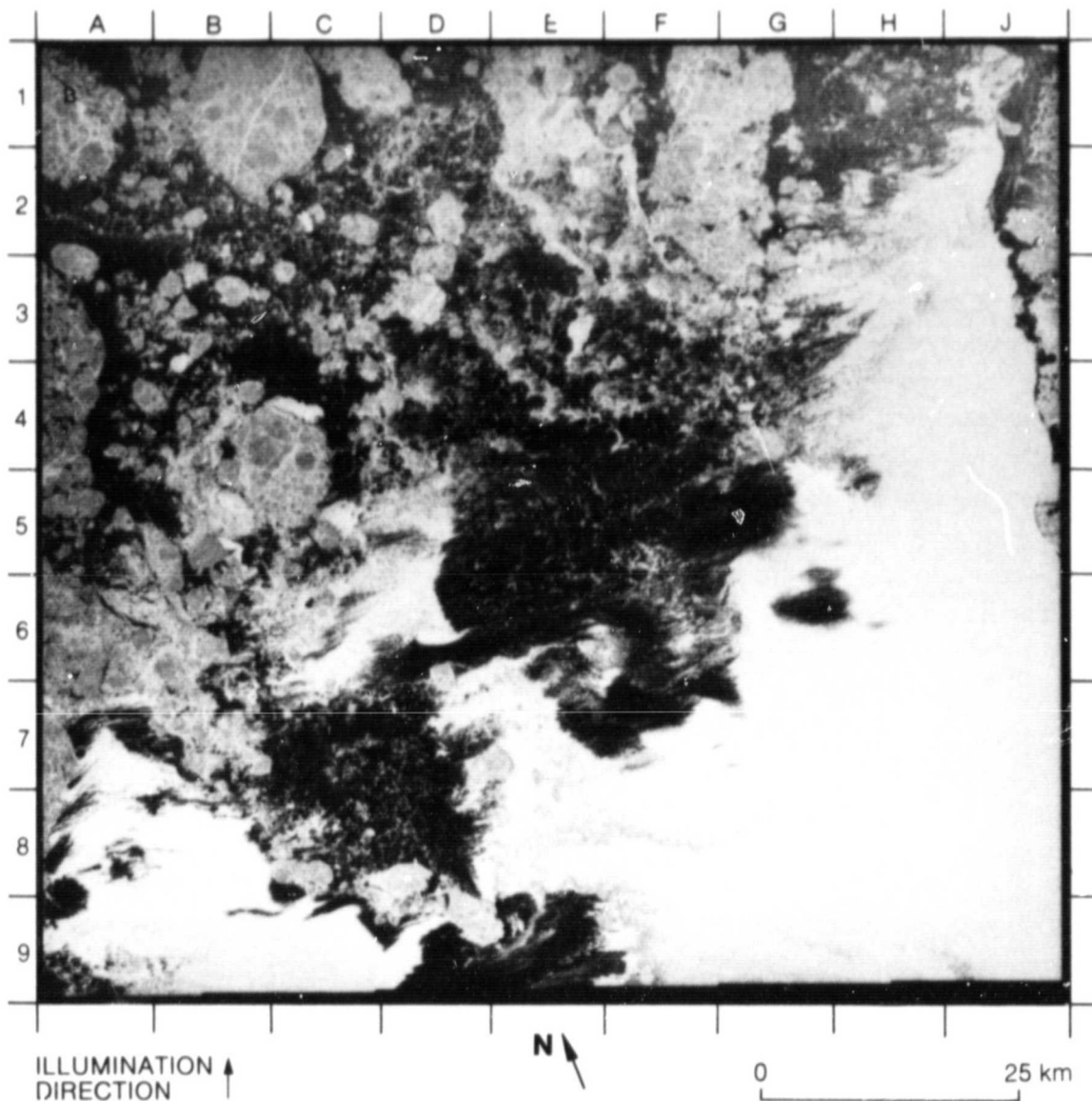
surface currents. The ice margin has broken floes of both first-year and multiyear ice as labeled a through f on the map (floes a and c appear just on the edge of Image A). The next image (B) shows that three floes (a, b, and c) have moved eastward 20 kilometers while the drift of two small floes (d and e) was more northward, each moving 38 kilometers and 14 kilometers, respectively (see the table). The amount of open water was reduced, with new ice forming within the darker areas, often combining to form fine curvilinear patterns most apparent in this image at the boundaries of the open water and new ice (A7, E9, and F6). Three days later (Image C), the percentage of open water is

ILLUMINATION DIRECTION

N

0   25 km
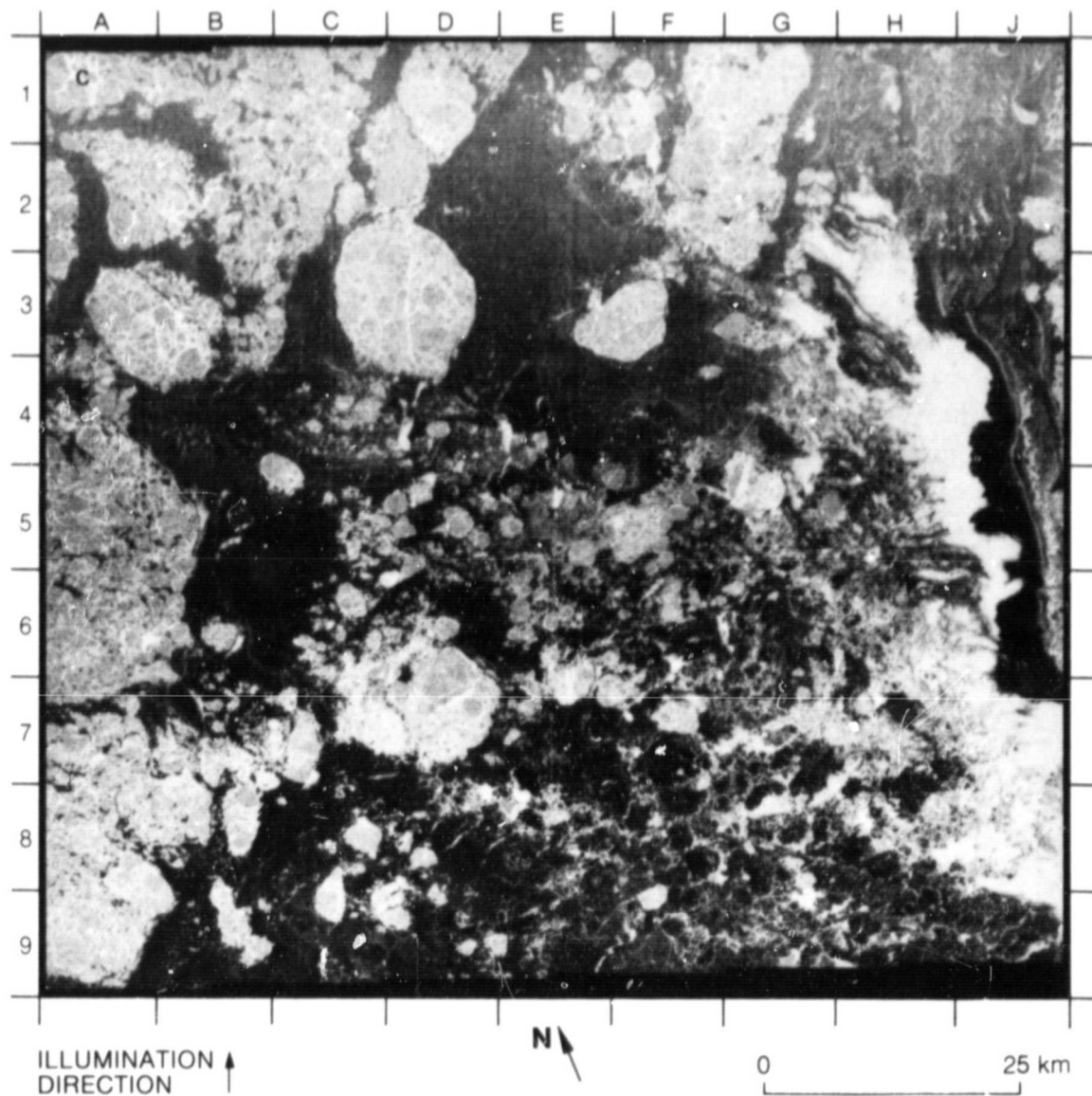
drastically reduced, occurring only near the coast of Banks Island, with large areas of new ice having formed (E9, F4, and H5). All the tracked floes moved southeast various distances with a change in direction of almost 90 degrees from their motion 3 days earlier. The five floes traveled an average of 35 kilometers, with floes b and d each drifting 43 kilometers. Note that floe f has not moved appreciably over the 6-day period, indicating that it may be grounded.

(A: Rev. 1339; 1533 GMT, September 28, 1978. B: Rev. 1382; 1545 GMT, October 1, 1978. C: Rev. 1425; 1559 GMT, October 4, 1978.)

129 A

BANKS ISLAND

---·---·---·--- SEPT 28
-------- OCT 1
———————— OCT 4

0   25 km
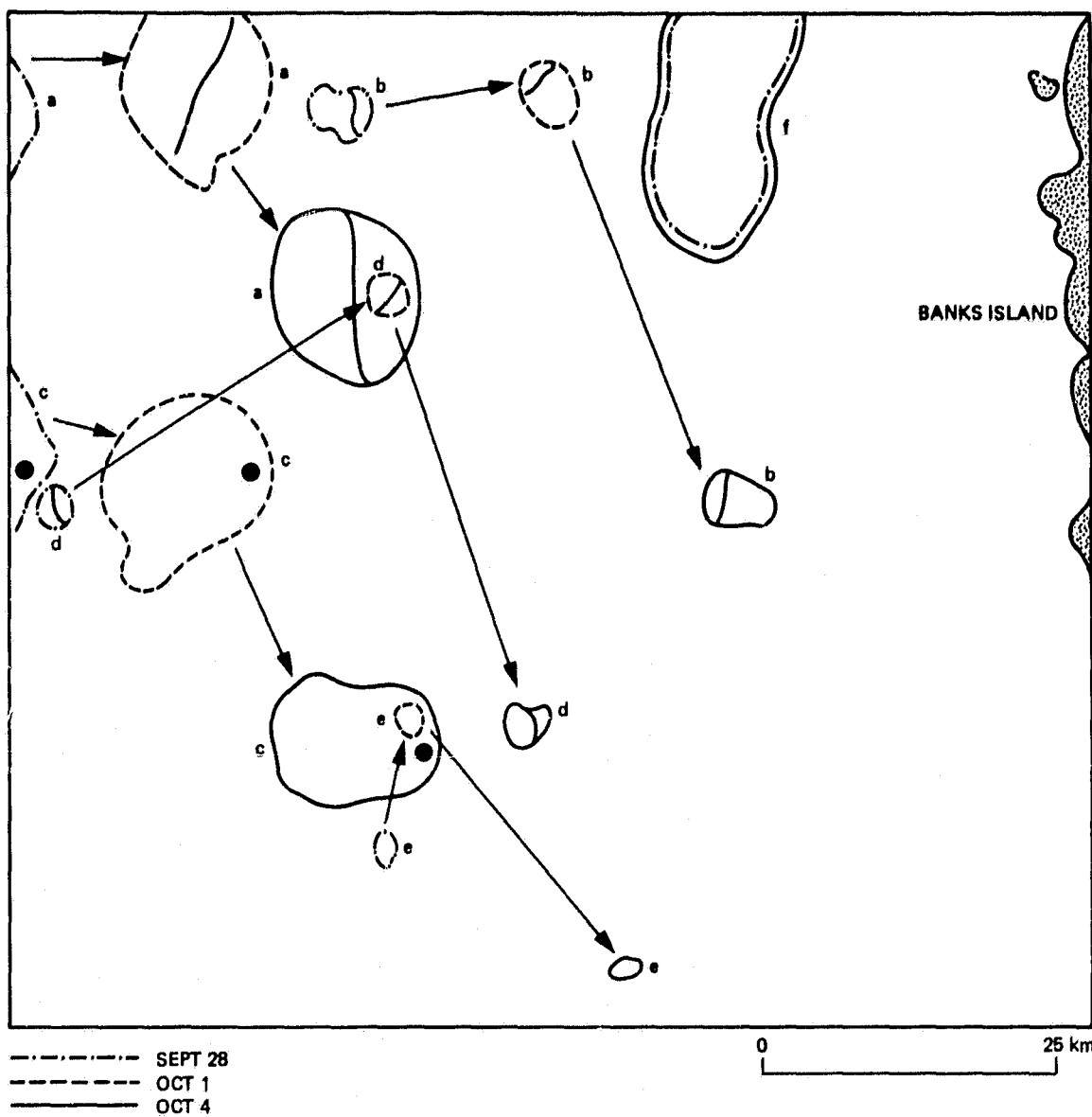
DISTANCE TRAVELED, kilometers

FLOES	a	b	c	d	e
28 SEPT TO 1 OCT	21	20	21	38	14
1 OCT TO 4 OCT	25	43	31	44	31

Motion of ice floes tracked over a six-day period. The table indicates the distance traveled by each floe.

129
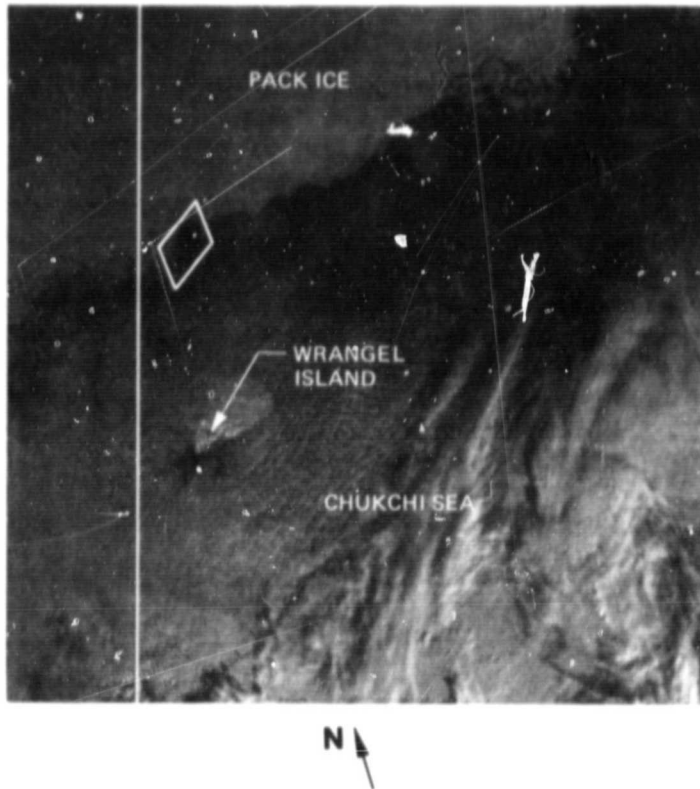
NOAA visible-channel image of the Chukchi Sea. The imaged
area is enclosed by a parallelogram.

The complexity of the interaction between surface waves, wind, and new ice at the
margin of the main ice pack is shown in this image, taken 150 kilometers north of
Wrangel Island in the Chukchi Sea (see the NOAA image for location). The pack ice is
identified by ice floes several kilometers in diameter (B3/B4 and A8/A9) and by a
portion of a larger floe about 15 kilometers in diameter (A1 to B2). Two areas of small,
dark patches (C1 and B4/B5) are most likely new ice. The bright band (D1 to B5) at the
margin of the pack ice may be small ice floes that have been fractured and then rafted
by surface waves. Between the bright band and main pack ice is a zone of intermediate
intensity that consists probably of loosely aggregated small floes. Surface waves with a
wavelength of roughly 150 meters, probably locally generated, can be seen impinging
the bright band at slight angles. Surface waves can propagate through ice, but will
eventually be attenuated by the ice itself at a rate that depends on the waves' charac-
teristics and the structure of the ice (Wadhams, 1973 and 1978). Note that surface
waves can be detected in the intermediate zone 2 to 3 kilometers from the bright border,
although the mechanisms that permit this detection are unknown. Conditions similar to
these at the margins of the pack ice (wave-induced ice breakup, subsequent rafting at
the edge, and an intermediate zone of small floes) have been observed in the Bering
Sea (Wadhams, 1980).

The dark zones next to the roughened open water (e.g., F4, G4, G8, and G12)
probably are made up of frazil ice (small discs of ice measuring 1 to 4 millimeters in
diameter) that has aggregated into a thick slurry called grease ice (e.g., Martin, 1981).
Grease ice effectively damps capillary waves and Bragg resonant waves (Martin and
Kauffman, 1981). Note that the surface waves seen at the pack ice margin are not
imaged in these dark zones. The grease ice was not as extensive three days earlier

during another Seasat pass (Revolution 1439); its rapid formation was presumably the result of northeasterly winds of 7.5 to 10 meters per second coming off the ice at the time of the image (as measured at Wrangel Island and generally confirmed by the cloud appearance and orientation on the NOAA image). Additionally, the grease ice has spread downwind, forming linear rows parallel to the wind direction and spaced about 100 meters apart. The rows are especially obvious at the boundaries shared by the grease ice and the open water (e.g., H3 and G11). Martin and Kauffman (1981) suggested that the convergence of grease ice into rows is the result of wind-induced Langmuir circulation.

A large zone of turbulent surface patterns lies between the dark grease-ice zones and the pack ice (e.g., D5 to D13). The surface waves mentioned earlier can be seen throughout the area. The origin of these surface patterns and their variation in back-scatter is unknown. We speculate that they may be caused by small ice floes oriented by a fluctuating, wind-driven current.

(Rev. 1482; 1547 GMT, October 8, 1978.)

APPENDIX A
Locations of Images

The following four maps show the geographic locations of the images presented in the atlas. The center of each image is represented by a closed circle labeled by the image number. Also shown on the maps are the locations of the five receiving stations, which are represented by closed triangles labeled with the following abbreviations: GDS (Goldstone, California); MIL (Merritt Island, Florida); SNF (Shoe Cove, Newfoundland, Canada); UKO (Oakhanger, United Kingdom); and ULA (Fairbanks, Alaska).
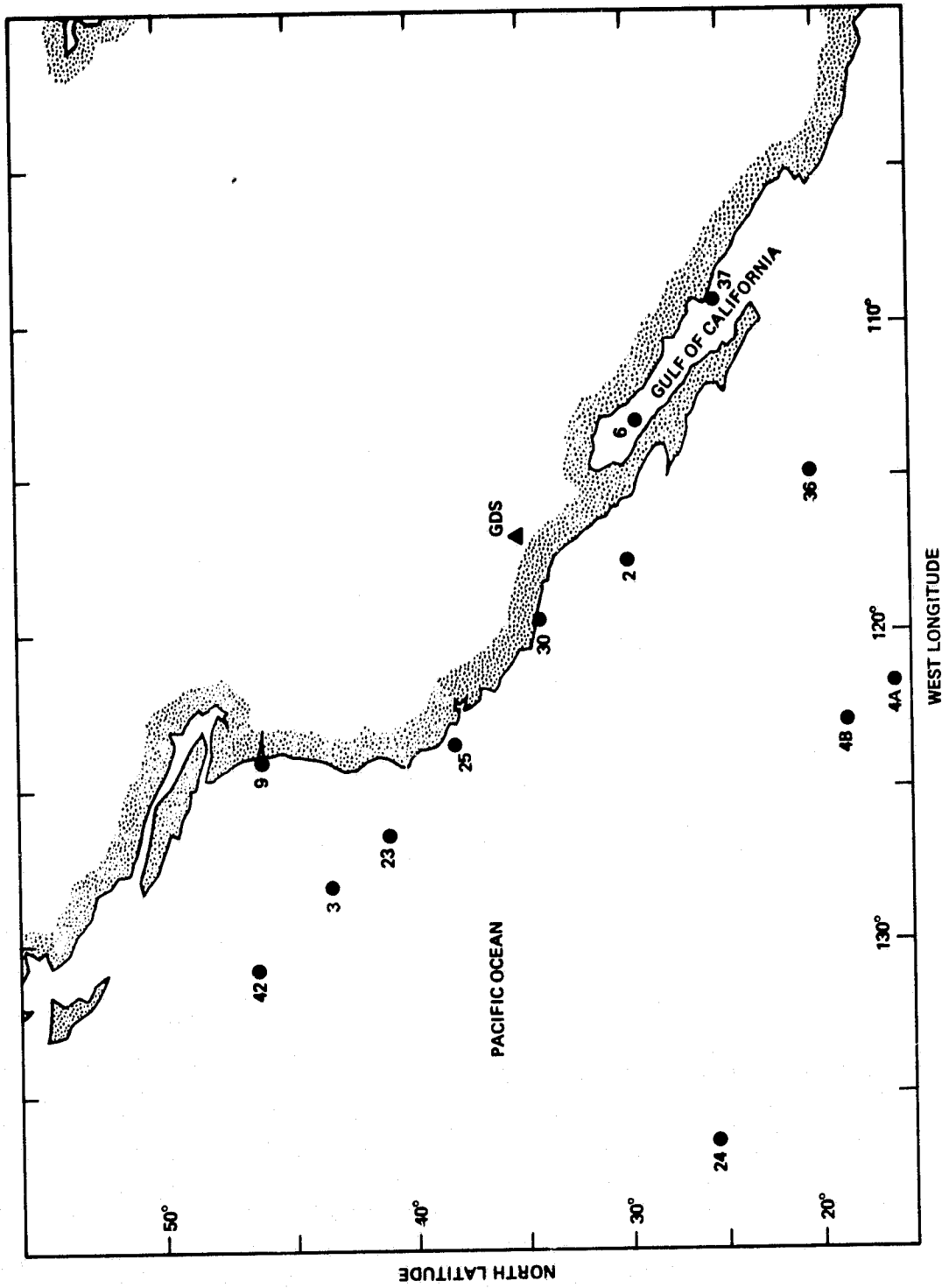
Figure A-1. Eastern North Pacific Ocean and Gulf of California.
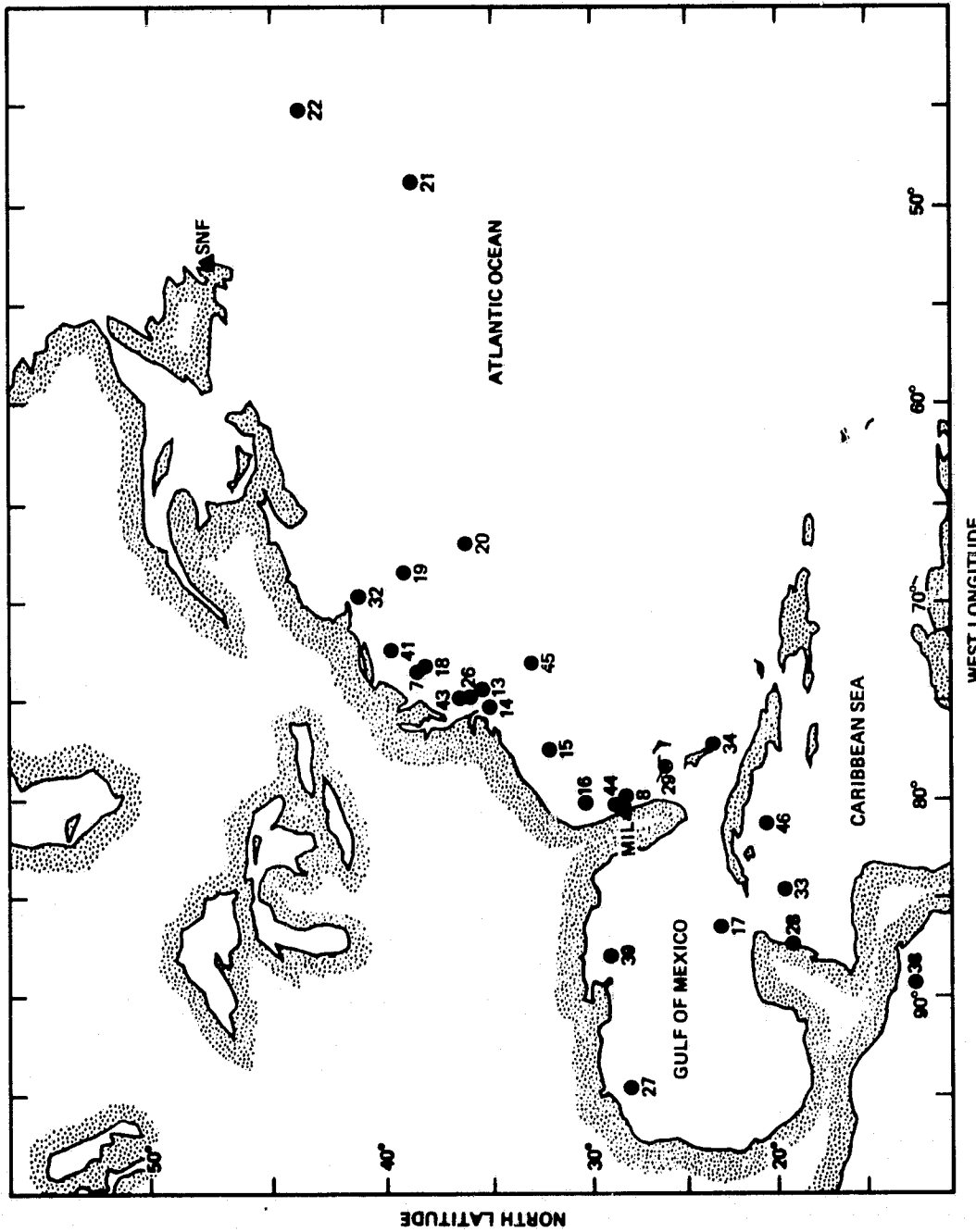
Figure A-2. Western North Atlantic Ocean, Gulf of Mexico, and Caribbean Sea.

135
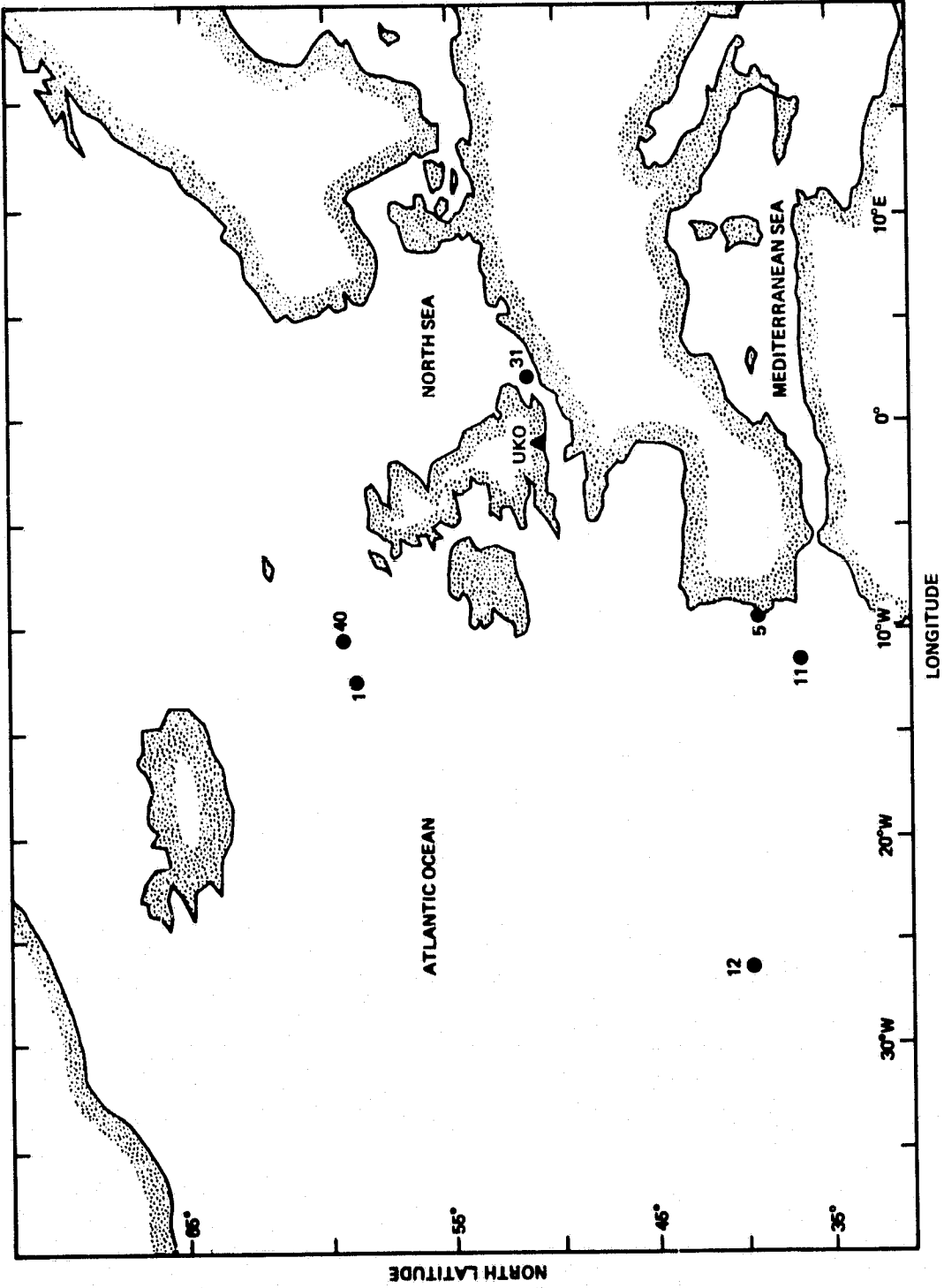
Figure A-3. Eastern North Atlantic Ocean, North Sea, and Mediterranean Sea.
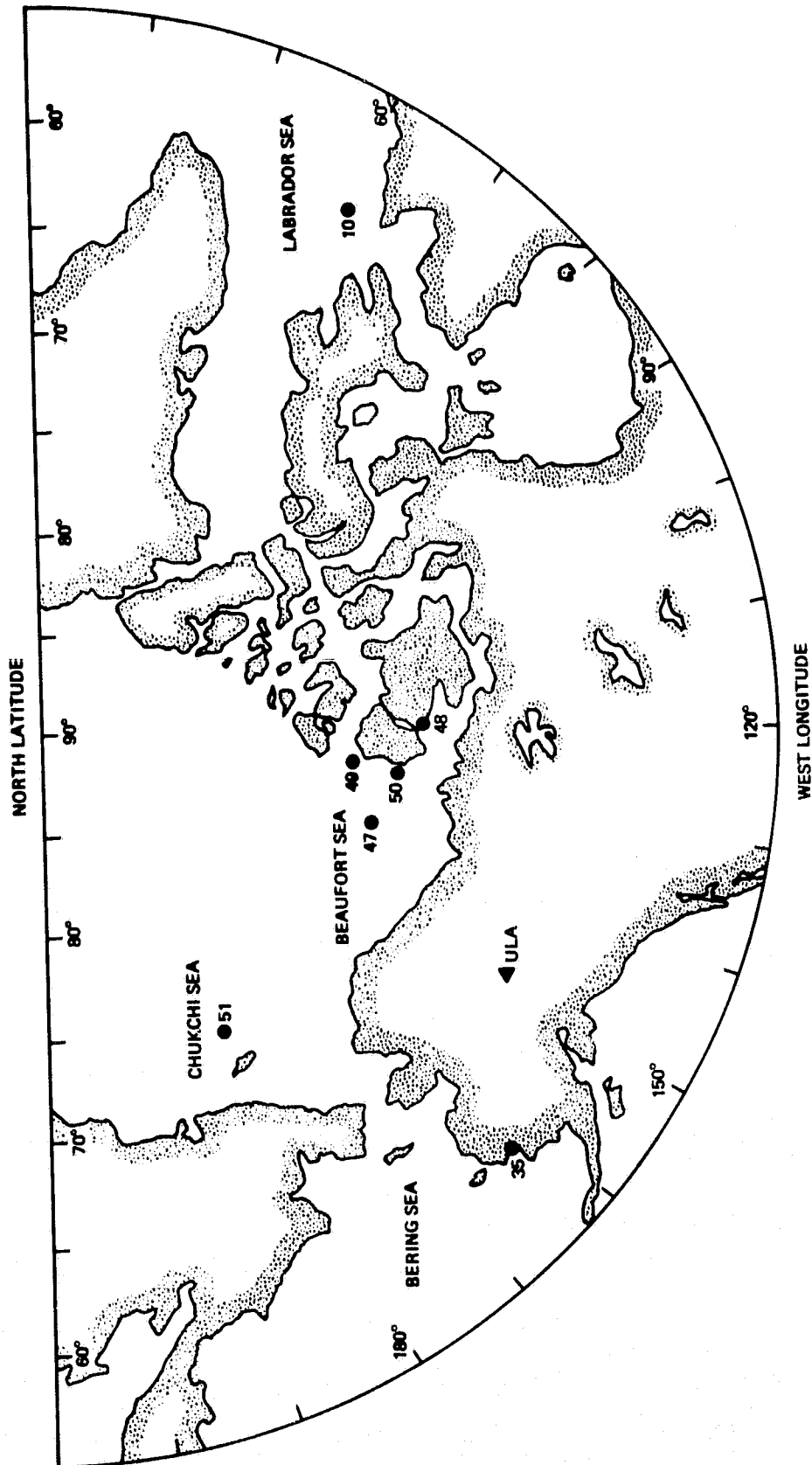
Figure A-4. Beaufort Sea, Chukchi Sea, Bering Sea, and Labrador Sea.

APPENDIX B

Index of Images

Image No.	Image Title	Seasat Rev. No.	Date, 1978	Center Locations Latitude, N	Longitude, W	
1	Wave Travel Oblique to the Flight Path	791	Aug. 21	59°00′	12°30′	
2	Wave Travel Parallel to the Flight Path	308	Jul. 18	29°56′	117°42′	
3	Waves Under a Spatially Variable Wind Field	1349	Sep. 29	43°30′	128°12′	
4	Waves Generated by a Hurricane	251	Jul. 14	A 15°54′	121°41′	
				B 18°31′	122°52′	
5	Wave Refraction by Bottom Topography	785	Aug. 20	39°22′	9°24′	
6	Gulf of California	1355	Sep. 29	29°27′	113°15′	
7	Mid-Atlantic Bight	931	Aug. 31	38°31′	73°35′	
8	Florida Coast	163	Jul. 8	28°19′	79°45′	
9	Oregon-Washington Coast	761	Aug. 19	46°08′	124°14′	
10	Labrador Sea (Off Hudson Strait)	1395	Oct. 2	60°20′	61°00′	
11	Ormonde Seamount (Off Portugal)	785	Aug. 20	36°46′	11°24′	
12	The Azores	556	Aug. 4	39°47′	26°22′	
13	The Gulf Stream Off Cape Hatteras (I)	1339	Sep. 28	35°27′	74°27′	
14	The Gulf Stream Off Cape Hatteras (II)	931	Aug. 31	35°07′	75°19′	
15	The Gulf Stream Off Charleston, South Carolina	400	Jul. 25	32°07′	77°33′	
16	The Gulf Stream Off Jacksonville, Florida	1110	Sep. 12	30°18′	80°10′	
17	The Loop Current in the Gulf of Mexico	393	Jul. 24	23°12′	86°30′	
18	A Warm-Core Ring Off Delaware Bay	1232	Sep. 21	38°07′	73°16′	
19	A Warm-Core Ring South of Cape Cod	880	Aug. 27	39°10′	68°31′	
20	A Cold-Core Ring in the Sargasso Sea	880	Aug. 27	36°12′	67°00′	
21	A Cold Eddy South of the Grand Banks of Newfoundland	1231	Sep. 21	38°42′	48°08′	
22	A Cold Eddy East of the Grand Banks of Newfoundland	1360	Sep. 30	43°46′	45°11′	
23	Eddies and Meanders of the California Current	710	Aug. 15	41°01′	126°37′	
24	The North Pacific Subtropical Front	230	Jul. 13	25°38′	136°29′	
25	Coastal Eddies Off Point Arena, California	1406	Oct. 3	38°11′	123°39′	
26	Interaction of Shelf Water With the Gulf Stream Near Cape Hatteras	1404	Oct. 3	35°59′	74°40′	
27	Coastal Eddies Off Galveston, Texas	465	Jul. 29	28°02′	94°34′	
28	Small Vortices East of the Yucatan Peninsula	795	Aug. 21	19°21′	87°22′	
29	Small Vortices South of Grand Bahama Island	1325	Sep. 27	26°15′	78°22′	
30	Oil Slicks and Platforms Off Santa Barbara, California	308	Jul. 18	34°10′	119°26′	
31	The English Channel	762	Aug. 19	51°23′	2°13′E	
32	Nantucket Shoals	880	Aug. 27	41°10′	69°40′	
33	Misteriosa Bank in the Caribbean Sea	1397	Oct. 2	19°42′	84°40′	
34	Tongue of the Ocean in the Bahama Bank	1411	Oct. 3	23°37′	77°07′	
35	The Kuskokwim River, Alaska	232	Jul. 13	59°40′	162°30′	
36	Hurricane Iva in the Tropical Eastern Pacific	674	Aug. 13	20°15′	114°53′	
37	A Tropical Storm in the Gulf of California	480	Jul. 30	25°10′	109°17′	
38	Squall Lines South of El Salvador	1211	Sep. 19	12°13′	89°20′	
39	Tropical Rain Cells in the Gulf of Mexico	1096	Sep. 11	29°03′	87°58′	
40	Windrows in the North Atlantic	1006	Sep. 5	59°30′	10°30′	
41	An Anomalous Feature South of Long Island, New York	1318	Sep. 27	39°46′	72°30′	
42	Ship With Stern Wake	1126	Sep. 13	46°24′	130°52′	
43	Ship With Bow Wake	1253	Sep. 22	36°35′	74°50′	
44	Ships in a Calm Ocean With Bow Wakes	407	Jul. 25	28°45′	80°10′	
45	Ship With Long Stern Wake	1210	Sep. 19	33°07′	72°58′	
46	Ships Displaced From Their Stern Wakes	1404	Oct. 3	20°42′	81°18′	
47	Pack Ice	1468	Oct. 7	73°20′	135°48′	
48	Shore-Fast Ice	220	Jul. 12	71°20′	119°16′	
49	Structural Variations Within Pack Ice	A 1409	Oct. 3	74°35′	126°05′	
		B 1452	Oct. 6	74°35′	126°05′	
50	Ice Motion and Morphology at Pack-Ice Margins	A 1339	Sep. 28	72°30′	127°00′	
		B 1382	Oct. 1	72°30′	127°00′	
		C 1425	Oct. 4	72°30′	127°00′	
51	Waves and New Ice Formation at Pack-Ice Margins	1482	Oct. 8	72°57′	179°41′	

[a] O for Optical; D for Digital.

[b] Dates indicated are for 1978.

[c] Acronyms:

DMA	Defense Mapping Agency	IOS	Institute of Oceanographic Sciences, Surrey, England	NO
DMSP	Defense Meteorological Satellite Program	IR	Infrared	R
GOES	Geostationary Operational Environmental Satellite	MSS	Multispectral Scanner	US

No.	Date, 1978	Latitude, N	Longitude, W	Processing[a] Mode	Corresponding Illustrations[b,c]
	Aug. 21	59°00′	12°30′	O	Wave spectra.
	Jul. 18	29°56′	117°42′		Hurricane path from Gunther (1979).
	Sep. 29	43°30′	128°12′		Weather map, 06:00:00 GMT, Sep. 29, National Weather Service.
	Jul. 14	A 15°54′	121°41′		Map of wind and wave height from Teleki et al. (1979).
		B 18°31′	122°52′		
	Aug. 20	39°22′	9°24′		DMA Chart 51120.
	Sep. 29	29°27′	113°15′		Bathymetric chart (Fisher et al., 1964).
	Aug. 31	38°31′	73°35′		DMA Chart 12200.
	Jul. 8	28°19′	79°45′		Geologic Map of U.S., USGS, 1974.
	Aug. 19	46°08′	124°14′	O	DMA Charts 18500 and 18520.
	Oct. 2	60°20′	61°00′	D	DMA Chart 15020.
	Aug. 20	36°46′	11°24′	D	IOS Chart C6568.
	Aug. 4	39°47′	26°22′	O	IOS Chart C6568.
	Sep. 28	35°27′	74°27′		NOAA-5 IR image; 00:19:00 GMT, Sep. 28; Rev. 9795, I2F.
	Aug. 31	35°07′	75°19′		Geologic Map of U.S., USGS, 1974.
	Jul. 25	32°07′	77°33′		Bathymetric chart from Hayes (1981).
	Sep. 12	30°18′	80°10′		Bathymetric chart from Hayes (1981).
	Jul. 24	23°12′	86°30′	O	Isotherm map adapted from Maul (1977).
	Sep. 21	38°07′	73°16′	D	NOAA-5 IR image, 00:21:28 GMT, Sep. 21; Rev. 9696, I2F.
	Aug. 27	39°10′	68°31′	O	Map from gulfstream (1978).
	Aug. 27	36°12′	67°00′	O	Map adapted from Cheney (1981).
	Sep. 21	38°42′	48°08′	D	DMSP IR image; 14:12:00 GMT, Sep. 24; Rev. 10535.
	Sep. 30	43°46′	45°11′	O	DMSP IR image; 14:35:00 GMT, Sep. 17; Rev. 10436.
	Aug. 15	41°01′	126°37′		NOAA-5 IR image; 04:16:36 GMT, Aug. 15; Rev. 9240, I3F.
	Jul. 13	25°38′	136°29′		Map of surface salinity from Robinson (1976).
	Oct. 3	38°11′	123°39′		NOAA-5 IR image; 17:18:01 GMT, Oct. 3; Rev. 9853, I2F.
	Oct. 3	35°59′	74°40′		Sketch map; bathymetry from Geologic Map of U.S., USGS, 1974.
	Jul. 29	28°02′	94°34′		Bathymetric chart (Uchupi, 1971).
	Aug. 21	19°21′	87°22′		Bathymetric chart (Uchupi, 1971).
	Sep. 27	26°15′	78°22′	O	Geologic Map of U.S., USGS, 1974.
	Jul. 18	34°10′	119°26′	D	Sketch map.
	Aug. 19	51°23′	2°13′E	D	DMA Chart 37130.
	Aug. 27	41°10′	69°40′	D	DMA Chart 13009/Landsat RBV image; Aug. 19; 30167-14444-D.
	Oct. 2	19°42′	84°40′	O	NOAA Nautical Chart 411.
	Oct. 3	23°37′	77°07′	O	Landsat MSS images (band 4); Oct. 31; 30240-14560/30240-14563.
	Jul. 13	59°40′	162°30′	D	Landsat MSS image (band 4), Jul. 30; 30147-21204.
	Aug. 13	20°15′	114°53′	O	GOES IR image; 03:45:00 GMT, Aug. 13; Full Disc.
	Jul. 30	25°10′	109°17′		GOES IR image; 13:00:00 GMT, Jul. 30; KC30N90W-2.
	Sep. 19	12°13′	89°20′		GOES VIS image; 16:00:00 GMT, Sep. 19; WB1
	Sep. 11	29°03′	87°58′	O	GOES IR image; 15:01:00 GMT, Sep. 11; RB23N85W-A.
	Sep. 5	59°30′	10°30′	D	Wind directions from Seasat scatterometer.
	Sep. 27	39°46′	72°30′	D	Wind speeds from Seasat scatterometer.
	Sep. 13	46°24′	130°52′	O	None.
	Sep. 22	36°35′	74°50′		None.
	Jul. 25	28°45′	80°10′		None.
	Sep. 19	33°07′	72°58′		None.
	Oct. 3	20°42′	81°18′	O	None.
	Oct. 7	73°20′	135°48′	D	Sketch map.
	Jul. 12	71°20′	119°16′	O	Sketch map.
	Oct. 3	74°35′	126°05′	D	Landsat MSS image (band 6); Jul. 5; 30122-20344.
	Oct. 6	74°35′	126°05′		
	Sep. 28	72°30′	127°00′		Sketch map.
	Oct. 1	72°30′	127°00′		
	Oct. 4	72°30′	127°00′	D	
	Oct. 8	72°57′	179°41′	O	NOAA-5 VIS image, 21:14:21 GMT, Oct. 8; Rev. 9917, V2F.

...tute of Oceanographic Sciences, Surrey, England NOAA National Oceanic and Atmospheric Administration   VIS Visible
...red   RBV Return Beam Vidicon
...ispectral Scanner   USGS United States Geological Survey

APPENDIX C
Catalog of the Seasat SAR Imagery

This appendix presents the catalog of SAR imagery acquired by Seasat. Included are areal coverage plots of all SAR data of sufficient quality to have been optically processed in a survey mode and tables of key orbital information for these data. This information will enable an investigator to identify closely which revolutions (if any) imaged an area of interest and to determine the dates and times of this imagery. Additionally, tables of digitally processed SAR imagery are provided. Finally, information is given concerning the distribution of both forms of processed Seasat SAR imagery.

C.1 Areal Coverage

The following 21 figures are computer-generated plots showing the areal coverage of all the Seasat SAR data that were of sufficient quality to have been optically processed in a survey mode. The plots have been grouped geographically by the location of the five receiving stations, which are labeled on the plots with their acronyms (see Appendix A). Each SAR swath is shown by two parallel lines enclosed at both ends and labeled in one of two ways: by revolution number (3 or 4 digits) or by node (1 to 3 digits followed by a decimal) (see Table C-1 for definition). The revolution number is used for a single swath; the node is used for two or more swaths of identical ground track. Additionally, swaths labeled with a node represent the maximum coverage of all revolutions during the time period specified in the caption for each plot. By finding in Table C-1 those revolutions that are labeled with the desired nodes, a specific revolution can be determined by noting the start and end latitudes.

These plots were generated using the Satellite Mission Design Program (Carlson, 1980) with osculating orbital elements taken from Klose (1979).
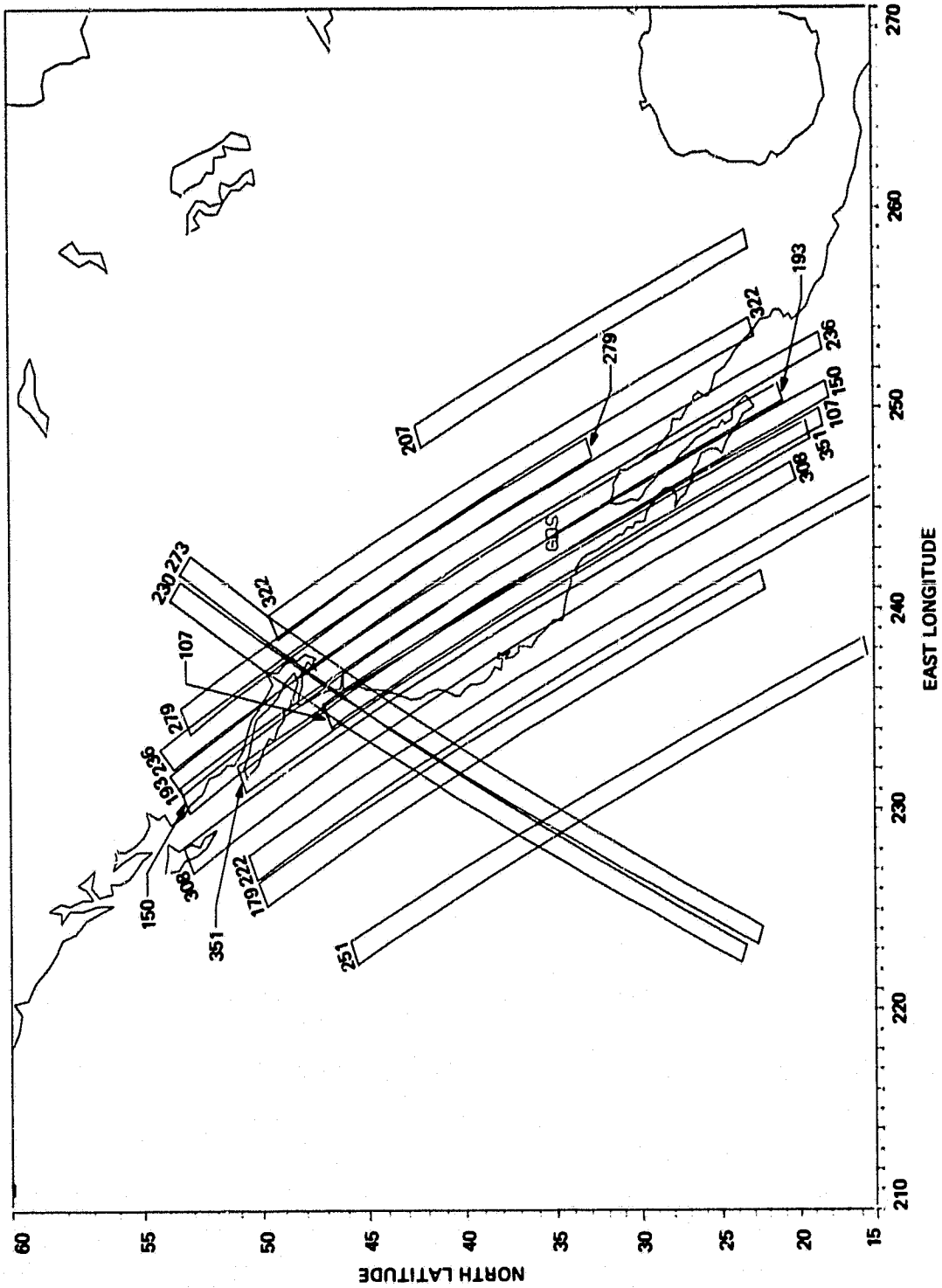
Figure C-1. Goldstone, California: July 4 through July 21, 1978.
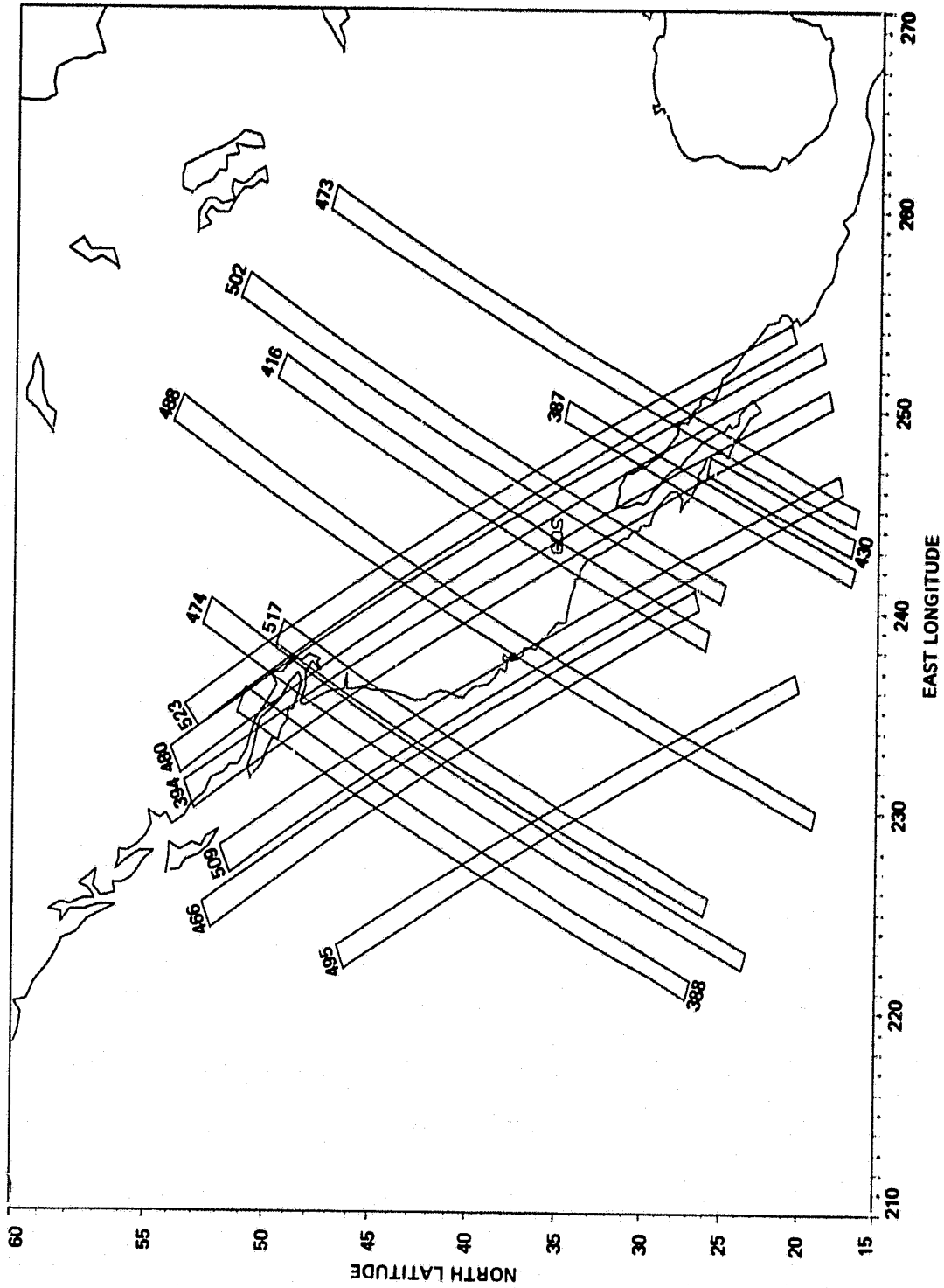
Figure C-2. Goldstone, California: July 22 through August 2, 1978.
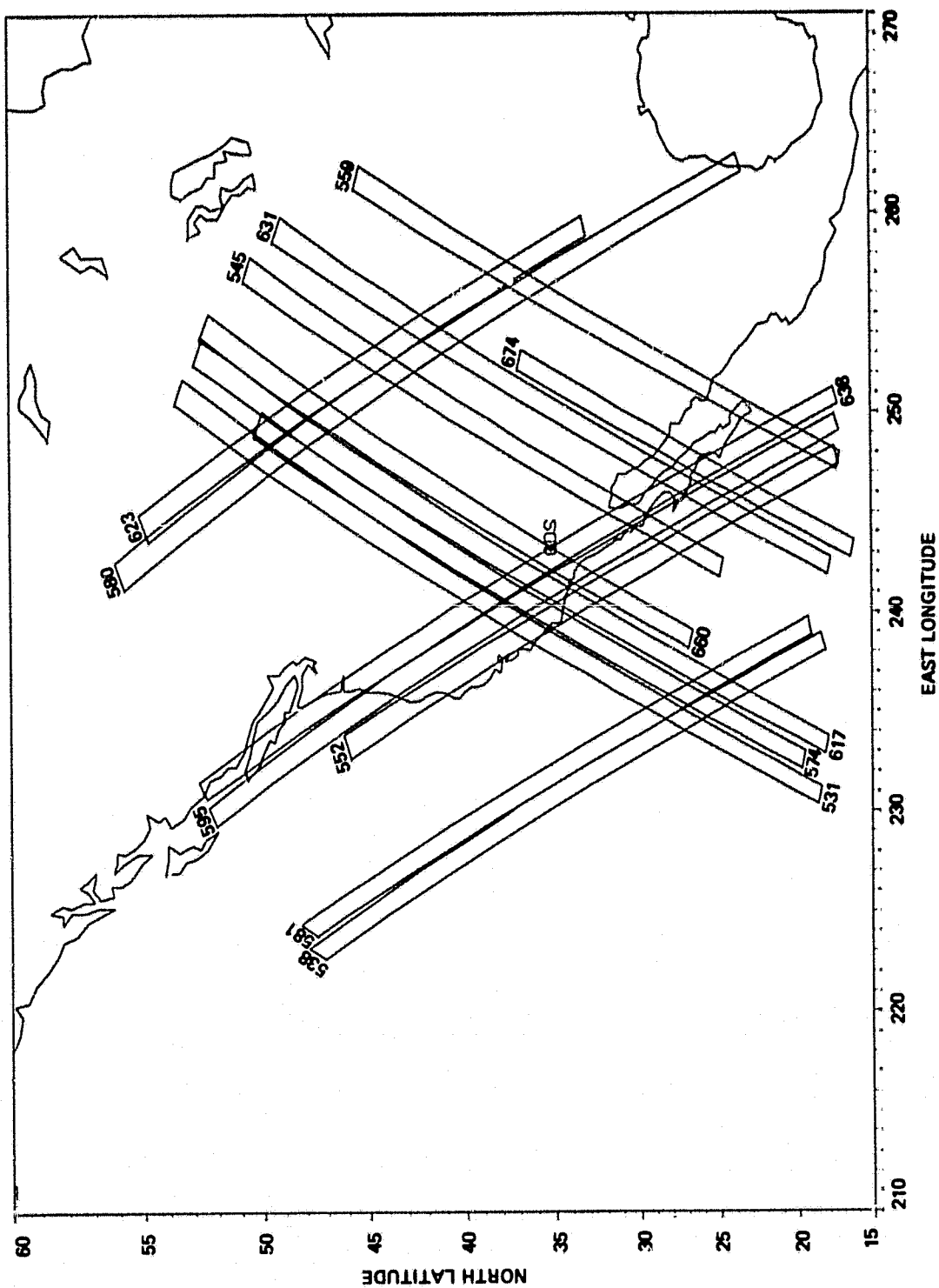
Figure C-3. Goldstone, California: August 3 through August 13, 1978.
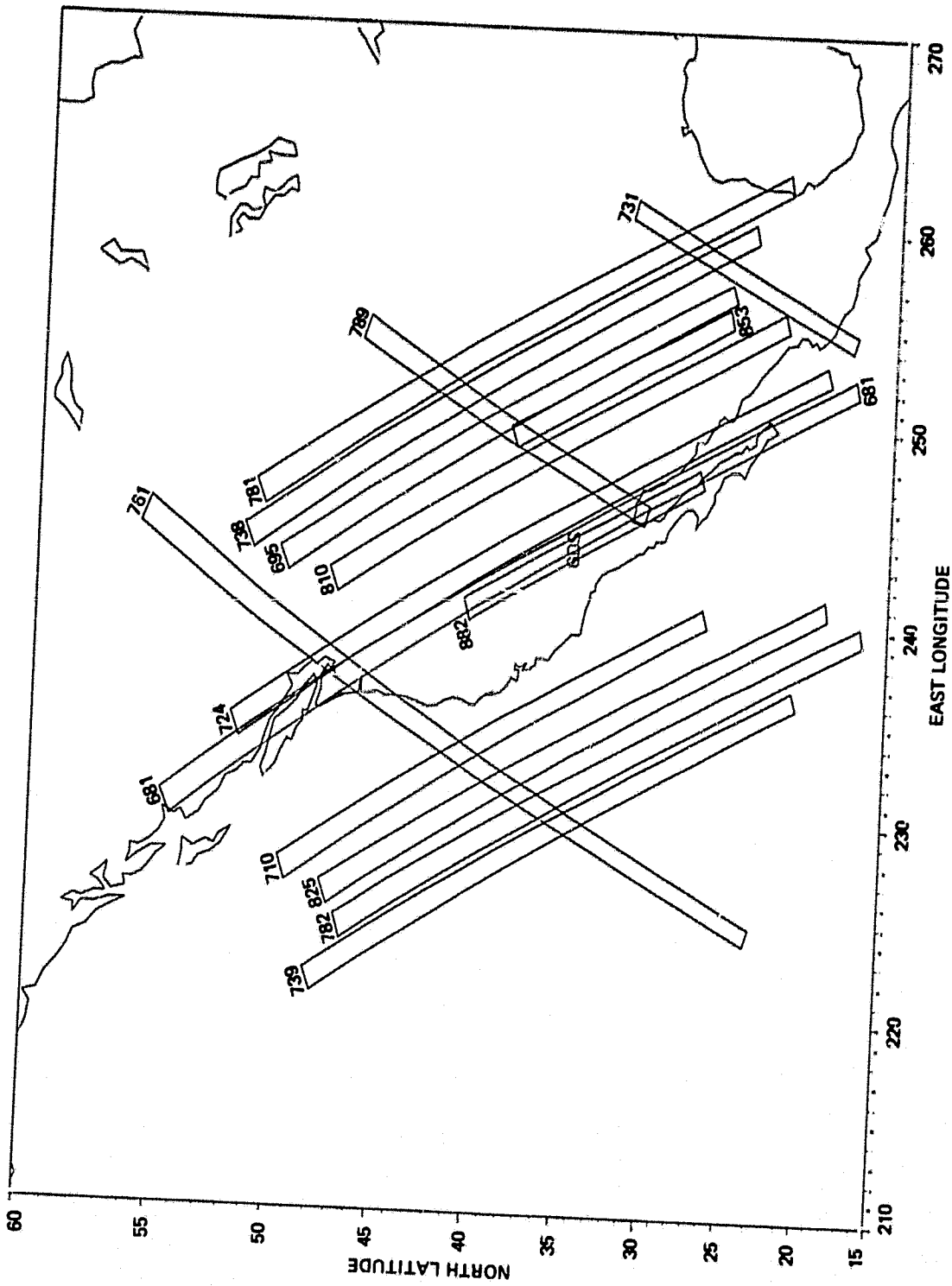
Figure C-4. Goldstone, California: August 13 through August 27, 1978.
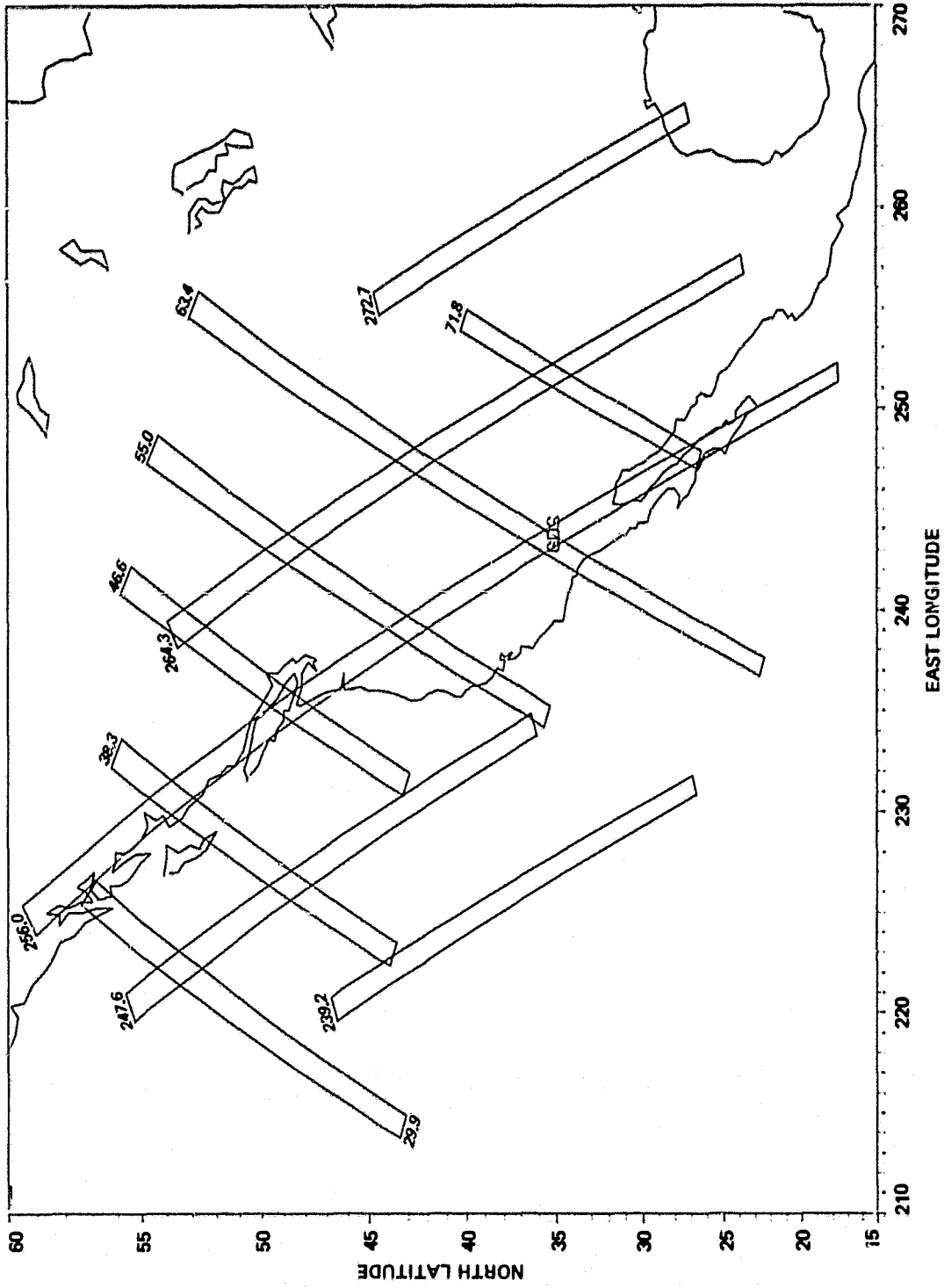
Figure C-5. Goldstone, California: August 28 through October 9, 1978.
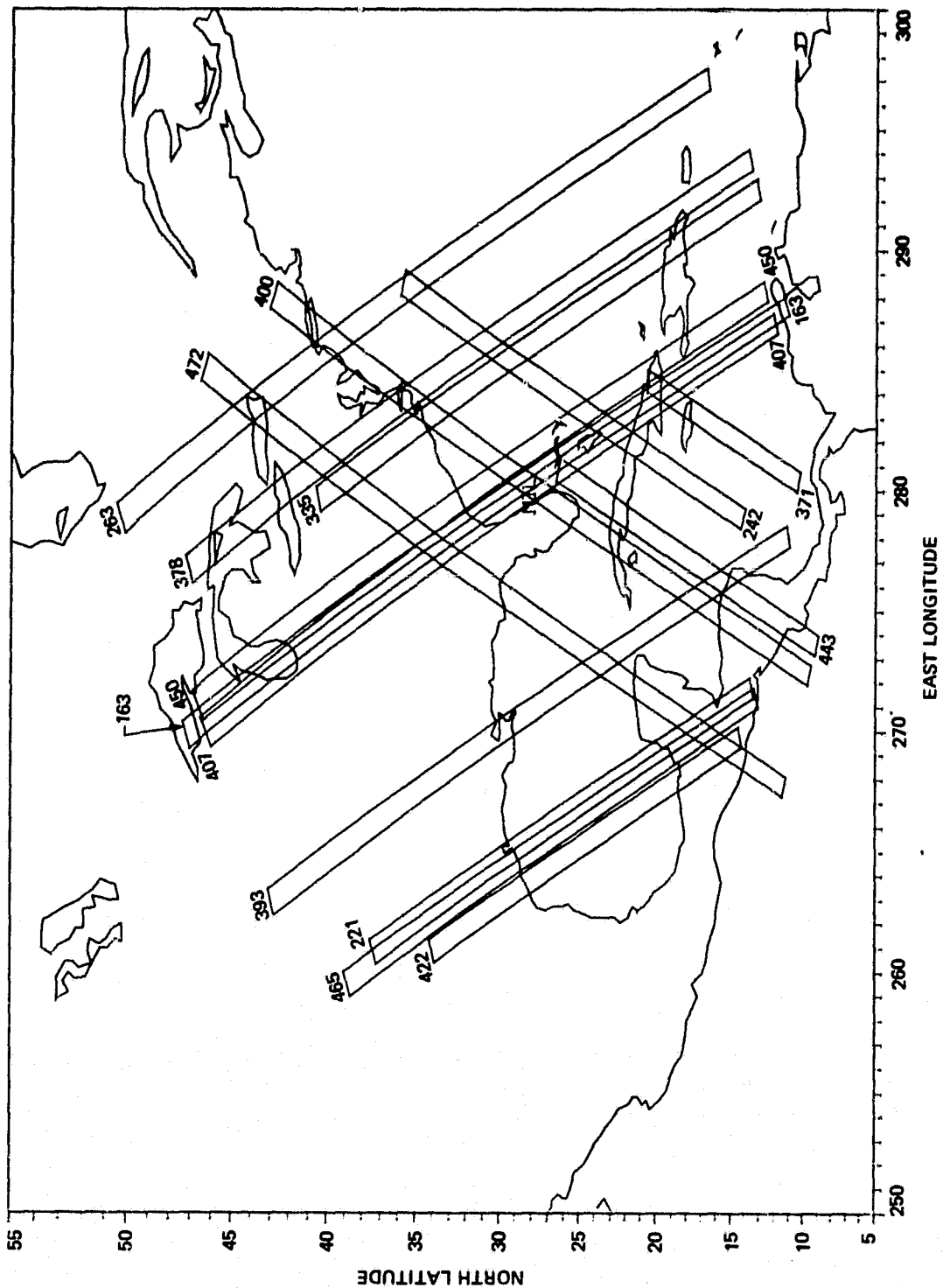
Figure C-6. Merritt Island, Florida: July 8 through July 30, 1978.

147
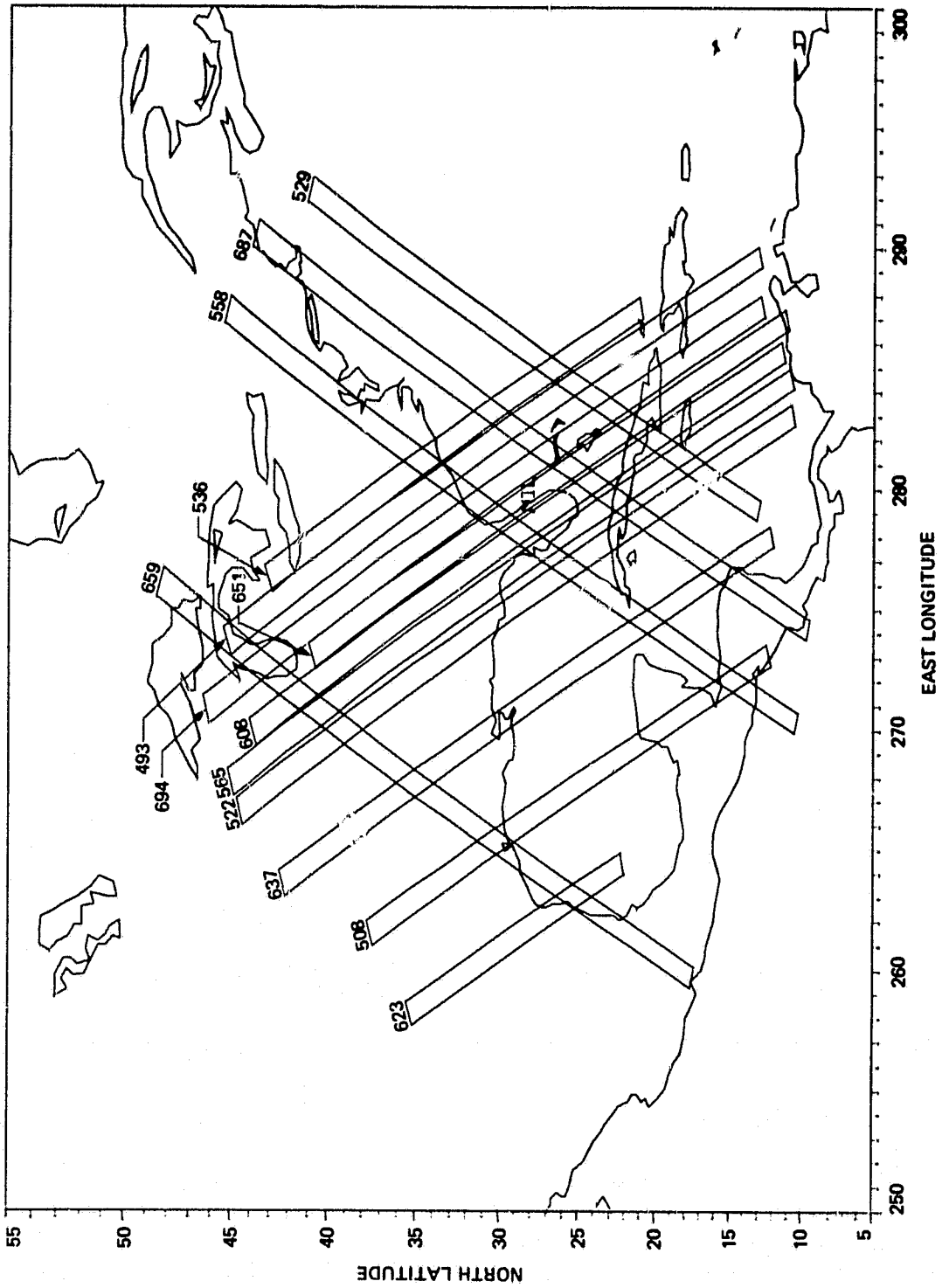
Figure C-7. Merritt Island, Florida: July 31 through August 14, 1978.
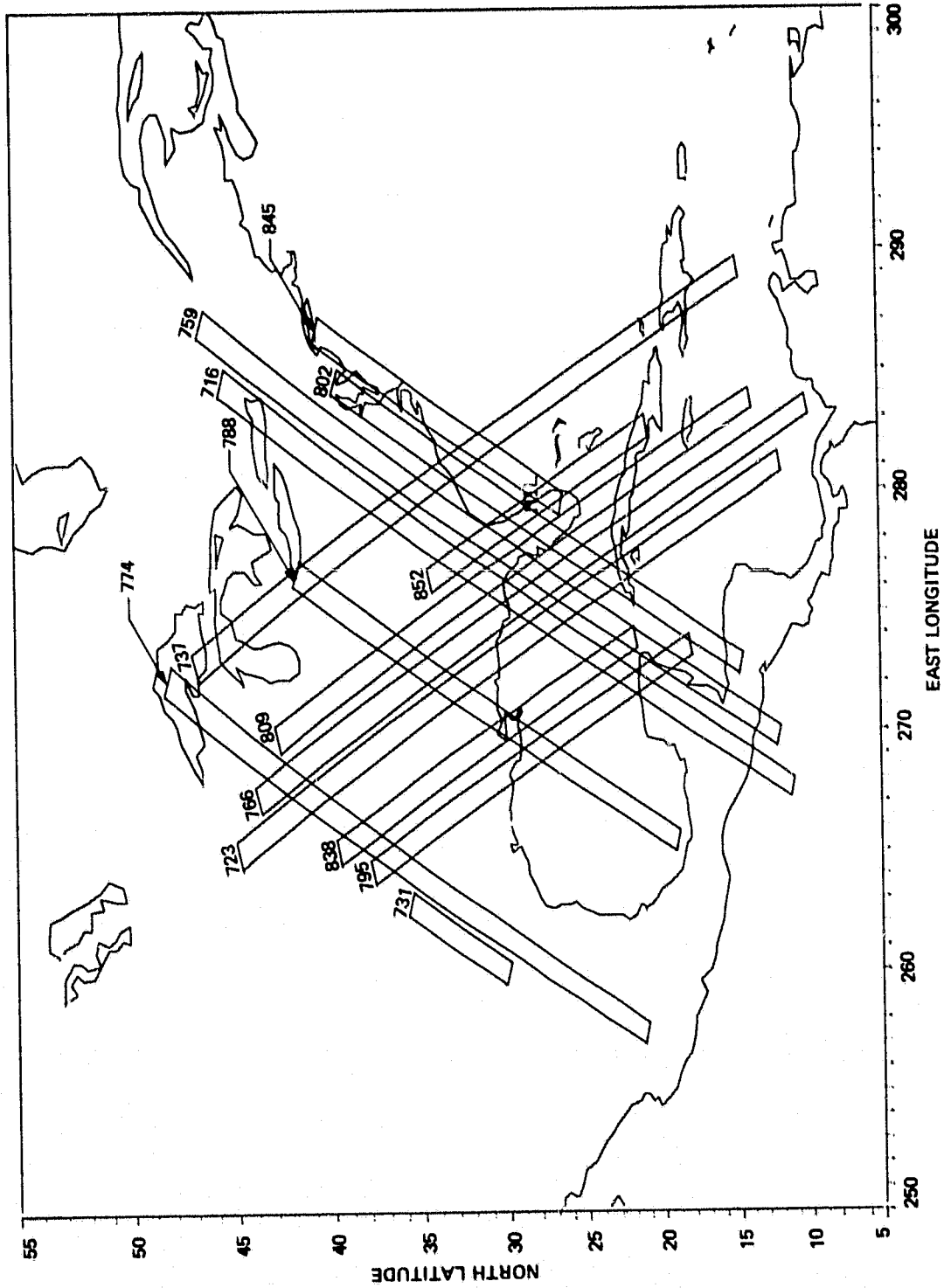
Figure C-8. Merritt Island, Florida: August 15 through August 25, 1978.

Figure C-9. Merritt Island, Florida: August 26 through October 9, 1978.
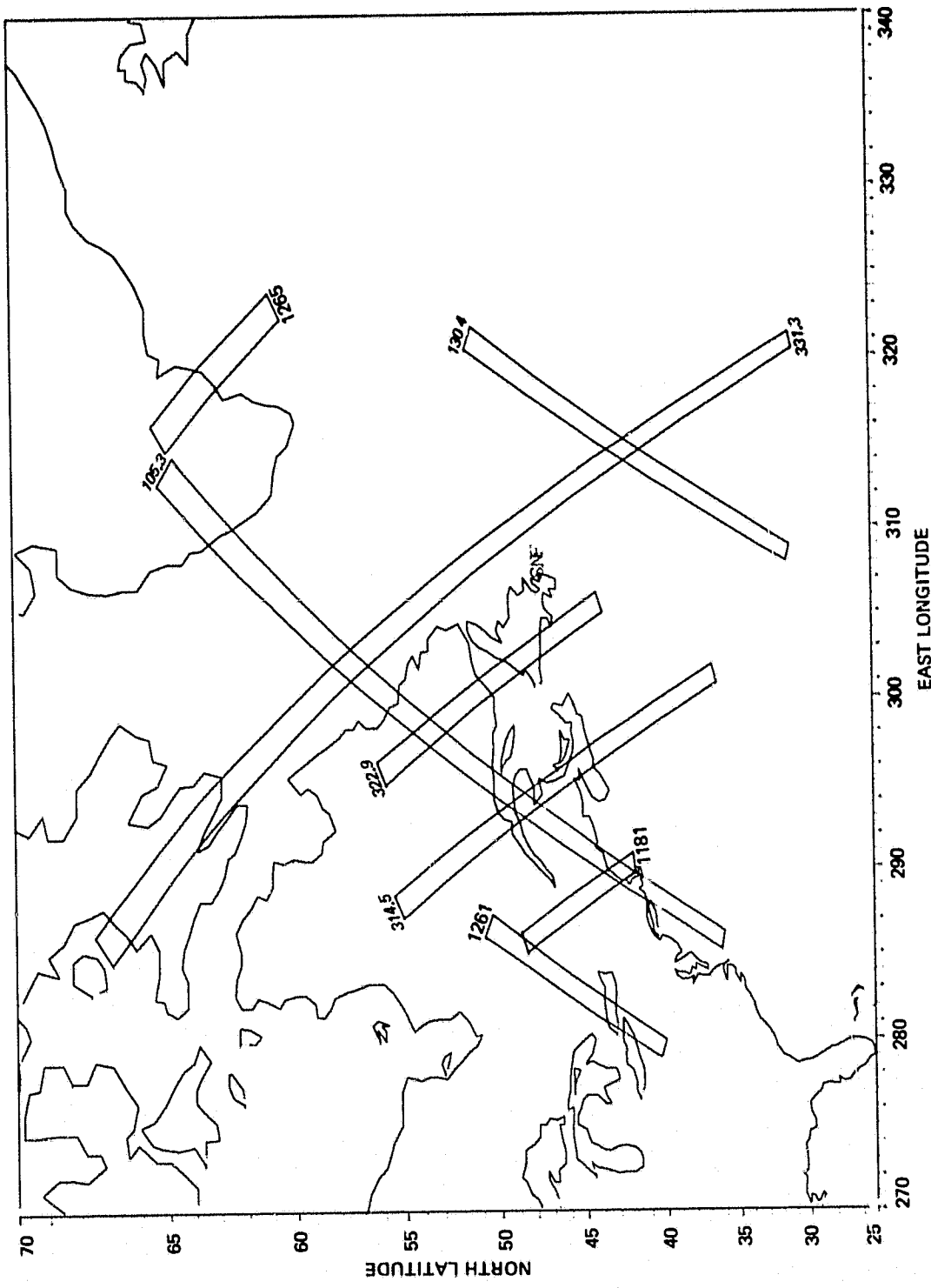
Figure C-10. Shoe Cove, Newfoundland: September 17 through October 9, 1978.
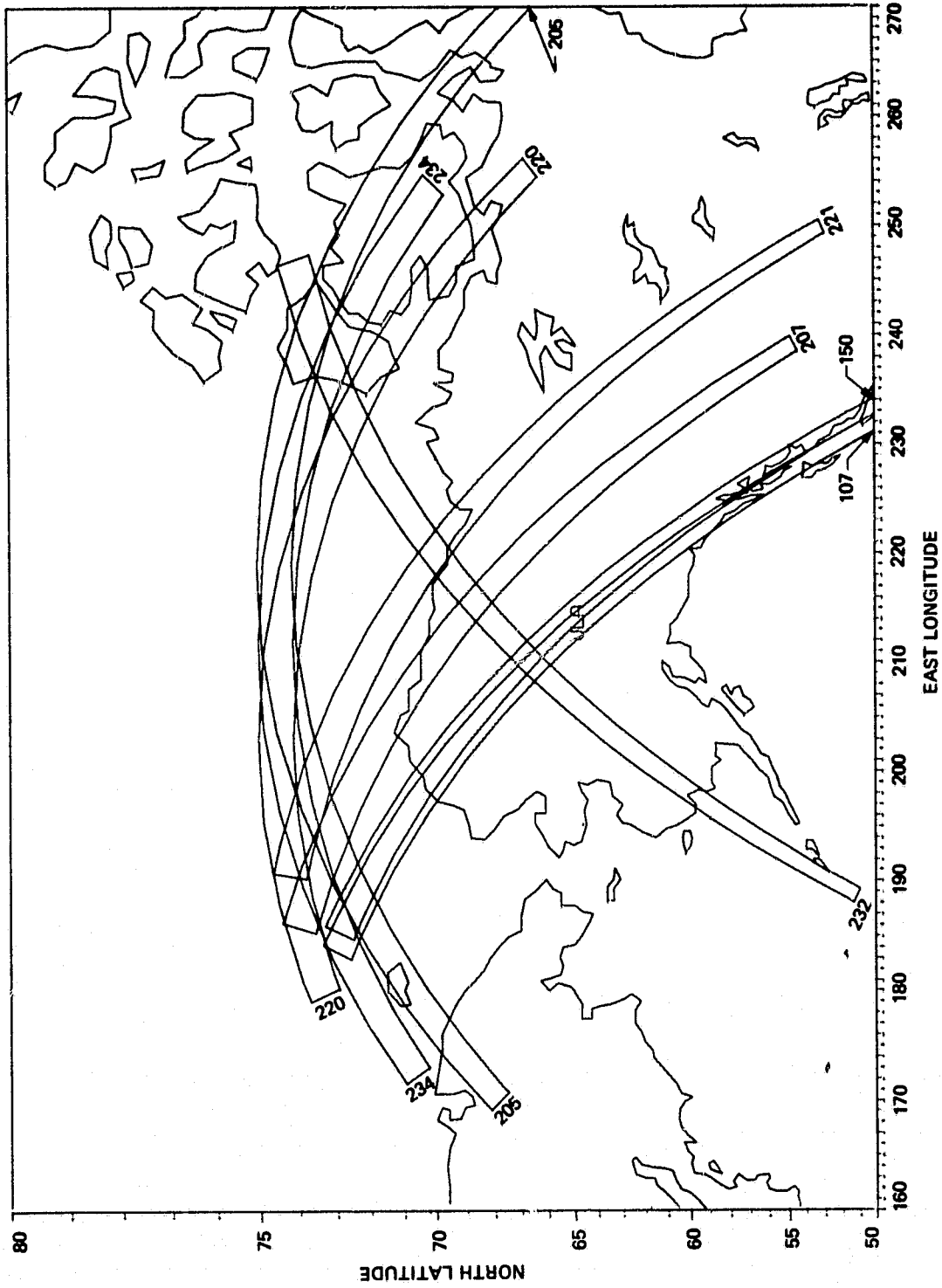
Figure C-11. Fairbanks, Alaska: July 4 through July 13, 1978.
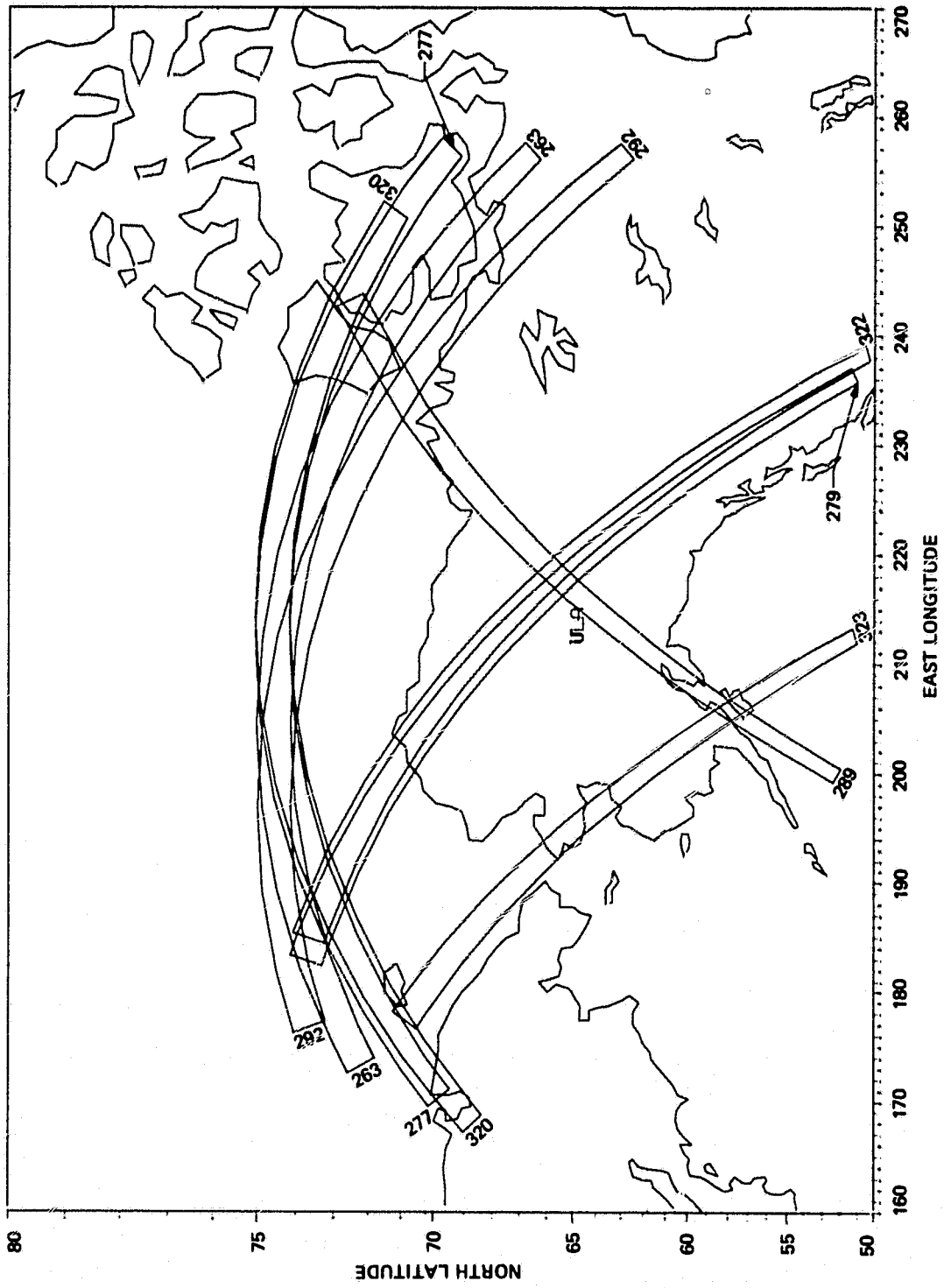
Figure C-12. Fairbanks, Alaska: July 14 through July 19, 1978.

Figure C-13. Fairbanks, Alaska: July 20 through July 23, 1978.

Figure C-14. Fairbanks, Alaska: July 24 through July 29, 1978.
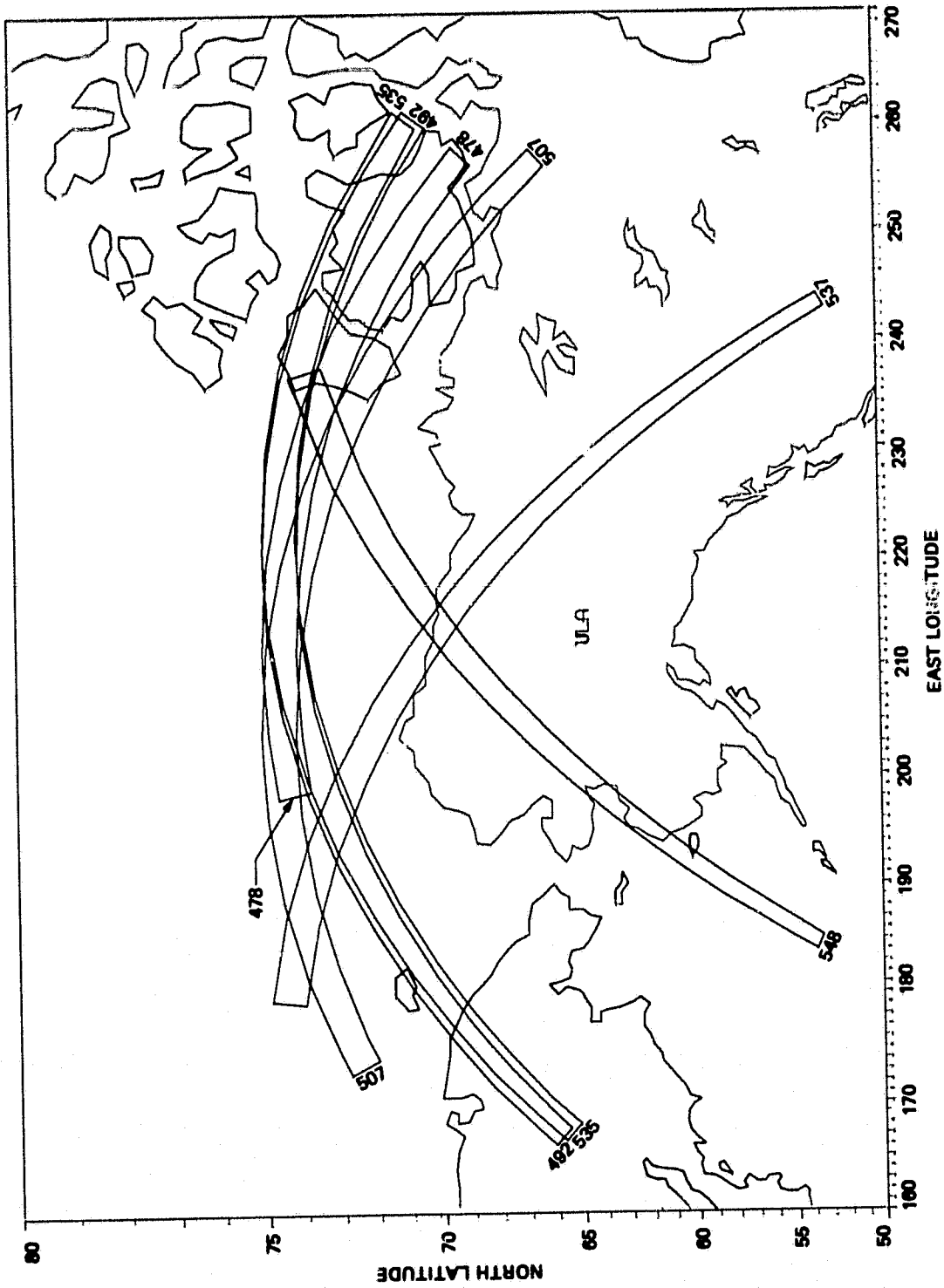
Figure C-15. Fairbanks, Alaska: July 30 through August 4, 1978.
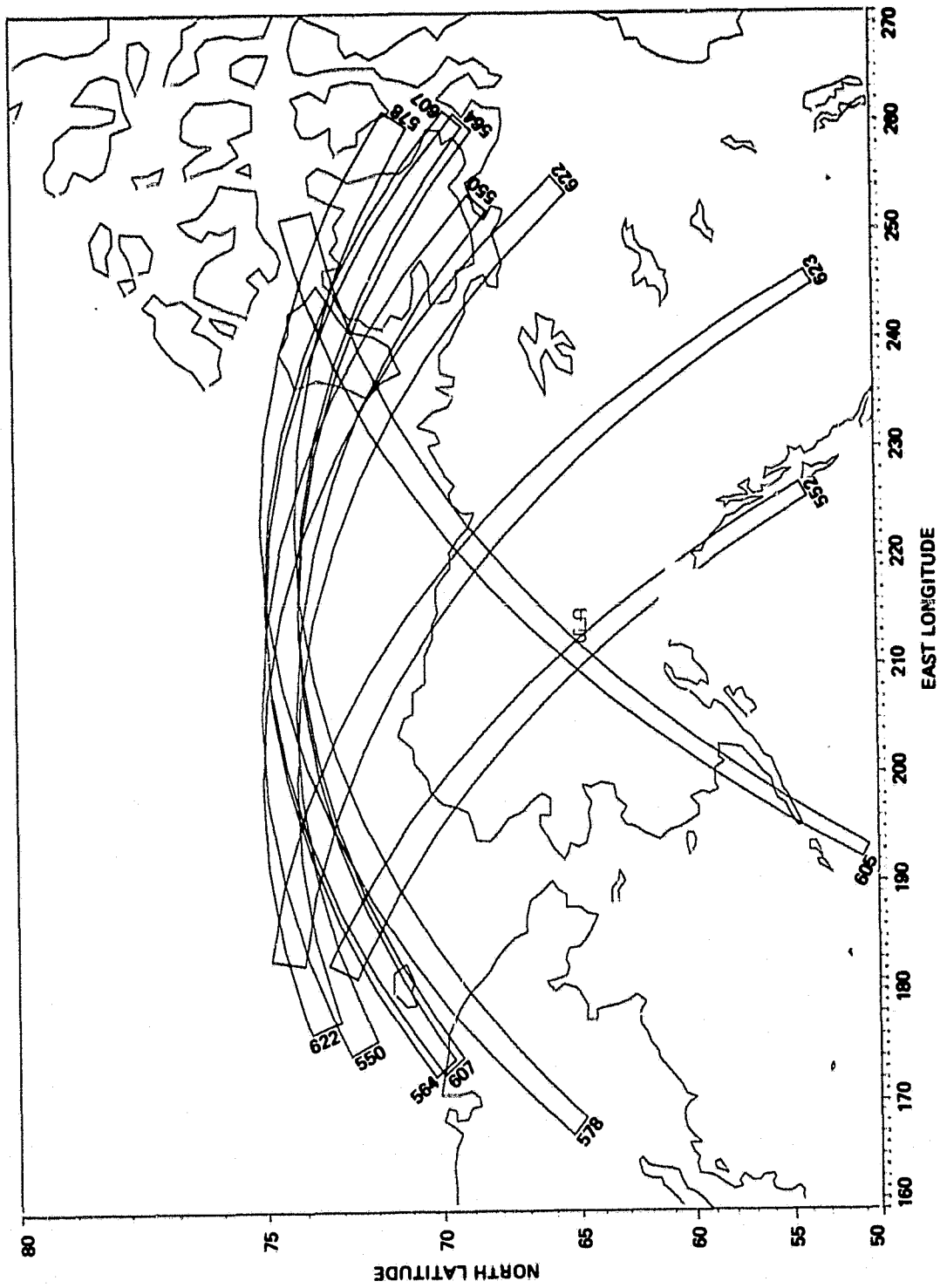
Figure C-16. Fairbanks, Alaska: August 4 through August 9, 1978.
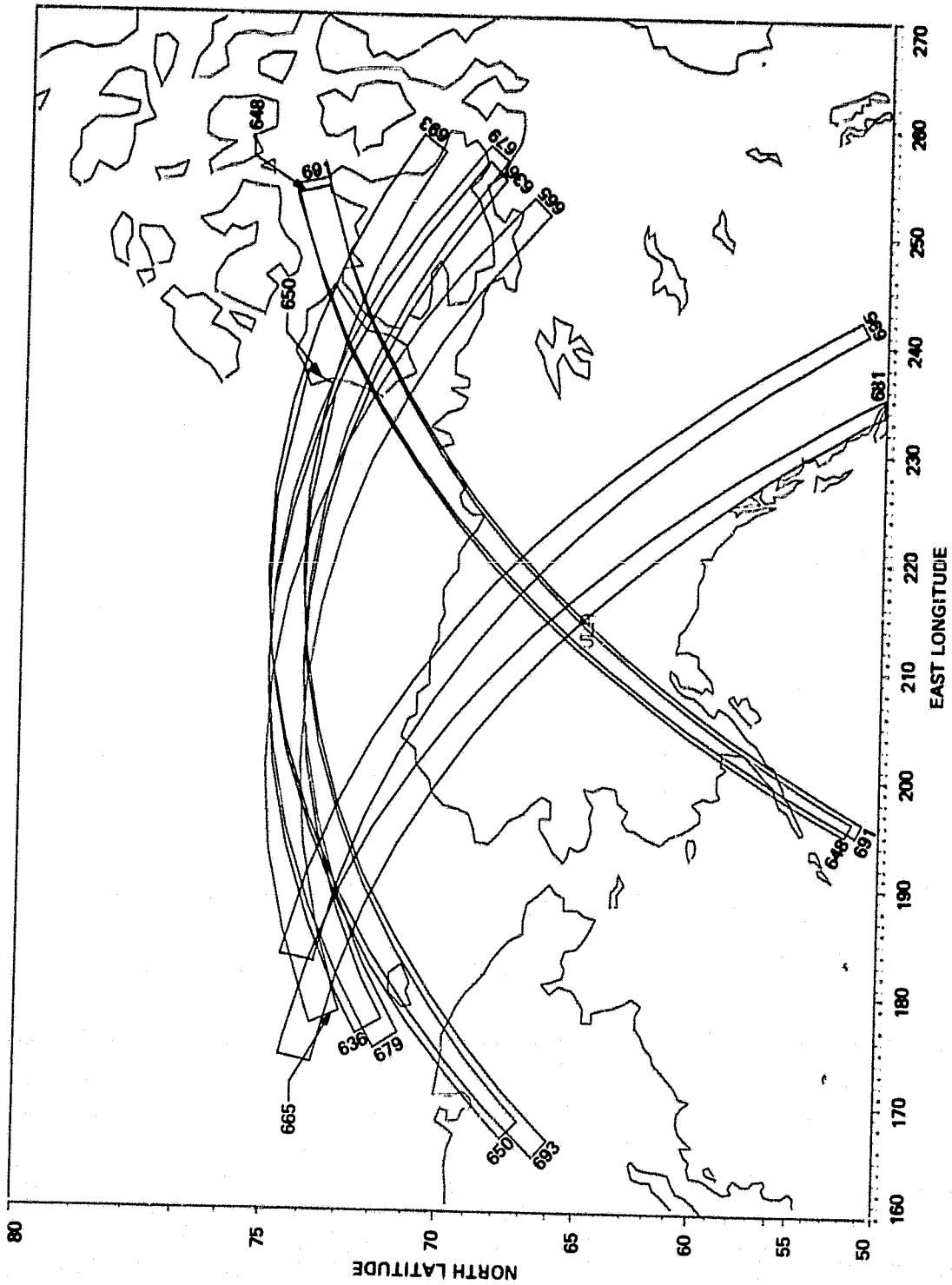
Figure C-17. Fairbanks, Alaska: August 10 through August 14, 1978.

158
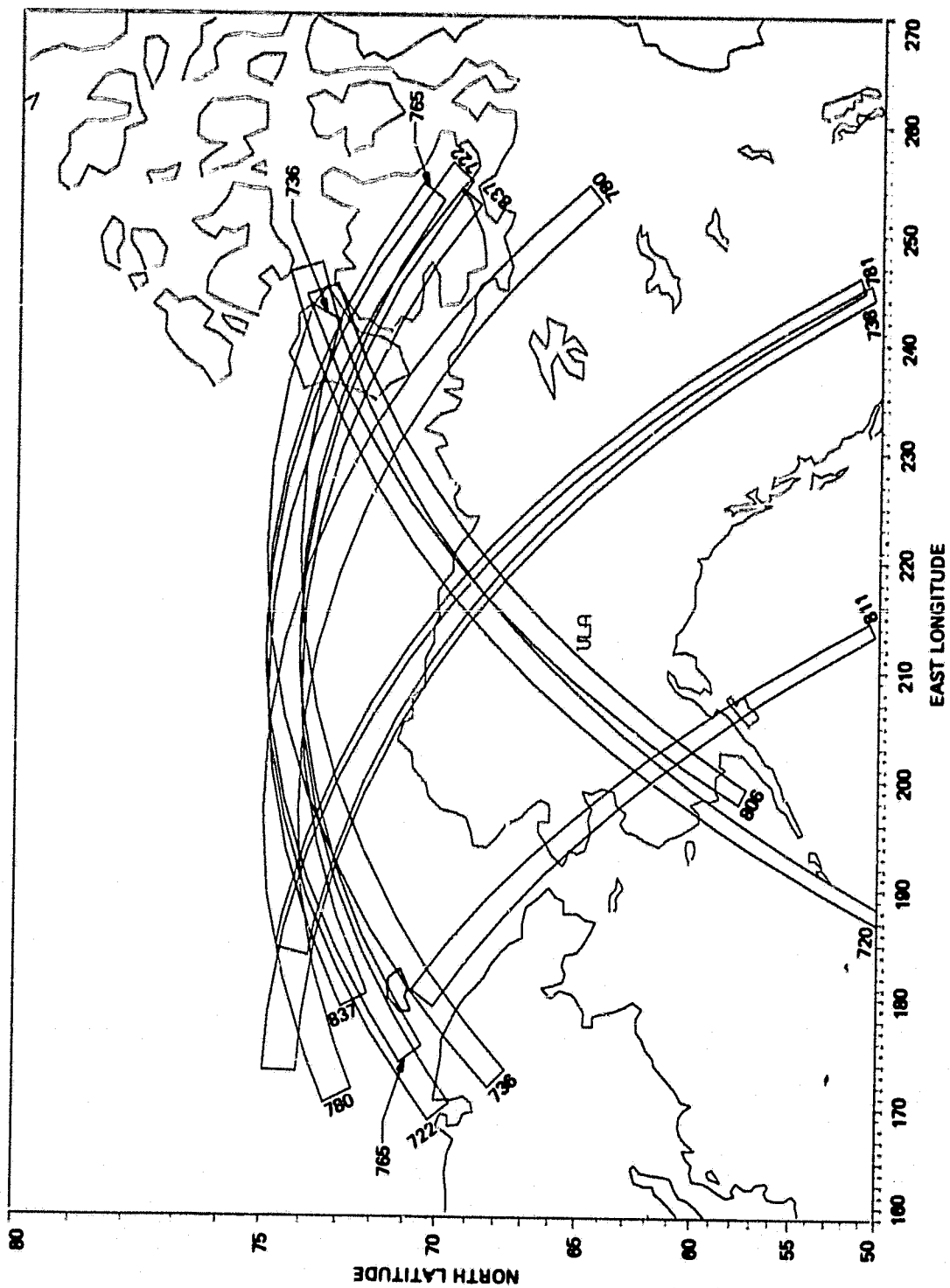
Figure C-18. Fairbanks, Alaska: August 15 through August 24, 1978.

Figure C-19. Fairbanks, Alaska: August 25 through October 9, 1978.
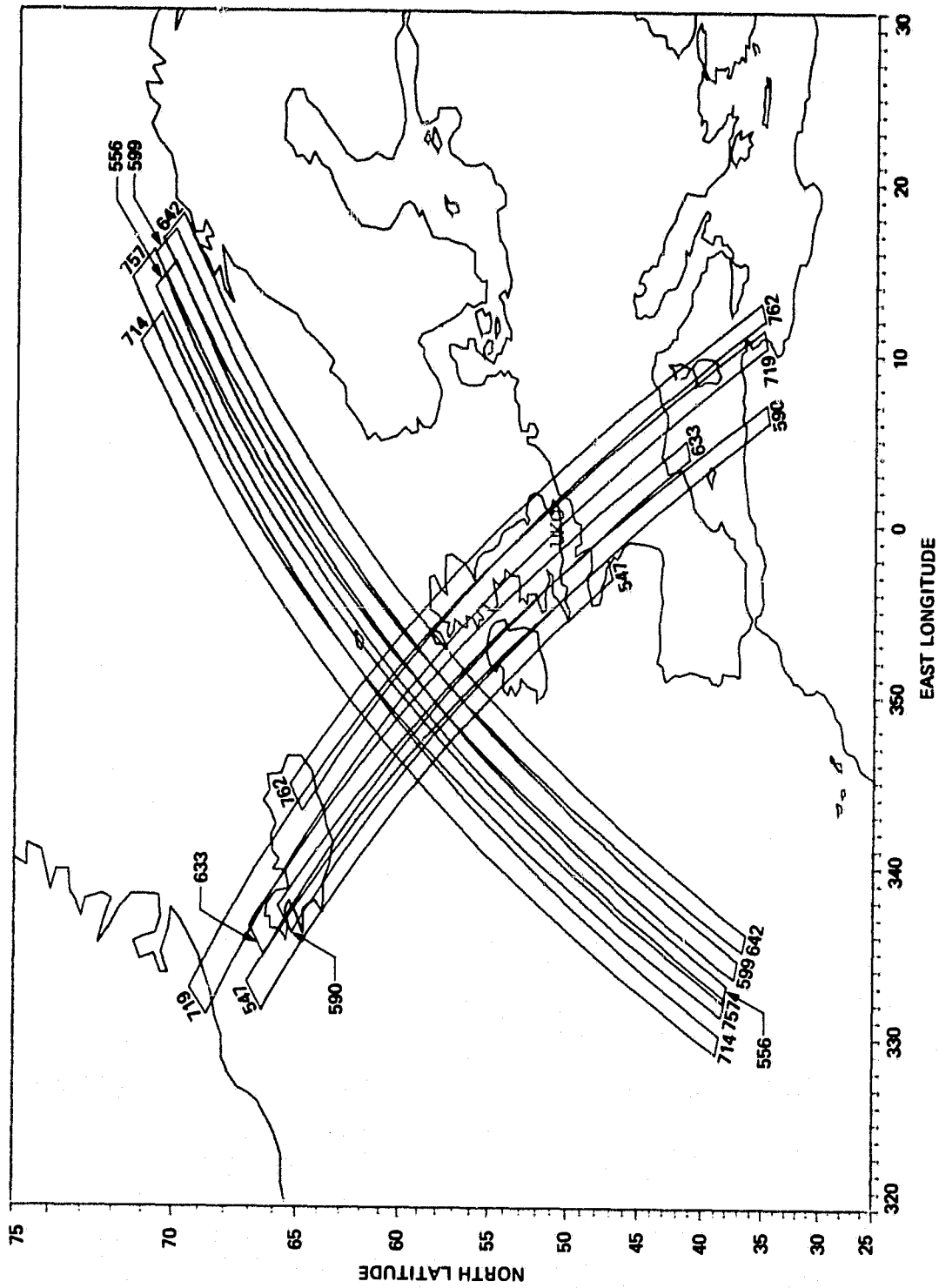
Figure C-20. Oakhanger, England: August 4 through August 19, 1978.
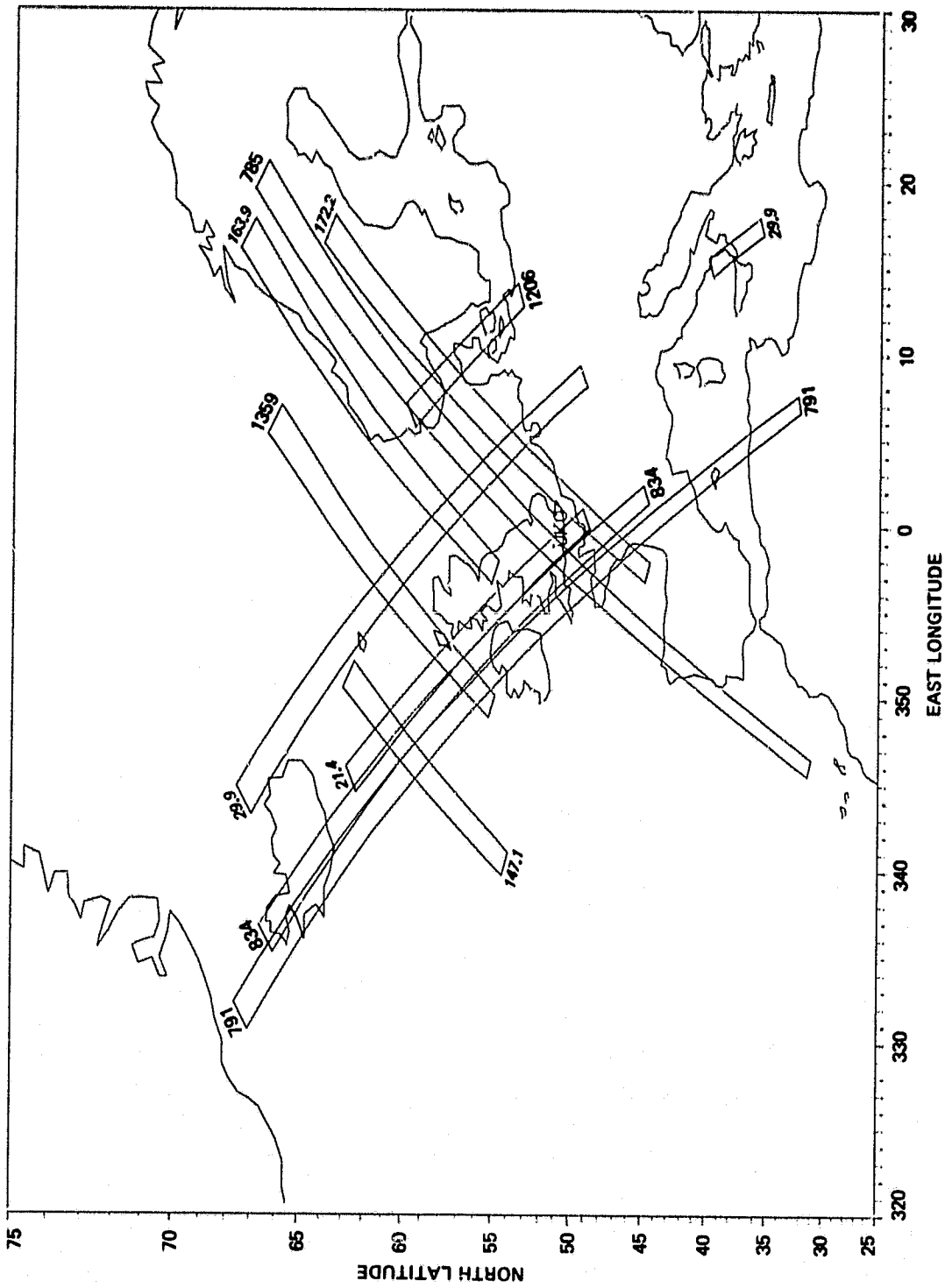
Figure C-21. Oakhanger, England: August 20 through October 10, 1978.

C.2 Key Orbital Information

Table C-1 presents key orbital information pertaining to the SAR swaths plotted on Figures C-1 through C-21. All the data in the table, which are listed by their revolution numbers, have been optically processed except as noted under "COMMENTS." Nodes and node times are taken from Klose (1979), and all times are standardized to Green~i~h Mean Time (GMT). Items listed include:

REV	revolution number
STA	receiving station acronym (see Appendix A)
NODE	east longitude in degrees where the spacecraft nadir track crosses the equator in an ascending mode (passing from south to north)
DAT	month and day of 1978
JLN	Julian day of 1978
NODETIM	time (hour:minute:second) of spacecraft node crossing
LTON	north latitude in degrees where imagery starts
LOFF	north latitude in degrees where imagery ends
TIMEON	time (hour:minute:second) when imagery starts
OFF	time (hour:minute:second) when imagery ends
COMMENTS	NP: entire revolution not optically processed unless followed by time (minute:second) and letter (S, start; M, middle; E, end), which indicates the duration and location of the segment of the revolution that is not optically processed
	NTC: no time code on original high-density digital tape
	ENG: engineering revolutions in which the configuration of the SAR was altered to test various features of the system

Table C-2 provides the approximate amount of time taken by the spacecraft to travel from the equator to the place where the SAR swath (not the nadir track) crosses a given latitude, either in an ascending mode (passing from south to north) or a descending mode (passing from north to south). Items listed in this table include:

LAT	north latitude in degrees
TA	time (minute:second) from equator to latitude crossing in an ascending mode
TD	time (minute:second) from equator to latitude crossing in a descending mode

Effective use of Tables C-1 and C-2 in conjunction with the coverage plots will enable the reader to determine the revolution numbers and the dates and times of the SAR images covering an area of interest, and will thus facilitate the process of ordering SAR images.

Table C·1. Orbital information for the Seasat SAR images

REV	STA	NODE	DAT	JLN NODE TIM	LTON	LOFF	TIME ON	OFF	COMMENTS
107	GDS	253.67	J 4	185-12: 1: 3	18.5	47.8	12: 6:15	15: 0	
107	ULA	253.67	J 4	185-12: 1: 3	47.8	73.4	12:15: 0	24:20	NP
150	GDS	255.10	J 7	188-12: 8: 6	18.2	54.6	12:13:22	24:10	
150	ULA	255.10	J 7	188-12: 8: 6	49.8	73.4	12:22:40	31:30	
163	MIL	289.03	J 8	189- 9:56:17	10.8	49.1	9:59:20	10:38	
179	GDS	247.70	J 9	190-12:46:21	22.6	50.1	12:52:45	1: 0	
193	GDS	256.54	J10	191-12:15: 9	21.1	53.6	12:21: 7	30:53	
205	ULA	315.55	J11	192- 6:22:48	65.8	68.0	8:44:32	53:25	
207	GDS	265.38	J11	192-11:43:58	23.6	42.6	11:50:40	56:20	
207	ULA	265.38	J11	192- 8:22:48	54.8	74.4	12: 0: 5	8:15	
220	ULA	299.30	J12	193- 9:32: 8	66.8	72.6	9:52:21	59:41	
221	MIL	274.22	J12	193-11:12:46	13.4	37.4	11:16:28	23:35	
221	ULA	274.22	J12	193-11:12:46	53.5	74.7	11:28:25	37:50	
222	GDS	249.14	J12	193-12:53:24	19.5	50.4	12:57:25	8:10	
230	GDS	48.48	J13	194- 2:18:26	53.8	23.4	2:53: 0	2:10	
232	ULA	358.51	J13	194- 5:39:41	74.6	51.2	6: 5:32	15: 3	
234	ULA	308.15	J13	194- 9: 0:56	69.9	70.1	9:22:25	29:45	
236	GDS	257.98	J13	194-12:22:12	18.6	52.5	12:27:25	38: 5	NP1:40M
242	MIL	107.48	J13	194-22:25:58	35.9	14.4	23: 6: 0	12:20	
251	GDS	241.74	J14	195-13:31:58	15.6	45.9	13:35:58	45: 0	
263	MIL	300.74	J15	196- 9:39:11	16.6	51.1	9:43:48	54: 8	
263	ULA	300.74	J15	196- 9:39:11	66.4	72.4	9:59:25	6:50	
273	GDS	49.92	J16	197- 2:25:28	53.4	22.5	3: 0:10	9:28	
277	ULA	309.59	J16	197- 9: 7:59	69.2	69.7	9:29:10	37: 0	
279	GDS	259.42	J16	197-12:29:14	33.2	54.2	12:38:46	45:10	
279	ULA	259.42	J16	197-12:29:14	51.5	73.9	12:44:15	53: 0	
289	ULA	8.59	J17	198- 5:15:32	72.5	51.8	5:43:10	50:43	
292	ULA	293.34	J17	198-10:17:25	63.5	73.3	10:36:25	44:30	
308	GDS	252.02	J18	199-13: 7:29	20.6	53.4	13:13:18	23:10	
320	ULA	311.03	J19	200- 9:15: 1	71.3	69.4	9:37:18	44:10	
322	GDS	260.86	J19	200-12:36:17	23.3	50.6	12:43: 4	51: 5	
322	ULA	260.86	J19	200-12:36:17	50.8	74.0	12:51:10	0: 9	
323	ULA	235.78	J19	200-14:16:54	51.4	70.6	14:31:57	38:40	
335	MIL	294.78	J20	201-10:24:27	13.0	41.4	10:28: 2	36:14	
337	ULA	244.62	J20	201-13:45:42	50.8	72.2	14: 0:35	8:17	
349	ULA	303.65	J21	202- 9:53:15	67.8	72.2	10:13:50	21:15	
350	ULA	278.54	J21	202-11:33:53	58.4	73.5	11:50:50	59:20	
351	GDS	253.46	J21	202-13:14:39	14.4	51.8	13:19:58	29:40	
351	ULA	253.46	J21	202-13:14:39	50.5	73.2	13:29:17	37:45	
363	ULA	312.47	J22	203- 9:22: 3	69.9	68.8	9:43:30	51:39	
365	ULA	262.30	J22	203-12:43:18	58.9	74.1	13: 0: 4	7:15	
371	MIL	111.81	J22	203-22:47: 5	20.9	10.9	23:31:30	34:30	
378	MIL	296.23	J23	204-10:31:29	13.6	46.3	10:35:15	45: 0	
378	ULA	296.23	J23	204-10:31:29	69.4	73.1	10:52:45	58:43	
380	ULA	246.06	J23	204-13:52:44	49.9	72.4	14: 7:20	15:25	
387	GDS	70.48	J24	205- 1:37: 8	34.7	16.7	2:17:30	22:40	
388	GDS	45.40	J24	205- 3:17:46	51.1	27.2	3:53:12	0:22	
392	ULA	305.07	J24	205-10: 0:17	68.4	73.5	10:21: 8	27:12	
393	MIL	279.99	J24	205-11:40:54	10.8	42.1	11:43:50	53:22	
394	GDS	254.91	J24	205-13:21:32	18.2	53.2	13:26:38	37:10	
400	MIL	104.41	J24	205-23:25:18	43.4	9.8	0: 2:40	13: 2	
406	ULA	315.91	J25	206- 9:29: 5	70.5	72.6	9:50:50	56:39	
407	MIL	288.83	J25	206-11: 9:42	11.8	47.1	11:12:55	23:25	
416	GDS	65.08	J26	207- 2:15:22	49.6	26.0	2:51:15	58:20	ENG

Table C-1 (contd)

REV	STA	NODE	DAT	JLN NODE TIM	LTON	LOFF	TIME ON	OFF	COMMENTS
422	MIL	272.59	J26	207-12:19: 8	14.2	34.1	12:23: 3	29:56	
430	GDS	71.93	J27	208- 1:44:10	25.8	16.3	2:27:10	30: 0	
435	ULA	306.51	J27	208-10: 7:18	69.3	73.5	10:28:30	34:16	
443	MIL	105.85	J27	208-23:32:20	27.0	9.6	0:14: 0	20: 7	
447	ULA	5.52	J28	209- 6:14:51	74.4	50.9	6:41: 0	50:20	
449	ULA	315.36	J28	209- 9:36: 6	71.6	72.2	9:57:50	3:50	
450	MIL	290.27	J28	209-11:16:44	12.5	47.0	11:20:10	30:26	NP4:30L
464	ULA	299.12	J29	210-10:45:32	66.8	72.5	11: 5:45	13:10	
465	MIL	274.03	J29	210-12:26: 9	13.1	38.7	12:29:45	37:21	
466	GDS	248.95	J29	210-14: 6:47	26.8	52.7	14:14:26	21:14	
472	MIL	98.45	J30	211- 0:10:33	47.4	12.0	0:47:16	57:48	
473	GDS	73.37	J30	211- 1:51:11	47.1	16.3	2:27:50	36:59	
474	GDS	46.29	J30	211- 3:31:49	53.6	23.6	4: 6:27	15:30	
478	ULA	301.96	J30	211-10:14:20	69.3	73.4	10:35:33	41:23	
480	GDS	251.79	J30	211-13:35:35	18.9	54.1	13:40:47	51:30	
488	GDS	51.13	J31	212- 3: 0:37	54.0	19.1	3:35: 7	45:38	
492	ULA	316.80	J31	212- 9:43: 7	71.0	65.4	10: 5: 5	13:49	PU4:30E
493	MIL	291.72	J31	212-11:23:45	12.8	45.8	11:27:16	37: 0	
495	GDS	241.55	J31	212-14:45: 1	20.5	46.4	14:50:48	58:32	
502	GDS	65.97	A 1	213- 2:29:25	51.1	25.2	3: 4:50	12:38	
507	ULA	300.56	A 1	213-10:52:33	66.7	72.5	11:12:43	20:10	
508	MIL	275.48	A 1	213-12:33:11	12.1	37.9	12:36:30	44: 8	
509	GDS	250.40	A 1	213-14:13:48	17.5	51.4	14:18:38	28:51	
517	GDS	49.73	A 2	214- 3:38:50	49.6	26.0	4:12:55	22:25	
522	MIL	284.32	A 2	214-12: 1:59	10.4	45.0	12: 4:48	15: 5	
523	GDS	259.24	A 2	214-13:42:36	20.9	54.6	13:47:55	58:40	
529	MIL	108.74	A 2	214-23:46:22	41.3	13.0	0:24:45	33: 6	
531	GDS	58.58	A 3	215- 3: 7:38	53.6	18.5	3:42:15	52:48	
535	ULA	318.24	A 3	215- 9:50: 9	71.3	64.7	10:12:17	21: 6	
536	MIL	293.16	A 3	215-11:30:46	21.3	43.9	11:37: 5	43:33	
537	ULA	268.08	A 3	215-13:11:24	53.5	74.6	13:27: 2	35:55	NP4:00S
538	GDS	243.00	A 3	215-14:52: 2	18.4	47.4	14:57:12	5:52	
545	GDS	67.42	A 4	216- 2:36:26	50.5	24.6	3:12: 2	19:48	
547	UKO	17.25	A 4	216- 5:57:41	47.4	69.6	6:11:31	18:12	NTC
548	ULA	352.17	A 4	216- 7:38:19	74.6	53.4	8: 3:10	13: 0	
550	ULA	302.00	A 4	216-10:59:34	68.6	72.3	11:20:27	27:16	
552	GDS	251.84	A 4	216-14:20:50	17.3	45.8	14:25:40	34:10	
552	ULA	251.84	A 4	216-14:20:50	54.1	73.1	14:36:45	44: 0	
556	UKO	151.51	A 4	216-21: 3:20	70.3	38.4	21:32: 3	42:38	NTC
558	MIL	101.34	A 5	217- 0:24:36	46.1	10.8	1: 1:33	12: 3	
559	GDS	76.26	A 5	217- 2: 5:14	45.0	17.0	2:42:35	50:50	
564	ULA	310.85	A 5	217-10:28:22	69.3	69.4	10:49:35	57:29	
565	MIL	285.76	A 5	217-12: 9: 0	10.5	45.5	12:11:51	22:18	
574	GDS	60.02	A 6	218- 3:14:39	50.0	19.4	3:50:25	59:54	
578	ULA	319.69	A 6	218- 9:57:10	71.6	64.2	10:19:25	28:17	
580	GDS	259.53	A 6	218-13:18:25	24.0	56.7	13:25:15	35: 0	
581	GDS	244.44	A 6	218-14:59: 3	19.3	48.2	15: 4:30	13: 8	
590	UKO	18.70	A 7	219- 6: 4:42	35.4	65.7	6:14:55	24:30	NTC
595	GDS	255.29	A 7	219-14:27:51	17.3	52.3	14:32:42	43:13	
599	UKO	152.95	A 7	219-21:10:22	70.3	37.7	21:39: 7	49:50	NTC
605	ULA	2.46	A 8	220- 7:14: 8	74.7	51.2	7:39:34	49:30	
607	ULA	312.29	A 8	220-10:35:23	69.7	69.0	10:56:45	4:40	
608	MIL	287.21	A 8	220-12:16: 1	11.1	44.4	12:19: 2	28:38	ENG

Table C-1 (contd)

REV	STA	NODE	DAT	JLN NODE TIM	LTON	LOFF	TIME ON	OFF	COMMENTS
617	GDS	61.47	A 9	221- 3:21:40	52.8	18.0	3:56:37	7: 0	ENG
622	ULA	296.05	A 9	221-11:44:49	65.8	73.2	12: 4:38	12: 0	
623	MIL	270.97	A 9	221-13:25:26	15.7	37.1	13:29:49	36: 9	
623	GDS	270.97	A 9	221-13:25:26	23.1	54.6	13:32: 0	41:30	NP4:30E
623	ULA	270.97	A 9	221-13:25:26	53.7	74.6	13:41:12	50: 0	
631	GDS	70.31	A10	222- 2:50:28	49.1	17.8	3:26:29	35:50	ENG
633	UKO	20.14	A10	222- 6:11:44	42.6	68.1	6:23:56	32:27	NTC
636	ULA	304.89	A10	222-11:13:37	68.5	71.6	11:34:30	41:45	
637	MIL	279.81	A10	222-12:54:14	11.0	42.5	12:57:30	7: 0	
638	GDS	254.73	A10	222-14:34:52	17.5	52.7	14:39:46	50:20	ENG
642	UKO	154.40	A10	222-21:17:23	70.1	36.9	21:46:13	57: 2	NTC
648	ULA	5.90	A11	223- 7:21: 9	74.6	51.8	7:46:52	56:40	
650	ULA	315.74	A11	223-10:42:24	74.6	68.0	11: 8: 8	12: 5	
651	MIL	288.66	A11	223-12:23: 2	10.8	41.2	12:25:58	34:59	
659	MIL	88.00	A12	224- 1:48: 4	48.7	17.6	2:24:12	33:31	
660	GDS	62.91	A12	224- 3:28:41	52.5	26.6	4: 3:39	10:30	NP3:00S
665	ULA	297.50	A12	224-11:51:50	67.1	73.1	12:12:10	19: 5	
674	GDS	71.75	A13	225- 2:57:29	37.0	16.7	3:37:10	43:11	
679	ULA	306.54	A13	225-11:20:38	68.5	71.1	11:41:35	49: 0	
681	GDS	256.18	A13	225-14:41:53	17.7	54.8	14:47: 0	56:30	NP1:30E
681	ULA	256.18	A13	225-14:41:53	49.2	73.4	14:56:15	5:17	
687	MIL	105.63	A14	226- 0:45:39	44.2	9.7	1:23:11	33:25	
691	ULA	5.35	A14	226- 7:28:10	74.5	50.6	7:54:10	3:43	
693	ULA	315.18	A14	226-10:49:25	70.9	66.8	11:11:20	29:35	
694	MIL	290.10	A14	226-12:30: 3	12.6	46.8	12:33:30	43:42	
695	GDS	265.02	A14	226-14:10:41	26.4	50.1	14:18:14	25:21	
695	ULA	265.02	A14	226-14:10:41	51.2	74.3	14:25:40	34:50	
710	GDS	248.06	A15	227-15:20: 6	27.6	50.4	15:28: 0	34:52	
714	UKO	148.45	A15	227-22: 2:37	70.4	39.2	22:31:17	41:41	NTC
716	MIL	98.34	A16	228- 1:23:38	46.1	10.9	2: 0:34	11: 2	NP5:00S
719	UKO	23.11	A16	228- 6:25:27	35.1	70.0	6:35:33	46:56	NTC
720	ULA	358.04	A16	228- 8: 6: 3	74.6	50.4	8:31:48	41:40	
722	ULA	307.88	A16	228-11:27:15	69.8	69.7	11:48:40	56:15	
723	MIL	282.81	A16	228-13: 7:52	11.6	45.4	13:11: 1	21: 5	
724	GDS	257.73	A16	228-14:48:28	19.7	51.9	14:54: 1	4:40	
731	GDS	82.19	A17	229- 2:32:42	31.6	14.2	3:12:43	18:12	NP
731	MIL	82.19	A17	229- 2:32:42	31.6	29.9	3:12:43	14:30	
736	ULA	316.81	A17	229-10:55:44	74.4	66.6	11:20: 0	26:59	
737	MIL	291.73	A17	229-12:36:20	14.6	47.7	12:40:23	50:15	NP5:00S
738	GDS	266.66	A17	229-14:16:56	24.6	51.4	14:24:38	32: 0	NP2:00C
738	ULA	266.66	A17	229-14:16:56	50.4	74.4	14:31:42	42: 0	
739	GDS	241.58	A17	229-15:57:33	21.4	48.6	16: 3:37	11:44	
757	UKO	150.27	A18	230-22: 8: 9	70.7	38.9	22:36:43	47:17	
759	MIL	100.13	A19	231- 1:29:18	47.2	11.9	2: 5:55	16:25	
761	GDS	50.00	A19	231- 4:50:27	55.9	23.6	5:24:21	34: 9	
762	UKO	24.92	A19	231- 6:31: 2	35.7	65.7	6:41:20	52: 7	NP1:20F
765	ULA	309.72	A19	231-11:32:45	70.1	70.5	11:54:18	1:24	
766	MIL	284.65	A19	231-13:13:19	9.6	44.2	13:15:54	26:10	
774	MIL	84.10	A20	232- 2:37:54	44.1	21.1	3:13:58	22:18	
780	ULA	293.68	A20	232-12:41:20	64.9	73.6	13: 0:50	8:10	
781	GDS	268.62	A20	232-14:21:55	22.6	51.5	14:28:20	38:30	
781	ULA	268.62	A20	232-14:21:55	51.0	74.7	14:36:50	46: 5	

Table C-1 (contd)

REV	STA	NODE	DAT	JLN NODE TIM	LTON	LOFF	TIME ON	OFF	COMMENTS
782	GDS	245.55	A20	232-16: 2:29	16.7	46.8	16: 7:19	16: 8	
785	UKO	168.34	A20	232-21: 4:12	67.2	31.8	21:34:12	45:26	
788	MIL	93.14	A21	233- 2: 5:55	42.1	18.8	2:44: 0	50: 0	NP1:00E
789	GDS	58.07	A21	233- 3:46:30	46.2	30.4	4:23:24	28:10	
791	UKO	17.73	A21	233- 7: 7:39	33.4	67.4	7:17:15	28: 5	NP2:00E
795	MIL	277.66	A21	233-13:49:56	18.1	38.3	13:55: 0	1: 0	
802	MIL	102.17	A22	234- 1:33:57	39.9	14.4	2:12:47	19:20	
806	ULA	1.40	A22	234- 8:16:14	74.0	57.3	8:42:46	49:30	
809	MIL	286.69	A22	234-13:17:57	13.6	43.3	13:21:45	30:32	
810	GDS	261.62	A22	234-14:56:32	22.6	47.5	15: 4:56	12:23	
811	ULA	236.56	A22	234-16:39: 6	50.8	70.3	16:53:59	0:43	
825	GDS	245.57	A23	235-16: 7:13	19.2	47.7	16:12:37	21: 7	
834	UKO	19.90	A24	236- 7:12:35	44.9	67.2	7:25:40	32:56	
837	ULA	304.68	A24	236-12:14:22	68.7	72.7	12:35:20	41:53	
838	MIL	279.60	A24	236-13:54:58	22.0	40.4	14: 1:12	6:40	
845	MIL	104.08	A25	237- 1:39: 7	40.9	26.3	2:17:39	22: 0	
849	ULA	5.78	A25	237- 8:21:31	74.6	67.9	8:47:20	55:10	
852	MIL	288.56	A25	237-13:23:18	21.1	34.9	13:29:16	35:56	
853	GDS	263.49	A25	237-15: 3:54	26.4	39.1	15:12:20	16: 7	
874	MIL	96.53	A27	239- 2:17:58	46.9	11.4	2:54:39	5:13	
880	MIL	305.84	A27	239-12:22:29	32.9	46.7	12:31:56	36: 0	
880	ULA	305.84	A27	239-12:22:29	71.8	74.0	12:44:50	49: 0	
882	GDS	255.62	A27	239-15:43:59	28.0	41.4	15:52: 0	56: 0	
888	MIL	104.93	A28	240- 1:48:31	51.9	32.2	2:23:39	29:39	
891	UKO	29.59	A28	240- 6:50:47	49.4	64.9	7: 5:24	10:24	NP BY JPL
894	ULA	314.24	A28	240-11:53: 2	70.9	73.5	12:14:57	19:59	
908	ULA	322.65	A29	241-11:23:34	73.1	73.9	11:46:41	50:11	ENG
909	MIL	297.53	A29	241-13: 4:20	31.7	38.4	13:13:26	15:26	
931	MIL	105.02	A31	243- 2: 0:53	41.5	28.6	2:38:15	42: 5	NP
947	GDS	63.19	S 1	244- 4:52:56	39.7	33.0	5:31:50	33:50	NP
957	UKO	172.05	S 1	244-21:40:28	55.4	49.0	22:14:31	16:31	NP
958	UKO	146.94	S 1	244-23:21:13	62.5	56.5	23:52:56	54:56	
963	UKO	21.37	S 2	245- 7:44:59	49.2	55.5	7:59:22	1:20	
966	ULA	306.02	S 2	245-12:47:14	73.4	74.7	13:10:36	12:36	
968	GDS	255.80	S 2	245-16: 8:45	43.7	50.2	16:21:27	23:27	NP
968	GDS	255.80	S 2	245-16: 8:45	32.6	39.3	16:18: 7	20: 7	NF
974	MIL	105.11	S 3	246- 2:13:16	50.0	32.7	2:49: 1	53:57	
980	ULA	314.43	S 3	246-12:17:47	74.0	74.6	12:41:38	43:38	
990	GDS	63.29	S 4	247- 5: 5:19	39.3	32.6	5:44:19	46:19	NP
991	GDS	38.17	S 4	247- 6:46: 4	51.2	44.8	7:21:24	23:24	
1001	UKO	147.03	S 4	247-23:33:36	61.5	68.7	0: 5:40	6:55	
1005	GDS	46.57	S 5	248- 6:16:36	51.4	44.9	6:51:55	53:55	
1006	UKO	21.46	S 5	248- 7:57:22	55.7	61.8	8:13:47	15:47	
1009	ULA	306.12	S 5	248-12:59:37	74.1	74.5	13:23:35	25:35	
1011	GDS	255.89	S 5	248-16:21: 7	43.2	49.8	16:33:40	35:40	NP
1011	GDS	255.89	S 5	248-16:21: 7	33.0	37.9	16:30:37	32: 4	
1017	MIL	105.20	S 6	249- 2:25:36	45.9	39.6	3: 2:37	4:36	
1020	GDS	29.86	S 6	249- 7:27:54	51.5	45.0	8: 3:11	5:11	
1023	ULA	314.52	S 6	249-12:30: 9	71.6	74.4	12:52:26	54:26	
1024	MIL	289.40	S 6	249-14:10:54	21.0	27.8	14:16:51	13:51	
1033	GDS	63.38	S 7	250- 5:17:41	41.2	34.5	5:56: 7	58: 7	NP
1034	GDS	38.26	S 7	250- 6:58:26	50.8	46.7	7:33:55	35:12	
1038	ULA	297.81	S 7	250-13:41:27	69.8	74.4	14: 2:52	5:42	
1038	MIL	297.81	S 7	250-13:41:27	32.7	36.1	13:50:52	51:52	

Table C-1 (contd)

REV	STA	NODE	DAT	JLN NODE TIM	LTON	LOFF	TIME ON	OFF	COMMENTS
1040	GDS	247.58	S 7	250-17: 2:57	44.7	48.0	17:15:58	16:58	NP
1044	UKO	147.12	S 7	250-23:45:58	62.9	56.8	0:17:33	19:33	
1048	GDS	46.67	S 8	251- 6:28:59	51.3	44.3	7: 4:20	6:20	
1049	UKO	21.55	S 8	251- 8: 9:44	55.8	61.9	8:26:10	28:10	
1052	ULA	306.21	S 8	251-13:11:59	71.0	74.1	13:33:57	35:57	
1054	GDS	255.98	S 8	251-16:33:40	31.3	38.0	16:42:42	44:29	
1080	ULA	323.00	S10	253-12:13: 8	73.2	74.2	12:36:22	38:17	
1081	ULA	297.88	S10	253-13:53:53	73.7	74.6	14:16:30	18:30	
1081	MIL	297.88	S10	253-13:53:53	33.4	36.8	14: 3:30	4:30	
1063	GDS	247.65	S10	253-17:15:25	42.7	49.5	17:27:59	29:59	
1087	UKO	147.18	S10	253-23:58:28	62.3	59.3	0:30:16	32:16	
1095	ULA	306.25	S11	254-13:24:33	74.3	74.4	13:38:42	50:42	
1096	MIL	281.14	S11	254-15: 5:19	22.7	29.4	15:11:45	13:45	
1097	GDS	256.02	S11	254-16:46: 5	47.3	53.8	16:59:53	1:53	NP
1097	GDS	256.02	S11	254-16:46: 5	31.8	38.5	16:55:13	57:13	NP
1109	ULA	314.62	S12	255-12:55:13	73.1	74.7	13:17:21	21:21	
1110	MIL	289.50	S12	255-14:35:59	18.3	38.5	14:41: 7	47: 7	
1112	GDS	239.27	S12	255-17:57:31	40.6	46.8	18: 9:17	11:10	
1122	ULA	348.11	S13	256-10:45: 8	73.3	69.4	11:12:15	14:15	
1126	ULA	247.64	S13	256-17:28:11	50.0	61.5	17:42:48	46:30	
1126	GDS	247.64	S13	256-17:28:11	42.7	55.7	17:40:35	44:36	
1138	ULA	306.24	S14	257-13:37:19	72.5	74.7	14: 0: 5	2:25	
1139	MIL	281.13	S14	257-15:18: 5	22.0	31.6	15:24:20	27:10	
1140	GDS	256.01	S14	257-16:58:51	23.6	53.7	17: 5:33	14:48	
1149	UKO	29.96	S15	258- 8: 5:42	53.8	67.3	8:21:30	26: 5	
1149	UKO	29.96	S15	258- 8: 5:42	36.0	40.3	8:16: 5	17:23	
1153	MIL	289.50	S15	258-14:48:45	20.8	34.3	14:54:38	58:38	
1155	GDS	239.27	S15	258-18:10:16	26.9	46.3	18:17:57	23:46	
1163	GDS	38.33	S16	259- 7:36:22	51.8	45.0	8:11:34	14:40	
1167	ULA	297.87	S16	259-14:19:25	65.4	73.0	14:39: 5	46:45	
1167	MIL	297.87	S16	259-14:19:25	15.1	30.8	14:23:17	28:16	
1169	GDS	247.64	S16	259-17: 4:56	36.6	49.5	17:51:30	55:24	
1177	GDS	46.70	S17	260- 7: 7: 2	51.2	44.7	7:42:24	44:24	
1181	SNF	306.24	S17	260-13:50: 5	41.7	48.3	14: 2:11	4:11	
1182	MIL	281.12	S17	260-15:30:51	30.3	35.5	15:39:33	41: 5	
1183	GDS	256.01	S17	260-17:11:36	20.7	52.5	17:17:26	26:55	
1193	ULA	4.84	S18	261- 9:59:14	73.4	63.6	10:26: 4	30:34	
1195	ULA	314.61	S18	261-13:20:45	72.6	74.7	13:43:35	46: 5	
1196	MIL	289.49	S18	261-15: 1:31	18.9	30.0	15: 6:51	10:21	
1197	GDS	264.38	S18	261-16:42:16	24.1	53.9	16:49: 7	58: 7	
1198	GDS	239.26	S18	261-18:23: 2	40.0	46.6	18:34:36	36:36	NP
1201	UKO	165.91	S18	261-23:25:19	67.8	63.3	23:55: 6	57: 6	
1204	MIL	88.56	S19	262- 4:27:36	49.7	16.5	5: 3:26	13:26	
1205	UKO	38.33	S19	262- 7:49: 8	53.7	59.9	8: 4:55	6:55	
1205	GDS	63.44	S19	262- 6: 8:22	39.9	31.4	6:47:12	49:42	
1206	GDS	38.33	S19	262- 7:49: 8	56.2	49.6	8:22:57	24:57	
1209	SNF	322.98	S19	262-12:51:25	44.1	56.0	13: 4:14	8:14	
1210	ULA	297.86	S19	262-14:32:11	72.6	74.7	14:55: 0	57: 0	
1210	MIL	297.86	S19	262-14:32:11	27.6	37.5	14: 4:14	8:14	
1211	MIL	272.74	S19	262-16:12:56	10.4	17.2	16:15:46	18:46	
1212	GDS	247.63	S19	262-17:53:42	44.0	50.6	18: 6:31	8:31	
1215	UKO	172.28	S19	262-22:55:59	58.6	52.6	23:29: 0	30:48	
1224	ULA	306.23	S20	263-14: 2:51	72.2	74.7	14:25:25	27:49	

Table C-1 (contd)

REV	STA	NODE	DAT	JLN NODE TIM	LTON	LOFF	TIME ON	OFF	COMMENTS
1225	MIL	281.11	S20	263-15:43:36	20.6	27.3	15:49:24	52:24	
1226	GDS	256.00	S20	263-17:24:22	24.5	37.4	17:31:20	35:10	
1231	SNF	130.42	S21	264- 1:48:11	45.0	38.4	2:25:28	27:28	
1232	MIL	105.30	S21	264- 3:28:56	44.3	30.0	4: 6:25	12:34	NP2:09E
1232	SNF	105.30	S21	264- 3:28:56	56.8	42.4	4: 2:34	4: 7	
1235	GDS	29.95	S21	264- 8:31:14	57.6	53.1	9: 4:35	6: 1	
1236	ULA	4.83	S21	264-10:11:59	73.1	64.3	10:39:15	43: 0	
1238	SNF	314.60	S21	264-13:33:31	42.3	55.3	13:45:48	49:48	
1239	MIL	289.46	S21	264-15:14:16	18.8	30.6	15:19:33	23: 3	
1241	ULA	239.25	S21	264-18:35:46	52.7	58.9	18:51:15	53:15	NP
1248	GDS	65.44	S22	265- 6:21: 8	40.0	33.6	6:59:54	1:54	NP
1249	GDS	38.32	S22	265- 8: 1:53	56.3	49.9	8:35:40	37:40	
1249	UKO	38.22	S22	265- 8: 1:53	53.7	59.9	8:17:40	19:40	NP BY JPL
1252	SNF	322.97	S22	265-13: 4:10	43.9	55.3	13:16:56	21:56	
1253	MIL	297.85	S22	265-14:44:56	15.3	39.9	14:49:12	57:12	
1254	MIL	272.74	S22	265-16:25:42	13.6	39.9	16:29:28	34: 5	
1254	GDS	272.74	S22	265-16:25:42	27.8	44.6	16:33:40	38:40	
1255	GDS	247.62	S22	265-18: 6:28	40.6	50.4	18:18:13	21:13	
1258	UKO	172.27	S22	265-23: 8:45	59.9	53.2	23:41:30	43:30	
1259	UKO	147.16	S23	266- 0:49:30	62.3	56.5	1:21:16	23:10	
1261	SNF	96.92	S23	266- 4:11: 2	50.0	40.1	4:46:47	49:48	
1263	GDS	46.69	S23	266- 7:32:33	50.8	45.3	8: 8: 2	9:45	
1265	SNF	356.46	S23	266-10:54: 5	60.9	65.6	11:12:10	13:50	
1267	MIL	306.22	S23	266-14:15:36	27.1	40.6	14:23:21	27:21	
1267	ULA	306.22	S23	266-14:15:36	73.9	74.6	14:39:21	41:21	
1269	GDS	255.99	S23	266-17:37: 7	27.2	59.1	17:44:53	54:38	
1269	ULA	255.99	S23	266-17:37: 7	53.0	60.4	17:52:40	55: 0	
1275	SNF	105.29	S24	267- 3:41:42	46.6	36.6	4:18:30	21:30	
1279	ULA	4.83	S24	267-10:24:45	73.8	65.3	10:51:28	55:28	
1261	ULA	314.59	S24	267-13:46:16	73.9	74.6	14:10: 0	12: 0	
1281	MIL	289.48	S24	267-15:27: 2	18.6	41.7	15:32:15	39:18	NP
1283	GDS	264.36	S24	267-17: 7:47	27.0	47.1	17:15:31	22:31	
1284	ULA	239.25	S24	267-18:48:33	55.0	61.2	19: 4:46	6:46	
1287	UKO	165.90	S24	267-23:50:50	66.7	61.0	0:21: 3	23: 3	NF
1290	MIL	88.55	S25	268- 4:53: 7	48.9	42.3	5:29:12	31:12	ENG
1291	GDS	63.43	S25	268- 6:33:53	52.6	26.0	7: 8:50	16:50	
1292	ULA	38.31	S25	268- 8:14:39	65.0	49.8	8:45:29	50:28	
1296	MIL	297.85	S25	268-14:57:41	28.8	42.9	15: 5:55	9:51	
1296	ULA	297.85	S25	268-14:57:41	70.0	74.7	15:19:10	23:10	
1298	GDS	247.62	S25	268-18:19:13	38.0	51.2	18:30:13	34:13	
1299	ULA	222.50	S25	268-19:59:59	56.0	62.0	20:16:29	18:29	
1306	GDS	46.69	S26	269- 7:45:18	55.8	42.8	8:19:14	23:14	
1307	UKO	21.57	S26	269- 9:26: 4	51.2	63.6	9:41: 5	45: 5	
1310	ULA	306.22	S26	269-14:28:21	68.6	73.9	14:49:15	55: 0	
1311	ULA	281.10	S26	269-16: 9: 7	58.6	72.9	16:26:27	32: 6	
1312	GDS	255.99	S26	269-17:49:52	17.4	44.2	17:54:45	2:42	ENG-NP2:45S
1316	UKO	155.52	S26	270- 0:32:55	66.3	55.4	1: 3:17	7:17	NP BY JPL
1318	SNF	105.29	S27	270- 3:54:27	50.1	36.9	4:30:10	34:10	
1321	GDS	29.94	S27	270- 8:56:44	55.8	43.1	9:30:40	34:35	
1322	ULA	4.82	S27	270-10:37:30	74.5	66.6	11: 3:44	7:44	
1324	SNF	314.59	S27	270-13:59: 1	37.2	43.8	14: 9:45	11:45	
1325	MIL	289.47	S27	270-15:39:46	20.2	33.7	15:45:28	49:28	
1327	GDS	239.24	S27	270-19: 1:18	33.6	46.8	19:10:57	14:57	

Table C-1 (contd)

REV	STA	NODE	DAT	JLN NODE TIM	LTON	LOFF	TIME ON	OFF	COMMENTS
1333	MIL	88.54	S28	271- 5: 5:52	50.2	43.8	5:41:33	43:30	
1334	GDS	65.43	S28	271- 6:46:38	53.0	26.2	7:21:26	29:22	ENG-NP3:00S
1335	ULA	38.31	S28	271- 8:27:24	65.2	48.5	8:58:10	3:37	
1339	ULA	297.85	S28	271-15:10:26	72.0	74.5	15:32:53	34:53	
1339	MIL	297.85	S28	271-15:10:26	28.4	41.8	15:18:34	22:54	
1340	GDS	272.73	S28	271-16:51:12	29.8	43.1	16:59:43	3:43	
1341	GDS	247.61	S28	271-18:31:57	38.6	51.7	18:43: 6	47: 6	
1344	UKO	172.26	S28	271-23:34:15	58.7	52.3	0: 7:16	9:16	NP BY JPL
1349	GDS	46.68	S29	272- 7:58: 3	55.9	42.6	8:31:58	35:58	
1352	SNF	331.33	S29	272-13: 0:20	45.9	61.8	13:13:42	18:42	
1353	ULA	306.22	S29	272-14:41: 6	73.8	72.4	15: 4:45	8:45	
1354	ULA	281.10	S29	272-16:21:51	58.5	72.9	16:39:10	44:49	NP
1355	GDS	255.99	S29	272-18: 2:37	26.5	43.3	18:10:11	15:11	
1359	UKO	155.52	S30	273- 0:45:40	67.0	55.6	1:15:45	19:45	
1360	SNF	130.40	S30	273- 2:26:25	48.7	35.4	3: 2:35	6:35	
1361	SNF	105.29	S30	273- 4: 7:11	52.4	36.2	4:42:30	47: 7	NP
1364	GDS	29.94	S30	273- 9: 9:28	56.0	43.4	9:43:20	47:13	
1365	ULA	4.82	S30	273-10:50:14	74.3	72.4	11:16:27	20:27	
1367	SNF	314.59	S30	273-14:11:45	37.1	43.8	14:22:26	24:28	
1368	MIL	289.47	S30	273-15:52:31	20.1	33.6	15:58:11	2:11	
1370	GDS	239.24	S30	273-19:14: 2	53.6	46.8	19:23:41	27:41	
1376	MIL	88.54	O 1	274- 5:18:36	49.1	42.6	5:54:37	56:37	NP
1377	GDS	65.43	O 1	274- 6:59:22	43.8	30.4	7:37: 1	41: 1	
1378	GDS	38.31	O 1	274- 8:40: 8	56.2	43.5	9:13:57	17:54	
1378	ULA	38.31	O 1	274- 8:40: 8	59.0	49.2	9:13: 0	16: 8	
1382	ULA	297.84	O 1	274-15:23:10	72.0	74.5	15:45:36	47:36	
1383	GDS	272.73	O 1	274-17: 3:56	31.8	43.0	17:13: 5	16:25	
1384	GDS	247.61	O 1	274-18:44:41	38.0	51.2	18:55:40	59:40	
1385	ULA	222.50	O 1	274-20:25:27	55.9	62.0	20:41:55	43:55	
1387	UKO	172.26	O 1	274-23:46:58	58.6	52.3	0:19:59	21:59	
1391	GDS	71.80	O 2	275- 6:30: 1	39.6	26.1	7: 8:57	12:57	
1395	ULA	331.33	O 2	275-13:13: 4	72.8	58.1	13:36: 2	46:15	
1395	SNF	331.33	O 2	275-13:13: 4	31.6	66.1	13:22: 4	33: 0	
1396	ULA	306.22	O 2	275-14:53:49	68.1	69.4	15:14:31	22:56	
1397	ULA	281.10	O 2	275-16:34:35	57.8	74.3	16:51:40	1: 0	NP3:20S
1397	MIL	281.10	O 2	275-16:34:35	10.2	23.7	16:37:20	41:20	
1398	GDS	255.99	O 2	275-18:15:21	17.6	44.4	18:20:17	27:25	ENG
1403	SNF	130.40	O 3	276- 2:39: 9	51.2	31.6	3:14:32	20:32	
1404	SNF	105.29	O 3	276- 4:19:55	57.0	44.0	4:53:27	57: 3	NP
1404	MIL	105.29	O 3	276- 4:19:55	44.8	22.4	4:57:15	3:57	
1404	MIL	105.29	O 3	276- 4:19:55	27.3	7.2	5: 2:30	8:26	NP
1406	GDS	55.06	O 3	276- 7:41:26	48.4	35.2	8:17:40	21:40	
1408	ULA	4.82	O 3	276-11: 2:57	74.6	63.5	11:28:36	34:20	
1409	ULA	339.71	O 3	276-12:43:43	73.6	66.5	13: 7:15	13:13	
1411	MIL	289.47	O 3	276-16: 5:14	17.9	37.7	16:10: 6	16: 8	
1412	GDS	264.36	O 3	276-17:46: 0	27.1	47.8	17:53:56	59:56	NP
1419	MIL	88.54	O 4	277- 5:31:20	48.8	29.1	6: 7:28	13:22	
1420	GDS	65.43	O 4	277- 7:12: 5	52.3	29.2	7:47: 7	54: 5	ENG-NP3:00S
1421	ULA	38.31	O 4	277- 8:52:51	65.2	49.7	9:23:36	28:41	NP
1425	ULA	297.85	O 4	277-15:35:53	65.8	71.7	15:55:43	3:57	
1425	MIL	297.85	O 4	277-15:35:53	18.8	39.3	15:41:10	47:10	ENG
1426	GDS	272.73	O 4	277-17:16:39	27.0	47.1	17:24:23	30:23	NP2:00SE
1428	ULA	222.50	O 4	277-20:38:11	50.2	68.0	20:52:52	58:52	
1430	UKO	172.27	O 4	277-23:59:42	63.9	45.2	0:30:56	36:56	

Table C-1 (contd)

REV	STA	NODE	DAT	JLN NODE TIM	LTON	LOFF	TIME ON	OFF	COMMENTS
1434	GDS	71.80	0 5	278- 6:42:44	38.0	26.4	7:22: 7	25:35	
1438	ULA	331.34	0 5	278-13:25:47	73.0	58.0	13:48:50	59: 0	
1438	SNF	331.34	0 5	278-13:25:47	31.6	67.1	13:34:47	46: 6	
1439	ULA	306.22	0 5	278-15: 6:33	68.0	69.5	15:27:13	35:38	
1440	ULA	281.10	0 5	278-16:47:18	57.7	74.3	17: 4:22	13:34	
1440	MIL	281.10	0 5	278-16:47:18	10.8	23.7	16:50:15	54: 1	
1441	GDS	255.99	0 5	278-18:28: 4	17.6	45.0	18:33: 0	41: 9	ENG
1446	SNF	130.41	0 6	279- 2:51:52	51.3	31.4	3:27:13	33:13	
1447	SNF	105.29	0 6	279- 4:32:38	57.2	41.4	5: 6: 8	11: 0	NP
1447	MIL	105.29	0 6	279- 4:32:57	44.3	15.3	5:10: 0	18:45	
1447	MIL	105.29	0 6	279- 4:32:57	17.0	7.2	5:18:30	21: 8	NP
1449	GDS	55.06	0 6	279- 7:54: 9	48.6	35.3	8:30:21	34:21	
1451	ULA	4.83	0 6	279-11:15:41	74.5	60.5	11:41:40	47: 5	NP3:00E
1452	ULA	339.71	0 6	279-12:56:26	73.8	71.0	13:20: 6	25:50	
1454	ULA	289.48	0 6	279-16:17:57	68.9	71.0	16:39: 1	45: 1	
1455	GDS	264.36	C 6	279-17:58:43	27.6	47.5	18: 6:37	12:37	NP
1462	MIL	88.55	0 7	280- 5:44: 3	48.8	29.2	6:20:10	26: 3	NP3:47S
1463	GDS	63.43	0 7	280- 7:24:48	52.3	22.4	7:59:50	8:53	
1464	ULA	38.32	0 7	280- 9: 5:34	65.3	49.8	9:36:18	41:23	NP
1468	ULA	297.85	0 7	280-15:48:36	65.6	71.7	16: 8:25	16:39	
1468	MIL	297.85	0 7	280-15:48:36	22.1	42.2	15:54:51	0:51	ENG
1469	GDS	272.74	0 7	280-17:29:22	27.0	47.0	17:37: 4	43: 4	NP2:00SE
1471	ULA	222.50	0 7	280-20:50:53	50.1	68.1	21: 5:33	11:33	
1473	UKO	172.27	0 6	281- 0:12:25	64.1	46.4	0:43:37	48:40	
1481	ULA	331.34	0 8	281-13:38:30	72.9	58.2	14: 1:30	11:40	
1482	ULA	306.23	0 8	281-15:19:15	68.6	64.3	15:40:10	48:20	
1483	ULA	281.11	0 8	281-17: 0: 1	59.8	74.3	17:17: 4	26:16	NP6:26E
1483	MIL	281.11	0 8	281-17: 0: 1	10.7	23.5	17: 2:55	6:42	
1484	GDS	256.00	0 8	281-18:40:47	12.6	55.0	18:45:42	57: 2	
1489	SNF	130.41	0 9	282- 3: 4:35	44.3	38.2	3:42: 4	43:56	
1490	SNF	105.30	0 9	282- 4:45:20	65.3	43.7	5:16: 5	23: 0	NP2:00E
1490	MIL	105.30	0 9	282- 4:45:20	45.4	14.4	5:22:48	31:42	
1490	MIL	105.30	0 9	282- 4:45:20	17.0	7.0	5:30:58	33:54	
1492	GDS	55.06	0 9	282- 8: 6:52	54.6	38.2	8:41:12	46:12	
1493	UKO	29.95	0 9	282- 9:47:38	49.2	55.6	10: 2: 1	4: 1	
1494	ULA	4.83	0 9	282-11:28:23	74.0	53.9	11:54:55	2:55	
1496	ULA	314.60	0 9	282-14:49:54	70.8	65.2	15:11:46	20:39	
1497	MIL	289.48	0 9	282-16:30:40	25.1	31.3	16:37:48	39:39	
1498	GDS	264.37	0 9	282-18:11:26	34.8	41.8	18:21:27	23:27	NP
1499	ULA	239.25	0 9	282-19:52:11	52.0	70.6	20: 7:27	13:57	
1502	UKO	163.90	010	283- 0:54:28	67.8	55.0	1:24:14	29:40	

Table C-2. Spacecraft travel time from the equator to image latitude

LAT	TA	TD	LAT	TA	TD
1	00:03	50:20	41	11:53	38:29
2	00:20	50:02	42	12:11	38:11
3	00:38	49:44	43	12:29	37:53
4	00:56	49:27	44	12:48	37:35
5	01:13	49:09	45	13:06	37:17
6	01:31	48:51	46	13:24	36:58
7	01:49	48:34	47	13:42	36:40
8	02:06	48:16	48	14:01	36:22
9	02:24	47:58	49	14:19	36:03
10	02:42	47:41	50	14:38	35:45
11	02:59	47:23	51	14:56	35:26
12	03:17	47:05	52	15:15	35:07
13	03:35	46:48	53	15:34	34:49
14	03:52	46:30	54	15:53	34:30
15	04:10	46:12	55	16:12	34:11
16	04:28	45:55	56	16:31	33:52
17	04:45	45:37	57	16:50	33:32
18	05:03	45:19	58	17:10	33:13
19	05:21	45:02	59	17:29	32:53
20	05:38	44:44	60	17:49	32:34
21	05:56	44:26	61	18:09	32:13
22	06:14	44:09	62	18:29	31:53
23	06:32	43:51	63	18:50	31:33
24	06:49	43:33	64	19:11	31:12
25	07:07	43:15	65	19:32	30:50
26	07:25	42:58	66	19:54	30:28
27	07:43	42:40	67	20:17	30:06
28	08:00	42:22	68	20:40	29:42
29	08:18	42:04	69	21:05	29:18
30	08:36	41:47	70	21:30	28:52
31	08:54	41:29	71	21:58	28:25
32	09:12	41:11	72	22:28	27:54
33	09:29	40:53	73	23:04	27:19
34	09:47	40:35	74	23:50	26:33
35	10:05	40:17	74.4	24:18	26:08
36	10:23	39:59	74.7	24:58	25:28
37	10:41	39:41			
38	10:59	39:24			
39	11:17	39:06			
40	11:35	38:47			

C.3 Digitally Processed SAR Images

Table C-3 lists, by revolution number, the SAR images that have been digitally processed by JPL up to October 1, 1981. Each image is 100 kilometers by 100 kilometers in area and has a nominal ground resolution of 25 meters in both range and azimuth (Wu, 1980). All processed digital imagery is available through the Environmental Data and Information Service (EDIS) of NOAA (see Section C.4 for address). Items listed include:

REV	revolution number
STA	receiving station acronym (see Appendix A)
LOCATION	site name, and state or country
LAT	north latitude in degrees for nominal center of image
LON	west longitude in degrees for nominal center of image
TIME	Julian day of 1978 followed by time (hour:minute: second) of center of image

Table C-4 lists, by revolution number and latitude, the digital SAR images processed in Europe up to August 1981. All processed imagery, available through ESRIN in Italy (see Section C-4 for address), have full 25-meter resolution and are 40 kilometers by 40 kilometers in size. Items listed include:

REV	revolution number
STA	receiving station acronym (see Appendix A)
DATE	month and day, 1978
LOCATION	site name and country
LAT	north latitude in degrees for center of image
LON	east or west longitude in degrees for center of image
ARCH	archive number
*	image slightly defocussed
**	larger scene 40 kilometers in azimuth and 50 kilometers in range

Table C-3. Digital images processed by JPL up to October 1, 1981

REV	STA	LOCATION	LAT		LON		TIME
107	ULA	PRINCE OF WALES IS	55	35	132	45	185-12:17:25
107	CDS	CA KERN COUNTY 1	35	7	119	6	185-12:11:10
107	CDS	CA POINT LOMA	32	5	117	5	185-12:10:19
107	CDS	CA MEDICINE LAKE	41	20	121	30	185-12:12:59
205	ULA	CAN BEAU SEA VIC I	73	32	114	15	192- 8:45:50
207	CDS	NM C MESA PRIETA	35	31	107	1	192-11:54: 9
207	CDS	NM ALBUQUERQUE	34	50	106	30	192-15:53:56
207	CDS	SW COLORADO	38	30	108	20	192-11:55: 2
207	CDC	MONTANA DILLON	45	13	112	38	192-11:57: 5
207	CDS	MONTANA ANACONDA	45	56	113	14	192-11:57:18
221	ULA	CAN FT STMPSON NWT	61	57	120	16	193-11:31: 9
221	MIL	OK CHICKASHA 2	35	0	98	0	193-11:22:46
221	MIL	KS COLBY 1	39	20	100	50	193-11:24:13
221	ULA	CAN MACKENZIE R.	68	59	135	25	193-11:33:45
230	CDS	CA STR. OF 2 B. C.	49	0	123	0	194- 2:54:29
232	ULA	AK KUSKOKWIM R.	60	0	162	30	194- 6:12:20
236	CDS	CA STR. OF 3 B. C.	49	0	123	0	194-12:36:27
242	MIL	BLAKE ESCARPMENT	32	30	73	0	194-23: 7: 4
251	CDS	HURRICANE FICO 3	18	50	122	52	195-13:36:51
251	CDS	HURRICANE FICO 1	16	46	122	2	195-13:36:15
251	CDS	HURRICANE FICO 2	17	48	122	27	195-13:36:33
263	MIL	NY NYC	40	30	74	15	196- 9:50:51
289	ULA	AK ANCHORAGE	61	13	150	25	198- 5:47:46
289	ULA	AK DELTA II	63	50	146	0	198- 5:46:48
289	ULA	AK KATMAI	58	25	154	15	198- 5:48:39
308	CDS	CA SAN NICHOLAS IS	33	45	119	20	199-13:17: 6
308	CDS	PAC OCEAN COASEX	30	18	117	40	199-13:16: 5
308	CDS	CA SUTTER'S BUTTE	39	13	121	50	199-13:18:45
308	SDS	CA SANTA BARBARA 1	34	10	119	36	199-13:17:17
322	CDS	AZ SAFFORD 1	32	50	109	40	200-12:45:35
322	ULA	AK DEASE INLET	70	48	156	25	200-12:58: 9
322	CDS	AZ GRAND CANYON 2	34	15	112	15	200-12:46:45
322	CDS	UT BLACK MTS. 1	38	10	112	50	200-12:47:14
322	CDS	UT SEVIER LAKE	38	55	113	10	200-12:47:27
335	MIL	DOM. REPUBLIC B	18	40	69	50	201-10:29:39
335	MIL	WV LOST RIVER	39	0	78	52	201-10:35:36
335	MIL	DOMIN REPUBLIC A	19	30	70	0	201-10:29:52
350	ULA	CAN LAC LA MARTE	63	17	118	15	202-11:52:48
351	CDS	CA GARLOCK FAULT	34	40	118	30	202-13:24:27
351	CDS	CA CINDER CONE	40	35	121	20	202-13:26:14
351	CDS	CA LOS ANGELES 1	34	0	118	20	202-13:24:18
351	CDS	CA LOS ANGELES 3	33	55	118	5	202-13:24:15
371	MIL	JAM PORT ANTONIO	18	2	76	32	203-23:32:25
371	MIL	CUBA MICARO MTS	20	20	75	30	203-23:31:43
378	MIL	VA PAMLICO/HALI. SW	35	20	76	0	204-10:41:38
378	MIL	VA WINCHESTER 2	39	20	78	8	204-10:42:49
378	MIL	PA BEDFORD	40	5	78	30	204-10:43: 3

Table C-3 (contd)

REV	STA	LOCATION	LAT		LON		TIME
378	MIL	VA FREDERICKSBURG2	38	7	77	24	204-10:42:25
380	ULA	AK RANGE GLACIER	62	56	150	50	204-14:11:32
380	ULA	AK KUSKOKWIM MTS.	64	5	151	50	204-14:11:55
393	MIL	MO CLINTON	38	15	93	45	205-11:51:55
393	MIL	MO GUILDFORD	40	9	94	52	205-11:52:30
393	MIL	LA MISS. DELTA 2	29	13	89	29	205-11:49:17
393	MIL	AR LITTLE ROCK	35	0	92	5	205-11:50:55
393	MIL	LA NEW ORLEANS 2	30	4	89	51	205-11:49:31
394	GDS	CA PANAMINT MTNS.	36	40	117	35	205-13:32: 7
407	MIL	IN KOKOMO	40	11	86	21	206-11:21:19
407	MIL	IN INDIANAPOLIS	39	51	85	56	206-11:21:12
416	GDS	CA LOS ANGELES 4	34	4	118	0	207- 2:55:57
422	MIL	TX TEMPLE	31	11	97	25	207-12:28: 3
447	ULA	N. ALASKA RANGE II	64	12	148	40	206- 6:46: 0
450	MIL	HAITI PORT-A-PIMEN	18	18	74	7	209-11:21:50
465	MIL	MX CALAKMUL	18	17	90	19	210-12:31:13
465	MIL	GUATEMALA TIKAL	17	13	89	38	210-12:30:55
465	MIL	TX HOUSTON	29	44	95	22	210-12:34:38
465	MIL	OK CHICKASHA 1	35	0	98	0	210-12:36:13
465	MIL	TX HONEY	33	32	96	50	210-12:35:47
472	MIL	PA ALTOONA	40	43	79	0	211- 0:49: 9
472	MIL	WV ALTA	37	52	80	33	211- 0:50: 1
472	MIL	PA EMPORIUM	41	30	78	22	211- 0:48:55
473	GDS	CO DENVER	39	30	105	0	211- 2:30:10
474	GDS	BC STR OF GEORGIA	49	15	123	17	211- 4: 7:50
474	GDS	BC JUAN DE FUCA 3	48	20	124	0	211- 4: 8: 3
480	GDS	CA STR. OF J. B. C.	48	54	122	54	211-13:49:50
480	GDS	WA SEATTLE 1	47	35	122	3	211-13:49:27
488	GDS	MT ELK RIVER	46	50	116	10	212- 3:37:18
493	MIL	SC KERSHAW COUNTY	34	20	80	35	212-11:33:36
493	MIL	WV BERNIE	38	11	82	1	212-11:34:45
502	GDS	UT SEVIER DESERT 2	39	0	112	28	213- 3: 8:30
502	GDS	UT BLACK MTS. II	38	13	112	50	213- 3: 8:43
502	GDS	WY EVANSTON 1	41	12	111	5	213- 3: 7:52
502	GDS	MT JORDAN	47	17	106	34	213- 3: 5:57
502	GDS	WY PINEDALE	45	55	110	0	213- 3: 7:19
502	GDS	CA ALGODONES DUNES	33	15	115	25	213- 3:10:14
508	MIL	OK TUSKAHOMA	34	25	95	45	213-12:43: 2
508	MIL	NICARAGUA	12	49	84	39	213-12:36:42
508	MIL	HONDURAS?	13	39	84	58	213-12:36:52
522	MIL	MINN TWIN CITIES	44	50	93	20	214-12:14:59
523	GDS	AZ SIERRITA	31	52	111	12	214-13:51:44
523	GDS	AZ HELVETIA 1	31	47	111	10	214-13:51:43
523	GDS	AZ SILVER BELL 1	32	30	111	40	214-13:51:54
523	GDS	AZ FOUR CORNERS	34	20	112	21	214-13:52:26
523	GDS	AZ PHOENIX	33	30	112	30	214-13:52:12
552	ULA	AK FAIRBANKS 1	64	40	147	15	216-14:40:12

Table C-3 (contd)

REV	STA	LOCATION	LAT		LON		TIME
552	GDS	CA SB CHANNEL 3	34	10	120	0	216-14:30:41
552	ULA	AK MALASPINA GLAC	60	15	140	0	216-14:38:41
552	ULA	AK UTUKOK RIVER	69	33	159	48	216-14:42: 6
552	ULA	AK DELTA	63	50	146	0	216-14:39:55
552	GDS	SACRAMENTO DELTA	38	12	121	51	216-14:31:48
552	ULA	AK YAKUTAT	59	24	139	7	216-14:38:21
552	GDS	CA SANTA BARB CH 1	34	10	120	0	216-14:30:36
558	MIL	VA FREDERICKSBURG	37	56	77	35	108- 1: 4: 1
558	MIL	VA FORT PICKETT	37	10	78	0	217- 1: 4:14
558	MIL	WASHINGTON, DC	38	55	76	55	217- 1: 3:39
559	GDS	NM CLAYTON 1	36	24	103	8	217- 2:45:15
565	MIL	IN PRINC.-EVANS.	38	20	87	40	217-12:19:58
565	MIL	KY POND R.	37	15	87	15	217-12:19:39
565	MIL	KY OWENSBORO	37	40	87	15	217-12:19:45
574	GDS	CA KETTLEMAN HILLS	36	0	120	0	218- 3:54:41
580	GDS	NM CLAYTON 2	36	24	103	8	218-13:28:52
580	GDS	CO DENVER	39	37	105	0	218-13:29:50
580	GDS	WY SHIRLEY MTS. 1	42	3	106	22	218-13:30:34
580	GDS	CO GRAND COUNTY	40	0	105	50	218-13:29:57
595	GDS	CA KERN COUNTY 2	35	7	119	6	219-14:37:54
595	GDS	CA KERN COUNTY 3	35	19	119	6	219-14:37:58
595	GDS	CA BUCK'S LAKE	39	53	121	11	219-14:39:20
595	GDS	OR HUMBOLDT	41	24	122	0	219-14:39:48
605	ULA	AK TAN./KANT. R.	64	44	150	35	220- 7:45: 4
605	ULA	AK KUSKOKWIM MTS.	64	11	151	57	220- 7:45:17
605	ULA	AK UNIMAK ISLAND	54	50	164	0	220- 7:48:23
608	MIL	FL OKEECHOBEE	27	23	80	50	220-12:23:46
608	MIL	W. IN. JAMAICA 1	18	2	77	5	220-12:21: 6
608	MIL	FL MIAMI	25	57	80	27	220-12:23:22
617	GDS	CA SANTA BARB 2	34	10	119	36	221- 4: 2:10
617	GDS	NV BEOWAWE	40	30	116	30	221- 4: 0:17
623	GDS	OK GUYMON	36	36	101	36	221-13:35:56
623	MIL	TX LLANO	30	45	98	45	221-13:34:11
623	GDS	MT MILK RIVER	49	0	110	20	221-13:39:41
631	GDS	TABLE MT SD	45	54	103	37	222- 3:27:30
631	GDS	AZ SILVER BELL 2	32	30	111	40	222- 3:31:25
631	GDS	WY SHIRLEY MTS. 1	42	3	106	22	222- 3:28:40
631	GDS	WY N POWDER R BAS	44	3	105	0	222- 3:28: 4
631	GDS	WY POWDER R. BAS S	43	18	105	26	222- 3:28:17
638	GDS	NV WALKER LAKE 2	39	0	119	0	222-14:46: 4
638	GDS	SAN BERNARDINO 1	34	5	117	15	222-14:44:40
651	MIL	GA THOMSON APPALAC	33	33	82	40	223-12:32:39
651	MIL	GA ALTAMAHA RIVER	31	30	81	45	223-12:32: 3
660	GDS	LOS ANGELES 2	33	50	118	10	224- 4: 9:15
681	GDS	WA MT ST HELEN	46	12	122	11	225-14:55:15
681	ULA	AK CRAZY MTS.	65	45	145	10	225-15: 1:40
681	GDS	CA KELBAKER	35	2	115	45	225-14:51:56

Table C-3 (contd)

REV	STA	LOCATION	LAT		LON		TIME
681	CDS	OR NEWBERRY	43	30	121	10	225-14:54:28
681	ULA	AK COLVILLE RIVER	69	15	154	20	225-15: 3: 0
691	ULA	AK FAIRBANKS 2	64	22	148	30	226- 7:59:17
694	MIL	KY SALYERSVILLE	37	45	83	5	226-12:40:53
694	MIL	LAKE MICHIGAN	44	0	87	0	226-12:42:47
695	CDS	NM MT. TAYLOR	35	20	107	20	226-14:20:50
719	UKO	ICELAND	65	0	16	45	228- 6:44:54
719	UKO	FRANCE ALPS 1	44	10	354	35	228- 6:38:14
719	UKO	SCOT GR GLEN FAULT	57	0	4	40	228- 6:42:12
719	UKO	FRANCE ALPS 2	45	5	355	10	228- 6:38:28
719	UKO	ENGLAND LONDON	51	34	359	44	228- 6:40:31
719	UKO	FRANCE PARIS	48	50	357	40	228- 6:39:39
723	MIL	IA AMES	42	20	93	18	228-13:20: 5
723	MIL	MO ST FRANCOIS MTS	37	30	90	30	228-13:18:38
724	CDS	BC STR OF GA 5	49	0	123	0	228-15: 2:42
737	MIL	HAITI PORT-A-PRINC	18	15	72	30	229-12:41:25
737	MIL	HAITI ISLE GONAVE	18	55	72	48	229-12:41:37
737	MIL	HAITI ST NICOLAS	19	40	73	8	229-12:41:50
738	CDS	TX COYANOSA 1	31	20	103	15	229-14:25:33
738	CDS	CO DEL NORTE	37	25	106	25	229-14:27:41
738	CDS	TX COYANOSA 2	31	20	103	15	229-14:25:31
738	CDS	MX OBALLOS	27	30	101	30	229-14:24:42
738	CDS	NM A	36	35	105	49	229-14:27:28
738	CDS	NM B	35	40	105	57	229-14:27:11
738	CDS	WY PARTICK'S DRAW	41	30	108	40	229-14:28:52
738	CDS	AZ NEW MEXICO 2	36	35	105	49	229-14:27:24
759	MIL	GUAT-SALVADOR II	13	45	90	0	231- 2:15:48
759	MIL	GUAT MONJAS	14	30	89	43	231- 2:15:35
759	MIL	SC KERSHAW 2	34	27	80	48	231- 2: 9:43
759	MIL	VA WINCHESTER	39	10	78	10	231- 2: 8:22
759	MIL	PA HARRISBURG 2	40	26	77	18	231- 2: 7:57
759	MIL	PA APPALACHIAN	41	10	77	0	231- 2: 7:44
759	MIL	GUAT AMATIGUE BAY	15	58	89	4	231- 2:15: 9
759	MIL	GUAT LAKE IZABEL	15	16	89	19	231- 2:15:22
761	CDS	WA SEATTLE 2	47	47	122	42	231- 5:26:51
761	CDS	OR/WA COLUMBIA R.	46	17	123	44	231- 5:27:20
762	UKO	N AT OC FAEROE BK	61	33	9	13	231- 6:49:17
762	UKO	SWITZERLAND GENEVA	46	27	353	50	231- 6:44:27
762	UKO	ENG CHANNEL	51	32	2	5	231- 6:46: 0
774	MIL	OK TULSA	36	20	95	56	232- 3:17:48
774	MIL	OK OOLAGAH LAKE 1	36	40	95	33	232- 3:17:39
781	ULA	AK NORTH SLOPE 1	70	30	148	0	232-14:43:36
781	CDS	WY COPPER MT. 1	43	20	107	55	232-14:34:21
781	ULA	AK N SLOPE 2	70	0	145	0	232-14:43:23
785	UKO	AT OC OROMONDE	36	46	11	24	232-21:44: 0
788	MIL	LA NEW ORLEANS 1	30	6	89	41	233- 2:47:39
788	MIL	KY LOUISVILLE	38	25	85	40	233- 2:45:13
788	MIL	KY BIG CLIFTY	37	30	86	10	233- 2:45:27

Table C-3 (contd)

REV	STA	LOCATION	LAT		LON		TIME
789	ODS	AZ MOHAWK 2	32	3	113	30	233- 4:27:19
789	ODS	WY BITTER CREEK	41	30	108	40	233- 4:24:48
789	ODS	AZ MOHAWK 3	32	10	114	0	233- 4:27:32
789	ODS	UT SAN RAFAEL	38	50	110	45	233- 3:57:28
791	UKO	ALGERIA CHOTT MELR	34	15	353	47	233- 7:17:31
791	UKO	ALGERIA BISKRA	34	58	354	9	233- 7:17:44
791	UKO	ALGERIA SETIF	35	41	354	30	233- 7:17:57
791	UKO	ALGERIA BEJAIA	36	25	354	54	233- 7:18:10
791	UKO	JASIN 1	59	0	12	30	233- 7:25: 2
791	UKO	NW IREL DRUMLIN FD	54	12	7	17	233- 7:23:29
795	MIL	LA ALEXANDRIA	31	25	92	30	233-13:58:50
795	MIL	OK OOLOGAH LAKE II	36	36	95	15	233-14: 0:26
795	MIL	OK MOODYS	36	3	94	56	233-14: 0:18
795	MIL	AR FORT SMITH	35	20	94	35	233-14: 0: 1
795	MIL	LA ACADIA 1	30	8	92	10	223-13:58:29
795	MIL	AR MENA	34	40	94	16	233-13:59:48
795	MIL	AR NASHVILLE	33	58	93	55	233-13:59:35
802	MIL	MD UPPER CHESAPEAK	39	15	76	20	234- 2:12:56
806	ULA	AK YUKON-TANANA R.	64	54	151	54	234- 8:47: 8
809	MIL	FL CYPRESS SWAMP	26	0	81	0	234-13:25:19
809	MIL	WI WISCONSIN RIVER	43	18	90	2	234-13:30:29
809	MIL	W. IN. JAMAICA 2	18	8	77	50	234-13:23: 0
809	MIL	JAM. MONTEGO BAY	18	21	77	50	234-13:23: 7
809	MIL	FL EVERGLADES	25	26	80	43	234-13:25: 8
810	ODS	UT TUSHA MTS.	38	25	112	10	234-15: 9:35
810	ODS	UT SEVIER DESERT 1	39	9	112	30	234-15: 9:48
810	ODS	NM SPRINGERVILLE	33	50	109	40	234-15: 8:11
838	MIL	MS VICKSBURG	32	20	91	14	236-14: 4:13
838	MIL	LA MISS DELTA 1	29	0	89	15	236-14: 3: 8
838	MIL	KANSAS CITY	39	8	94	37	236-14: 6:13
845	MIL	NC DUCK	34	11	75	56	237- 2:19: 2
853	ODS	UT SAN RAFAEL	39	15	110	40	237-15:15: 8
853	ODS	NM ST AUGUSTINE FL	33	50	108	0	237-15:13:35
853	ODS	NM BANDERA LAVA FL	34	30	108	0	237-15:13:45
853	ODS	UT COMB RIDGE	37	15	109	38	237-15:14:35
853	ODS	UT ORANGE CLIFFS 1	37	56	110	5	237-15:14:48
874	MIL	ONTARIO BOBCAYGEON	44	32	78	30	239- 2:55:24
874	MIL	KY HUNTINGTON	38	22	82	34	239- 2:57:22
874	MIL	IN ZEBULON	37	34	82	28	239- 2:57:30
874	MIL	NY HAM., ONT/BUF.	43	8	79	18	239- 2:55:50
880	MIL	MA NANTUCKET IS.	41	10	69	40	239-12:34:23
880	MIL	ATL OC COLD RING 3	37	6	67	30	239-12:33: 7
882	ODS	CA IMPERIAL VAL 1	33	0	115	30	239-15:53:27
882	ODS	CA PISGAH	34	50	116	40	239-15:54: 8
882	ODS	CA COLDSTONE	35	10	116	52	239-15:54: 2
888	MIL	MA MOOSEHEAD LAKE	45	35	69	25	240- 2:25:37
931	MIL	DE BAY I/WAVES A	38	49	73	28	243- 2:40: 3

Table C-3 (contd)

REV	STA	LOCATION	LAT		LON		TIME
931	MIL	DE BAY I/WAVES B	38	4	73	55	243- 2:40:17
931	MIL	DE BAY I/WAVES C	37	19	74	22	243- 2:40:31
974	MIL	NC CAPE HATTERAS	35	52	74	54	246- 2:53:20
974	MIL	NC CAPE HATTERAS 1	35	0	75	20	246- 2:53:33
1006	UKO	ATL OC N-JASIN 2	59	30	10	30	248- 8:15: 1
1049	UKO	ATL OC JASIN 3	59	30	10	30	251- 8:27:21
1126	ULA	AK CONTROLLER BAY	60	13	144	25	256-17:46: 5
1140	GDS	CA DEATH VALLEY	36	20	116	50	257-17: 9:20
1140	GDS	NV WALKER LAKE 1	38	20	118	10	257-17: 9:56
1140	GDS	MEX. SONORA DUNES	31	55	114	15	257-17: 7:57
1140	GDS	NV GOLDFIELD	37	40	117	15	257-17: 9:44
1140	GDS	CA ALGODONES	32	56	115	0	257-17: 8:17
1149	UKO	SHETLAND ISLAND	59	55	2	36	258- 8:23:25
1169	GDS	PAC OCEAN OCNOGPHR	48	40	132	53	259-17:55: 4
1183	GDS	ANGEL DE LA GUARDA	29	45	113	40	260-17:20: 9
1197	GDS	WY EVANSTON 2	41	20	111	5	261-16:54:11
1197	GDS	UT CANYONLANDS	38	13	109	32	261-16:53:17
1197	GDS	NM FARMINGTON	36	44	108	12	261-16:52:51
1197	GDS	UT UTE PEAK	37	30	108	52	261-16:53: 4
1204	MIL	MO ST FRANCOIS MTS	37	30	90	30	262- 5: 7: 9
1204	MIL	MO ST LOUIS	38	45	90	30	262- 5: 6:48
1211	MIL	GUAT LAKE AYARZA	14	20	89	55	262-16:16:53
1211	MIL	GUAT RIO SALINAS	0	0	0	0	262-16:17:18
1211	MIL	MEX RIO LACANTUM	16	23	90	49	262-16:17:30
1211	MIL	GUAT SALAMA	15	5	90	15	262-16:17: 6
1211	MIL	GUAT-SALVADOR 1	13	31	89	40	262-16:16:40
1231	SNF	GRAND BANKS EDDY	38	18	48	15	264- 2:27:22
1232	MIL	ATL OC WARM RING	38	7	73	16	264- 4: 8:19
1253	MIL	PUERTO RICO	18	15	66	30	265-14:50: 2
1253	MIL	PA LOCK HAVEN	41	4	77	56	265-14:56:51
1254	GDS	KS SUBLETTE 5	37	44	100	50	265-16:36:36
1267	MIL	ATL OC CLD RING 1	34	22	65	48	266-14:25:22
1267	MIL	ATL OC COLD RING 2	34	22	65	48	266-14:25:29
1267	MIL	BERMUDA	32	23	64	39	266-14:24:51
1269	GDS	BC JUAN DE FUCA 2	48	0	124	0	266-17:51:15
1269	GDS	BC JUAN DE FUCA 1	48	55	124	32	266-17:49: 1
1291	GDS	SAN BERNARDINO II	34	5	117	15	268- 7:14:26
1292	ULA	WILLOW LAKE	62	14	119	17	268- 8:46:31
1296	MIL	PA HARRISBURG 2	40	20	77	0	268-15: 9:20
1296	MIL	PA HARRISBURG 1	40	9	77	3	268-15: 9:20
1296	MIL	CHESAPEAKE BAY 2	37	50	75	52	268-15: 8:33
1296	MIL	CHESAPEAKE BAY 1	38	9	75	52	268-15: 6:21
1296	ULA	BEAUFORT SEA 4	72	30	127	0	268-15:20:20
1306	GDS	PAC OC OCLD 1306	48	43	125	19	269- 8:21:26
1318	SNF	HUDSON CANYON	39	46	72	30	270- 4:33:23
1339	MIL	ATL OCEAN DUCK-X	36	20	74	56	271-15:20:55
1339	ULA	BEAUFORT SEA 5	72	30	127	0	271-15:33: 5
1340	GDS	KS SUBLETTE 2	37	44	100	50	271-17: 2: 6

Table C-3 (contd)

REV	STA	LOCATION	LAT		LON		TIME
1382	ULA	BEAUFORT SEA 3	72	30	127	0	274-15:45:50
1382	ULA	BEAUFORT SEA 6	73	38	135	2	274-15:46:35
1383	GDS	KS SUBLETTE 1	37	44	100	50	274-17:14:52
1391	GDS	AZ HELVETIA 2	31	35	110	28	275- 7:11:20
1391	GDS	NM MAAR VOLCANOS	34	20	106	45	275- 7:10:29
1395	SNF	LABRADOR SEA	60	20	61	0	275-13:31: 0
1404	MIL	AT OC WARM RING 2B	37	2	74	6	276- 4:59:30
1404	MIL	WARM RING 2 A	37	50	73	43	276- 4:59:24
1406	GDS	CA MT. SHASTA LAKE	41	35	121	30	276- 8:19:45
1406	GDS	WA SPOKANE 1	47	36	117	38	276- 8:17:55
1409	ULA	BANKS ISLAND 1 CAN	0	0	0	0	276-13: 9:34
1425	ULA	BEAUFORT SEA 2	72	30	127	0	277-15:58:34
1426	GDS	KS SUBLETTE 3	37	44	100	50	277-17:27:34
1434	GDS	AZ SAFFORD 2	32	45	109	50	278- 7:23:42
1441	GDS	OR NEWBERRY 2	43	40	121	0	278-18:40:44
1441	GDS	CA IMPERIAL VAL. 2	33	0	115	30	278-18:37:29
1446	SNF	AT OC ROCKAWAY B	34	26	50	23	279- 3:32:22
1446	SNF	AT OC ROCKAWAY A	35	13	49	58	279- 3:32: 8
1447	MIL	MA BOSTON	42	42	71	5	279- 5:10:41
1449	GDS	WA SPOKANE 2	47	36	117	39	279- 8:30:38
1452	ULA	BANKS ISLAND 2 CAN	74	40	125	35	279-13:22:16
1463	GDS	CA LOS ANGELES 4	33	56	117	33	280- 8: 5:27
1468	MIL	WASHINGTON DC 2	39	5	77	0	280-15:59:54
1468	ULA	ZERO BEAUFORT SEA	73	20	135	48	280-16:12: 1
1468	MIL	VA CHESAPEAKE BAY3	37	0	76	0	280-15:59:20
1469	GDS	KS SUBLETTE 4	37	44	100	50	280-17:40:17
1490	SNF	GREENLAND GLACIERS	64	0	49	0	282- 5:16:33
1492	GDS	OR NEWBERRY 3	43	40	121	0	282- 8:44:38
1494	ULA	AK NENANA-TANANA R	64	18	149	6	282-11:59:28
1498	GDS	CO PARADOX BASIN	38	10	109	20	282-18:22:24

Table C-4. Digital images processed in Europe up to August 1981

REV	STA	DATE	LOCATION	LAT	LON	ARCH
757	UKO	Aug 18	Faroer	62.28	7.15W	907**
			Faroer	62.22	6.57W	902
			Faroer	62.14	6.51W	901
			Faroer	62.12	7.42W	906**
			Faroer	62.04	7.19W	905
			Faroer	61.58	6.52W	903
762	UKO	Aug 19	Sardegna/G. di Orosei	40.04	9.34E	2101**
			Sardegna/Tortoli	40.06	9.50E	2801**
			Sardenga/G. di Orosei	40.18	10.20E	2103**
			Sardegna/Orosei	40.28	9.37E	2114**
			Sardegna/Capo Comino	40.37	10.09E	2106**
			Olbia	40.48	09.24E	6701
			Olbia	40.56	09.19E	6704
			Corsica/Str. of Bonifacio	41.13	9.09E	2401**
			Corsica/G. de Porto	42.14	8.14E	1901**
			Sardegna, Corsica/Isola Caprera	41.22	9.42E	2403**
			Sardegna, Corsica/Porto Vecchio	41.31	8.58E	2404**
			Corsica/G. de Porto Vecchio	41.40	9.31E	2406**
			Corsica/G. de Porto	42.19	8.28E	1911**
			Corsica/Calvi	42.29	9.01E	1913**
			Mont Blanc/Annecy	45.44	5.54E	2001**
			Annecy	45.49	06.09E	2011
			Mont Blanc	45.59	6.44E	2003**
			Mont Blanc/Thonon	46.07	5.56E	2004**
			Geneva	46.09	6.16E	204
			Mont Blanc/Geneva	46.13	6.18E	2006**
			Mont Blanc/Thonon	46.17	6.31E	2016**
			Jura	46.18	5.54E	003*
			Geneve/Oyonnax	46.23	5.45E	0214**
			Jura	46.26	6.10E	002*
			Lake of Geneva	46.32	6.30E	001*
			Geneve/Lac de Joux	46.34	6.20E	0216**
			W. Flanders/Hazebrouck	50.39	2.26E	4501**
			W. Flanders/Kortrijk	50.50	3.04E	4503**
			W. Flanders/Dunkerque	50.57	2.11E	4504**
			W. Flanders/Oostende	51.08	2.49E	4506**
			Channel/E. Margate	51.19	1.53E	2501**
			Channel/N. Dunkerque	51.30	2.31E	2503**
			Channel/N. Margate	51.37	1.37E	2504**
			Channel/N. E. Margate	51.48	2.16E	2506**
			E. Anglia/R. Ouse	52.41	0.39E	4001**
			E. Anglia/Cromer	52.53	1.19E	4003**
			E. Anglia/The Wash	52.59	0.23E	4004**
			E. Anglia/The Wash	53.11	1.02E	4006**
			Dundee/Firth of Forth	56.07	2.45W	3901**
			Dundee/Firth of Forth	56.20	2.03W	3903**
			Dundee/Tay	56.25	3.05W	3904
			Dundee/Dundee	56.31	2.42W	3905
			Dundee/Arbroath	56.37	2.22W	3906
			JASIN	59.58	7.10W	501
			JASIN	59.50	7.30W	503

Table C-4 (contd)

REV	STA	DATE	LOCATION	LAT	LON	ARCH
762 (contd)			JASIN	59.57	7.26W	0513
			JASIN	60.05	7.03W	0512
			JASIN	60.06	6.45W	502**
			JASIN	60.12	6.41W	0523**
785	UKO	Aug 20	Sweden/Stora Lulevatten	67.03	19.30E	7503
			Sweden/Björkholmen	66.49	18.54E	7506
			Sweden/Muddus Park	66.46	20.19E	7501
			Sweden/Lovos	66.36	18.37E	7203
			Sweden/Jokkmokk	66.31	19.44E	7504
			Sweden/Rappen	66.21	18.03E	7206
			Sweden/Pärl ävl	66.21	19.19E	7201
			Sweden/Forsnäs	66.06	18.45E	7204
			Sweden/Hornavan	66.05	17.28E	7303
			Sweden/Storyindeln	65.49	16.54E	7306
			Sweden/Storavan	65.47	18.17E	7301
			Sweden/Forgberg	65.36	16.25E	7403
			Sweden/Sorsele	65.32	17.44E	7304
			Sweden/Gardikfors	65.20	15.53E	7406
			Sweden/Blattnicksele	65.19	17.15E	7401
			Sweden/Storuman	65.04	16.43E	7404
			UK/Cape Spurn	53.58	00.28E	6903
			UK/Cape Spurn	53.45	01.07E	6901
			UK/Cape Spurn	53.39	00.10E	6906
			UK/Cape Spurn	53.27	00.50E	6904
			UK/Grimsby	53.24	00.03W	7003
			UK/Mablethorpe	53.13	00.37E	7001
			UK/Horncastle	53.07	00.15W	7006
			UK/The Wash	52.56	00.20E	7004
			England/Oxford	51.49	01.25W	7103
			England/Slough	51.37	00.46W	7101
			England/Swindon	51.31	01.41W	7106
			England/Reading	51.21	01.00W	7104
			UK/Salisbury	51.12	01.57W	8303
			UK/Southampton	51.01	01.18W	8301
			UK/The Stour	50.54	02.12W	8306
			UK/The Solent	50.43	01.33W	8304
			UK/Weymouth	50.39	02.25W	8203
			UK/Durlston Head	50.28	01.46W	8201
			Channel	50.21	02.40W	8206
			Channel	50.10	02.01W	8204
			Bretagne/Sept Isles	49.01	03.43W	6403
			Bretagne/Paimpol	48.51	03.06W	6401
			Bretagne/Roscoff	48.47	03.54W	6406
			Bretagne/Guingamp	48.36	03.17W	6404
			France/Brest	48.20	04.15W	7803
			France/Mont. noires	48.09	03.38W	7801
			France/Pte du Raz	48.02	04.28W	7806
			France/Audierne	47.56	04.33W	7703
			France/Quimper	47.51	03.52W	7804
			France/Concarneau	47.46	03.56W	7701

Table C-4 (contd)

REV	STA	DATE	LOCATION	LAT	LON	ARCH
785 (contd)			France/Atlantic	47.37	04.44W	7706
			France/Atlantic	47.27	04.10W	7704
			Atlantic	46.36	05.28W	7603
			Atlantic	46.26	04.52W	7601
			Atlantic	46.18	05.41W	7606
			Atlantic	46.07	05.05W	7604
			Portugal/Barcelos	41.35	08.44W	8403
			Portugal/Guimaraes	41.26	08.14W	8401
			Portugal/Povoa	41.16	08.55W	8406
			Portugal/Porto	41.06	08.22W	8404
			Portugal/Atlantic	41.00	09.05W	8103
			Portugal/Ovar	40.50	08.32W	8101
			Portugal/Atlantic	40.41	09.17W	8106
			Portugal/Aveiro	40.32	08.44W	8104
			Portugal/Atlantic	40.24	09.27W	8003
			Portugal/Figueira	40.15	08.54W	8001
			Portugal/Atlantic	40.07	09.37W	8006
			Portugal/Vieira	39.58	09.04W	8004
791	UKO	Aug 21	Algeria	35.28	5.20E	018
			Algeria	35.38	5.45E	027
			Algeria	35.47	5.10E	026
			Algeria	35.54	5.36E	023
			Barcelona West	41.23	1.58E	1601
			Barcelona	41.27	2.16E	1602
			Barcelona/Mataro	41.31	2.32E	1603**
			Barcelona/Manresa	41.41	1.47E	1604
			Barcelona/Manresa	41.46	2.04E	1605
			Barcelona/Vich	41.51	2.20E	1606**
			France/Blaye	45.11	00.26W	6601
			France/Emb. Gironde	45.30	00.39W	6604
			Royan	45.46	0.51W	1401
			Saintes	45.52	0.32W	1402
			St. Jean d'Angély	45.56	0.15W	1403**
			St. Jean d'Angély	45.56	0.15W	1413
			La Rochelle	46.05	1.04W	1404
			Surgères	46.10	0.45W	1405
			Niort	46.15	0.28W	1406**
			France/Pertuis Breton	46.19	1.14W	2701**
			France/Fontenay	46.29	0.38W	2703**
			France/La Roche	46.36	1.26W	2704**
			Nantes	47.03	1.42W	3401**
			Nantes/Loire	47.13	1.09W	3403**
			Nantes/St. Nazaire	47.21	1.56W	3404**
			France/St. Nazaire	47.27	1.59W	3301**
			Nantes/Erdre	47.32	1.20W	3406
			France/Redon	47.44	2.13W	3304**
			Bretagne/St. Brieuc	48.31	2.48W	1701
			Bretagne/Baie de St. Brieuc	48.36	2.29W	1702
			Bretagne/St. Malo	48.41	2.12W	1703**
			Bretagne/Tréguier	48.49	3.02W	1704

Table C-4 (contd)

REV	STA	DATE	LOCATION	LAT	LON	ARCH
791 (contd)			Bretagne/Pte de Plouézec	48.55	2.44W	1715
			Bretagne/G. de St. Malo	48.59	2.25W	1706**
			Ireland/Cahore Pt	52.32	6.10W	4101**
			Ireland/Irish Sea	52.44	5.31W	4103**
			Ireland/Wicklow	53.02	5.47W	4106**
			Dublin/Kildare	53.08	6.42W	3601**
			Dublin	53.20	6.03W	3603**
			Dublin/Edenderry	53.26	6.59W	3604**
			Dublin/Drogheda	53.37	6.19W	3606**
			Dundalk/Cavan	53.40	7.13W	3501**
			Dundalk	53.52	6.33W	3503**
			Dundalk/Longford	53.57	7.30W	3504
			Dundalk/Monaghan	54.09	6.50W	3506**
			Donegal/Fermanagh	54.19	7.46W	3801**
			Donegal/Tyrone	54.30	7.09W	3803**
			Donegal/Donegal	54.36	8.04W	3804**
			Donegal/Strabane	54.48	7.24W	3806**
			Irish N. Coast/Gweebarra	54.52	8.19W	2601**
			Irish N. Coast/L. Swilly	55.03	7.39W	2603**
			Irish N. Coast/Bloody Foreland	55.09	8.37W	2604**
			Irish N. Coast/Sheep Haven	55.21	7.56W	2606**
			JASIN	59.08	11.50W	701
834	UKO	Aug 24	Cherbourg/Carantan	49.22	1.30W	4201**
			Cherbourg/B. de la Seine	49.33	0.53W	4203**
			Cherbourg/Cherbourg	49.40	1.44W	4204**
			Cherbourg/B. de la Seine	49.51	1.07W	4206**
			Channel/N. Cherbourg	49.54	1.56W	3001**
			Channel/N. E. Cherbourg	50.06	1.19W	3003**
			Channel/S. W. Wight	50.13	2.11W	3004**
			Channel/S. Wight	50.24	1.33W	3006**
			Bournemouth/Weymouth	50.29	2.25W	4601**
			Bournemouth/Bournemouth	50.41	1.47W	4603**
			JASIN	59.08	11.00W	1101
			Iceland/Medallandsbugur	63.31	17.40W	6101
			Iceland/Skeidarasandur	63.46	16.54W	6103
			Iceland/Landbrot	63.47	18.10W	6104
			Iceland/Skeidararjökull	64.03	17.23W	6106
			Iceland/Langjökull	64.50	20.09W	6201
			Iceland/Audkuluheidi	65.05	20.40W	6204
			Iceland/Audkuluheidi	65.07	19.23W	6203
			Iceland/Hrutafjördhur	65.19	21.08W	6301
			Iceland/Audkuluheidi	65.22	19.53W	6206
			Iceland/Fjardharhorn	65.33	21.38W	6304
			Iceland/Thingeyrar	65.49	20.49W	6306
			Iceland/Hunafloi	65.35	20.21W	6303
891	UKO	Aug 28	Bonn	50.40	7.07E	1011**
			Bonn	50.41	7.10E	051
			Bonn/Koeln	50.51	7.07E	108
			East of Bonn	50.51	7.45E	1012**

Table C-4 (contd)

REV	STA	DATE	LOCATION	LAT	LON	ARCH
891 (contd)			East of Bonn	50.51	7.41E	004
			Koeln	50.57	6.56E	003
			Koeln	50.58	6.51E	1013**
			Gummersbach	51.07	7.28E	006
			Gummersbach	51.10	7.29E	1014**
			Duesseldorf	51.14	6.38E	1015**
			Duesseldorf	51.15	6.41E	109
			Wuppertal	51.26	7.16E	112
			Wuppertal	51.26	7.16E	1016**
957	UKO	Sep 1	North Sea	51.37	02.00E	5403
			N. Sea/N. W. Ostend	51.25	02.39E	5401
			N. Sea/Goodwin Sands	51.19	01.45E	5406
			N. Sea/Dunkerque	51.08	02.24E	5404
			Strait of Dover	51.03	01.32E	5503
			France/St. Omer	50.52	02.10E	5501
			France/Boulogne	50.45	01.17E	5506
			France/La Canche	50.34	01.55E	5504
963	UKO	Sep 2	Channel	50.25	00.53W	5201
			Channel	50.36	00.15W	5203
			Isle of Wight	50.42	01.07W	5204
			England/Worthing	50.53	00.29W	5206
			England/Denbigh	53.11	03.21W	5301
			England/Liverpool	53.24	02.42W	5303
			UK/Colwyn Bay	53.30	03.39W	5304
			UK/Southport	53.41	02.57W	5306
			Irish Sea	53.45	03.54W	6801
			UK/Morecambe Bay	53.57	03.13W	6803
			Irish Sea	54.03	04.11W	6804
			UK/Barrow	54.15	03.30W	6806
1044	UKO	Sep 8	Atlantic	62.03	09.57W	8901
			JASIN	59.48	13.51W	1502
			JASIN	59.40	13.27W	1501
			JASIN	59.31	14.13W	1505
1149	UKO	Sep 15	Mediterranean	36.54	16.38E	8501
			Mediterranean	37.02	17.07E	8503
			Mediterranean	37.12	16.28E	8514
			Mediterranean	37.22	16.59E	8506
			Mediterranean	37.25	16.21E	8601
			Mediterranean	37.34	16.52E	8603
			Mediterranean	37.44	16.10E	8604
			Mediterranean	37.53	16.42E	8606
			Calabria/C. Spartivento	38.02	16.00E	2201**
			Calabria/Siderno	38.12	16.32E	2203**
			Calabria/C. di Gioia	38.20	15.50E	2204**
			Calabria/Monasterace	38.30	16.21E	2206**
			Italy/Scalea	39.22	15.14E	8701
			Italy/Belv. Mar.	39.31	15.46E	8703
			Italy/Scalea	39.41	15.03E	8704

Table C-4 (contd)

REV	STA	DATE	LOCATION	LAT	LON	ARCH
1149 (contd)			Italy/Scalea	39.50	15.35E	8706
			G. di Salerno/S. Licosa pt.	40.00	14.52E	2901**
			G. di Salerno/Mt. Cervati	40.12	15.22E	2903**
			G. di Salerno/Licosa pt.	40.15	14.43E	2904**
			G. di Salerno/F. Sele	40.28	15.13E	2906**
			Fair Isle	59.37	1.45W	404
			Shetland	59.50	1.25W	401
			South of Foula	59.58	2.00W	403
			S. W. Foula	60.03	2.32W	2304**
			Shetland	60.04	1.30W	402
			Shetland	60.18	1.46W	2306**
			Atlantic	62.12	05.44W	9301
			Atlantic	62.27	04.57W	9303
			Faroer	62.28	06.11W	9304
			Norwegian Sea	62.44	05.33W	9306
			Bakkafloi	66.15	13.28W	9601
			Bakkafloi	66.29	14.03W	9604
			Bakkafloi	66.33	12.38W	9603
			Bakkafloi	66.47	13.12W	9606
1249	UKO	Sep 22	Denmark/Vordingborg	54.57	11.54E	4801
			Denmark/Fakse Bay	55.10	12.35E	4803
			Denmark/Naestved	55.15	11.36E	4804
			Denmark/Köge	55.28	12.17E	4806
			N-Sjaelland/Slagelse	55.30	11.19E	4701**
			N-Sjaelland/Roskilde	55.43	12.01E	4703**
			Denmark/Samsö Belt	55.48	11.00E	4704
			Denmark/Isefjord	56.01	11.42E	4706
			Arhus bugt	56.03	10.44E	1301
			Kattegatt	56.10	11.06E	1302
			Kalø Vig	56.21	10.25E	1303
			Grena	56.28	10.47E	1305
			Kattegat	56.34	11.07E	1306
1307	UKO	Sep 26	UK/Isle of Man	54.16	04.13W	9401
			UK/Whitehaven	54.28	03.32W	9403
			UK/Burrow Head	54.35	04.27W	9404
			UK/Solway Firth	54.46	03.49W	9406
			UK/Arran	55.22	05.15W	9001
			UK/Prestwick	55.34	04.34W	9003
			UK/Kintyre	55.39	05.34W	9004
			UK/Firth of Clyde	55.52	04.52W	9006
1316	UKO	Sep 27	N. Atlantic	61.46	01.59W	8801
			N. Atlantic	61.45	03.12W	8806
			N. Atlantic	61.30	02.24W	8804
1344	UKO	Sep 29	NL/Vlieland	53.28	04.43E	7901
			NL/Texel	53.10	04.27E	7904
1473	UKO	Oct 8	Norway/Oslo	59.53	10.53E	5603
			Norway/Ostervallskog	59.39	11.39E	5601

Table C-4 (contd)

REV	STA	DATE	LOCATION	LAT	LON	ARCH
1473 (contd)			Norway/Oslo Fjord	59.36	10.31E	5606
			Norway/Sarpsborg	59.22	11.16E	5604
			Norway/Horten	59.21	10.12E	6503
			Norway/Fredrikstad	59.07	10.56E	6501
			Norway/Porsgrun	59.04	09.50E	6506
			Norway/Oslo Fjord	58.50	10.35E	6504
			Norway/Kragerø	58.48	09.31E	5703
			N. Skagerrak	58.34	10.15E	5701
			Norway/Arendal	58.31	09.09E	5706
			N. Skagerrak	58.18	09.54E	5704
			S. Skagerrak	57.43	08.12E	5803
			S. Skagerrak	57.30	08.56E	5801
			S. Skagerrak	57.25	07.52E	5806
			Denmark/Lild Strand	57.13	08.36E	5804
			North Sea	51.28	2.05E	4903**
			Oostende	51.17	2.44E	4901**
			Calais	51.10	1.50E	4906**
			Dunkerque	50.59	2.28E	4904**
			France/Dieppe	49.52	00.46E	9203
			France/St. Saëns	49.41	01.23E	9201
			France/Seine	49.33	00.31E	9206
			France/Rouen	49.23	01.09E	9204
			France/Le Havre	49.19	00.20E	9103
			France/Elboeuf	49.08	00.57E	9101
			France/Lisieux	49.00	00.05E	9106
			France/Eure	48.50	00.43E	9104
1493	UKO	Oct 9	Frankfurt/Worms	49.38	8.19E	4401**
			Frankfurt/Darmstadt	49.49	8.56E	4403**
			Frankfurt/Wiesbaden	49.56	8.04E	4404**
			Frankfurt/Mainz	50.02	8.24E	4405
			Frankfurt/Frankfurt	50.07	8.42E	4406
			Frankfurt/Frankfurt	50.07	8.42E	4416**
			Koenigswinter	50.39	7.30E	803
			Siegen	50.50	8.05E	801
			Olpe	51.06	7.54E	802
			Holland/O. Flevoland	52.33	5.47E	1202
			Holland/Zwolle	52.41	6.08E	1203
			Holland/Meppel	52.46	6.28E	1201
			Holland/Ijsselmeer	52.52	5.30E	1204
			Holland/Heerenveen	52.56	5.54E	1205
			Holland/Drachten	53.04	6.11E	1206
			Holland/Alsluitdijk	53.06	5.18E	1801
			Holland/W. Leeuwarden	53.12	5.39E	1802
			Holland/E. Leeuwarden	53.18	5.58E	1803**
			Holland/Terschelling	53.23	5.01E	1804**
			Holland/Ameland	53.35	5.41E	1806**
1502	UKO	Oct 10	Norway/Frohavet	64.09	09.04E	5103
			Norway/Frohavet	63.53	09.53E	5101
			Norway/Frøya	63.52	08.39E	5106
			Norway/Orland	63.38	09.24E	5104

Table C-4 (contd)

REV	STA	DATE	LOCATION	LAT	LON	ARCH
1502 (contd)			England/Carlisle	54.59	03.05W	5003
			England/Alston	54.46	02.25W	5001
			England/Workington	54.40	03.20W	5006
			England/Ullswater	54.29	02.42W	5004
			UK/River Esk	54.22	03.38W	5903
			UK/Morecambe Bay	54.10	02.57W	5901
			Irish Sea	54.04	03.55W	5906
			UK/Blackpool	53.52	03.15W	5904
			Irish Sea	53.48	04.10W	6003
			UK/Liverpool Bay	53.36	03.30W	6001
			UK/N. Anglesey	53.31	04.26W	6006
			UK/Conway Bay	53.19	03.46W	6004

C.4 Distribution of Seasat SAR Processed Data

Public sale and distribution of all Seasat SAR data processed by the Jet Propulsion Laboratory (Tables C-1 and C-3) are being handled by the Environmental Data and Information Service (EDIS) of the National Oceanic and Atmospheric Administration. SAR imagery is available in the form of photographic prints, negatives, transparencies, and computer-compatible tapes (9 tracks, 1600 bits/inch for digitally processed imagery only). Additionally, individuals may order a SAR image, digitally processed by JPL, of any area along a swath by contacting:

Environmental Data and Information Service
National Climatic Center
Satellite Data Services Division
World Weather Building, Room 100
Washington, D C. 20233
Phone: (301) 763-8111

Seasat SAR data received at Oakhanger, United Kingdom, have been processed also in Europe (Tables C-1 and C-4), and can be obtained through the European Space Agency at the following address:

ESRIN – Earthnet Programme Office
Via Galileo Galilei
00044 Frascati
Italy

C – 3

References

Active Microwave Workshop Report, 1975, R. E. Matthews, ed., NASA SP-376, National Aeronautics and Space Administration, Washington, D.C.

Alpers, W. R., and C. L. Rufenach, 1979, "The Effects of Orbital Motions on Synthetic Aperture Radar Imagery of Ocean Waves," *IEEE Trans. Antennas and Propagation*, Vol. AP-27, pp. 685-690.

Apel, J. R., 1981, "Nonlinear Features of Internal Waves as Derived from the Seasat Imaging Radar," in *Oceanography from Space*, J. F. R. Gower, ed., Plenum, New York, N.Y., 978 pp.

Apel, J. R., H. M. Byrne, J. R. Proni, and R. L. Charnell, 1975, "Observations of Oceanic Internal and Surface Waves from the Earth Resources Technology Satellite," *J. Geophys. Res.*, Vol. 80, pp. 865-881.

Batchelor, G. K., 1967, *An Introduction to Fluid Dynamics*, Cambridge University Press, New York, N.Y., 615 pp.

Beal, R. C., 1980, "Spaceborne Imaging Radar: Monitoring of Ocean Waves," *Science*, Vol. 208, pp. 1373-1375.

Beal, R. C., 1981, "Spatial Evolution of Ocean Wave Spectra," in *Spaceborne Synthetic Aperture Radar for Oceanography*, R. C. Beal, P. S. DeLeonibus, and I. Katz, eds., Johns Hopkins University Press, Baltimore, Md. 215 pp.

Beal, R. C., P. S. DeLeonibus, and I. Katz, eds., 1981, *Spaceborne Synthetic Aperture Radar for Oceanography*, Johns Hopkins Univ. Press, Baltimore, Md. 215 pp.

Behringer, D. W., R. L. Molinari, and J. F. Festa, 1977, "The Variability of Anticyclonic Current Patterns in the Gulf of Mexico," *J. Geophys. Res.*, Vol. 82, pp. 5469-5476.

Bernstein, R. L., L. Breaker, and R. Whritner, 1977, "California Current Eddy Formation: Ship, Air, and Satellite Results," *Science*, Vol. 195, pp. 353-359.

Bina, R. T., and E. R. Ombac, 1979, "Effects of Tidal Fluctuations on the Spectral Patterns of Landsat Coral Reef Images," *Proc. 13th International Symp. on Remote Sensing of Environment*, Vol. 3, pp. 1293-1308, Environmental Research Institute of Michigan, Ann Arbor, Mich.

Brooks, D. A., and J. M. Bane, Jr., 1978, "Gulf Stream Defection by a Bottom Feature off Charleston, South Carolina," *Science*, Vol. 201, pp. 1225-1226.

Brown, W. E., Jr., C. Elachi, and T. W. Thompson, 1976, "Radar Imaging of Ocean Surface Patterns," *J. Geophys. Res.*, Vol. 81, pp. 2657-2667.

Campbell, W. J., R. O. Ramseier, H. J. Zwally, and P. Gloersen, 1980, "Arctic Sea-Ice Variations from Time-Lapse Passive Microwave Imagery," *Boundary-Layer Meteorology*, Vol. 18, pp. 99-106.

Campbell, W. J., J. Wayenberg, J. B. Ramseyer, R. O. Ramseier, M. R. Vant, R. Weaver, A. Redmond, L. Arsenault, P. Gloersen, H. J. Zwally, T. T. Wilheit, T. C. Chang, D. Hall, L. Gray, D. C. Meeks, M. L. Bryan, F. T. Barath, C. Elachi, F. Leberl, and T. Farr, 1978, "Microwave Remote Sensing of Sea Ice in the AIDJEX Main Experiment," *Boundary-Layer Meteorology*, Vol. 13, pp. 309–337.

Cardone, V. J., D. B. Ross, and M. Ahrens, 1977, "An Experiment in Forecasting Hurricane-Generated Sea States," *Proc. 11th Tech. Conf. on Hurricanes and Tropical Meteorology*, pp. 688–695, American Meteorological Society, Boston, Mass.

Carlson, R. J., 1980, *User's Guide for the Satellite Mission Design Program (SAMDP 4.0)*, Engineering Memorandum No. 312/80-106, Jet Propulsion Laboratory, Pasadena, Calif. (JPL Internal document).

Cheney, R. E., 1981, "A Search for Cold Water Rings," in *Spaceborne Synthetic Aperture Radar for Oceanography*, R. C. Beal, P. S. DeLeonibus, and I. Katz, eds., Johns Hopkins University Press, Baltimore, Md. 215 pp.

Cheney, R. E., P. L. Richardson, and B. P. Blumenthal, 1980, "Air Deployment of Satellite-Tracked Drifters," *J. Geophys. Res.*, Vol. 85, pp. 2773–2778.

Clarke, R. A., H. Hill, R. F. Reiniger, and B. A. Warren, 1980, "Current System South and East of the Grand Banks of Newfoundland," *J. Phys. Oceanogr.*, Vol. 10, pp. 25–65.

Curlander, J. C., and W. E. Brown, Jr., 1981, "A Pixel Location Algorithm for Spaceborne SAR Imagery," *Proc. 1981 International Geoscience and Remote Sensing Symposium*, Washington, D.C., pp. 843–850, IEEE Geoscience and Remote Sensing Society, Piscataway, N.J.

Curtin, T. B., and C. N. K. Mooers, 1975, "Observation and Interpretation of a High-Frequency Internal Wave Packet and Surface Slick Pattern," *J. Geophys. Res.*, Vol. 80, pp. 882–894.

deLoor, G. P., and H. W. Brunsveld Van Hulten, 1978, "Microwave Measurements Over the North Sea," *Boundary-Layer Meteorology*, Vol. 13, pp. 119–131.

Egan, W. C., 1980, "Optical Remote Sensing of the Sea — A Caribbean Example," *Proc. of 14th International Symp. on Remote Sensing of Environment*, Vol. I, pp. 563–586, Environmental Research Institute of Michigan, Ann Arbor, Mich.

Elachi, C., and J. R. Apel, 1976, "Internal Wave Observations Made with an Airborne Synthetic Aperture Imaging Radar," *Geophys. Res. Lett.*, Vol. 3, pp. 647–650.

Elachi, C., and W. E. Brown, Jr., 1977, "Models of Radar Imaging of the Ocean Surface Waves," *IEEE Trans. Antennas and Propagation*, Vol. AP-25, pp. 84–95.

Elachi, C., T. W. Thompson, and D. King, 1977, "Ocean Wave Patterns Under Hurricane Gloria: Observation with an Airborne Synthetic Aperture Radar," *Science*, Vol. 198, pp. 609-610.

Environmental Atlas of the Tongue of the Ocean, Bahamas, 1967, Report SP 24, U.S. Naval Oceanographic Office, Washington, D.C.

Estes, J. E., M. Wilson, and E. Hajic, 1980, *Analysis of Seasat-A SAR Data for the Detection of Oil on the Ocean Surface*, University of California, Santa Barbara, Calif., 99 pp.

Ewing, G., 1950, "Slicks, Surface Films and Internal Waves," *J. Mar. Res.*, Vol. 9, pp. 161-187.

Fisher, A., Jr., 1972, "Entrainment of Shelf Water by the Gulf Stream Northeast of Cape Hatteras," *J. Geophys. Res.*, Vol. 77, pp. 3248-3255.

Fisher, R. L., G. A. Rusnak, and F. P. Shepard, 1964, "Submarine Topography of the Gulf of California," in *Symposium on Marine Geology of Gulf of California*, American Association of Petroleum Geologists, Tulsa, Okla.

Fofonoff, N. P., 1980, "The Gulf Stream System," in *Evolution of Physical Oceanography*, B. Warren and C. Wunsch, eds., MIT Press, Massachusetts Institute of Technology, Cambridge, Mass., 623 pp.

Ford, J. P., R. G. Blom, M. L. Bryan, M. I. Daily, T. H. Dixon, C. Elachi, and E. C. Xenos, 1980, *Seasat Views North America, The Caribbean, and Western Europe with Imaging Radar*, Publication 80-67, Jet Propulsion Laboratory, Pasadena, Calif., 141 pp.

Ford, W. L., J. R. Longard, and R. E. Banks, 1952, "On the Nature, Occurrence and Origin of Cold Low Salinity Water Along the Edge of the Gulf Stream," *J. Mar. Res.*, Vol. 11, pp. 281-293.

Fu, L-L, 1981, "Observations and Models of Inertial Waves in the Deep Ocean," *Rev. Geophys. Space Phys.*, Vol. 19, pp. 141-170.

Gargett, A. E., 1976, "Generation of Internal Waves in the Strait of Georgia, British Columbia," *Deep-Sea Res.*, Vol. 23, pp. 17-32.

Gargett, A. E., and B. A. Hughes, 1972, "On the Interaction of Surface and Internal Waves," *J. Fluid Mech.*, Vol. 52, pp. 179-191.

Gloersen, P., H. J. Zwally, A. T. C. Chang. D. K. Hall, W. J. Campbell, and R. O. Ramseier, 1978, "Time-Dependence of Sea-Ice Concentration and Multiyear Ice Fraction in the Arctic Basin," *Boundary-Layer Meteorology*, Vol. 13, pp. 339-359.

Gonzalez, F. I., R. C. Beal, W. E. Brown, P. S. DeLeonibus, J. W. Sherman III, J. F. Gower, D. Lichy, D. B. Ross, C. L. Rufenach, and R. A. Schuchman, 1979, "Seasat Synthetic Aperture Radar: Ocean Wave Detection Capabilities," *Science*, Vol. 204, pp. 1418-1421.

Gonzalez, F. I., C. L. Rufenach, and R. A. Shuchman, 1981a, "Ocean Surface Current Detection by Synthetic Aperture Radar," in *Oceanography from Space*, J. F. R. Gower, ed., Plenum, New York, N.Y., 978 pp.

Gonzalez, F. I., T. W. Thompson, W. E. Brown, Jr., and D. E. Weissman, 1981b, "Seasat Wind and Wave Observations of Northeast Pacific Tropical Storm IVA, 1978," to be published.

Goodman, J. W., 1968, *Introduction to Fourier Optics*, McGraw-Hill, New York, N.Y.

Gower, J. F. R., and B. A. Hughes, 1979, "Radar and Ship Observations of Coastal Sea Surface Roughness Patterns in the Gulf of Georgia," *Proc. of the 13th International Symp. on Remote Sensing of Environment*, Vol. 1, pp. 103–115, Environmental Research Institute of Michigan, Ann Arbor, Mich.

gulfstream, 1978, "Gulf Stream Position," Vol. IV, No. 8, p. 2, National Oceanic and Atmospheric Administration, Washington, D.C.

Gunther, E. B., 1979, "Eastern North Pacific Tropical Cyclones, 1978," *Mariners Weather Log*, Vol. 23, pp. 152–165, National Oceanic and Atmospheric Administration, Washington, D.C.

Hansen, D. V., 1970, "Gulf Stream Meanders Between Cape Hatteras and the Grand Banks," *Deep-Sea Res.*, Vol. 17, pp. 495–511.

Harger, R. O., 1970, *Synthetic Aperture Radar Systems*, Academic Press, New York, N.Y.

Haury, L. R., M. G. Briscoe, and M. H. Orr, 1979, "Tidally Generated Internal Wave Packets in Massachusetts Bay," *Nature*, Vol. 278, pp. 312–317.

Hayes, R. M., 1981, "Detection of the Gulf Stream," in *Spaceborne Synthetic Aperture Radar for Oceanography*, R. C. Beal, P. S. DeLeonibus, and I. Katz, eds., Johns Hopkins University Press, Baltimore, Md. 215 pp.

Hickey, B. M., 1979, "The California Current System — Hypotheses and Facts," *Progress in Oceanography*, Vol. 8, pp. 191–279.

Hovanessian, S. A., 1980, *Introduction to Synthetic Array and Imaging Radars*, Artech House, Inc., Dedham, Mass., 156 pp.

Hovis, W. A., D. K. Clark, F. Anderson, R. W. Austin, W. H. Wilson, E. T. Baker, D. Ball, H. R. Gordon, J. L. Mueller, S. Z. El-Sayed, B. Sturm, R. C. Wrigley, and C. S. Yentsch, 1980, "Nimbus-7 Coastal Zone Color Scanner: System Description and Initial Imagery," *Science*, Vol. 210, pp. 60–63.

Hughes, B. A., 1976, "On the Interaction of Surface and Internal Gravity Waves: Uniformly Valid Solution by Extended Stationary Phase," *J. Fluid Mech.*, Vol. 74, pp. 667–683.

Hughes, B. A., 1978, "The Effect of Internal Waves on Surface Wind Waves: 2. Theoretical Analysis," *J. Geophys. Res.*, Vol. 83, pp. 455-465.

Hughes, B. A., and H. L. Grant, 1978, "The Effect of Internal Waves on Surface Wind Waves: 1. Experimental Measurements," *J. Geophys. Res.*, Vol. 83, pp. 443-454.

Huhnerfuss, H., and W. D. Garrett, 1981, "Experimental Sea Slicks: Their Practical Applications and Utilization for Basic Studies of Air-Sea Interactions," *J. Geophys. Res.*, Vol. 86, pp. 439-447.

Huneycutt, B. L., T. J. Bicknell, B. M. Holt, and C. Wu, 1981, *User's Manual for Existing EDIS Data from the SEASAT Synthetic Aperture Radar*, Jet Propulsion Laboratory, Pasadena, Calif. (in preparation).

IEEE J. of Oceanic Eng., 1980, Vol. OE-5.

Jain, A., 1978, "Focusing Effects in the Synthetic Aperture Radar Imaging of Ocean Waves," *Applied Physics*, Vol. 15, pp. 323-333.

Jones, W. L., V. E. Delnore, and E. M. Bracalente, 1981, "The Study of Mesoscale Ocean Winds," in *Spaceborne Synthetic Aperture Radar for Oceanography*, R. C. Beal, P. S. DeLeonibus, and I. Katz, eds., Johns Hopkins University Press, Baltimore, Md. 215 pp.

Jordan, R. L., 1980, "The Seasat-A Synthetic-Aperture Radar System," *IEEE J. of Oceanic Eng.*, Vol. OE-5, pp. 154-164.

Kasischke, E. S., R. A. Shuchman, and J. D. Lyden, 1980, *Detection of Bathymetric Features Using Seasat Synthetic Aperture Radar — A Feasibility Study*, Final Report 135900-2-F, Environmental Research Institute of Michigan, Ann Arbor, Mich.

King, D. B., and O. H. Shemdin, 1978, "Radar Observations of Hurrican Wave Directions," *Proc. 16th Coastal Engineering Conf.*, ASCE/Hamburg, West Germany, pp. 209-226.

Klose, J. C., 1979, *Seasat Node Tables and Osculating Orbital Elements*, Report 622-215, Jet Propulsion Laboratory, Pasadena, Calif. (JPL internal document).

Kuettner, J. P., 1971, "Cloud Bands in the Earth's Atmosphere: Observations and Theory," *Tellus*, Vol. 23, pp. 404-425.

Kupferman, S. L., and N. Garfield, 1977, "Transport of Low-Salinity Water at the Slope Water — Gulf Stream Boundary," *J. Geophys. Res.*, Vol. 82, pp. 3481-3486.

LaFond, E. C., 1962, "Internal Waves, Part 1", in *The Sea*, Vol. 1, pp. 731-751, Interscience, New York, N.Y.

Lai, D. Y., and P. L. Richardson, 1977, "Distribution and Movement of Gulf Stream Rings," *J. Phys. Oceanogr.*, Vol. 7, pp. 670-683.

LaViolette, P. E., S. Petherych, and J. F. R. Gower, 1980, "Oceangraphic Implications of Features in NOAA Satellite Visible Imagery," *Boundary-Layer Meteorology*, Vol. 18, pp. 159-175.

Leberl, F., M. L. Bryan, C. Elachi, and T. Farr, 1979, "Mapping of Sea Ice and Measurement of Its Drift Using Aircraft Synthetic Aperture Radar Images," *J. Geophys. Res.*, Vol. 84, pp. 1827-1835.

LeBlond, P.H., T.R. Osborn, D.O. Hodgins, R. Goodman, and M. Metge, 1981, "Surface Circulation in the Western Labrador Sea," *Deep-Sea Res.*, Vol. 28 A, 683-693.

Lee, C.Y., and R.C. Beardsley, 1974, "The Generation of Long Nonlinear Internal Waves in a Weakly Stratified Shear Flow," *J. Geophys. Res.*, Vol.79, 453-462.

Lee, T.N., 1977, "Coastal Currents Along the Southern Shore of Grand Bahama Island," *Bulletin of Marine Science*, Vol. 27, pp. 802-820.

Legeckis, R.V., 1978, "A Survey of Worldwide Sea Surface Temperature Fronts Detected by Environmental Satellites," *J. Geophys. Res.*, Vol. 83, pp. 4501-4522.

Legeckis, R. V., 1979, "Satellite Observations of the Influence of Bottom Topography on the Seaward Deflection of the Gulf Stream off Charleston, South Carolina," *J. Phys. Oceanogr.*, Vol. 9, 483-497.

Leipper, D.F., 1970, "A Sequence of Current Patterns in the Gulf of Mexico," *J. Geophys. Res.*, Vol. 75, pp. 637-657.

LeMone, M.A., 1973, "The Structure and Dynamics of Horizontal Roll Vortices in the Planetary Boundary Layer," *J. Atmos. Sci.*, Vol. 30, pp. 1077-1091.

Lichy, D.E., M.G. Mattie, and L.J. Mancini, 1981, "Tracking of a Warm Water Ring," in *Spaceborne Synthetic Aperture Radar for Oceanography*, R.C. Beal, P.S. DeLeonibus, and I. Katz, eds., Johns Hopkins University Press, Baltimore, Md. 215 pp.

Lighthill, J., 1978, *Waves in Fluids*, Cambridge University Press, New York, N.Y., 504 pp.

Lohmann, P., and H. van der Piepen, 1981, "Evaluation of Ocean Bottom Features from Ocean Color Scanner Imagery," *Photogrammetria*, Vol. 36, pp. 81-89.

Lyzenga, D.R., 1981, "Remote Sensing of Bottom Reflectance and Water Attenuation Parameters in Shallow Water Using Aircraft and Landsat Data," *Int. J. Remote Sensing*, Vol. 2, pp. 71-82.

Mann, C.R., 1967, "The Termination of the Gulf Stream and the Beginning of the North Atlantic Current," *Deep-Sea Res.*, Vol. 14, pp. 337-359.

Martin, S., 1981, "Frazil Ice in Rivers and Oceans," *Annual Review of Fluid Mechanics*, Vol. 13, pp. 379-397.

Martin, S., and P. Kauffman, 1981, "A Field and Laboratory Study of Wave Damping by Grease Ice," *J. Glaciology*, Vol. 27, pp. 283-313.

Maul, G. A., 1977, "The Annual Cycle of the Gulf Loop Current Part I: Observations During a One-Year Time Series," *J. Mar. Res.*, Vol. 35, pp. 29-47.

Maxworthy, T., 1979, "A Note on the Internal Solitary Waves Produced by Tidal Flow Over a Three-Dimensional Ridge," *J. Geophys., Res.*, Vol. 84, pp. 338-345.

McCartney, M. S., L. V. Worthington, and W. J. Schmitz, Jr., 1978, "Large Cyclonic Rings From the Northeast Sargasso Sea," *J. Geophys. Res.*, Vol. 83, p. 901-914.

Molinari, R. L., 1976, "The Formation of the Yucatan Current Based on Observations of Summer 1971," *J. Phys. Oceanogr.*, Vol. 6, pp. 596-602.

Molinari, R. L., M. Spillane, I. Brooks, D. Atwood, and C. Duckett, 1981, "Surface Currents in the Caribbean Sea as Deduced From Lagrangian Observations," *J. Geophys. Res.*, Vol. 86, pp. 6537-6542.

Mollo-Christensen, E., 1981, "Surface Signs of Internal Ocean Dynamics," in *Spaceborne Synthetic Aperture Radar for Oceanography*, R. C. Beal, P. S. DeLeonibus, and I. Katz, eds., Johns Hopkins University Press, Baltimore, Md., 215 pp.

Mollo-Christensen, E., and A. Mascarenhas, Jr., 1979, "Heat Storage in the Oceanic Upper Mixed Layer Inferred From Landsat Data," *Science*, Vol. 203, pp. 653-654.

Moskowitz, L. I., 1973, "The Feasibility of Ocean Current Mapping Via Synthetic Aperture Radar Methods," *Proc. Amer. Soc. of Photogrammetry*, Part II, pp. 760-771.

Mountain, D. G., and J. L. Shuhy, 1980, "Circulation Near the Newfoundland Ridge," *J. Mar. Res.*, Vol. 38, pp. 205-213.

Onstott, R. G., G. J. Dome, C. V. Delker, J. S. Patel, and R. K. Moore, 1980, *Radar Backscatter Study of Sea Ice*, Technical Report RSL-TR-331-14, University of Kansas/Remote Sensing Laboratory, Lawrence, Kansas.

Osborne, A. R., and T. L. Burch, 1980, "Internal Solitons in the Andaman Sea," *Science*, Vol. 208, pp. 451-460.

Page, D. F., and R. O. Ramseier, 1975, "Application of Radar Techniques to Ice and Snow Studies," *J. Glaciology*, Vol. 15, No. 73, pp. 171-191.

Phillips, O.M., 1977, *The Dynamics of the Upper Ocean*, Second Edition, Cambridge University Press, New York, N.Y., 336 pp.

Phillips, O. M., 1981, "The Structure of Short Gravity Waves On the Ocean Surface," in *Spaceborne Synthetic Aperture Radar for Oceangraphy*, R. C. Beal, P. S. DeLeonibus, and I. Katz, eds., Johns Hopkins University Press, Baltimore, Md., 215 pp.

Pollard, R. T., 1978, "GARP Topics, the Joint Air-Sea Interaction Experiment — JASIN 1978," *Bull. Amer. Meteor. Soc.*, Vol. 59, pp. 1310-1318.

Richardson, P. L., R. E. Cheney, and L. A. Mantini, 1977, "Tracking of a Gulf Stream Ring With a Free Drifting Surface Buoy," *J. Phys. Oceanogr.*, Vol. 7, pp. 580-590.

Rihaczek, A. W., 1977, *Principles of High-Resolution Radar*, Mark Resources, Marina Del Rey, Calif.

Robinson, M. K., 1976, *Atlas of North Pacific Ocean Monthly Mean Temperatures and Mean Salinities of the Surface Layer*, NOORP-2, Naval Oceanographic Office, Washington, D.C., 194 pp.

Rodahl, K., 1954, "Ice Islands in the Arctic," *Scientific American*, Vol. 191, pp. 41-45.

Roden, G. I., 1975, "On North Pacific Temperature, Salinity, Sound Velocity and Density Fronts and Their Relation to the Wind and Energy Flux Fields," *J. Phys. Oceanogr.*, Vol. 5, pp. 557-571.

Ross, D. B., 1981, "The Wind Speed Dependency of Ocean Microwave Backscatter," in *Spaceborne Synthetic Aperture Radar for Oceanography*, R. C. Beal, P. S. DeLeonibus, and I. Katz, eds., Johns Hopkins University Press, Baltimore, Md., 215 pp.

Ross, D. B., and V. J. Cardone, 1978, "A Comparison of Parametric and Spectral Hurricane Wave Prediction Products," in *Turbulent Fluxes Through the Sea Surface, Wave Dynamics, and Prediction*, A. Favre and K. Hasselmann, eds., Plenum Press, New York, N.Y.

Saunders, P. M., 1971, "Anticyclonic Eddies Formed From Shoreward Meanders of the Gulf Stream," *Deep-Sea Res.*, Vol. 18, pp. 1207-1219.

Science, 1979, Vol. 204, pp. 1405-1424.

Seasat Gulf of Alaska Workshop II Report, 1980, Barrick, D. E., J. C. Wilkerson, P. M. Woiceshyn, G. H. Born, and D. B. Lame, eds., Report 622-107, Jet Propulsion Laboratory, Pasadena, Calif. (JPL internal document).

Shand, J. A., 1953, "Internal Waves in the Georgia Strait," *Trans. Amer. Geophys. Union*, Vol. 34, pp. 849-856.

Shemdin, O. H., W. E. Brown, Jr., F. G. Staudhammer, R. Shuchman, R. Rawson, J. Zelenka, D. B. Ross, W. McLeish, and R. A. Berles, 1978, "Comparison of in Situ and Remotely Sensed Ocean Waves off Marineland, Florida," *Boundary-Layer Meterology*, Vol. 13, pp. 193-202.

Shuchman, R. A., and E. S. Kasischke, 1979, "The Detection of Oceanic Bottom Topographic Features Using Seasat Synthetic Aperture Radar Imagery," *Proceedings of the 13th International Symposium on Remote Sensing of Environment*, Vol. 3, pp. 1277–1292, Environmental Research Institute of Michigan, Ann Arbor, Mich.

Shuchman, R. A., and E. S. Kasischke, 1981, "Refraction of Coastal Ocean Waves," in *Spaceborne Synthetic Aperture Radar for Oceanography*, R. C. Beal, P. S. DeLeonibus, and I. Katz, eds., Johns Hopkins University Press, Baltimore, Md., 215 pp.

Smith, N. P., 1980a, "Temporal and Spatial Variability in Longshore Motion Along the Texas Gulf Coast," *J. Geophys. Res.*, Vol. 85, pp. 1531–1536.

Smith, N. P., 1980b, "On the Hydrography of Shelf Waters off the Central Texas Gulf Coast," *J. Phys. Oceanogr.*, Vol. 10, pp. 806–813.

Stommel, H., 1965, *The Gulf Stream*, Second Edition, University of California Press, Berkeley, Calif., 248 pp.

Sverdrup, H. U., M. W. Johnson, and R. H. Fleming, 1942, *The Oceans*, Prentice-Hall, Englewood Cliffs, N. J., 1087 pp.

Teleki, P. G., W. J. Campbell, R. O. Ramseier, and D. Ross, 1979, "The Offshore Environment: A Perspective From Seasat-1 SAR Data," *Proc. 11th Annual Offshore Technology Conference*, Houston, Texas, pp. 215–220.

The Ring Group, 1981, "Gulf Stream Cold-Core Rings: Their Physics, Chemistry, and Biology," *Science*, Vol. 212, pp. 1091–1100.

Tidal Current Tables, 1978, *Atlantic Coast of North America*, National Oceanic and Atmospheric Administration, National Ocean Survey, Rockville, Md.

Tomiyasu, K., 1978, "Tutorial Review of Synthetic-Aperture Radar (SAR) With Applications to Imaging the Ocean Surface," *Proceedings of the IEEE*, Vol. 66, pp. 563–583.

Uchupi, E., 1971, *Bathymetric Atlas of the Atlantic, Caribbean and Gulf of Mexico*, Report 71-72, Woods Hole Oceanographic Institution, Woods Hole, Mass.

Valenzuela, G.R., 1978, "Theories for the Interaction of Electromagnetic and Oceanic Waves — A Review," *Boundary-Layer Meteorology*, Vol. 13, pp. 61–85.

Vesecky, J. F., H. M. Assal, and R. H. Stewart, 1981, "Remote Sensing of the Ocean Waveheight Spectrum Using Synthetic-Aperture-Radar Images," in *Oceanography from Space*, J. F. R. Gower, ed., Plenum, New York, N.Y., 978 pp.

Vesecky, J. F., and R. H. Stewart, 1981, "The Observation of Ocean Surface Phenomena Using Imagery From the Seasat Synthetic Aperture Radar — An Assessment," submitted to *J. Geophys. Res.*

Wadhams, P., 1973, "Attenuation of Swell by Sea Ice," *J. Geophys. Res.*, Vol. 78, pp. 3552-3563.

Wadhams, P., 1978, "Wave Decay in the Marginal Ice Zone Measured From a Submarine," *Deep-Sea Res.*, Vol. 25, pp. 23-40.

Wadhams, P., 1980, "Ice Characteristics in the Seasonal Sea Ice Zone," *Cold Regions Science and Technology*, Vol. 2, pp. 37-87.

Weissman, D. E., T. W. Thompson, and R. Legeckis, 1980, "Modulation of Sea Surface Radar Cross Section by Surface Stress: Wind Speed and Temperature Effects Across the Gulf Stream," *J. Geophys. Res.*, Vol. 85, pp. 5032-5042.

Williams, R. S., and W. D. Carter, eds., 1976, *ERTS-1, A New Window on Our Planet*, Geological Survey Professional Paper 29, U.S. Government Printing Office, No. 024-001-02757-7, Washington, D.C., 362 pp.

Woodcock, A., 1941, "Soaring Over the Open Sea," *The Scientific Monthly*, Vol. 25, pp. 226-232.

Wu, C., 1980, "A Digital Fast Correlation Approach to Produce Seasat SAR Imagery," in *Proceedings of IEEE 1980 International Radar Conference*, Arlington, Va., pp. 153-160, IEEE Aerospace and Electronic System Society.

Wu, C., B. Barkan, H. Huneycutt, C. Leang, and S. Pang, 1981, *An Introduction to the Interim Digital SAR Processor and the Characteristics of the Associated Seasat SAR Imagery*, Publication 81-26, Jet Propulsion Laboratory, Pasadena, Calif.

Wyrtki, K., L. Magaard, and J. Hager, 1976, "Eddy Energy in the Oceans," *J. Geophys. Res.*, Vol. 81, pp. 2641-2646.